Microwave Dielectric Heating Through Interference Modulation with Narrow Band High Power Sources

Ingolf Meier

Dissertation presented for the Degree of Doctor of Philosophy
in Engineering at the University of Stellenbosch

Supervisor/Promoter: Professor Dr J.B. de Swardt

Date: 7 August, 2002

Declaration

I, the undersigned, hereby declare that work contained in this dissertation is my own original work and that I have not previously in its entirety or in part submitted it at any university for a degree.

Signed: Date:

Abstract

One of the most difficult problems in microwave dielectric heating is the generation and control of field and heating patterns. A technique allowing the synthesis of different, pre-determinable heating patterns by interference modulation is proposed.

The proposed concept may be described by the term 'interference modulation'. Interference modulation is a technique which enables particular patterns, called features, to be obtained by signals from several sources interfering with each other. The relative phases of the signals are modulated, by which process known features may be selected. Weights are assigned to these features, which may be combined over time to form a new heating pattern. Phase changes may then be used to switch to specific, known features, with weights which will determine the contribution of each feature to the desired overall pattern.

In the practical implementation described, magnetron tubes are the sources. Each of these narrow-band high-power sources was injection locked to a low power control signal. The control signals are derived from a reference source and their phase is set to select a corresponding feature.

Calculation and measurement showed that reliable locking occurs with a control signal power of at least 3% of the magnetron's emitted power.
Measurements of patterns were carried out with materials formed into sheets and blocks. Some were chemically prepared to reveal the overall heating pattern. The observed patters, simulations and field measurements concur, thus validating the concept and operation of the proposed topology.

Opsomming

Een van die moeilikste probleme in mikrogolf diëlektriese verhitting is die opwekking en beheer van veld- en verhittingspatrone. 'n Tegniek wat voorsiening maak vir die sintese van verskillende, voorafbepaalde verhittingspatrone deur interferensie word hier voorgestel.

Die voorgestelde beginsel kan beskryf word deur die term "interferensie modulasie". Interferensie modulasie is 'n tegniek wat spesifieke patrone, genoem kenmerke, moontlik maak deur seine van verskillende bronne met mekaar te laat interfereer. Bekende kenmerke kan geselekteer word deur die relatiewe fases van die seine te moduleer. Gewigte word aan hierdie kenmerke toegeken wat oor tyd gekombineer kan word om nuwe verhittingspatrone te vorm. Faseveranderings kan dan gebruik word om na 'n spesifieke, bekende kenmerk te skakel met gewigte wat die bydrae van elke kenmerk van die verlangde algehele patroon bepaal.

Magnetrons word gebruik as bronne in die praktiese implimentering wat beskryf word. Elkeen van hierdie nouband, hoë drywing bronne is injeksie-gesluit met 'n lae drywing beheersein. Die beheerseine is afgekoppel van 'n verwysingsbron en hul fases is gestel om 'n ooreenstemmende kenmerk te verkry.

Berekening en meting toon dat betroubare sluiting voorkom wanneer die beheersein ten minste 3% van die magnetron se uittree-drywing is. Metings van patrone is gemaak met materiale wat in lae en blokke gevorm is. Sommiges is met chemikalië voorberei sodat die algehele verhittingspatroon gesien kan word. Die waargeneemde patrone, simulasies en veldmetings stem goed ooreen en bevestig die beginsel en werking van die voorgestelde topologie.

Table of Contents

List of Figures

List of Symbols

α	Attenuation constant [Np/m] or phase offset [°]
β	Phase constant [rad/m] or phase offset [°]
β_c	Cut-off wave number [rad/m]
γ	Propagation constant $\alpha + j\beta$ [1/m]
Γ	Reflection coefficient
$\tan\delta_E$	Electric loss tangent
$\tan\delta_M$	Magnetic loss tangent
ε	Complex permittivity of material [C/V m]
ε_{eff}	Effective dielectric constant
ε_r	Relative permittivity
$\Theta°$	Relative phase shift [°]
λ_0	Free space wave length [m]
λ_c	Cut-off wave length [m]
λ_g	Wavelength in applicator [m]
μ	Permeability [Wb/A m] [H/m]
μ_0	Permeability of free space = 4 π 10^{-7} [H/m]
ρ	Density of matter [kg/m^3]
σ_E	Electric conductivity [A/V m]
σ_M	Magnetic conductivity [V/A m]
$\varphi(t)$	Instantaneous phase difference [rad or °]
ω_0	Natural or undisturbed resonant frequency [rad]
ω_i	Frequency of injected signal [rad]
ω_{Res}	Resonance frequency [rad]
ω_a, ω_b	Frequencies of sources A and B [rad]
a_0	Peak amplitude constant [V/m]
B	Susceptance = Im(Y), e.g. B_0 [$1/\Omega$]
BW_{Lock}	Locking bandwidth [Hz]
C	Capacitor or Capacitance [F]
c	Speed of light in free space, 299792458 m/s [m/s]
c_p	Specific heat [J/kg C°]
d_a, d_b	Delays from ports A or B. [m]
D_ϕ	Domain of phases
D_I	Domain of features
E	Electric field [V/m]
E_y	Electric field in yz-plane [V/m]
E_{ya}, E_{yb}	Electric field sources at ports A and B. [V/m]
Δf	Frequency difference [Hz]
f_0	Natural or undisturbed resonant frequency [Hz]
f_{inj}	Frequency of injected signal [Hz]

f_{Res}	Resonance frequency [Hz]
G	Conductance = Re(Y), e.g. G_0 [$1/\Omega$]
H	Voltage gain
H_0	Magnitude of magnetic field [A/m]
I(V)	Voltage dependent current source [A]
I_a	Anode current [A]
I_D	Desired intensity pattern
I_E	Dependent intensity distribution or feature variable
I_{Err}	Discrepancy between desired and obtained intensity pattern
I_{inj}	Injected current signal [A]
I_{Res}	Current into resonator [A]
J_S	Supplied electric current density [A/m^2]
L	Inductor or Inductance [H]
l	Length [m]
M_S	Supplied magnetic current density [V/m^2]
m, n	Integer values
P_D	Power dissipated or absorbed [W]
P_D	Power dissipated [W]
P_E	Power exiting or not absorbed [W]
P_{in}	Incident power [W]
P_{osc}	Power emitted by oscillator
P_{out}	Emitted power [W]
P_P	Power potential, stored as energy [W]
P_S	Power supplied [W]
Q, Q_E	Quality factor, external quality factor
R	Resistor or Resistance [Ω]
R_I	Subset or range of features
S_{av}	Average pointing vector [W/m^3]
ΔT	Change in temperature [°]
Δt_n	Time weighting factor
V	Voltage or Volume of matter [V]
V_0	Voltage at ω_0 [V]
V_{in}	Incident voltage signal [V]
V_{max}	Standing wave voltage maximum [V]
V_{min}	Standing wave voltage minimum [V]
V_{out}	Emitted voltage signal [V]
X_a, X_b	Offset relative to port A or B [m]
Y	Admittance, e.g. Y_0 [$1/\Omega$]
Y_{active}	Admittance of active part [$1/\Omega$]
Y_L	Load admittance [$1/\Omega$]
$Y_{passive}$	Admittance of passive part[$1/\Omega$]
Z(t)	Complex impedance or impulse impedance response [Ω]
Z_0	Free space wave impedance [Ω]
Z_g	Impedance of guided structure [Ω]
Z_{Res}	Impedance of resonator [Ω]
Z_{yz}	Wave impedance in yz-plane [Ω]

Notation:

$L\langle\ \rangle$, $L^{-1}\langle\ \rangle$	Laplace transform and its inverse
$*$	Linear convolution
A^*	Conjugate of A
A^T	Transpose of A
$\bullet$	Dot product
$\times$	Cross product
∇	Differential (vector) operator

Decibels, dB, are used to express power relative to one watt. Other dB derivatives in use are dBm, dBc, dBi and dBv. These are defined as follows:

dB = 10 log 10 (P [W] / 1 W)

dBm = 10 log 10 (P [W] / 1 mW)

dBc = dB value relative to (dominant) carrier

dBi = dB value relative to an isotropic radiator

dBv = 20 log 10 (V [V] / 1 V)

Chapter 1

Introduction

A technology born in the 1950s, microwave heating is now widely used in the home and industry alike [1]. Its popularity arose from the compact, efficient and fast heating solutions that it makes possible, especially in household, catering, and food processing applications. Applicator and cavity designs have, however, not kept pace, and have remained essentially unchanged and application specific.
Application specific applicators are required to ensure efficient processing of different materials, volumes and shapes. This, together with the high initial investment cost associated with microwave heating equipment [2][3], precludes the use of microwave heating in production runs that require processing of a variety of different items, each of which is likely to have its own particular characteristics and requirements which can not be satisfied by current, conventional designs. As a result industrial microwave dielectric heating is commonly confined to niche applications.
This needs to change. New applications and uses for microwave heating arise almost daily in industry and material science. These demand flexibility and precise control of the heating process. At the same time environmental concerns, energy efficiency [4] and EMC/EMI compliance [5]-[8] play an increasing role, in addition to heating requirements.

1.1 Problem statement

The distribution of microwaves in applicators is generally not uniform. This is so because they are indeed waves, and hence standing wave patterns are produced in the applicator. These result in an uneven heating distribution in the target materials.

1.1.1 Heating requirement

Appropriate heating patterns and the way they are applied to objects is important in microwave dielectric heating. For example, during the synthesis of super-conducting ceramic material, quality and yield are improved when the raw material is sintered from the inside out [9]-[12]. Sintering of conventional ceramics, on the other hand, is sensitive to thermal runaway and material cracking [13]. 'Shaped', yet controlled variable heating can be applied to produce quality products [2][9][14][15], with randomly distributed switching of the location of patterns making it possible to reduce thermal runaway.
An example from the food processing industry is the thawing of frozen foods with microwaves [15][16].
While thawing, a phase transition occurs, and with it a change in microwave material properties [16]. Even when a uniform heating field is applied, the changes in the material cause the food to be prone to overheating at edges and corners [15][17]. Special care must be taken to avoid this.
In this example, an adaptable heating profile is desirable to provide flexibility while ensuring product quality.

1.1.2 Problem

Dynamically variable and controllable microwave heating patterns are required to solve the problem described previously. Currently available microwave heating apparatuses are, however, not able to provide the flexibility required to implement this.

Instead, current methods to achieve uniformity tend to focus solely on applicator design [18]-[20], and are therefore static. This is the result of traditional design techniques which view the source as a fixed, unchangeable component of the microwave system, in which only the applicator or cavity is seen as a variable for change. The focus of current methods is hence on applicator design to achieve heating uniformity [18]-[20].

Examples of this include:

- Single and multi-mode applicators [3][17][21][22],
- Applicators with mode-stirrers [3][23][24],
- Applicators with turn-tables and conveyor belts [3][22]-[24], and
- Meandered leaky waveguides, as well as arrays of these [22][23].

Combinations of these techniques have also been used.

But conventional (magnetron based) sources are peculiar in that both their output power and frequency depend on their supply and load. Mode stirrers represent a repetitively changing load, while multi-mode applicators exhibit multiple resonant frequencies. Load and supply conditions interfere with the behaviour of the source and determine the heating profile in the applicator. Techniques based on manipulating the cavity alone, therefore, do not lead to general uniform heating (e.g. Figure 1) [22][25].

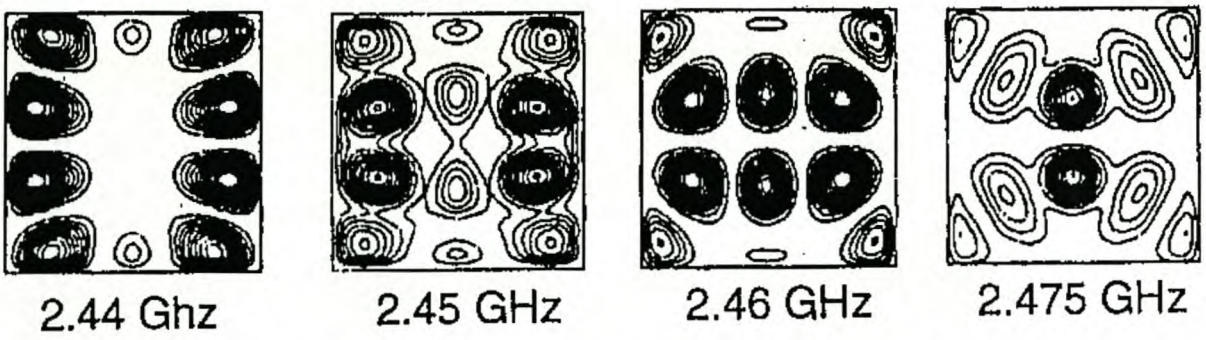

Figure 1: Heating results of a plastic block in a multi mode cavity (after [22]).

The combination of two cascaded applicators, described in [26], whose heating patterns are displaced by 90°, is tailored to the needs of a specific application only. It too is static.

The characteristics and capabilities required to produce uniform heating, and that are not present in current designs are summarised as follows:

- Power uniformity,
- Active control and change of heating patterns,

- Direct online change without structural modification, and
- Application diversity.

Lauf [19][20] came to the same conclusion and proposed a broadband microwave heating system operating from 2 to 18 GHz (Figure 2). Lauf's system solves a number of the above issues, but also introduces new ones. These include the:

- Shielding to comply with the respective regulatory requirements concerning safety and spectrum [8],
- Limitation of use to low power microwave applications [3][20],
- Design of broadband components, which is more involved and hence costly [3], and
- Increased cost of broadband sources.

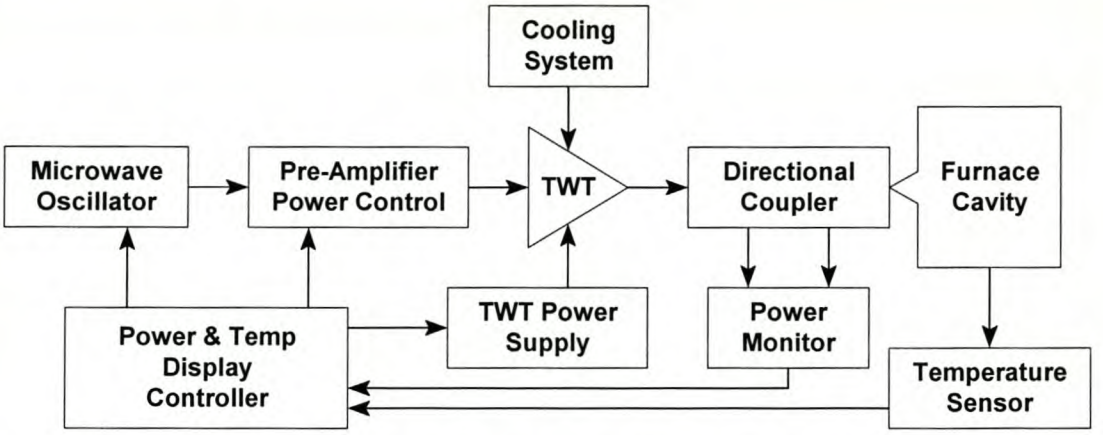

Figure 2: Broadband microwave heating system as proposed by [19][20].

A system that circumvents these issues is required, with emphasis on low cost and compliance. It should also cater for microwave heating profiles which can be adapted under diverse conditions and in variable environments.

1.1.3 Proposed solution

Signals from two or more fixed frequency narrow band magnetron based sources are interfered to produce different, distinct, interference patterns, called features [27][28]. A low-power control signal injection locks the sources to ensure frequency coherence as well as to provide phase control. The phase difference, in turn, effects and selects the features.

A subsequent synthesis technique assigns weights to appropriate features. These are averaged by the slow thermal time constant of matter, to yield smooth time averaged heating patterns.

The single frequency nature of this topology facilitates shielding and EMI compliance. Its distinct advantage is to allow use of simpler narrow band microwave components for its implementation, thus reducing overall design time and system cost. In addition, robust, narrow band magnetron tubes, which constitute one example of a source suitable for this design, are known for their high power conversion efficiencies

exceeding 70% [1][3][29]-[33], and their low cost per kW of microwave power compared to other technologies [3].
The result is a simple, resource conscious and environmentally friendly process, which caters for direct online change of heating profiles without the need for structural modifications. Furthermore, this is achieved at low cost.

1.2 Aims and contributions of dissertation

The dissertation presents an injection locked microwave-heating topology that makes use of narrow band magnetron tubes to synthesise heating patterns. Emphasis is placed on low cost, ease of manufacture and high local content.
The behaviour of matter in time varying fields and its equivalent electrical model are assumed, and not covered, to prevent distraction from the aim. A full coverage of this topic is found in references [13][17][34]-[44].

The primary contributions of this work include [18][45]-[47]:

- The development, description and application of a technique to synthesise microwave heating patterns [18][45]-[47],
- The control of features and heating patterns through injection locking of sources for microwave heating [18][45]-[47],
- The generalisation of a Rieke diagram based oscillator model [45], and
- The development and verification of a general solution to the Van der Pol equation (section 2.3 and appendix A).

Secondary contributions are:

- The derivation of known oscillator equations from the general solution to the Van der Pol equation in the time domain (appendix A),
- The design of low cost, easily manufactured, yet versatile standard microwave components for the 2.45 GHz range as technology and research enablers (appendix E),
- The standardisation, implementation and organisation of a microwave-heating infrastructure to support component design, research and manufacture (appendix E), and
- The formulation of a castable transition metal salt ($CoCl_2$, $NiCl_2$) impregnated composite for pattern visualisation (appendix D).

1.3 Brief description of contributions

In this section contributions are briefly summarised. The significance of each contribution is discussed and relevant results are outlined.

1.3.1 Pattern synthesis technique

Conventional techniques focus on applicator design only, attempting to enhance the heating uniformity. The proposed novel topology provides a different way to achieve

this. In this method heating patterns are synthesised by controlling the phase of several incident waves. Coupled with principles from image recognition theory, the synthesis of flexible and repeatable microwave field patterns becomes possible. The same hardware can thus be re-used for very different materials of varying shapes, sizes and with different dielectric properties and heating requirements. Changes of the heating characteristic can be effected, online, by change of time-weighting factors and phase. This type of topology aims at modern industrial synthesis solutions and processes. Just-in-Time production would be one such example.

1.3.2 Rieke diagram model

Closed form solutions of oscillators like the magnetron have, to date, been unsuccessful despite over half a century of research [3][48]-[60]. Numerical particle based simulations are possible [54], but are highly computationally intensive and time consuming. The information of most interest to microwave designers is impedance, frequency and power. Models that make use of polynomial approximations to measured data provide a helpful means of modeling the magnetron source.

The polynomial approximations for magnetron oscillators proposed by [61] and [62] are based more on what happens graphically on a Smith chart than on physical reasoning. Practical design, on the other hand, focuses on gain and bandwidth. In using these parameters, a gain-bandwidth dependent vector polynomial that models the admittance of oscillators is derived. It includes all effects modelled by [61] and [62], but is more general.

In practice, the low order model produced excellent interpolated and **extrapolated** results of the active region of oscillators.

1.3.3 General Van Der Pol time domain solution

Van der Pol's famous equation [63], describing the behaviour of oscillators, is exclusively used for the theoretical description of oscillatory processes in the frequency domain. A general solution to the Van der Pol equation in the time-domain is obtained. From it, equations necessary to describe injection locking are derived (appendix A).

The solution shows good prospects for inclusion into time-domain circuit simulators and the study of injection locking and oscillatory phenomena. For example, the start-up of oscillation out of noise can be predicted without assumptions, simplifications or approximations. A detailed study is, however, beyond the scope of this dissertation.

1.3.4 Time domain magnetron operational description

Current textbooks base the operational description of the magnetron on the assumption that after switch-on output at the natural resonant frequency is present. This is not the case. A time-domain description improves on this by explaining effects from start-up to steady state oscillation.

1.3.5 Pattern visualisation technique

The verification of three-dimensional electromagnetic fields obtained by simulation is a common problem in microwave dielectric heating, because measurements inside

applicators interfere with the electromagnetic fields. A different approach measures fields by passive means. Techniques that make use of fax paper and liquid crystals, both of which change colour depending on their temperature, already exist. Transition metal compounds like cobalt-chloride as the 'active' ingredient provide an alternative. These can be embedded into open-pored materials like silica gel, paper, cornstarch and flour. The impregnated items are placed into the applicator to measure the heating distributions and are evaluated afterwards. The result is a perceivable colour gradient in the case of cobalt-chloride, ranging from a light purple when moist to a deep cobalt blue when dry. The process is repeatable with the same sample.
For this technique a suitable, castable compound was formulated (appendix D).

1.4 Tools, instruments and facilities

The principal activities can be categorised into:

- Design and manufacture, and
- Measurement and characterisation.

Each required different tools and facilities.

Design was carried out using a combination of simulation and mathematical tools, together with information available in the literature. Tools in this category included:

Simulation for which finite element packages such as Maxwell Eminence®[1], Microwave Lab®[1] and HFSS®[1] were used for evaluation of possible structures prior to manufacture. Simulation catered for field visualisation that was essential to a more intuitive waveguide component design approach. Simulation tools were also necessary for pattern simulation. The software is further detailed in [64]-[66].

Mathematical Analysis tools such as MuPad®[2] and Mathematica®[3] provided symbolic analysis, while numerical packages such as Matlab®[4] and Octave[5] aided with modelling, optimisation and presentation of results.

Measurement and characterisation of components made use of:

Coaxial to waveguide transitions to connect WR340 waveguide devices to coaxial measurement facilities. These are vital components, necessary for evaluation and measurement.

Waveguide Calibration Kit consists of shorting plate, two offset shorts and a load. With this kit the Vector Network Analyser was accurately calibrated. Load match is approximately -30 dB, which is sufficient for the purpose of this investigation.

Vector Network Analyser measured the complex reflection coefficients of devices. Both the HP8753C and HP8510 were used (often in conjunction with coaxial to

---

[1] © 1999, Ansoft Corporation, USA
[2] Version 1.4.1, © 1998, The MuPAD Group, University of Paderborn, Germany
[3] Version 2.0, © 1991, Wolfram Research Inc., USA
[4] Version 5.1, © 1999, The MathWorks Inc., USA
[5] GNU Octave, Version 2.0.14, © 1999, John W. Eaton, University of Wisconsin-Madison, USA

waveguide transitions). Components could be evaluated and characterised to obtain data for modelling and simulation. Before each measurement, the correct calibration kit was loaded and the instrument calibrated for full two port measurement.

Spectrum Analyser (HP8569A) obtained magnetron spectra under various conditions of load, operation and supply.

Oscilloscope with Down-converter allowed for the capture of time-domain waveforms of magnetron and locking phenomena. A high-speed sampling oscilloscope (TDS380), together with a down-converter consisting of mixer and local oscillator, served as a sufficiently broadband platform for 2.45 GHz signals.

1.4.1 Creation of infrastructure

The development of theoretical concepts forms but one aspect of the research process. Construction of the proposed topology is the subsequent, important step necessary to prove the theory correct. Before a complete system could be built, all its components had to be designed and the infrastructure for their construction established.
Requirements for the infrastructure included:

- Standardisation of component interfaces, right down to sizes and types of bolts,
- Location of waveguide suppliers,
- Close liaison with the various workshops,
- Establishing acceptable practices for component manufacture and
- Liaison with possible external component suppliers, notably for circulators and magnetron tubes, but also to enforce compliance with the waveguide component interfaces used in industry.

From the beginning, emphasis was placed on low cost, ease of manufacture and high local content, this necessity arising from tight budgetary constraints and the high cost of imported components. The result included components such as:

- Flanges,
- Transitions,
- Calibration kit,
- Waveguide bends (E and H plane),
- Launchers,
- Slotted waveguide,
- Variable high power probe,
- Phase compensated T-piece,
- 3-Stub tuner,
- 15dB coupler and
- Double slug tuner.

All components were designed, optimised, built and tested for use in the 2450 MHz industrial, scientific and medical (ISM) band. The quality, performance, and ease of manufacture of the components with standard workshop tools prompted interest from within the research group, from other institutions (Universitè de la Réunion), from industry (reference in Siemens internal report) and the military (RAF in Mildenhall). These are basic components that were found to enable or aid others to perform their research in microwave dielectric heating, without the need to concern themselves with component design. Full dimensions and measured characteristics are available in Appendix E, allowing others to rebuild the topologies and structures described.

The substantial amount of time that had to be invested into the proper design of these versatile waveguide components did, however lead to a better understanding of the behaviour of microwaves inside the structure.
Similarly, understanding of magnetron tubes, particularly their supply and operation, had to be established prior to commencement of studies. For the operation, a high-voltage measurement bench was set up, suitable for magnetron testing and operation. It consisted of manually controlled transformer-rectifier-filter based high-voltage direct current power supplies, with a separately controlled filament supply [52].

1.5 Limitations and their impact

Constraints in finances and facilities meant that a substantial amount of time had to be diverted to the design of the various new components, in addition to the organisation of the respective facilities. Notably, Rieke diagram measurements could be only partially carried out due to a lack of appropriate directional couplers. Instead, published data was used in the modelling process, with no resulting restriction on the validity of the model. The model predicts complex impedance, power and frequency accurately.

Temperature measurements of the load were not carried out and fortunately have no bearing on the topic. In general, temperature measurements in microwave fields with moving loads are extremely difficult. Instead, an indirect approach using cobalt-chloride impregnated silica gel (appendix D), was applied for pattern visualisation and to confirm results. Measurements obtained by sliding a high power probe along a slotted line also confirmed simulated results.

A recurring nuisance during the design and research process was the constantly expiring license of Maxwell Eminence®, Microwave Lab® and especially Matlab®. The backward compatibility issue of newer versions also hindered the research process.

However, these constraints resulted in a deeper understanding and produced a lower-cost approach.

1.6 Organisation

The problem, its importance and the new ideas and concepts that will be introduced have been briefly discussed. Microwave generators, their high-voltage supplies and their working principles are briefly outlined in section 2.1, and a verbal time domain description is presented, followed by a discussion of Rieke diagrams for magnetron performance evaluation in section 2.2. Equations and theory concerning injection locking is introduced in section 2.3, the full derivation being left for appendix A. Numbers need to be assigned to the sources, by means of which their behaviour can be modelled. Therefore section 2.4 introduces an oscillator model suitable for magnetron tubes. Chapter 2 is rounded off with aspects and problems associated with microwave heating in section 2.6. A summary of microwave heating uses and fields of applications is provided, highlighting the penetration of microwave dielectric heating already achieved in industry.
The theory of the new pattern synthesis topology is covered in depth in chapter 3. Practical measurements and performance evaluation are the subject of chapter 4 and the conclusion is reached in chapter 5.

Chapter 2

Background

The magnetron tube is but one high power source used to generate the electromagnetic radiation for heating of materials. Magnetron tubes are cheap, simple, efficient and robust [3][29]. These characteristics make them a common choice for application in microwave dielectric heating. In this chapter, the device is examined and a verbal explanation of its operation, from start-up out of noise until steady state oscillation, is given. The time domain explanation is found to improve on the standard frequency domain descriptions which are commonly found.
With a view toward the facilitation of the measurement and characterisation of oscillators in later chapters, a detailed description of the Rieke diagram and its measurement process is given. This is followed by a summary of some of the many application areas of microwave dielectric heating (MDH) which serve to highlight its importance to modern industry. The discussion of the advantages and the disadvantages then lead to the one equation that governs MDH. This equation points to the need for online controllable, uniform heating fields.

2.1 Microwave sources

A suitable, high power microwave source is required. Many types of microwave sources have been developed over the years including klystrons, gyratrons, vircators [68][69], cross-field amplifiers and solid state devices. The magnetron, however, has had the greatest impact on MDH as an efficient and robust high power microwave oscillator.
The first magnetron was proposed around 1913 by A.W. Hull [49]. Generally, its output power is determined by the anode structure, and the frequency of operation by its size [50]. Figure 3 is representative of a typical magnetron source used today in microwave ovens. Figure 4 is a close-up of the magnetron tube. It shows the vanes, straps and cathode with filament parts of the assembly.
The complex interactions evade a concise closed-form analytical expression that describes the magnetron's operation. Perhaps the most complete closed analytical treatment of the magnetron to date is that given in [51]. Simulation and numerical treatment of magnetron behaviour proved more appropriate to further understanding and insight [54][70]. Even these numerical models do not include all physical effects, particularly those of a particle nature that are due to the interaction of the space-charge [6] with its surroundings [71]-[73].

[6] Electrons are particles.

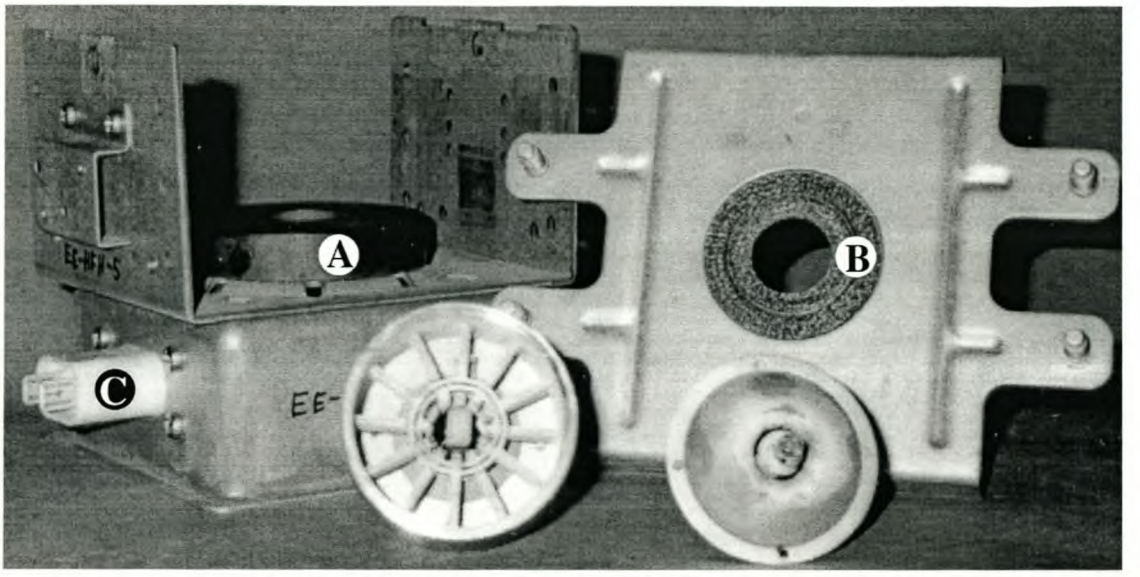

Figure 3: Disassembled microwave-oven magnetron with permanent magnet and mounting. Notable features include a pair of permanent magnets **A** (a second magnet which is not visible is present behind label **B**), gasket for good RF seal **B** and the supply terminals for filament and cathode **C** with integral filter capacitor. A disassembled magnetron tube is visible in the foreground.

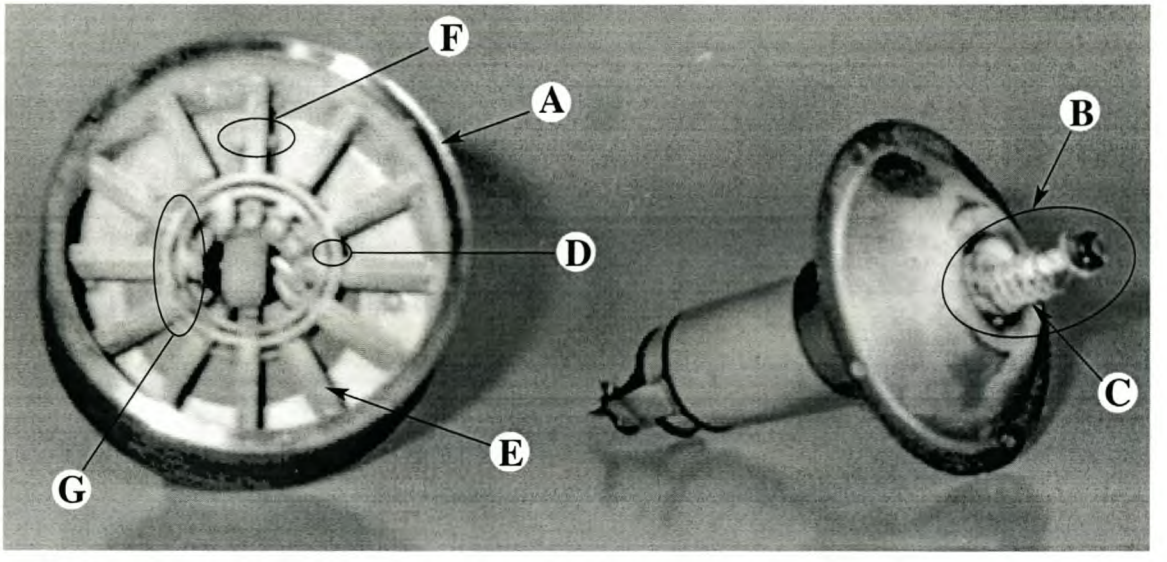

Figure 4: Close-up of the disassembled magnetron tube.
Features: Anode structure **A**, Cathode with (broken) filament **B**, (burnt out) filament **C**, Straps **D**, Vanes **E**, and connection to Antenna **F**. **G** encircles an area of straps molten as a result of moding.

The intricate nature of the magnetron's workings do tend to result in it being taking for granted as a given in most microwave heating systems. Designers prefer not to delve into its inner workings and hence tend not to consider the implications of possible structural changes, virtual cathodes, and how these might impact on the performance of the source under consideration. So as not to fall into this trap, the magnetron as well as its constituents are examined to gain the necessary insight into its operating principles before a time domain description of the magnetron's principle of operation is given [50].

2.1.1 Electron cloud formation

The 'active ingredients' in a magnetron are the electrons emitted from the cathode by the process of thermionic emission. After power is applied to the filament the cathode heats up, increasing the electron's kinetic energy until the cathode emitter's work function is overcome [36]. At this point electrons escape from the surface of the heated cathode [36] and form an electron cloud with randomly distributed electrons around the cathode. Electron emission angle and velocity vary significantly amongst these electrons, which generates noise [70].
The permanent magnets in Figure 3 set up a magnetic field but, until an electric field is present, its effect on the electrons is of no concern. As soon as an electric field is applied, however, electrons try to move away from the cathode towards the anode but are prevented from reaching the anode by the applied magnetic field (magnetic isolation). The electrons thus form an electron layer, a virtual cathode so to speak, at a distance around the cathode, known as the 'Brillouin layer'. Electrons in this layer are in equilibrium, balanced by the applied electric and magnetic fields and their velocity-momentum. Figure 5 depicts the electron density around the cathode. The figure indicates an increased electron density about the Brillouin layer, with a lower density of electrons occupying the space between it and the cathode. As a result of magnetic isolation, almost no electrons are located between the anode and the Brillouin layer.

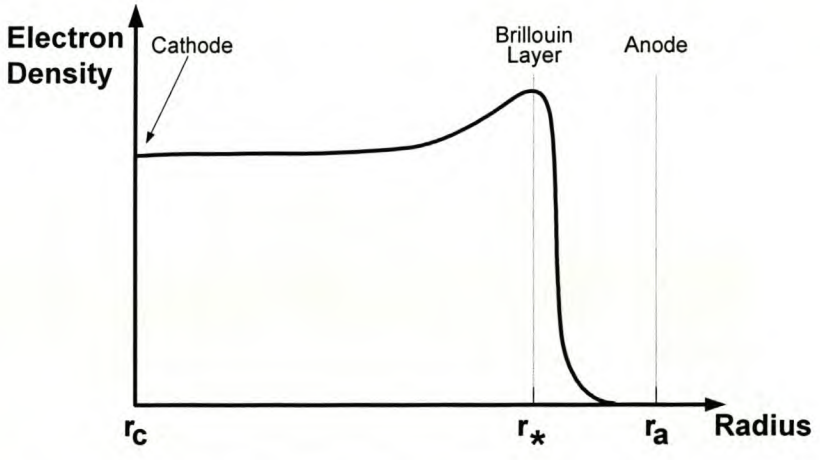

Figure 5: Electron density distribution between cathode and anode in an operating magnetron.
r_a, r_c and r_* are the radii of anode, cathode and Brillouin layer respectively [57].

The Brillouin layer represents a substantial space-charge away from the cathode, altering the initial overall E-field [57]. In effect the Brillouin electron layer may be considered a virtual cathode whose effective cathode radius changes and, with it, the frequency [52].

2.1.2 Onset of oscillation: A time domain view

At this point the Brillouin layer has formed concentrically between anode and cathode as described in the previous subsection. Slight variations in its position would cause a shift of surface electrons in the anode by static electric repulsion. The perturbations that initiate oscillation in the magnetron arise from ambient noise, originating either from electrons drifting in the Brillouin Layer or from an externally injected signal in the case of injection-locking [57]. Start-up times until oscillation commences range from nano-seconds to seconds [50][52][53] (see also Figure 6). The frequency domain description often found in the appropriate literature [15][23][50] [52][53][57][58] argues that at this point energy is present at the resonant frequency in the noise spectrum, but this does not explain start-up phenomena per se. It merely implies that suitable excitation for start-up exists. Looking at the build-up of oscillation in the time-domain provides a slightly different picture, which improves understanding.

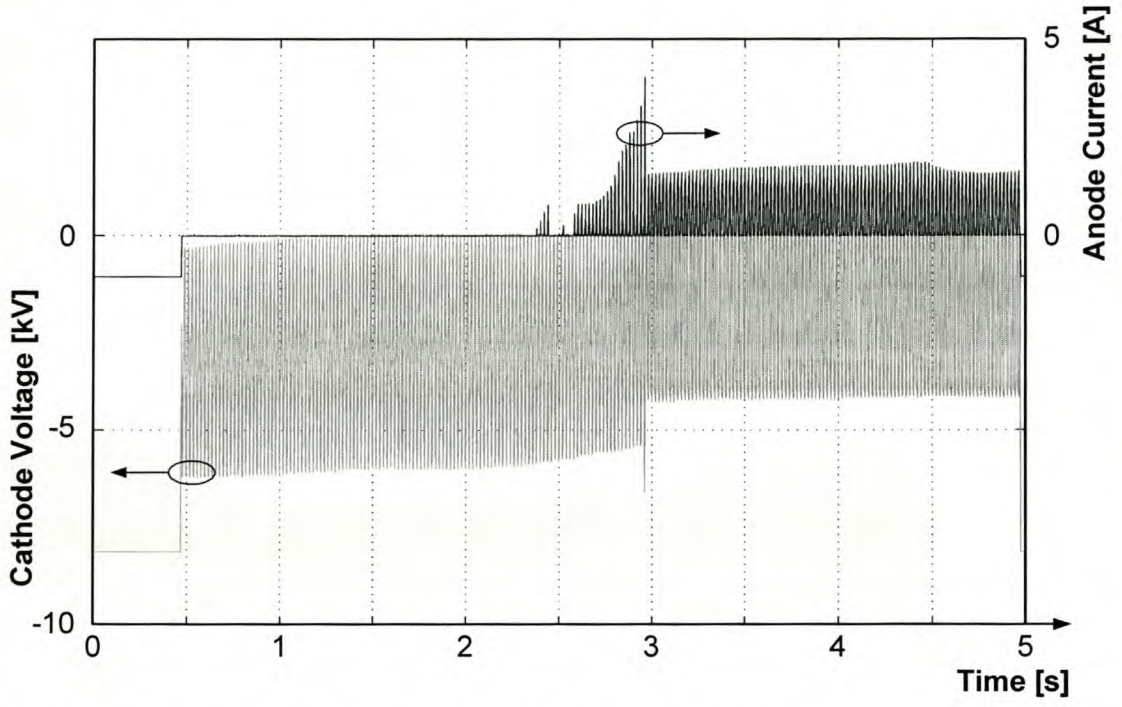

Figure 6: Anode current and cathode voltage during start-up (after this author in [50]).

Electrons in the Brillouin layer have a particular drift velocity. Were it any faster, then through their interaction with the magnetic field present, they would return to the cathode. On the other hand, if the drift velocity were any slower then this particular velocity, they would mode towards the anode. Their drift velocity, and the fact that the cathode emits electrons at random angle and with random velocity, results in a constant noise current being induced in the anode structure. Electrons that move charge on the anode surface perform work, and are thus slowed down and tend to move closer towards the anode. At the same time electrons on the anode surface may perform work on electrons in the Brillouin layer, causing them to return to the

cathode. This process establishes a balance that exists as long as a symmetrical 'quasi-smooth' statistical distribution of electrons is present about the axis of symmetry.

How current flows in the Brillouin layer, as well as *how it flows in the anode surface,* must be considered next. In the Brillouin layer current flows as a result of a number of individual electrons moving independently at their drift velocity, whereas in the anode surface, as in all metals, current flows by electrons 'pushing' each other [36][70]. Charge movement on the anode surface is faster than in the Brillouin layer. Hence the wave-velocity on the anode surface must be slowed down to the wave velocity in the Brillouin layer to allow the electrons and the surface wave to interact — the purpose of the slow wave structure.

Suppose now that, due to noise and turbulence in the Brillouin layer, an electron on the anode surface shifts. The charge-distribution on the surface travels faster than the drift velocity of the Brillouin layer, but is slowed down by the slow-wave structure (item 'E' in Figure 4) to be in phase with the Brillouin layer at resonance. The electrons that caused this to happen are slowed down, move towards the anode and begin to trail behind. In the meantime the surface wave reaches the neighbouring vane which, as a result, tends to be more negative. This in turn moves electrons in the Brillouin layer. They receive momentum, fall back to the cathode and this results in a process known as 'Back-bombardment'. The process contributes to cathode heating as well as to the liberation of 'secondary electrons'. The deformed Brillouin layer continues to rotate and reaches the next vane. This now represents a new, less random, occurrence increasing as long as the electric fields coincide constructively.
Should anode surface wave velocity and Brillouin layer electron drift velocity not be the same, then the disturbances cannot interact constructively and their net effect fades away until it ceases to exist. Similarly, permanent conduction is not possible because this results in increased electron velocity, which again causes them to curl towards the cathode in the magnetic field.

It is interesting to note that electron movement in the slow-wave structure is back and forth, while in the Brillouin layer movement takes place in only one direction [59].

2.1.3 Spoke formation

The feedback process that leads to start-up continues to remove energy from the electrons in the Brillouin layer. Naturally a limit is set on this process by the number of electrons available and emitted but, until this is reached, electrons are accelerated and decelerated which tends to bunch them azimuthally. Slower electrons in the region of the anode and faster ones in the cathode region create a saw blade-like shape with backward bending saw-teeth (Figure 7).

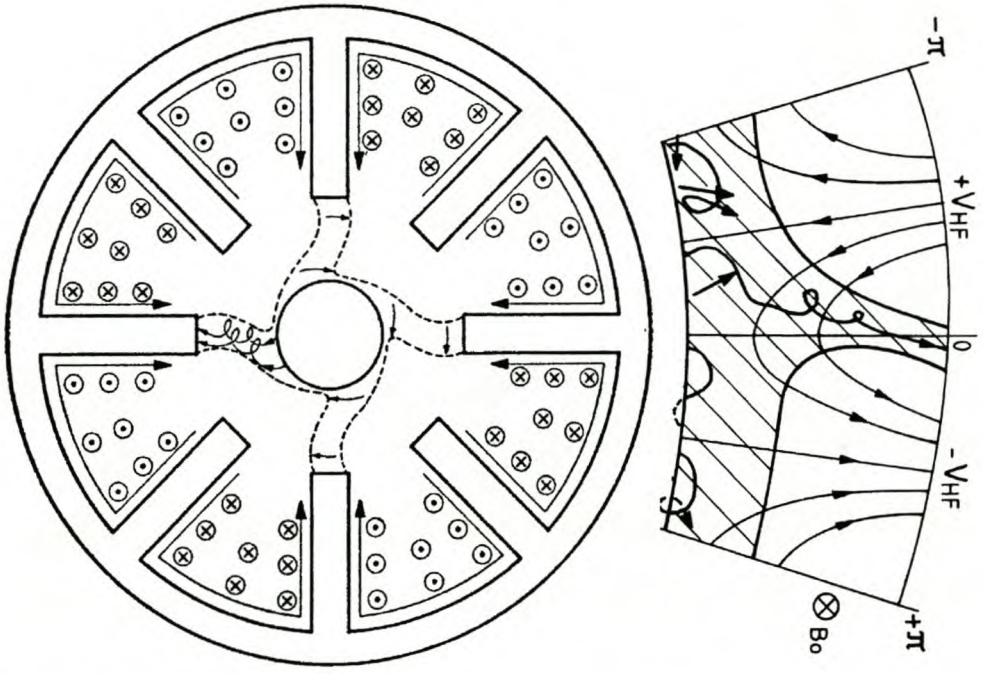

Figure 7: Schematic of spoke rotation in π-mode.
The path taken by electrons can be seen in the close-up [58][59].

Motion in three dimensions complicates the picture further.

2.1.4 Origin of electrons in the magnetron

In conventional magnetron tubes most of the electrons originate from secondary emission caused by back-bombardment. Primary electrons, derived from thermionic emission, are required to initiate the process [58]. These electrons gain kinetic energy and fall back to the cathode thus 'bombarding' its surface. The kinetic energy of these primary electrons is transferred to the cathode, manifesting itself as heat but more importantly, they liberate secondary electrons at the cathode's surface. This liberation process only takes place if sufficient energy to overcome the work function of the surface is transferred (by heat, back-bombardment or otherwise) and is an important mechanism by which electrons are generated in the magnetron [70].
In Figure 7 it is noticed that emission of secondary electrons takes place only in specific regions along the formed spoke wheel on the surface of the cathode. In other words, the process is not as random as primary thermionic emission. Instead, it represents a bounded stochastic process. As mentioned in [31] a magnetron can operate at relatively low noise, low enough even to be suitable for communication systems, after ignition (spoke formation may also be referred to as 'ignition') with the filament supply removed.

2.1.5 De-coupling of RF-energy

At this point, the magnetron is in steady state operation. To de-couple microwave energy to the outside, several possibilities exist:

- Loop coupling from the resonator to an antenna,
- Coupling hole or slot in the resonator to couple to a waveguide, and
- Connection of a vane to an antenna by means of a transmission line.

Magnetron tubes, like the one shown in Figure 3, use the latter method, feeding an antenna via a strip or transmission line (see Figure 8).
The antenna is placed either into a connector for transmission in coaxial cables (found in low power applications, for instance diathermy) or into a launcher, which represents a transition between the antenna and an appropriate waveguide.
A launcher is a piece of waveguide with a *short* positioned at a particular distance away from the antenna. Tube manufacturers usually have appropriate dimensions, including mounting instructions, available on request. A typical configuration is illustrated in Figure 8.

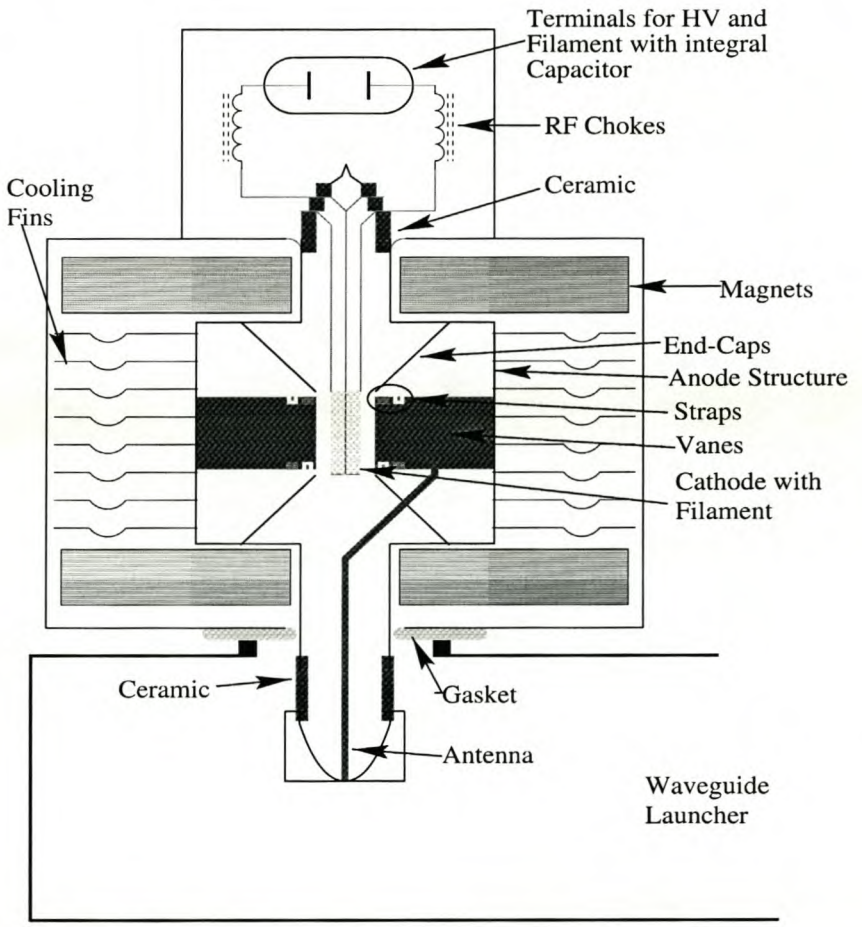

Figure 8: Schematic cross-section of magnetron mounted in launcher.

2.1.6 Influence of power supply waveform on frequency spectrum

A spectrally pure (or narrow band spectrum) output from the magnetron is required. However, the performance of the magnetron is strongly influenced by both the high-voltage supply and the filament supply.

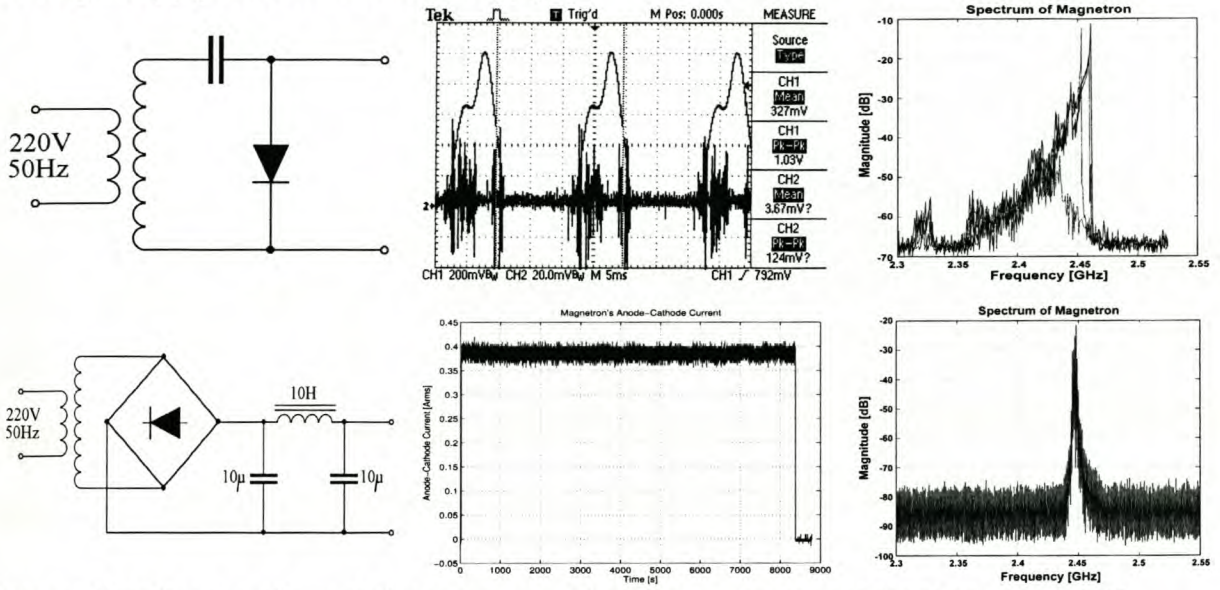

Figure 9: Influence of supply type and current on magnetron operational spectrum [50].
Top row: Conventional half-wave doubler produces broader spectrum.
Bottom row: Full-wave rectified with π-filter results in cleaner spectrum.
The magnitude of the spectrum is attenuated by about 60 dB.

Figure 9 shows the output spectrum of the same tube for two different supplies:

- The conventional ubiquitous half-wave doubler: Produces a broad spectrum swept every second half-cycle (Figure 9, top row). Due to the current-frequency dependence of the magnetron (Figure 10) [52] the frequency is swept every half-cycle and its spectrum is not strictly confined to the 2.4 GHz ISM band.
- The full wave rectified high-voltage supply (single or three phase) with π-filter: Although the remaining supply ripple still modulates the spectrum, it is considerably cleaner and more narrow band (Figure 9, bottom row). Also, the noise floor is approximately 10 dB lower than that of the half-wave doubler.

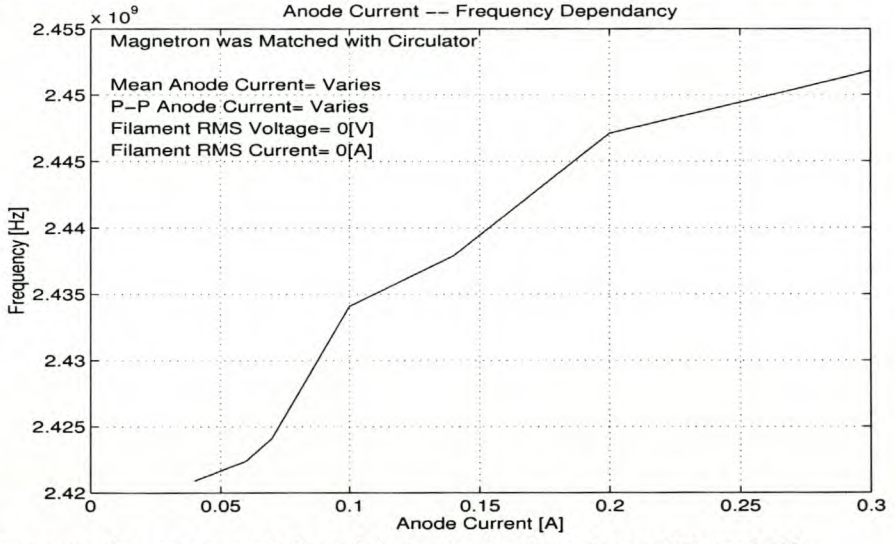

Figure 10: Current - frequency relationship under matched conditions [50].

The filament supply is another significant disturbance mechanism. The difference between operating the tube with and without the filament supply is seen in Figure 11. The reason for this difference is as follows:

> The filament supply is an AC supply, in this case 3 V at 8 A. A current of 8 A flowing through a spirally wound filament produces a magnetic field disturbance sufficient to modulate the electron cloud and, with it, the frequency. The relation between magnetic field and frequency has already been shown by [52], and [31] confirms that removal of the filament, and thereby its resulting magnetic modulation, does produce a cleaner spectrum, suitable even for transmitters in some cases. Also, the noise floor is slightly lower with filament supply removed.

The π-filter in Figure 12 tends to remove fast, high frequency fluctuations that affect the operation of the magnetron tube. Slow fluctuations are removed by inserting an incandescent light bulb into the HV path. In this setup two 60 W, 250 V glow-bulbs in series formed a simple negative feedback method, which at the same time protects against fault currents. An increase in current caused by a change in supply voltage increases the current through the bulb's filament, thereby heating it and causing an increase in its resistance. An increased resistance results in a larger voltage drop, thereby partially compensating for slow supply fluctuations. If, due to a fault condition, too large a current is drawn, the incandescent bulb fuses, thus interrupting the fault current.

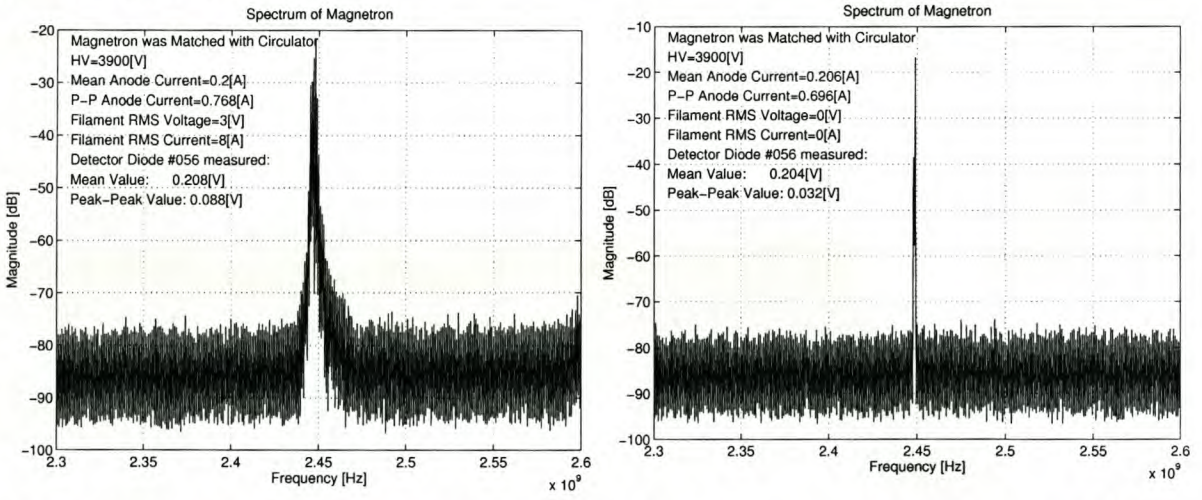

Figure 11: Influence of filament supply on spectrum of magnetron (after this author in [50]).
Left: Filament supply on
Right: Filament supply off.
A π-filtered full-wave rectified power supply was applied.

A circuit diagram of the supply used is shown in Figure 12. The single-phase supply indicated could also be replaced by a three-phase supply. Single-phase supplies have a larger associated supply ripple, but were found to exhibit a lower long-term variance, whereas the opposite was noticed on three phase supplies.

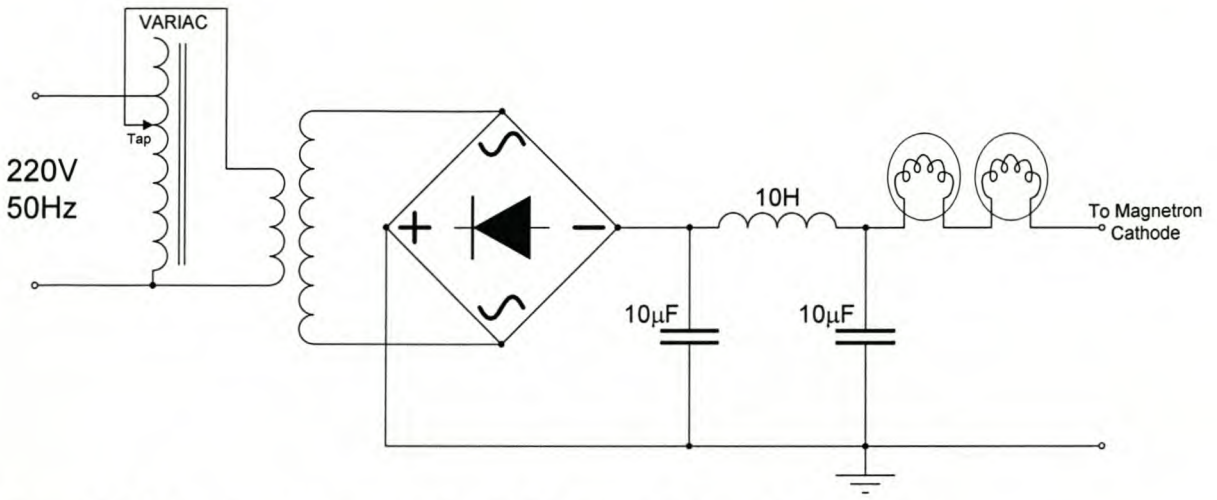

Figure 12: Magnetron power supply with Variac, π-filter and stabilisation.

Therefore, a tube operated using a stable high voltage power supply (preferably with constant anode-cathode current) and with the filament turned off after ignition produces a spectrally pure high power microwave signal suitable for injection locking.

2.2 Rieke diagram

A magnetron mounted in its launcher can be considered as a fixed 'microwave supply unit'. From a design point of view the interface is a waveguide, and parameters such as complex impedance, frequency and output power need to be considered. These parameters depend on bias[7] conditions. Fortunately, the bias conditions of a magnetron tube are fixed or kept constant under normal operating conditions. Only the microwave load may vary. This situation is charted on a 'load diagram', also known as 'Rieke diagram' or 'Rieke's diagram', named after F.F. Rieke who together with J.E. Evans first used it around 1940 to plot oscillator performance characteristics [75]. It is exclusively encountered with high power microwave oscillators like magnetron tubes for which no simple means exists to obtain the performance under varying load conditions. Keeping this in mind, the focus is on magnetron tubes used in waveguide launchers.

The Rieke diagram indicates the output performance of the device under various load conditions and with bias conditions kept constant. Both frequency and output power of the oscillator are measured and graphed on a polar plot or Smith chart. On a polar plot the load is indicated as Voltage Standing Wave Ratio (VSWR) or as magnitude of the reflection coefficient and phase in degrees or fractions of wavelength under matched conditions. By convention, points of constant power are connected by solid lines, while points of constant frequency are drawn as dotted or dashed lines.

Manual [52] and automatic [76][77] Rieke diagram measurement set-ups are very similar to each other. Both use the same basic measurement technique, consisting of slotted waveguide with double slug tuner as variable load, and either a dual directional coupler or a sliding probe with detector and volt meter to measure VSWR,

[7] The author refers to *supply conditions* of the magnetron as *bias* in analogy with terminology used for other discrete active devices such as transistors and valves.

power and frequency. For manual measurements the double slug tuner has the distinct advantage over a three-stub tuner in that movement along a slotted line corresponds to VSWR circles on the Smith chart, easing manual data acquisition considerably.

Making use of a slotted line with a sliding probe the voltage maximum, V_{max}, and the voltage minimum, V_{min}, are measured to find the VSWR as V_{max}/V_{min}. The phase is calculated from (1) with x_{Vmin}, the distance between the first V_{min} away from the antenna of the magnetron [34][59]. By convention, the reference position (x=0) is the centre position of the antenna.

$$\Theta° = 720\left(\frac{x_{Vmin}}{\lambda} - \frac{1}{4}\right) \tag{1}$$

The frequency is calculated indirectly from the distance between the extrema. A calibrated detector diode provides a voltage reading, which is converted to an equivalent power value via its calibration chart.

The following summarises a systematic Rieke diagram measurement procedure as outlined in [52]:

Information to be recorded is:

- Anode current (average),
- Anode-cathode voltage,
- Duty cycle or wave shape for pulsed or cycled operation,
- Output power (average),
- Frequency, and
- Load condition, magnitude and phase.

It is essential to maintain a constant magnetic field and anode current throughout the measurement process or, preferably, to perform the measurement as close to operating conditions as possible. For this, the magnetron is presented with a matched load, and its bias conditions are adjusted to the desired value. Anode-cathode voltage, output power and frequency are recorded. Thereafter the measurement is conducted by repeating the following steps until a sufficient amount of data has been gathered, always taking care that the absolute maximum ratings of the magnetron are *not* exceeded:

- Present a new load to the magnetron (change of VSWR on double slug tuner and/or movement along slotted waveguide),
- Readjust anode current to recorded bias value,
- Record anode-cathode voltage, output power and frequency.

During the measurement the magnetron should not be operated in its sink region, to prevent damage and overheating. The sink region refers to a region of complex load conditions on the Rieke diagram under which the magnetron ceases to oscillate. Supply power is still absorbed, but no microwave radiation is produced. Therefore sufficient cooling is necessary throughout the entire measurement cycle.

It is essential to adhere to the set bias conditions throughout the measurement process. Alternatively, it is sensible to measure the magnetron under the same bias conditions it will encounter during operation.

An example of a Rieke diagram on a Smith chart is shown in Figure 13.

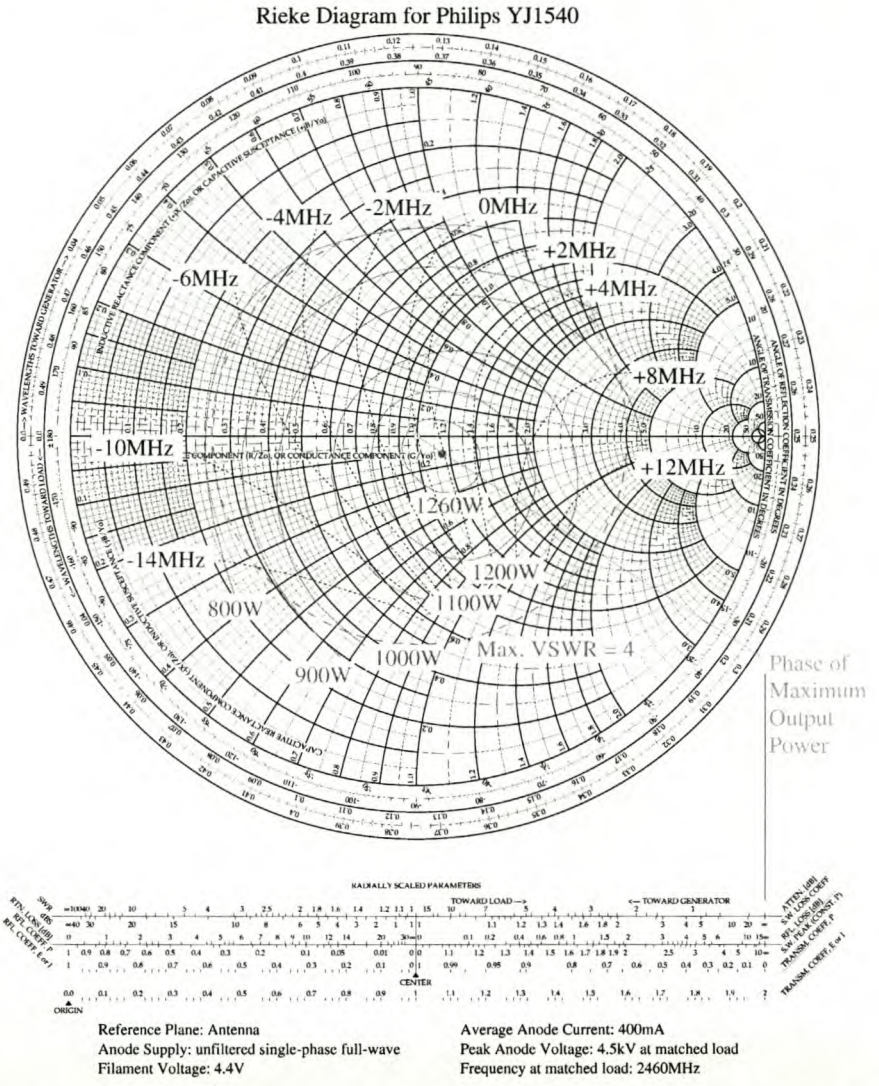

Figure 13: Rieke Diagram for the Philips YJ1540 magnetron tube (2M137 equivalent) [33].

2.2.1 Sources in HFSS and Maxwell Eminence

The finite element packages mentioned in section 1.4 assume ideal sources. The use of isolators makes the magnetron sources behave fairly close to that ideal. The topology makes use of isolators in such a way that the assumption of ideal in simulations is reasonable. In the intended operation several sources are attached to an applicator, and their phase is varied. Simulation packages such as HFSS and Maxwell Eminence allow the parameters of the sources to be adjusted independently of each other, i.e. they cater for multiple simultaneously excited independently adjustable sources, as described by this author in [18]. Details on adjustment and placement can be found in either the online references or the accompanying manuals [64]-[66].

2.3 Essentials of Injection Locking

The phenomenon of synchronisation and locking of oscillating processes is common in nature. The Dutch physicist Christian Huygens first documented it in 1665. He

noticed that the pendulums of clocks positioned in close proximity to each other swung in synchronism. The first analytical treatment of injection locking of electronic oscillators was conducted 260 years later by Balth van der Pol [63][78] in his analysis of the amplitude dependence of injected signal and oscillator. Robert Adler later established bounds for the instantaneous phase shift between injected signal and oscillator, within which locking can take place [79]. Locking has subsequently been described for various oscillator types and configurations [63][78] [80]-[82] [85]-[88].

Injection locking theory will be covered briefly, starting with the single tuned oscillator, also known as Van der Pol oscillator [63][78][82][85][86][88]. Only the essential concepts will be introduced in the body of text below. The full derivation is left for appendix A.

The results of the derivations are applied to predict the locking performance of a commercial magnetron tube. These are later verified by measurements.

2.3.1 Mathematical Description of Oscillator

The single frequency oscillator of Figure 14 is mathematically described by differential equation 2.

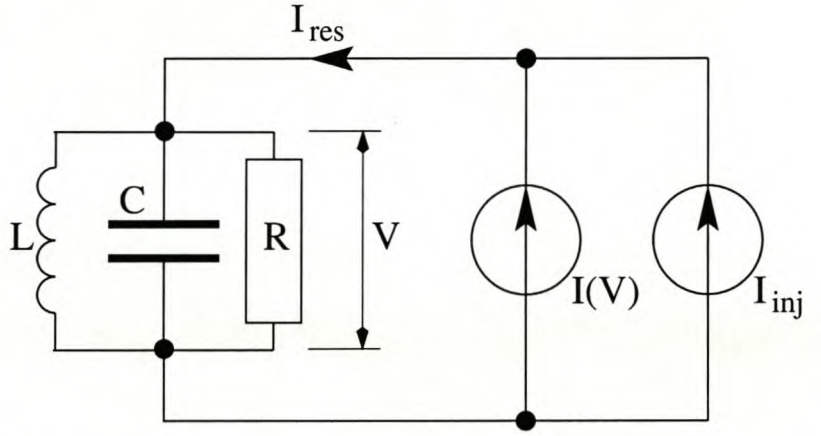

Figure 14: Van der Pol oscillator.

$$\frac{d^2}{dt^2}V(t)+\frac{\omega_0}{Q}\frac{d}{dt}\left(V(t)-R\,I_{Res}(V(t))\right)+\omega_0^2\,V(t)=0 \qquad (2)$$

with

$$\frac{\omega_0}{Q}=\frac{1}{RC} \text{ and } \omega_0=\frac{1}{LC}$$

$I(V)$ of Figure 14 represents the non-linear saturating gain element of the circuit and I_{inj} an externally injected signal as well as noise[8]. The quantities ω_0 and Q represent the resonant frequency of the oscillator and its quality factor respectively [89][90]. These quantities may be obtain from measurements [90][91] or otherwise.

[8] Noise will not be considered.

Before applying the Laplace transform $L\langle\ \rangle$ to the previous equation, components relating to resonators and sources are re-arranged to arrive at equation 3. Subsequently solving for V(t), one arrives at the recursive differential convolute describing all oscillating processes in equation 4 – the symbol '$*$' indicating convolution.

$$s^2 L\langle V(t)\rangle + \frac{\omega_0}{Q}\left(s L\langle V(t)\rangle\right) + L\langle V(t)\rangle \omega_0{}^2 = \frac{R\,\omega_0}{Q} L\left\langle \frac{d I_{Res}}{dt} \right\rangle \tag{3}$$

$$V(t) = I_{Res}(V(t)) * \frac{d\,Z(t)}{dt} \tag{4}$$

$$\text{where } Z(t) = L^{-1}\left\langle \frac{R\,\omega_0}{Q s^2 + \omega_0\, s + Q\,\omega_0^2} \right\rangle$$

Equation 4 is a general solution to equation 2. It describes the fact that an oscillator is the superposition of resonator impulse impedance responses in the time domain, excited by its own signal – hence oscillation requires recursion.
I_{Res} is the combined current into the resonator, consisting of transconductance current I(V) and injected signal current I_{Inj}, and Z(t) is the impulse impedance response characteristic describing the resonator.

2.3.2 Injection Locking Equations

Equation 4 represents a general description of any oscillating process. It is therefore suitable for use in finding some essential injection locking equations. These will be briefly explained in the following subsections (a full derivation is found in appendix A).

The aims are to determine:

- The amplitude of an injected signal necessary to lock an oscillator (Van der Pol), and
- The frequency range over which a source can be locked (Adler).

2.3.3 Van der Pol equation

Van der Pol's aim was to establish a relationship between the signal amplitude and the bandwidth of the injected signal, allowing it to lock an oscillator [63][78]. Oscillators tend to be high-Q circuits. This allows loss and higher order frequency components to be neglected. Thereby the focus is on the natural frequency of the oscillator and its injected signal amplitude. The relationship

$$\frac{E}{a_0\sqrt{2}} = \frac{\omega_0 - \omega_i}{\omega_i} \tag{5}$$

could thus be established by Van der Pol (appendix A).

Equation 5 predicts the relationship between the injected signal amplitude E and the injected frequency ω_i that can lock the oscillator even with undisturbed frequency ω_0. In effect, all frequencies between ω_0 and ω_i will lock the oscillator. This is described by (6), and establishes the locking region for a given amplitude and frequency.

$$\frac{E}{a_0\sqrt{2}} \geq \frac{\omega_0 - \omega_i}{\omega_i} \tag{6}$$

The dynamics of the system were not of so much interest to Van der Pol. His equation hence applied to 'sufficiently long times' to ensure locking (should such be possible).

2.3.4 Adler injection locking equation

Robert Adler [79], however, was concerned with the dynamics of the system. He considered amplitude and instantaneous phase to arrive at (7).

$$\frac{d}{dt}(\varphi) = |\omega_i - \omega_0| - \frac{\omega_0 |\Gamma|}{Q_E \sin(\varphi)} \tag{7}$$

Here the instantaneous phase difference in time $\varphi(t)$ between two sources and their amplitude ratio $|\Gamma| = |V_{in}|/|V_{out}|$ are related to the oscillator's parameters ω_0 and Q_E. Two important conditions can thus be derived from (7), namely the 'locking bandwidth' and the 'locking time' of an oscillator with an injected signal.

For a suitable injected signal, the instantaneous phase will tend towards zero. Hence $d\varphi/dt = 0$ under locked conditions, leading to the injection locking bandwidth given by (8).

$$BW_{Lock} = \frac{2f_0}{Q\sqrt{P_{out}/P_{in}}} \tag{8}$$

The time required for an oscillator to lock onto an injected signal is the second parameter of interest. This determines the speed with which the injected signal's phase can be changed and still keep the oscillator locked. The maximum instantaneous phase excursions is given by $\sin(\varphi) = \pm 90^\circ$. Substitution into (7) and integrating, the locking time is found in (9).

$$t = \frac{2\dfrac{\omega_0 |\Gamma|}{Q_E |\omega_i - \omega_0|}}{\left(\left(\dfrac{\omega_0 |\Gamma|}{Q_E}\right)^2 - |\omega_i - \omega_0|^2\right)^{\frac{1}{2}}} \tag{9}$$

Equations 8 and 9 are particularly convenient to apply because they make use of determinable quantities: BW_{Lock}, ω_0, Q_E and Γ.

The simplicity of Adler's equation, however, hides one important fact: It includes only linear contributions. Higher order terms are not considered. As a result, (8) and (9) provide reasonable but conservative estimates only. This is confirmed by [85], and reflected in section 4.1 as well as appendix A.2.

2.4 Magnetron modelling (electrical point of view)

A manual version of the Rieke diagram was described in section 2.2. Alternatively the same information can be parameterized, as is shown by this author in [45]. For this purpose the magnetron model in Figure 15 is used. It aims to relate output power, frequency and impedance of the magnetron oscillator to each other.

2.4.1 Parts of a magnetron

To model the magnetron (or any oscillator for that matter) it is sub-divided into its active and passive parts (Figure 15), which are described separately.

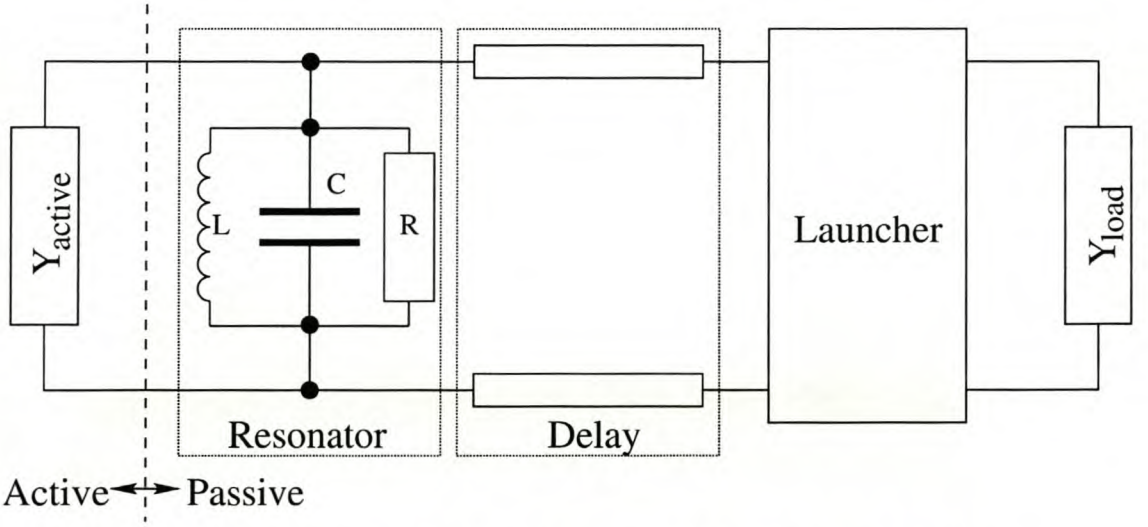

Figure 15: Magnetron model separated into its active and passive components.

The passive parts can be measured in the cold state of the magnetron with a network analyser and extracted if necessary (see section 4.2). For the active part no complete expression exists, despite valuable attempts, analytically by [51][92][93], numerically by [54][70], and through impedance approximations by [94][95]. These techniques assume substantial intrinsic oscillator knowledge that is not always obtainable.

2.4.2 Rieke diagram based magnetron model

A different approach to obtaining the information desired is the Rieke diagram based magnetron model. [61] had already proposed a mathematical relationship between the power, frequency and impedance of oscillators by approximation to measured

Rieke diagram data of the admittance G(V(s)) in (10). A good graphical description of each of the coefficients is found in the same reference.

$$\begin{aligned} Y(j\omega,|V|^2) &= -G_0 + jB_0 + (G_\omega + jB_\omega)\,\Delta\omega \\ &\quad + (G_V + jB_V)\,|V|^2 + (G_C + jB_C)\,\Delta\omega|V|^2 \\ &\quad + (G_{\omega^2} + jB_{\omega^2})\,\Delta\omega^2 \\ &= -Y_0 + Y_\omega\,\Delta\omega + Y_V|V|^2 + Y_C\,\Delta\omega|V|^2 + Y_{\omega^2}\,\Delta\omega^2 \end{aligned} \tag{10}$$

where

$$|V|^2 = \frac{P_{osc}}{Re(Y_L)}$$

Closer examination reveals (10) to be a truncation of the series expression in (11). Grouping terms and simplifying, a more physically related interpretation in terms of gain-bandwidth product and admittance is obtained in (12) (see [45] by this author). The model includes all the factors contained in (10), but it is extended.

$$Y(j\omega,|V|) = -Y_0 + (k_{V1}|V| + k_{\omega 1}\,\Delta\omega) + (k_{V2}|V| + k_{\omega 2}\,\Delta\omega)^2 + \ldots \tag{11}$$

$$Y(j\omega,|V|) = -Y_0 \sum_{n=0}^{N} (\overrightarrow{k_n}^T \cdot \vec{X})^n \tag{12}$$

where

$$\overrightarrow{k_n} = \begin{pmatrix} k_{\omega_n} \\ k_{V_n} \\ k_{\omega V_n} \end{pmatrix}, \quad \vec{X} = \begin{pmatrix} \Delta\omega \\ H \\ \Delta\omega H \end{pmatrix}$$

$$\Delta\omega = \omega - \omega_0 = \text{Bandwidth}$$

$$H = \frac{|V|}{|V_0|} = \text{Gain}$$

$$\omega_0 = \text{Resonant frequency into matched load}$$

$$V_0 = \text{Voltage at } \omega_0$$

To obtain the relevant constants, error function (13) is minimised by simultaneous solution of equations (14), and each solution must pass conditions (15) to be classified as a minimum. If numerical optimisation techniques are used, then they may as well be applied directly to (13) for Error=0.
Caveats with polynomial equations are local minima, because derivative based algorithms tend to falsely detect an optimum where there is none. Simulated annealing is a technique suitable to overcome this restriction [96].

$$\text{Error} = Y(j\omega, |V|) - Y_{\text{Rieke}} \tag{13}$$

$$\text{Re}\left(\frac{d\,\text{Error}}{d\Delta\omega}\right) = 0,\ \text{Im}\left(\frac{d\,\text{Error}}{d\Delta\omega}\right) = 0,\ \text{Re}\left(\frac{d\,\text{Error}}{dH}\right) = 0,\ \text{Im}\left(\frac{d\,\text{Error}}{dH}\right) = 0 \tag{14}$$

$$\frac{d^2\,\text{Error}}{d\,\Delta\omega^2} > 0 \text{ and simultaneously } \frac{d^2\,\text{Error}}{d\,H^2} > 0 \tag{15}$$

The multi-dimensional extension of the polynomial leads to artificial neural networks (ANNs). They have recently been demonstrated to represent Rieke diagram data closely, and it appears possible to include operating conditions [97]. The ANN approach has, however, the disadvantage of removing physical insight, and it is only valid within the bounds of the 'learned' set of data.

2.4.3 Future model improvements

Currently the valid operating region of the model is limited to particular fixed bias conditions only. As stated earlier, artificial neural networks (ANNs) appear as possible candidates to bridge this gap [97]. The polynomial model presented can be integrated into ANNs to reduce neural complexity and serve as 'intrinsic neural knowledge' whereby training and complexity of the ANN are reduced, and the ANN is directed towards a more feasible solution. The latter is advantageous because ANNs tend only to interpolate results very well, but exhibit poor behaviour outside their training bounds. With pre-knowledge included, it is more likely that data outside the bounds of the training set will result in a meaningful output. The use of ANNs does, however, remove much of the physical meaning gained by (12).

2.5 Similar or identical tubes

Magnetron tubes can be locked to a low-power injected reference signal [63][78], and made to form reflection amplifiers [31][80]. Equation 9 predicts that the locking time decreases [95]

a) with increased incident power ($P_{in} \rightarrow P_{out}$, i.e. $\Gamma \rightarrow 1$), and
b) for the injected signal's frequency ω_i (or its harmonics) close to the resonant frequency ω_0 of the oscillator (or its harmonics).

Conversely, time becomes large towards the edges of the locking band. The injected frequency ω_i should therefore be kept close to the resonant frequency ω_0 to ensure fast locking, and to simultaneously ensure that locking is maintained, even with changes in circuit parameters. Using magnetron tubes of the same type and at their resonant condition ensures that this condition is met for injection locking.

Tubes of the same type and from the same manufacturer will therefore be used.

2.6 Summary of common microwave heating application in industry

Microwaves can be generated and applicators designed, but their purpose and their application should not be overlooked.
An overview of microwave dielectric heating applications is found in [1][15][17][22] [23] and [59]. Many other references exist. The major areas of application to date can be summarised as:

- Food Industry
  - Thawing of fish and meat [15]
  - Drying and microwave assisted freeze drying [15]
  - Pre-cooking of foodstuffs
  - Pest control of corn and flour [4]
  - Re-working of confectionery [98]
  - Sterilisation [99]
- Chemical Processes
  - Polymerisation and polymer curing [100]
  - Increased reaction speed
  - Waste treatment [2][101]
  - Regeneration of spent active carbon [2] or catalysts [102]
  - Microwave assisted (selective) ore extraction [2][103][104]
  - Mineral oil refining[9]
- Pharmaceutical Applications
  - Sterilisation
  - Microwave assisted drying
- Medical Applications
  - Hyperthermia for cancer treatment
  - Treatment of dental caries [105]
- Ceramics and Material Science
  - Material synthesis
  - Synthesis of nano-particles [106][107]
  - Joining of Materials [108]
  - Sintering [14][109]
  - Ablation coating
- High-Energy Physics
  - Plasma
  - Accelerators
- Household
  - Microwave oven for thawing, cooking and baking

All of the above mentioned applications have one common trait: They can be described in terms of equation 16 [18][34][41]. This equation describes the power dissipated, P_D, in a volume of material exposed to electromagnetic waves.

[9] Informal talk with CPI representative at the Second World Congress on Microwave and Radio Frequency processing, USA, Florida, Orlando, April 2000.

$$P_D(t) = \frac{1}{2}\iiint_V (\sigma_E + \omega\varepsilon \tan\delta_E)|E|^2 + (\sigma_M + \omega\mu \tan\delta_M)|H|^2 \, dV \quad (16)$$

where

σ_E : Electric conductivity
ε : Complex permittivity
$\tan\delta_E$: Electric loss tangent
σ_M : Magnetic conductivity
μ : Complex permeability
$\tan\delta_M$: Magnetic loss tangent

Power dissipated in a material translates into heat generated within it, which, in turn, appears as a change in temperature, ΔT, of the matter (see equation 17 [44]).

$$\Delta T = \int \frac{P_D(t)}{V \rho c_p} dt \quad (17)$$

where

V : Volume of matter
ρ : Density
c_p : Specific heat

This implies that heat is only generated in the presence of matter and, as soon as matter is present, heat is generated instantaneously in its volume. This is contrary to conventional heating where one is accustomed to heat slowly diffusing into the volume of an object and away from the contact surface area of the source, with the terminal temperature intrinsically limited by the temperature of the source itself.

In contrast, equation 16 and 17 predict that microwave heating exhibits the following traits:

- Heat is developed in the material and is caused by its dielectric and magnetic loss properties when inside an electromagnetic field. As soon as the microwave field is applied heating takes place, and as soon as it is removed heating ceases.
- As long as the material is in the microwave field its temperature increases. A temperature ceiling is potentially only produced by changes in the material's phase, electromagnetic properties, or when countered by loss of heat.
- The heating characteristic is determined by electromagnetic material properties. Lossy materials such as carbon heat faster when compared to a low loss material such as Teflon.

Equation 16 also points to intrinsic problems found with microwave dielectric heating. For uniform heating it is required that

- a uniform field is applied; however:
  - waves possess peaks and troughs, and their reflections result in stationary modal patterns, and
  - the wavelength tends to be comparable to the size of the object to be heated, or the resolution required.
- a uniform dielectric property with negative or constant $\mathrm{d\,loss}/\mathrm{d\,T}$ is present or else
  - thermal runaway takes place as is commonly found in transition metal oxide compounds like ceramics [13]
  - uneven heating occurs

Different applications, therefore, have specific heating requirements. The proposed technique does not aim to satisfy each and every application's requirements, but many of the requirements are common to a range of applications, making feasible an applicator that can be adapted to suit a number of these applications if its heating patterns can be suitably adjusted.

2.7 Conclusion

Magnetron tubes are used predominantly to generate high power microwave radiation for MDH. The magnetron's operation from start up to stable oscillation and spoke formation was explained using a time domain description.
Analysis revealed that objects exposed to microwave fields do not possess fixed temperature profiles, but exhibit constant temperature differentials instead. The concern of microwave dielectric heating is therefore not so much the heat produced in the material, but rather the applied heating field. Hence the ability to control the field, and with it the heating patterns, is crucial to the successful application of microwave dielectric heating.
A topology that can achieve this by synthesising a uniform or pre-determined, controllable field, and consequent heating patterns, will now be described.

The tubes can be locked to an injected signal in order to synchronise them. Locking happens faster with the injected signal closer to the natural frequency of the oscillator, even for small injected signal amplitudes. This is ideal for injection locking of magnetron tubes of the same kind.

Chapter 3

Interference Modulation: Theory and Topology

The synthesis of patterns necessitates a look at various magnetron based single source and injection locked multi-source interference modulation topologies. High-power phase shifters are discussed with a view to the necessary practical implementation of the interference modulator. They are components essential to the pattern synthesis process.

The approach is as follows:

- Outline various interference modulation topologies,
- Propose a topology suitable for implementation later on,
- Investigate high power phase shifters,
- Describe the synthesis of features by interference modulation, and
- Describe the synthesis of patterns using features.

In this chapter, the theoretical description outlining the various topologies is given. Results based on theory are presented, and are tested by way of measurements which are presented in subsequent chapters.

3.1 Interference modulation topologies

Interference modulation requires frequency coherence. In section 2.5 it is noted that it is advantageous in a multi source topology to use identical sources and operate these under similar operating conditions. The result: Driving points and frequencies of these high power narrow band magnetron based sources are close to each other. This facilitates their control by injection locking.

3.1.1 Interference Modulation Topologies

Both subdivided single sources and multiple, injection locked sources can be used to produce the required interference. The microwave interferometer topologies of Figure 16 have been used. This work is described in more detail by this author in [18][45][46].

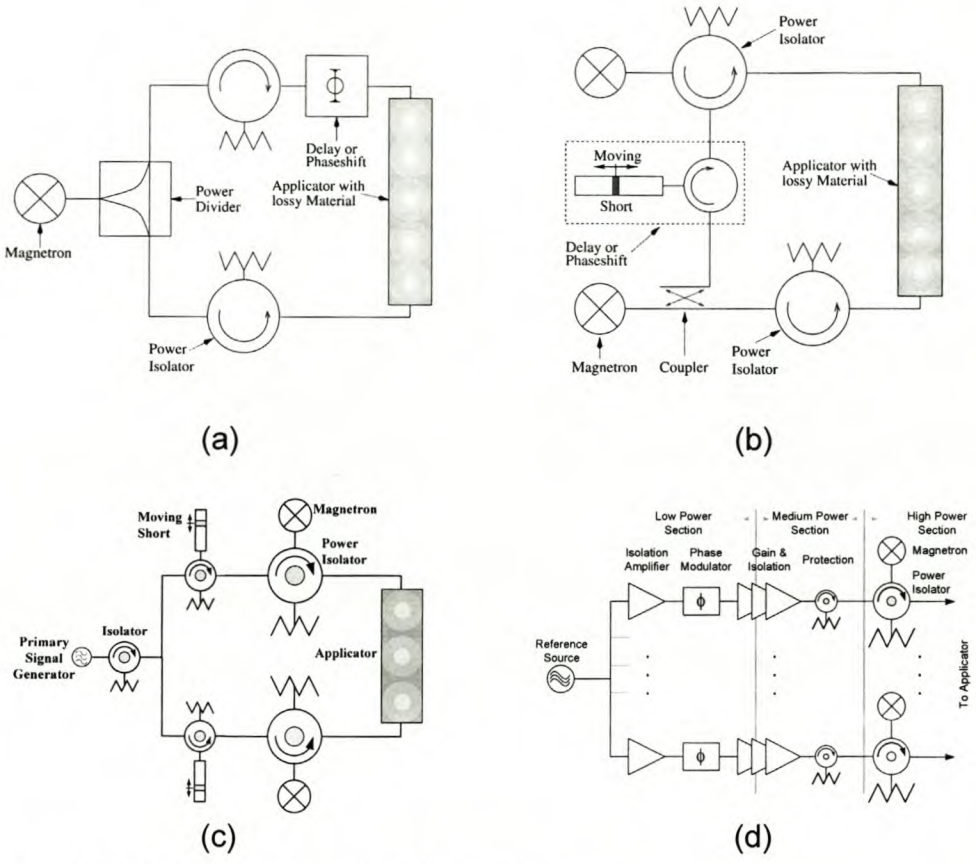

Figure 16: Interference modulation topologies.
Single subdivided source in (a) and multi-source injection locked topology in (b) or with separate reference in (c) and (d) (after this author in [18]).

Figure 16a is a direct adaptation of the optical bench, but implemented with waveguides for microwave use. The signal emanating from a magnetron is split by a power divider, a variable delay or phase shifter introduced in the upper path, and both signals are re-combined in an applicator producing features by interference. Power isolators in both paths protect the source from reflections.
Although simple in construction, a single subdivided source exhibits the following drawbacks:

- Graceful failure does not exist,
- Long high-power waveguides are required for physically large applicators (long line effect!), and
- Delay and phase shifter components are located in the high power path.

These drawbacks are overcome using the topology shown in Figure 16b. Here multiple sources are injection locked for frequency coherence. Only a fraction of the main path's power is required for injection locking [31], resulting in a low-power section for injection locking and phase control. This implementation features:

- Lower power control components resulting in lower cost,
- Higher power scalability,
- Complexity which is comparable to the single source topology, and
- Sources' heads can be located at the point of application, interconnected solely by low-power signal runs required for injection locking.

For improved spectral purity a modification of the multi-source topology is shown in Figure 16c. A separate source (not necessarily magnetron based) provides the reference signal. Further refinement of the topology leads to that shown in Figure 16d, where the source's heads contain phase modulators, medium power amplifiers and high gain magnetron based sources. The medium power amplifier provides isolation, and at the same time serves as the driver for the reflection amplifier (formed by magnetron and circulator). The amplifier is followed by a circulator based isolator for protection against high incident power. These heads require only a very low power reference signal to maintain frequency synchronism between the sources. A phase modulator in each path is used to change the relative phase difference between the sources and provides the means to control the synthesis process. The added advantage of this topology is that the microwave sources become independent microwave power modules, a desirable feature for industrial applications [3][50].

The topology that will be considered in the following subsections is that of Figure 16b. Details of its implementation are provided in Chapter 4. In this topology, a variable-delay phase shifter is used to introduce a phase shift between sources.

3.1.2 Variable delay and phase shifter

These are briefly discussed since they are required for automated control. A number of techniques, particularly suitable to low-power applications, can be found in [110]. PIN diodes are also suitable for low and medium power applications. Their use is described in [111]. For high power applications and designs based on waveguides, the structures in Figure 17 are most suitable. Moving shorts change the delay, while circulators or 3-dB hybrid couplers separate signals and ensure matching at the ports [112].

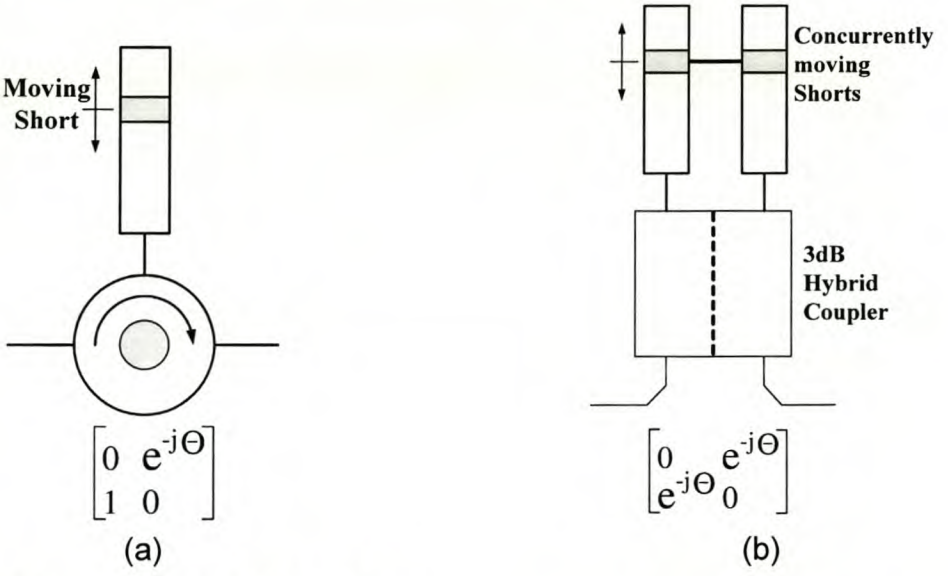

Figure 17: High power phase shift structures.
Variable shorts can be combined with a circulator (a) or with 3-dB hybrid couplers (b) to form high power phase shift structures.

Stepped variable delays are sufficient for the technique described and the moving shorts in Figure 17 can be replaced by an array of switched PIN diodes.

3.2 Pattern Synthesis

The concept of features and patterns, as used in this context, is briefly described before developing the theory of interference modulation using multiple frequency coherent signals to obtain them.

> Features are the basic elements that compose a pattern. A picture may be a pattern composed of features such as colours, textures and shapes. This concept is illustrated by the sequence of pictures in Figure 18.
> While the term 'field patterns' is also used to refer to what are in fact 'field features', they are not generally interchangeable. As such, it is important to understand the distinction between the two concepts, in order to understand this chapter.

It can therefore be said that 'field features' obtained by interference modulation are used to synthesise pre-determinable 'field patterns', which are directly related to heating patterns.

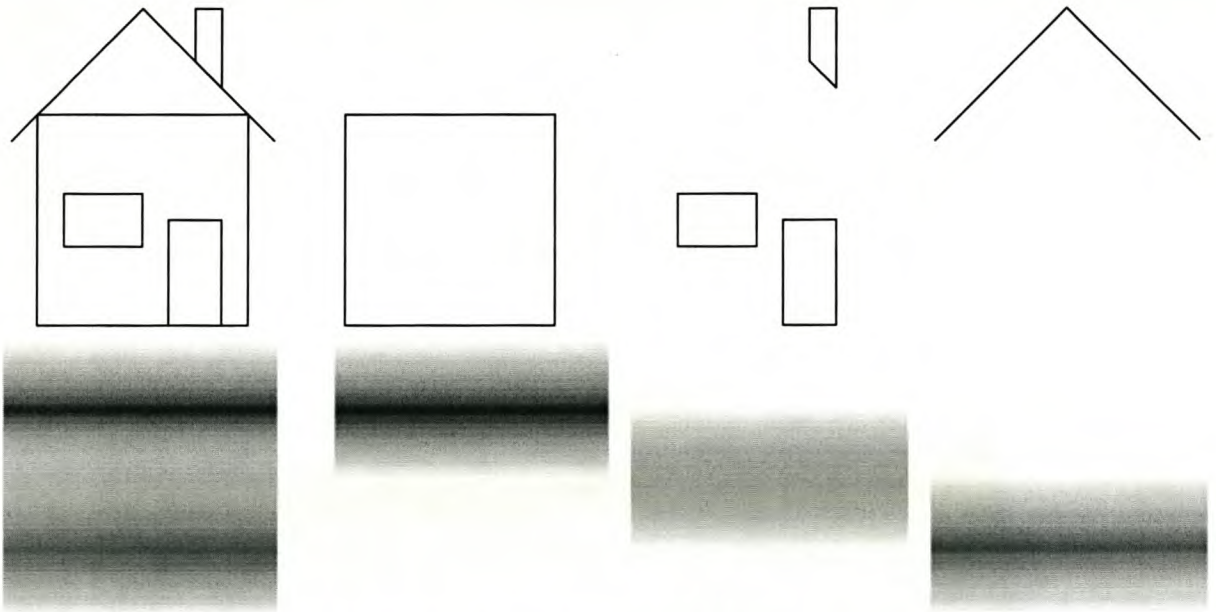

Figure 18: Illustrating how patterns are composed of features.
Each pattern in the first column is composed by equal weighted superposition of the three features on its right hand side.

This can also be described with set-theory, where features are referred to as *bases* [28][113][114]. With the definitions in (18), (19) and (20), the statement above is expressed in set-theory notation by equation (21).

$$D_{\phi} \in \text{Domain of Phases} \tag{18}$$

$$D_{I} \in \text{Domain of Features} \tag{19}$$

$$R_{I} \in \text{Subset or Range of } D_{I} \tag{20}$$

I_E in Figure 19 is obtained as follows:

$$I_E = I(\phi) \text{ or } D_\phi \rightarrow R_I : \phi \rightarrow I_E(\phi) \quad (21)$$

In equation (21) the independent variable $\phi \in D_\phi$ is mapped to the dependent variable $(I_E \in R_I) \in D_I$. The process may produce a fragmented range R_I, but is a subset of D_I, i.e. $R_I \in D_I$. In addition, different elements of D_ϕ may map to the same element in R_I, a unique mapping from D_ϕ to R_I. However, the reverse does not hold, leading to ambiguous solutions (see Figure 19).

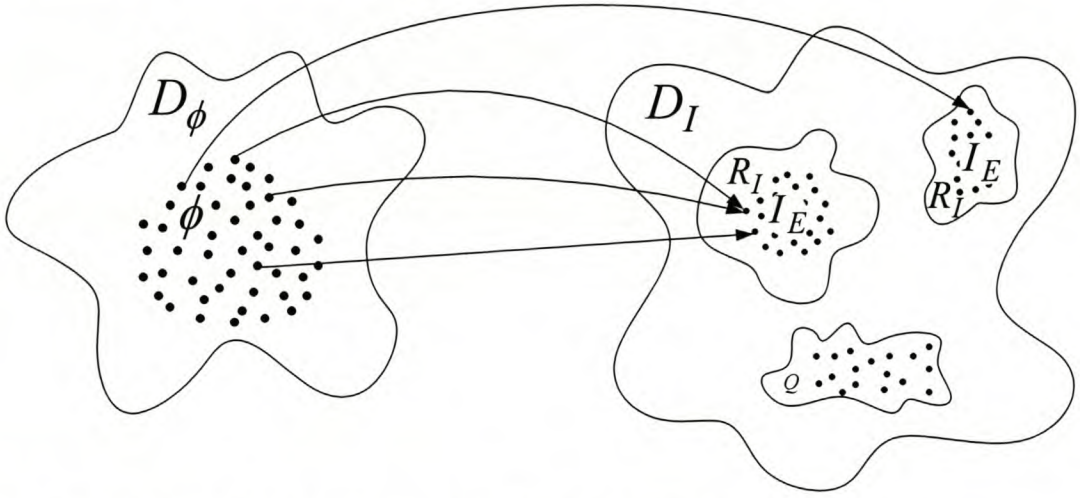

Figure 19: Depiction of set-theory equation (21) (after [113]).

The object is to find I_E s sufficient to span the range R_I by their linear combination. These I_E s are called the bases of R_I, denoted I_{EB}, and form the subset $I_{EB} \subseteq R_I$. The elements in the subset of I_{EB} are sufficient to represent the entire range R_I by linear combination. In the example of Figure 18, the range R_I is represented by the pattern on the left hand side, which can be spanned by the linear combination of the three I_{EB} s on its right hand side.

Applied to microwave heating, features (in D_I) are obtained by interference of incident frequency coherent signals. This process is described in the following subsections.

3.3 Interference Modulation for Feature Generation

Assume a waveguide is used as applicator, with co-ordinates and dimensions as shown in Figure 20. Electric field sources are present on either side, and are represented by equations (22) and (23) [34][41]. Both sources may have associated absolute delays d_a and d_b and are not in phase.

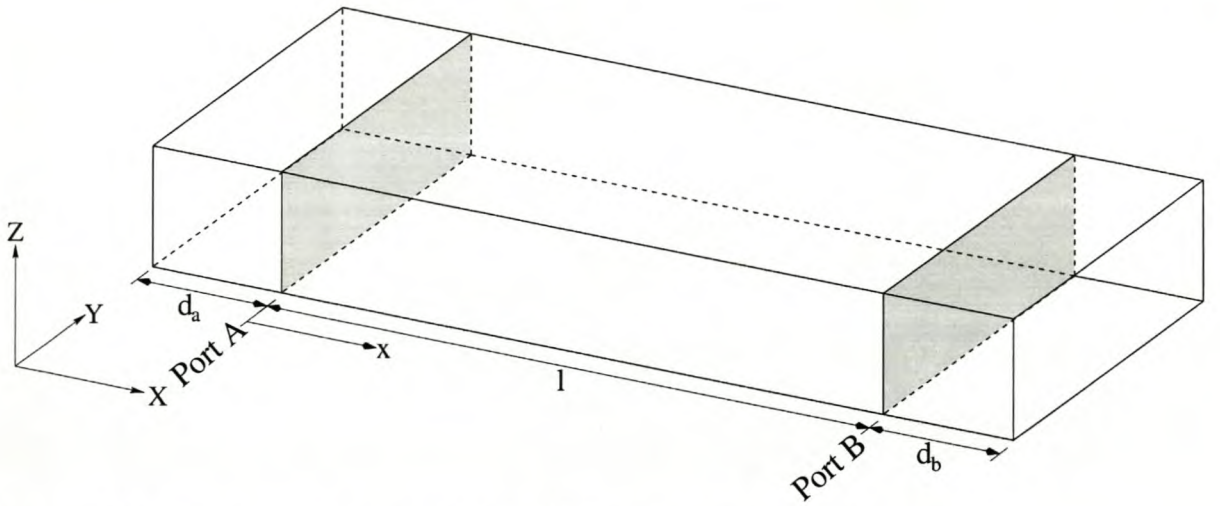

Figure 20: Dimensions and co-ordinates of waveguide set-up used.

$$E_{ya} = \frac{\gamma Z_{yz} H_0}{\beta_c^2} \frac{\pi}{Z_l} \sin\left(\frac{\pi Z}{Z_l}\right) e^{-\gamma X_a} = p_a(Y,Z) e^{-\gamma X_a} \quad (22)$$

$$E_{yb} = \frac{\gamma Z_{yz} H_0}{\beta_c^2} \frac{\pi}{Z_l} \sin\left(\frac{\pi Z}{Z_l}\right) e^{-\gamma X_b} = p_b(Y,Z) e^{-\gamma X_b} \quad (23)$$

where

γ = Propagation constant $\alpha + j\beta$ [1/m]

Z_{yz} = Transverse wave impedance $= \frac{Z_0}{\sqrt{\varepsilon_{eff}}}$ [Ω]

H_0 = Magnitude of magnetic field [A/m]

$\beta_c = \sqrt{\left(\frac{n\pi}{Y_l}\right)^2 + \left(\frac{m\pi}{Z_l}\right)^2}$ = cutoff wave number [rad/m]

$X_a = x + d_a$ = Offset relative to port A [m]

$X_b = l - x + d_b$ = Offset relative to port B [m]

$\varepsilon_{eff} = 1 - \left(\frac{\lambda_0}{\lambda_c}\right)^2$ = effective dielectric constant of waveguide [1]

Interference E_y described by (24) occurs in the presence of E_{ya} and E_{yb} inside a waveguide. Its field at position 'x' along a waveguide of length 'l' with $p_a=p_b=p$ is given by (25). Both the available average power density described by the Poynting vector (26) [34] and the power dissipated in a dielectric material (16) rely on $|E_y|^2$ (27) (by this author in [46]). Therefore both are directly related to the electric field distribution. Similarly, for magnetic materials, $S_{av} = (1/2)|H_z|^2 \, Re(Z_0)$.

$$E_y = E_{ya} + E_{yb} = p(Y,Z)(e^{-\gamma X_a} + e^{-\gamma X_b})$$

$$= p(Y,Z)\,(e^{-\gamma(x+d_a)} + e^{-\gamma(l-x+d_b)}) \quad (24)$$

$$E_y = p(Y,Z) e^{-\gamma X_a} (1 + e^{-\gamma d}) \quad (25)$$

where

$$d = X_b - X_a = l - 2x + (d_b - d_a) \text{ [m]}$$

$$S_{av} = \frac{1}{2}\mathrm{Re}\left(\frac{E_y E_y^*}{Z_0}\right) = \frac{1}{2}|E_y|^2 \mathrm{Re}\left(\frac{1}{Z_0}\right) \quad (26)$$

$$|E_y|^2 = E_y E_y^* = |p(Y,Z)|^2 e^{-2\mathrm{Re}(\gamma)X_a}(1 + e^{-2\mathrm{Re}(\gamma)d} + 2e^{-\mathrm{Re}(\gamma)d}\cos(\mathrm{Im}(\gamma)d)) \quad (27)$$

3.3.1 Features through Phase Shift

Consider, now, the effect of changing the relative phase difference d_b - d_a on the position of peaks and troughs of $|E_y|^2$ for the cases of no load, lossless sample and real-life lossy sample inside the applicator.

Lossless empty applicator: With $\mathrm{Re}(\gamma) = 0$ (27) reduces to (28).

$$|E_y|^2 = 4|p(Y,Z)|^2 \cos^2\left(\frac{\pi}{\lambda_g}d\right) \quad (28)$$

The extrema of the cosine term are therefore uniquely determined by the relative phase shift between incident signals. This is demonstrated in Figure 21 for an empty 0.5 m long WR340 waveguide with imposed signals at 2450 MHz. It is noted that none of the features on their own represents a desirable uniform field distribution, but the peaks of 0° and the troughs of 180° appear to complement each other and, indeed, their average in Figure 22 remains uniform in the x-direction.

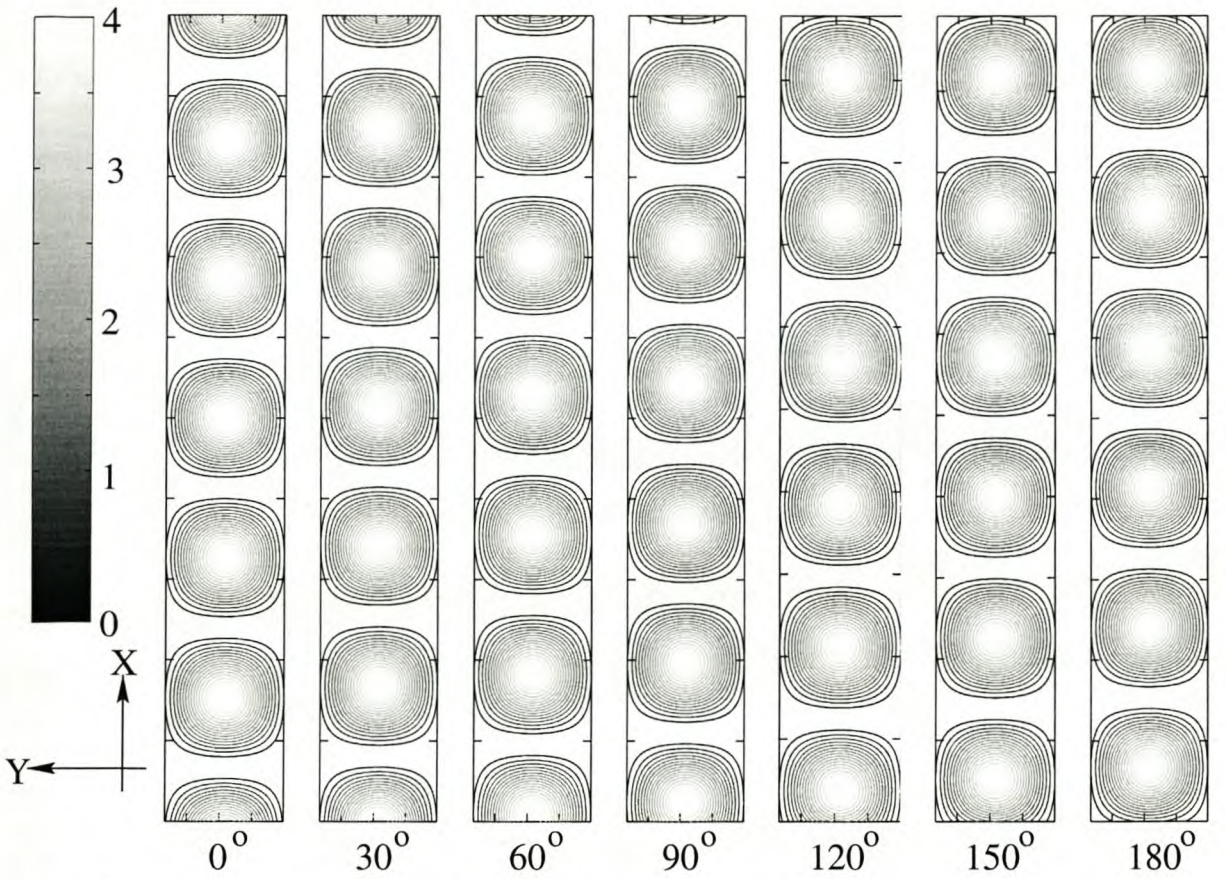

Figure 21: Energy concentration zones of features in the X-Y plane.
$|E|^2$ representative of energy concentration zones of features in the X-Y plane in Figure 20 produced by interference at various relative phase differences between incident signals in a 0.5 m long WR340 waveguide at 2450 MHz in the absence of material.

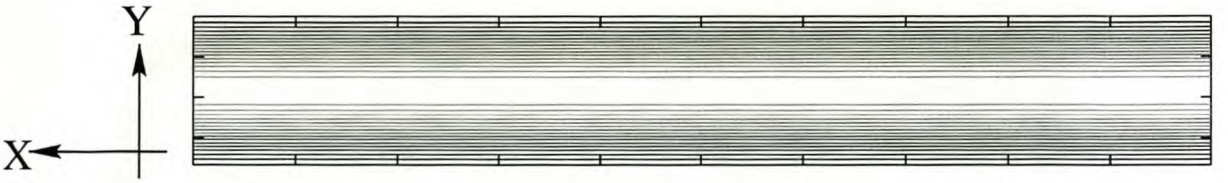

Figure 22: Average of 0° and 180° features of Figure 21.

Lossless sample: A 25.4 mm (1") thick slab of lossless material with $\varepsilon_r = 10 - j0$ is centred in the same waveguide (Figure 21).

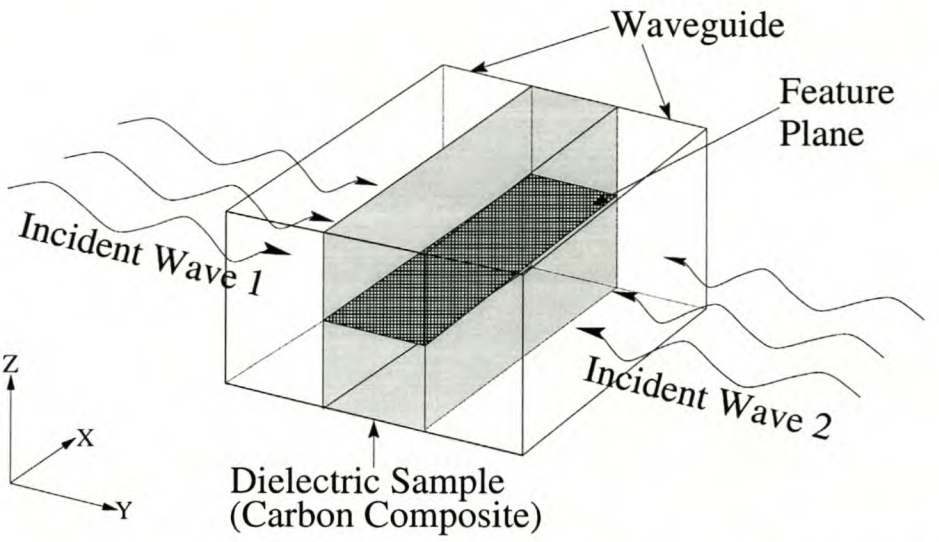

Figure 23: Diagram of sample placement inside waveguide and feature plane used.

Focusing on the fields inside the slab we find in Figure 24 that, as before, changing the relative phase difference can easily shift peaks and troughs. Also, the average of the 0° and 180° features is uniform along the x-axis (see Figure 25). A difference found with respect to the previous example is a change in wavelength and reflections at the discontuniuty, as is expected.

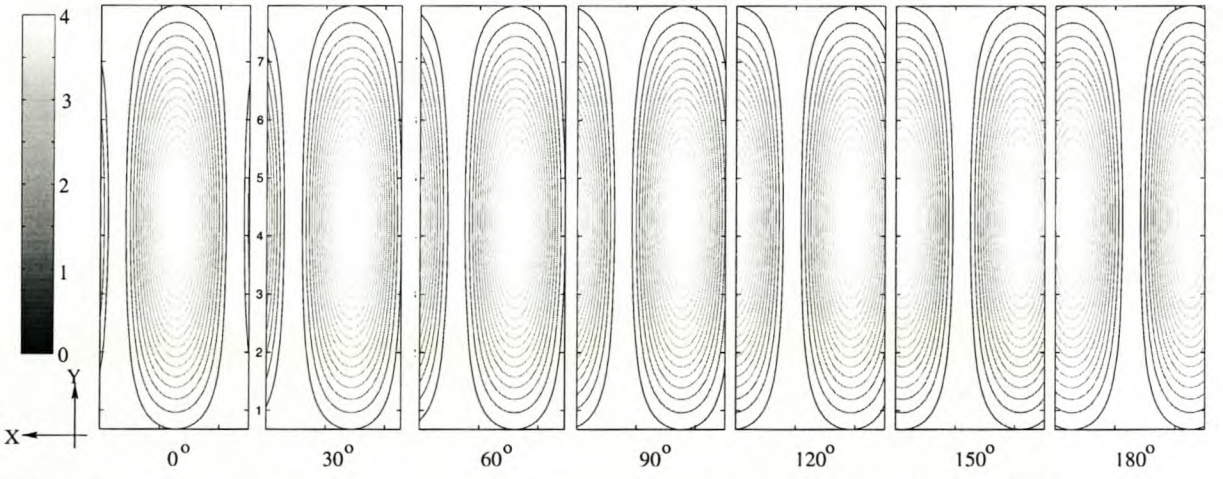

Figure 24: Energy concentration zones in the X-Y plane with sample of $\varepsilon_r = 10 - 0\mathrm{j}$.
$|E|^2$ representative of energy concentration zones in the X-Y plane produced by interference at various relative phase differences between incident signals in a 0.5 m long WR340 waveguide at 2450 MHz with centred 25.4 mm thick sample of $\varepsilon_r = 10 - 0\mathrm{j}$.

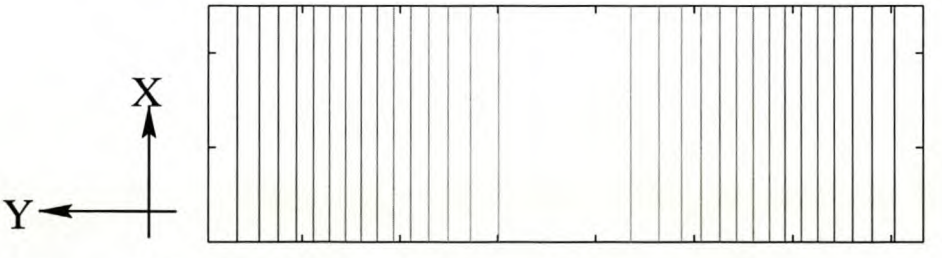

Figure 25: Average of 0° and 180° features of Figure 24.

Lossy sample: The same set-up as before; this time with granular active carbon composite of approximate relative dielectric constant $\varepsilon_r = 10 - 2.5j$ [115] used as the material. Under microwave exposure the slab now heats up and in the process weakens the field travelling through it (note the change in scale in Figure 26). Interference still takes place but the intensity of the features changes with depth into the lossy material. Consequently the average of 0° and 180° features is no longer uniform (Figure 27).

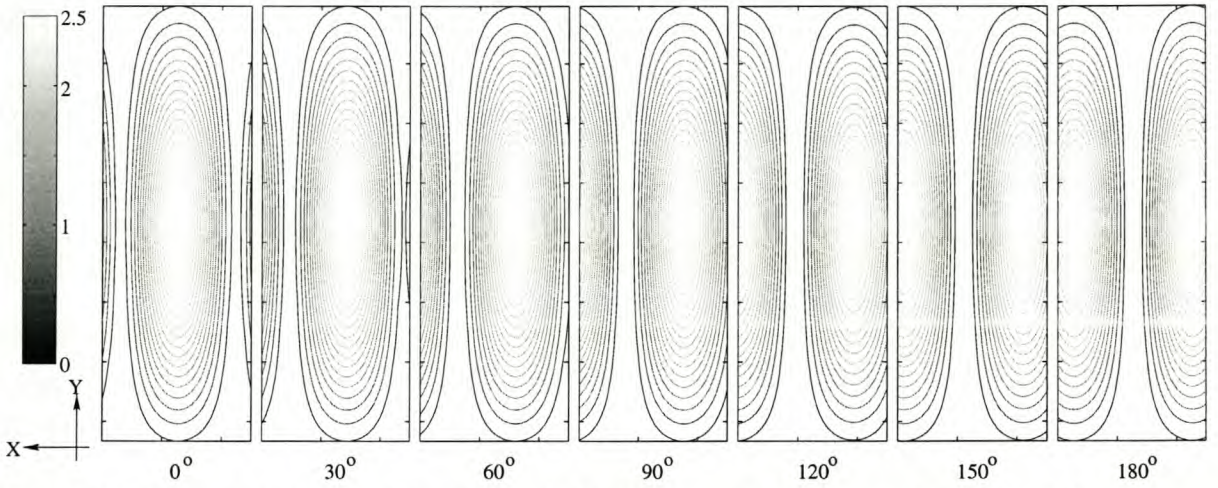

Figure 26: Energy concentration zones in the X-Y plane with sample of $\varepsilon_r = 10 - 2.5j$. $|E|^2$ representative of energy concentration zones in the X-Y plane produced by interference at various relative phase differences between incident signals in a 0.5 m long WR340 waveguide at 2450 MHz with centred 25.4 mm thick sample of $\varepsilon_r = 10 - 2.5j$.

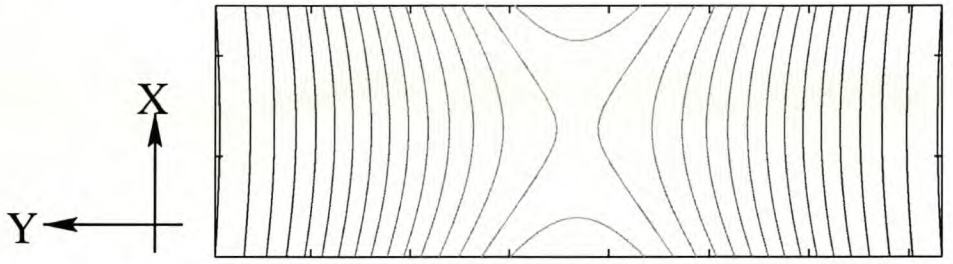

Figure 27: Average of 0° and 180° features of Figure 26.

3.3.2 Resolution of features

Typically, a uniform field distribution is desired. If heating is to be applied to specific areas, then the resolution at which the features can be placed in the material becomes important. From Figure 22, Figure 24 and Figure 26 it is seen that singular heating is only guaranteed in the presence of a single peak inside the material. Such a single peak corresponds to half a wavelength, and hence represents the resolution limit.

The wavelength inside a material depends on the real part of its dielectric constant. For surface treatment the resolution tends not to be an issue. Resolution does, however, tend to be an issue in the case of volumetric heating. In volumetric heating

the loss of the material affects the resulting heating pattern inside a material (see Figure 25). It can therefore not as easily be compensated for, say for example by adding another feed, as would be the case for surface treatment. Instead, a resolution limit exists, imposed by physical constraints.

For surface treatment and near-surface treatment it is possible to increase the resolution, using a technique suggested in [14]. Basically, a high resolution scanning beam, or field obtained from a laser source or a steered antenna array at sufficiently high a frequency is applied to a material. The material used by [14] was a ceramic that increases its microwave loss at higher temperatures in the microwave bias field. The method has prospects for surface and near-surface treatment, as well as for thin sheets of ceramics.

The resolution limit is a boundary which can be approached but not exceeded. Pattern synthesis is a means to approach this limit.

3.4 Pattern synthesis from features

In Figure 22 and Figure 25 one finds that averaging of certain features, produced by incident signals of specific relative phase difference, results in a reasonably uniform pattern in the lossless case, but the same does not apply when losses come into play (Figure 27). Weighting of features before averaging can compensate for attenuation and enhance the uniformity of the overall pattern.

3.4.1 Description of pattern synthesis

The synthesis of patterns from features is divided into two steps:

De-composition: At first a given pattern is de-composed into known features. Time-weights of each feature on the overall pattern are obtained through pattern recognition [27][28] or optimisation.

Re-composition: The overall heating pattern is synthesized by application of the weights from the de-composition step to the individual features in, for example, a subsequent time averaging manner. The result is a redistribution over time of the effective energy that heats the material.

Re-composition only requires time-weighting factors because the features are intrinsically known to the system. All computational effort, therefore, resides in the de-composition stage alone.

Mathematically each E-field intensity distribution feature $I_E(\phi_n)$ is associated with a time weighting factor Δt_n, where the ϕ-space has been discretized by N. By time-averaging a new intensity distribution pattern, $\overline{I_E}$ is synthesised according to (29) [18], completing re-composition.

$$\overline{I_E} = \frac{\Delta t_1 I_E(\phi_1) + \cdots + \Delta t_N I_E(\phi_N)}{\Delta t_1 + \cdots + \Delta t_N} = \frac{\sum_{n=1}^{N} \Delta t_n I_E(\phi_n)}{\sum_{n=1}^{N} \Delta t_n} \tag{29}$$

Equation 16 links field intensities to power dissipated in materials which, in turn, is related to the change in material temperature by equation 17.

Based on section 3.3.2, which deals with the resolution limit, a residual error $I_{Err} = I_E - I_D$ remains between the desired intensity pattern I_D and the synthesised pattern $\overline{I_E}$ resulting from:

- Sharp discontinuities which cannot be resolved,
- Insufficient coverage of features, due to lack of freedom of features, and
- Poor choice of time-weights.

It is the task of an optimisation algorithm to reduce the residual error and to produce an optimum pattern from a set of given base features. A least square approach where $I_{Err} = \sum \left| \partial \overline{I_E} / \partial x \right|^2$ is minimised has been taken by this author in [18] to obtain a uniform pattern. Various other optimisation techniques [96][97][116]-[119] may be possible but are beyond the scope of this research.

3.4.2 Influence of the applicator on the pattern

A waveguide is used to demonstrate the idea, but other applicators are feasible. The slanted reactor in Figure 28 also produces different patterns for varying relative phase differences.
Gravity flow is used to move material such as granular carbon through the applicator. The features depicted in the same figure are oriented in the direction of material flow.

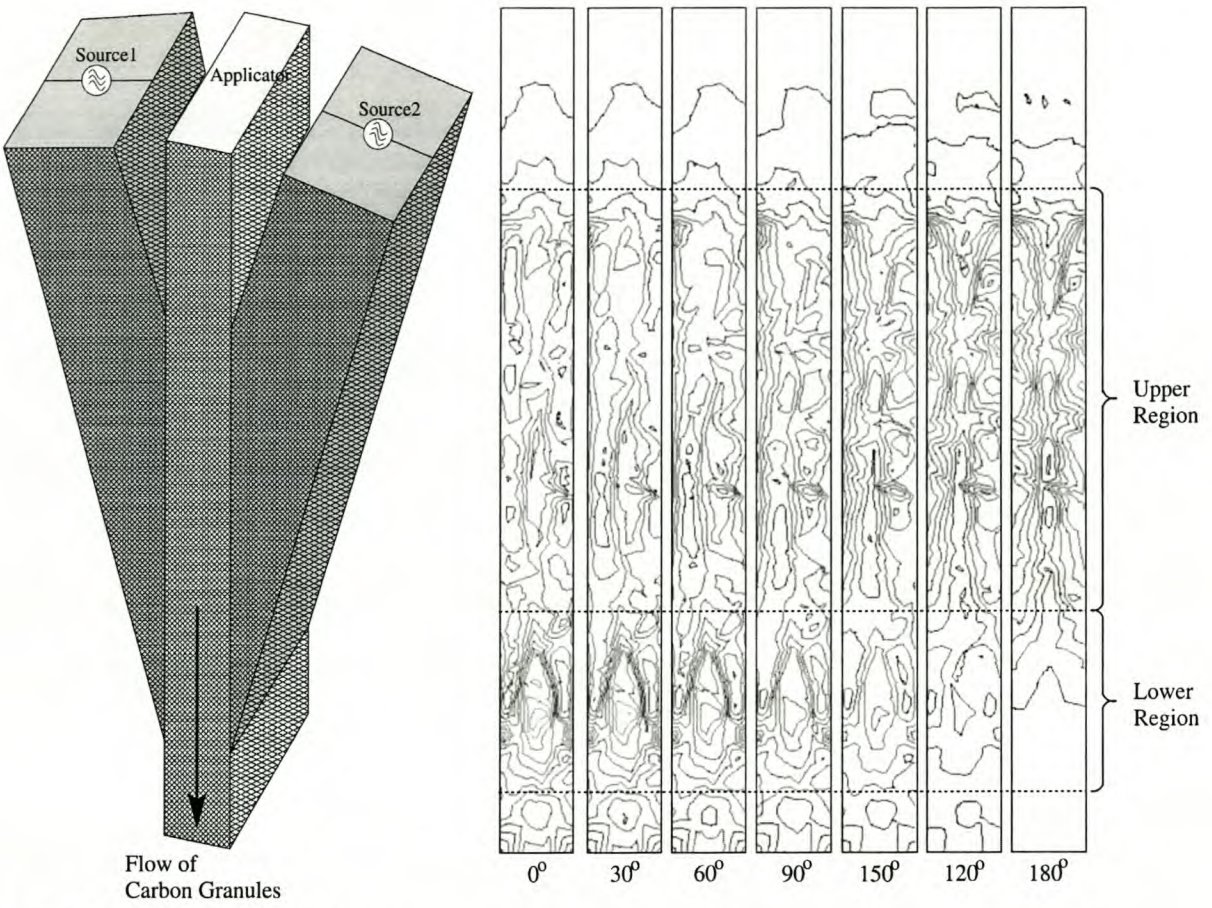

Figure 28: Slanted applicator.

The material ($\varepsilon_r = 10 - 2.5j$) is located in the centre between the two waveguide feeders and flows in the direction indicated (by this author in [45]). The feature slices were taken in the centre of the narrow wall of the applicator.

The total energy of each plane is the same; they differ only in their distribution densities. Moving from left to right, the density moves from the lower region into the upper region. Since the lower region is somewhat shorter, a higher energy concentration results. Since the features are, again, a function of the relative phase shift between sources, heating distribution can again be affected by a change of phase. As material moves through the applicator, heating requirements are adapted, resulting in gentler heating in some regions, by a change of the heating profile. The same principle can be applied to move the heating zone in zonal-heating apparatuses used for material purification.

Other applicators, including multi-mode cavities or leaky feeders, are possible, but the design and analysis of these is beyond the scope of this investigation [21].

3.5 Conclusion on implementation of topology

The control of fields and heating patterns is essential to microwave heating. Interference modulation, combined with a technique to synthesize patterns, was developed. It was shown theoretically to fulfil the requirement for a simple, controllable and, most importantly, pre-determinable method to obtain heating patterns.

The single frequency property of the topology allows narrow band sources such as magnetron tubes to be used. The sources are injection locked to ensure frequency coherence and, simultaneously, to control their relative phase difference. The latter determines the features used by the synthesis process. Lossy and lossless cases were covered, and it was found that the topology can produce a uniform or particular heating pattern in either. The topology is limited only by pattern resolution constraints.

Implementations of several interference modulation topologies and phase shifting topologies were discussed in detail, and a topology suitable for a practical implementation was determined. Its principles were explained and exemplified with a waveguide as applicator. The synthesis procedure time-averages features. These result from varying the relative phase amongst different sources. The notion of discrete relative phase steps was introduced. It simplifies implementation considerably.

The proposed topology and its theoretical description predict good results. This prediction needs to be confirmed by measurements made using a practical implementation of the topology, which follows in the subsequent chapter.

Chapter 4

Measurement and Results

The theory, the underlying principles and the tools for interference modulation are described in chapters 2 and 3. The first sections of this chapter show measurements that confirm this theory. In the subsequent sections, measurements regarding the synthesis of patterns by interference modulation are presented.
Measurements presented in the first sections confirm that:

- The magnetron model introduced in section 2.4 is an alternative to the Rieke diagram,
- The frequency coherence predicted does in fact exist,
- The relative phase shift between the sources is sufficient and directly related to the phase shifter, and that
- The required frequency coherence is not disrupted by the phase shifter over its operating range.

In subsequent sections, measurements pertaining to interference modulation, its application in the production of features and the synthesis of heating patterns in lossy materials are presented. Furthermore, theoretical predictions, simulations and patterns obtained by a visualisation technique are compared and discussed.

4.1 Injection locking of magnetrons for the multi-source topology

The goal is to build the structure shown in Figure 29.

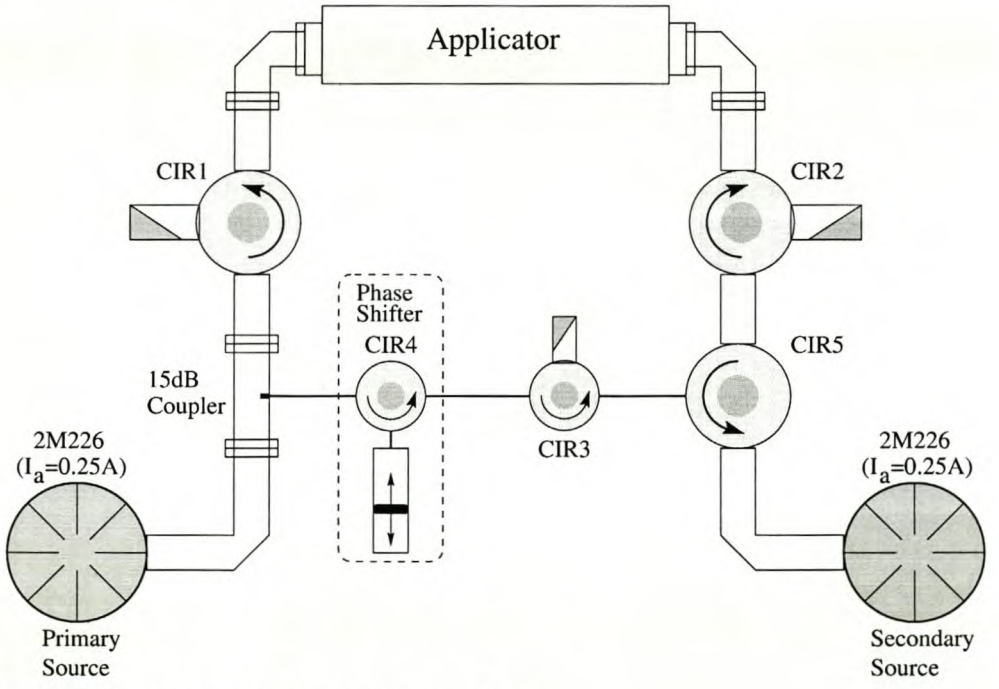

Figure 29: Target injection locking configuration.

The oscillator model in chapter 2 describes the phenomena of injection locking. From the model, an equation for the injection locking bandwidth is derived as shown by equation 8. Using the model and its associated equations, the locking bandwidth is calculated and verified by measurements, and a suitable locking frequency is determined.
The locking time is also determined, because this time sets the upper bound on how frequently the phase can be altered while the oscillator remains locked.

4.1.1 Locking bandwidth

The locking bandwidth is obtained from (8) for which the following values are obtained from measurements made of the magnetron oscillator (see section 4.2 later):

$$\omega_0 = 2\pi 2450 \text{ MHz}$$

$$R = (5297.8\ \Omega \| 533.16\ \Omega) = 484.4\ \Omega$$

$$C = 17.1931 \text{ pF}$$

$$Q = \omega_0 R C = 128.1$$

Substituting these into (8) with an effective gain of

$$\sqrt{P_{out}/P_{in}} = \sqrt{825/25} = 5.745 \equiv 15.2 \text{ dB}$$

yields a predicted locking bandwidth of 6.658 MHz. Measurements of the locking bandwidth under dynamic and quasi-static conditions (Figure 30) produced bandwidths of 8 MHz and 9 MHz respectively, with the difference arising from dynamic effects and locking time constraints. The frequency contours of Figure 31 were measured according to [51][91], and confirm this bandwidth for $|\Gamma| = 0.174$.

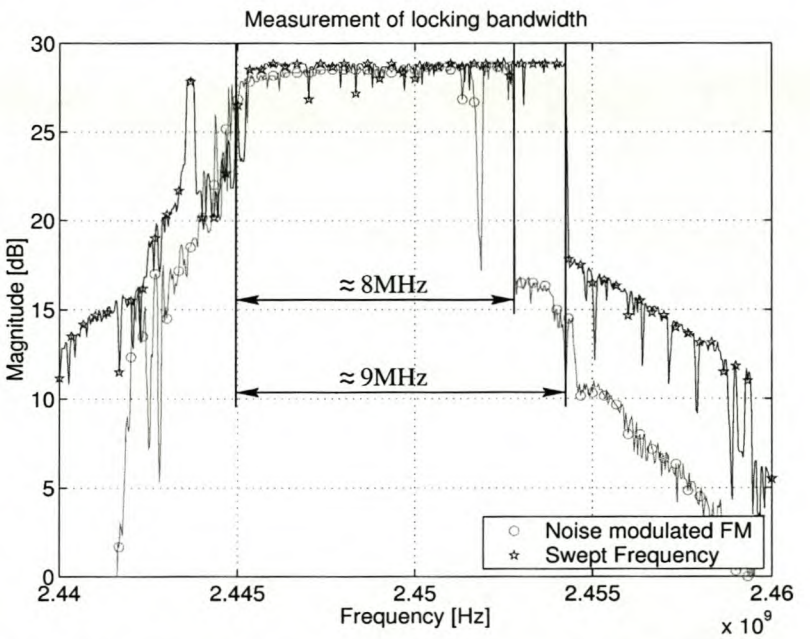

Figure 30: Injection locking bandwidth measured by two different methods.

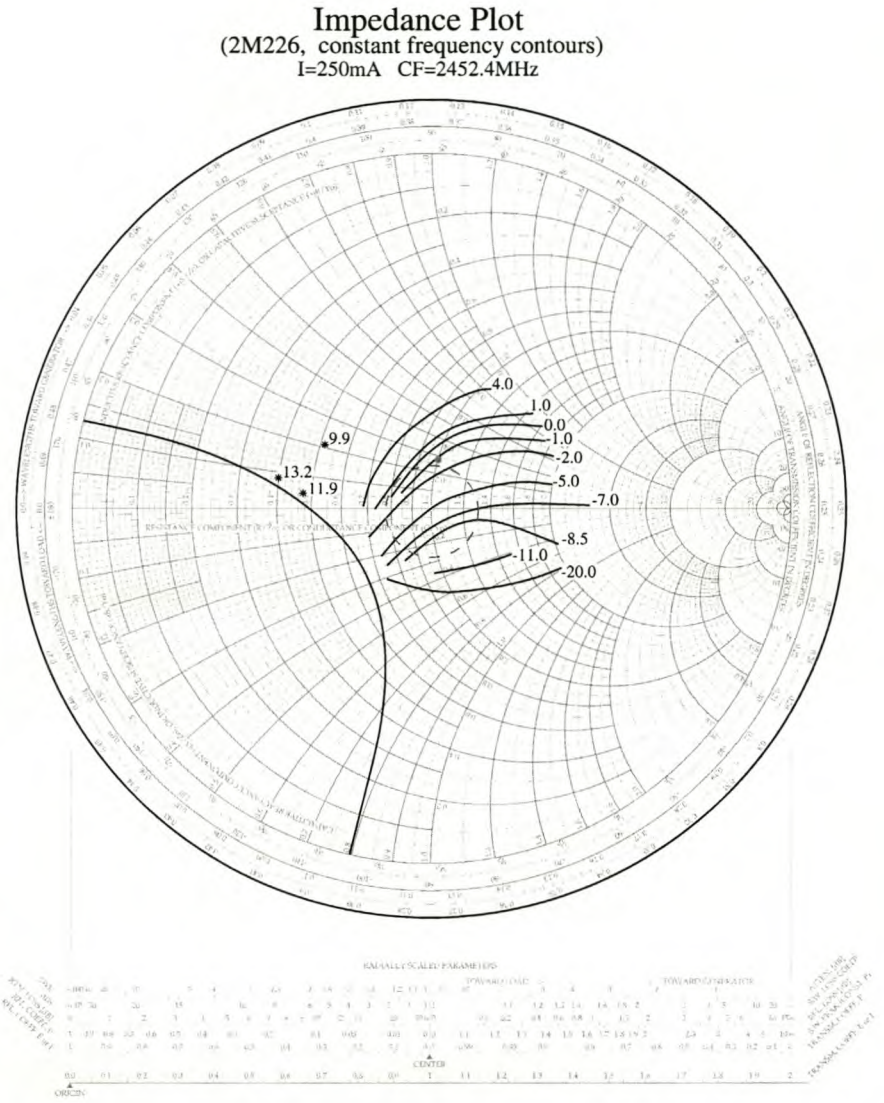

Figure 31: Frequency contours for the 2M226 magnetron tube measured according to [51] [91]. The frequency offset is stated in MHz from the Centre Frequency (CF).

The predicted bandwidth is approximately 1.8 MHz narrower than the measured one. This agrees well with the measurements, considering that [85] states that a conservative estimate may be obtained from (8) only. Theoretically, as well as by measurement, 2450 MHz is the frequency at which locking is ensured with the lowest injected signal power. This frequency is thus henceforth used, as the injection locking frequency.

4.1.2 Locking-time

Using the values above, the locking-time is computed from (9) as $t = 0.455\ \mu s$, equivalent to 1115 periods at 2450 MHz. This represents the time it takes theoretically to regain phase-lock after a ±90° instantaneous phase change has occurred. Therefore the frequency with which phases, and hence features, can be switched is theoretically limited to 2.2 MHz – in the extreme.
In fact, it can be shown (appendix A.2) that (8) only accounts for linear terms, which suggests that 2.2 million features per second is, again, a conservative estimate.

4.2 Magnetron model

An electronic Rieke diagram represents an alternative to its printed equivalent. Magnetron characteristics are, however, expressed in the form of operating curves in datasheets and not as model parameters. Model parameters must therefore be extracted from the published data. The modelling process to obtain these is detailed as follows:

- Measure cold source parameters,
- Extract active data, and
- Model and parameter extraction of active circuit from Rieke diagram.

For the modelling process, the Rieke diagram in Figure 13 is used.

4.2.1 Determination of model parameters

The aim is to determine and model Y_{active} of Figure 15. The launcher, delay line and resonator must be removed mathematically from the Rieke diagram. Parameters for the delay line and the resonator are found from cold measurements of the tube, using a network analyser (Figure 32), after mathematical removal of the launcher.

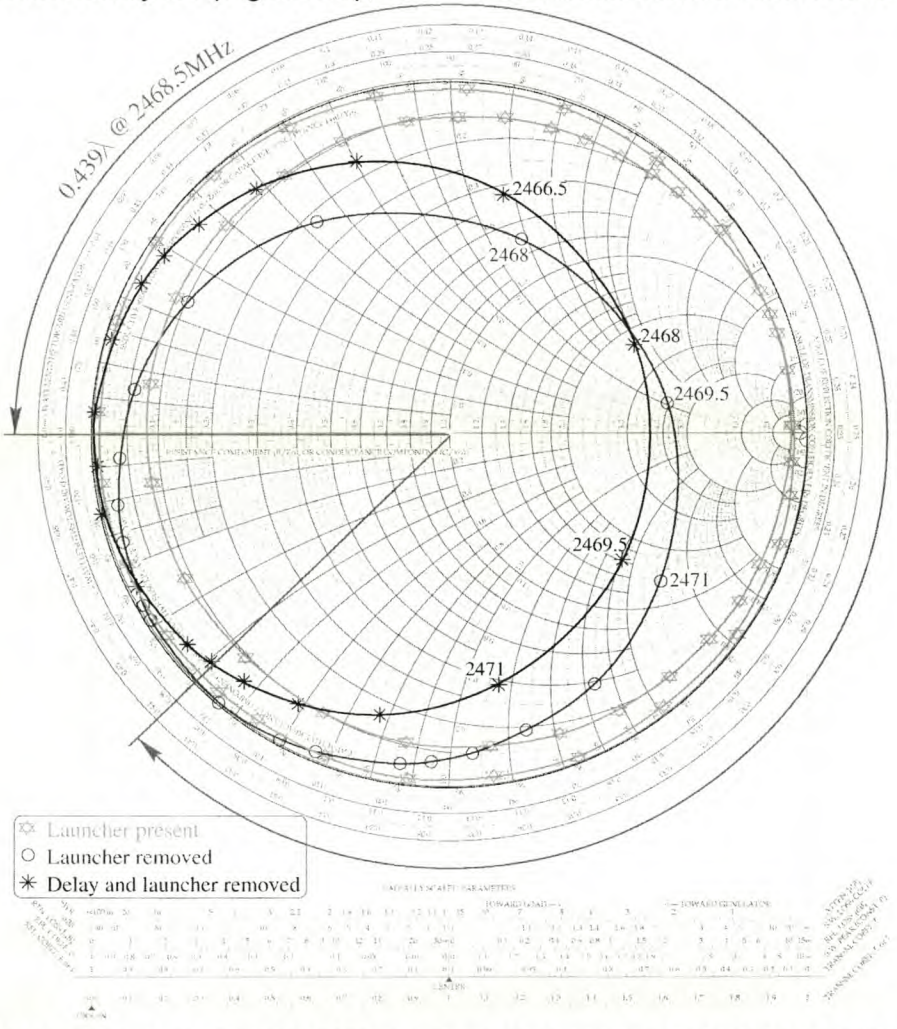

Figure 32: Cold measurement of 2M137 tube and steps in the removal of passive components to obtain resonator parameters.

The load, as seen by the tube's antenna, appears as an offset short and a dispersive transmission line, both connected in parallel. The latter represents the launcher. Hence a rotation, of 232.2 mm in our case, moves the measurement plane to the antenna leaving only an offset short of 17.8 mm to be removed. From Figure 32 a counter clockwise rotation of 0.439λ at 2468.5 MHz removes the intrinsic delay and moves the graph to the position of a parallel resonator. Values for the RLC modelled resonator are obtained as follows:

The intersection of the real axis on the Smith chart provides both the coupling coefficient of $\beta = 3.75$ [90] and the resonance frequency of $f_{Res} = 2468.5\ \text{MHz}$. Together with (30) to (36) [90] $R = 5297.8\ \Omega$, $L = 24.18\ \text{nH}$ and $C = 17.19\ \text{pF}$ are obtained as the RLC elements in Figure 33.

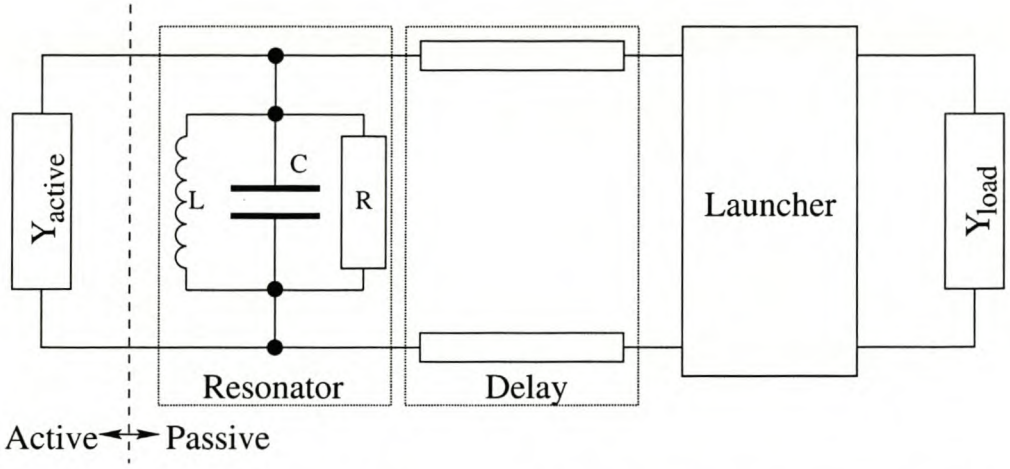

Figure 33: Magnetron model separated into its active and passive components.

$$Z_0 = \mu_0 c = 376.73\ \Omega \tag{30}$$

$$Z_g = \frac{Z_0}{\sqrt{1-\left(\frac{f_C}{f}\right)^2}} = 533.16\ \Omega \tag{31}$$

$$Z_{Res} = Z_0 \beta \tag{32}$$

$$\omega_{Res} = 2\pi f_{Res} \tag{33}$$

$$R = Z_0 \beta^2 \tag{34}$$

$$L = \frac{\beta}{\omega_{Res}} \tag{35}$$

$$C = \frac{1}{\beta \omega_{Res}} \tag{36}$$

The passive parameters are mathematically removed to reveal the behaviour of the active component as illustrated by Figure 34.

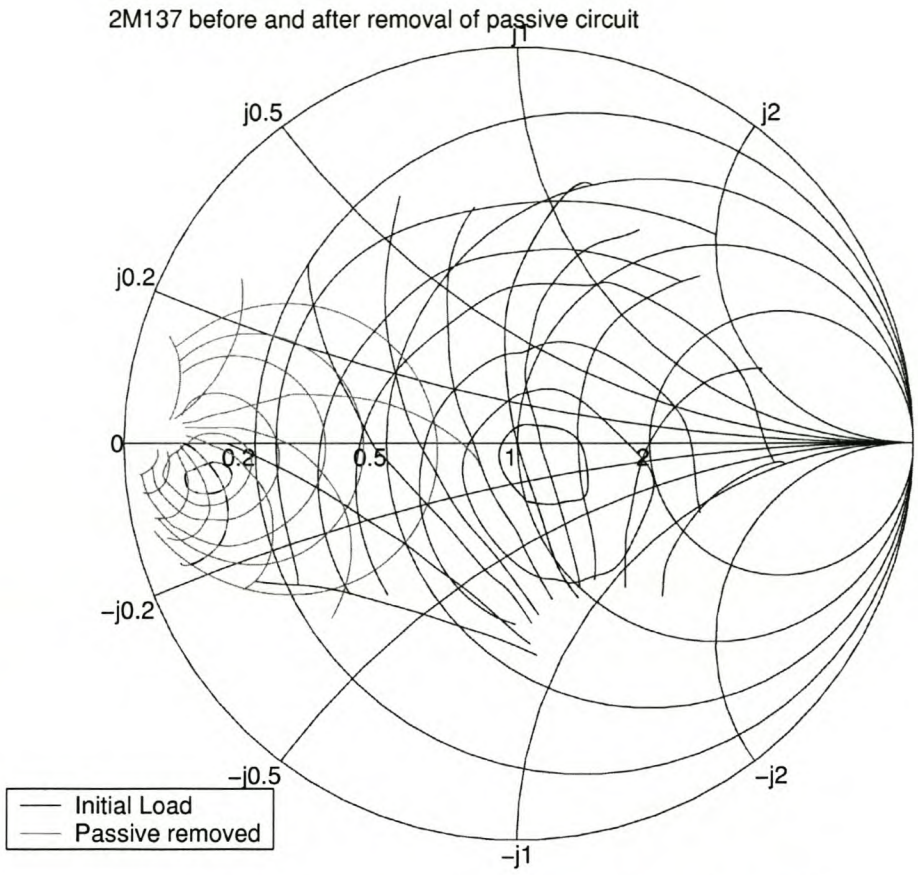

Figure 34: 2M137 before and after removal of the passive circuit elements.

For N=3 in equation 12 good agreement was found between the given and modelled values of the active impedance. Higher odd order approximations hardly improved results and were therefore not investigated further. The optimised coefficients of the 3rd order vector polynomial used in Figure 35 are as follows:

$$Y_0 = 34.31687 - 9.824220\,j$$

$$k_1 = \begin{bmatrix} 2.622433 + 3.853343\,j \\ -0.061125 + 0.006255\,j \\ -0.079684 + 0.271246\,j \end{bmatrix}$$

$$k_2 = \begin{bmatrix} 3.999364 + 4.697766\,j \\ -0.030624 + 0.000554\,j \\ -0.009879 - 0.002129\,j \end{bmatrix}$$

$$k_3 = \begin{bmatrix} 28.63449 - 27.77619\,j \\ 0.069900 - 0.243299\,j \\ -0.353102 - 2.134100\,j \end{bmatrix}$$

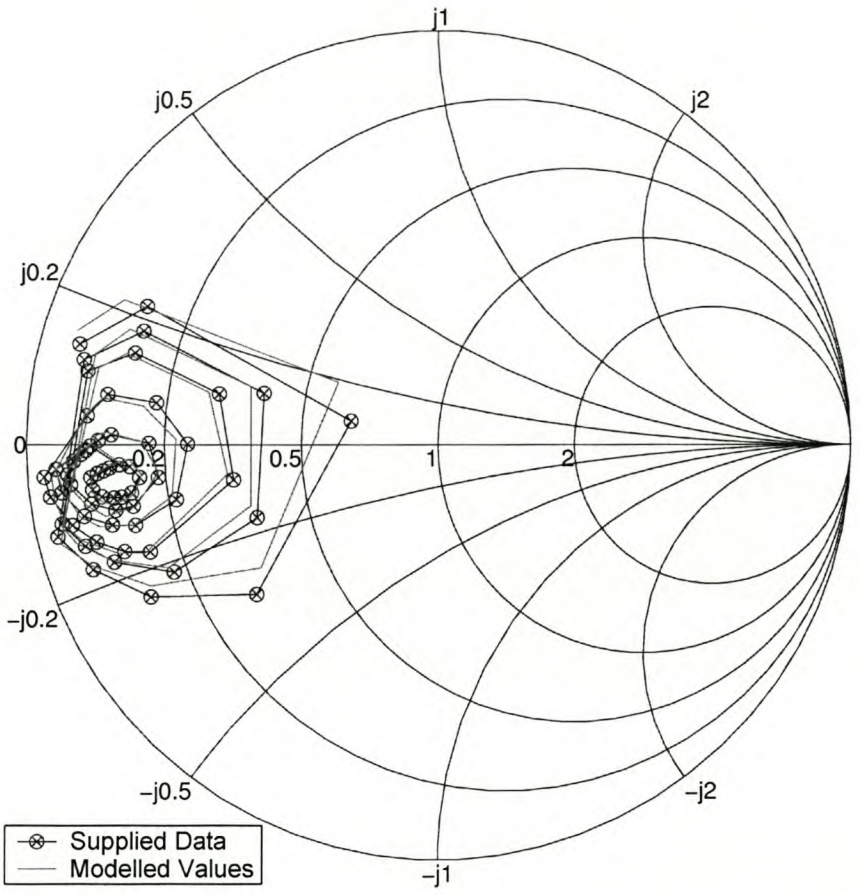

Figure 35: Comparison between supplied and modelled values for a 3rd order vector polynomial.

The final task in the modelling process is to show that useful data can be extracted using the passive model values and coefficients given above. Since this is a multi-variable polynomial problem, simulated annealing (see appendix C.2) was chosen as a suitable method for the reversing process. Instead of simply verifying and testing previously trained points to see that these are indeed correctly determined by the algorithm, the complex impedance was computed for a power-frequency field such that the model could be verified over a wider operating range.
Results shown in Figure 36 are very satisfactory indeed. Not only is interpolation carried out smoothly, but extrapolated results are also well behaved and appear reasonable. Problems were encountered only close to the sink region or for power-frequency-impedance requests inside the sink region. In contrast, the authors of [61], for example, do not go so far as to test their model in this domain.

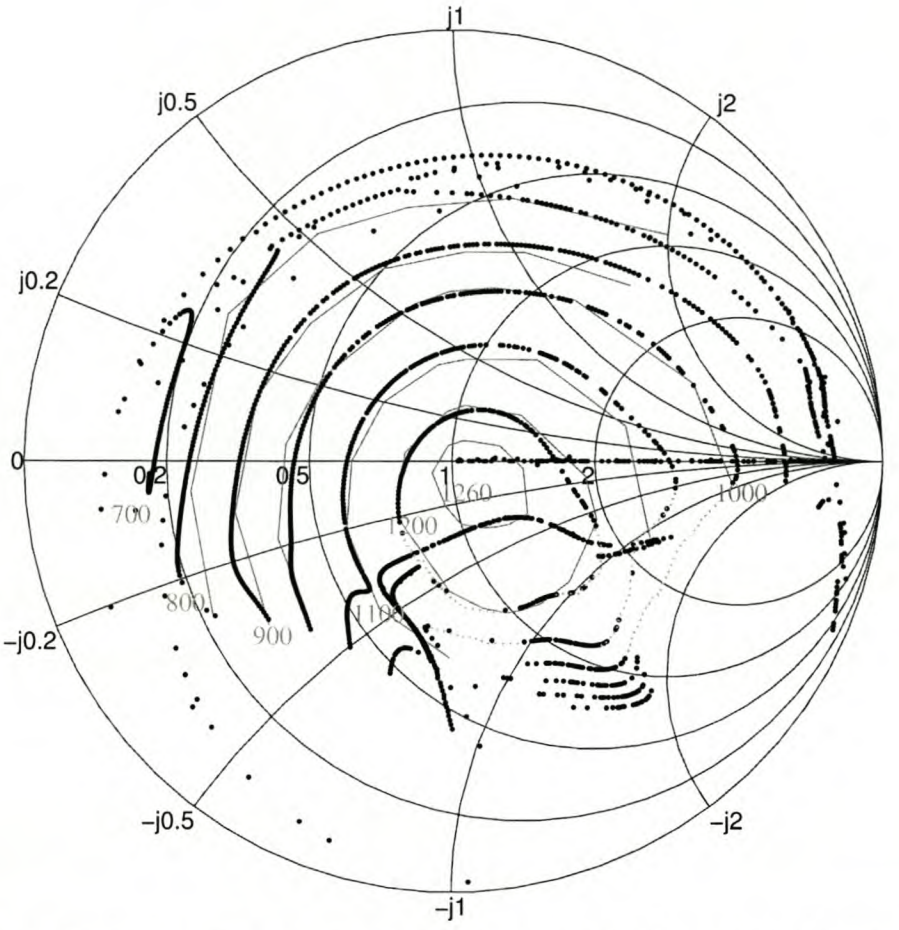

Figure 36: Model generated Rieke diagram data (dark dots) compared to information given (grey lines).

4.2.2 Conclusion on magnetron model

The extraction of passive model parameters and the isolation of the active region is a straightforward process. Vector polynomial coefficients of only 3rd order were found to be sufficient to reproduce the initial data accurately. Extrapolated data, that is data outside the training range of values, appears reasonable and is not erratic outside of the sink region.

4.3 Injection Locking Measurements

Frequency coherence between the sources is a necessary precondition for the synthesis of patterns by interference modulation. To achieve this goal, the minimum amplitude that securely locks the sources at 2450 MHz must be determined. Dropout effects resulting from an injected signal of too low an amplitude and those resulting from the movement of the injection frequency, both towards and then beyond the locking bounds, are also measured.

The measurement is carried out in both the frequency and the time domains. In the time domain the clearer X-Y plot of locked versus injected signal is used, whereas in the frequency domain the conventional power spectrum plot is used. Figure 37

shows the measurement setup with the time and frequency domain options. The signal from the primary source (a magnetron in the setup shown), passed through a variable high power attenuator formed by the combination of two circulators with a moving short in a T-piece, is measured. It then enters the source under test (SUT) through a directional coupler. The signal from the coupler and that from a coupling port at the circulator are measured. The RF signal may be displayed directly on the spectrum analyzer. To view the signals in the time domain, two mixers first perform a frequency shift down to approximately 50 MHz, such that the signals are suitable for display on a storage oscilloscope.

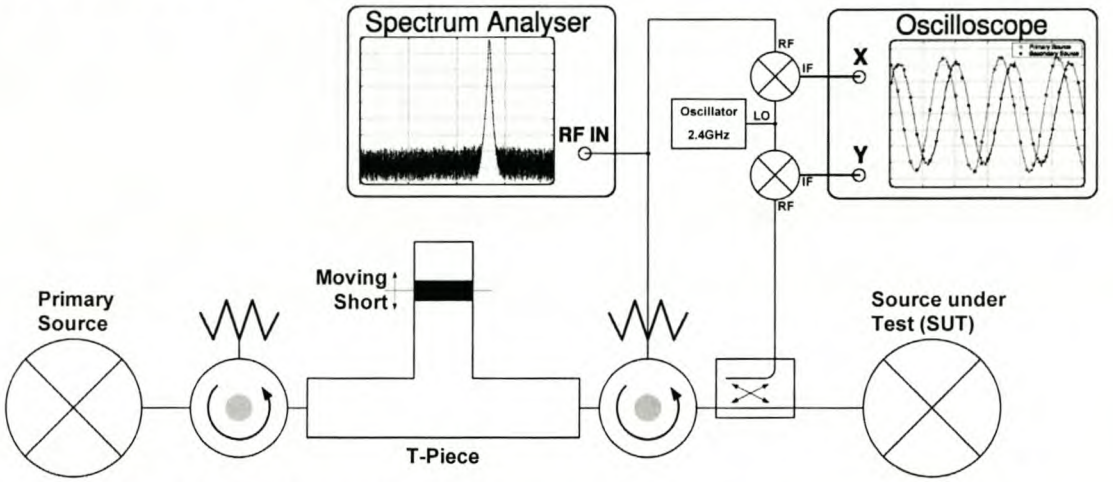

Figure 37: Setup for injection-locking tests.

First, a suitable amplitude that reliably locks the sources must be found. The signal of the primary source is set to 2450 MHz, the optimum frequency as found in Section 4.1. The amplitude is adjusted to the minimum possible, which is approximately 3½ W (Figure 38) and verified to be sufficiently stable and free of short-term jitter (Figure 38b). This signal is then injected into the SUT, which responds with the spectrum shown in Figure 39. As can be seen, the SUT is not properly locked by the injected signal as its amplitude is too low (less than 0.5% of the SUTs emitted power).

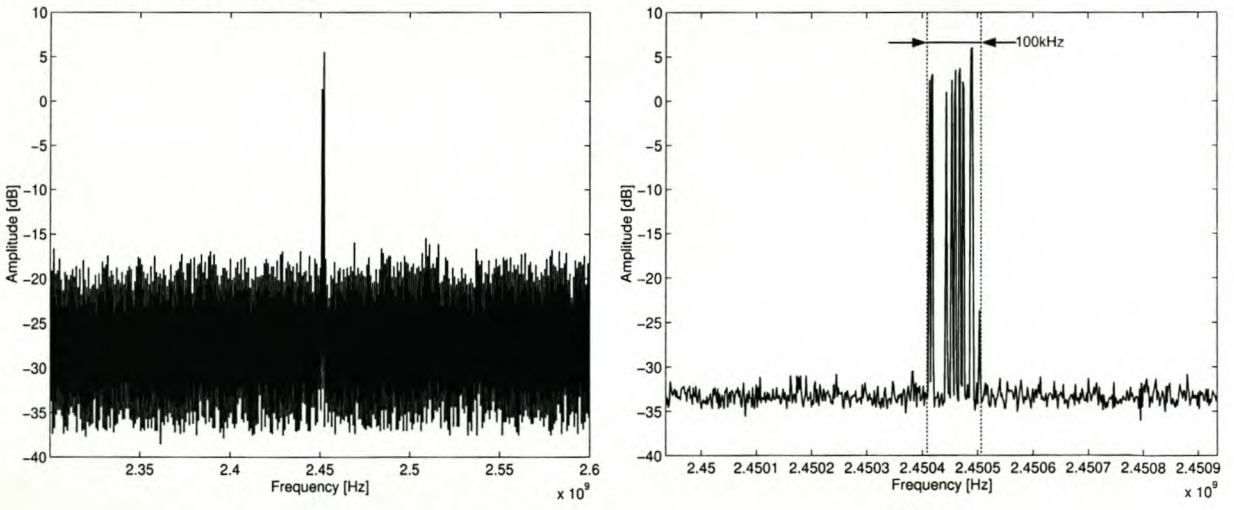

(a) (b)

Figure 38: Injected signal adjusted for minimum amplitude (a), zoomed in to reveal long term jitter of about 100 kHz (b). Note the scale of (b)!

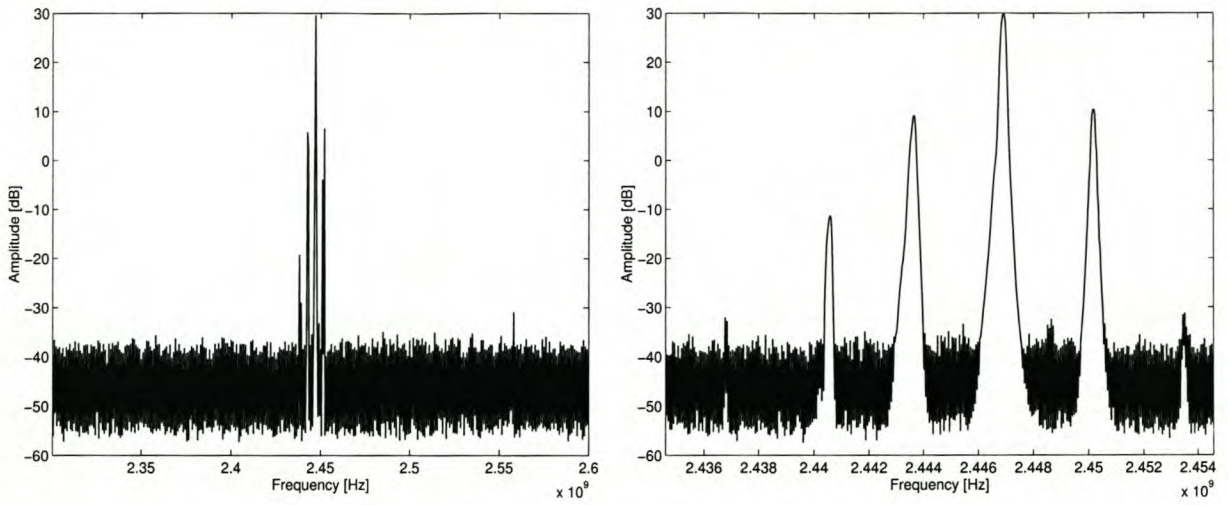

Figure 39: Resulting spectrum of the secondary source into which the signal in Figure 38 was injected.

Increasing the injected signal above 15 W, this is equivalent to about 12 dB or 1.75% of the SUT's free running signal power, results in locking. At this point, the difference in injected signal power to locked signal power, also known as locking gain, is about 18 dB. Further increasing the injected signal amplitude produces no additional, significant improvement. Instead, this merely increases the output power by the same amount as the additional input power added, implying that the locking gain drops to unity because of saturation.
In Figure 40 the injected amplitude is increased by 6 dB to about 18 dB. The locked SUT delivers about 30 dB under this condition, viz. the gain is 12 dB, a decrease of 6 dB, a saturation effect common to oscillators for they operate in their gain limited region (gain equal to unity).

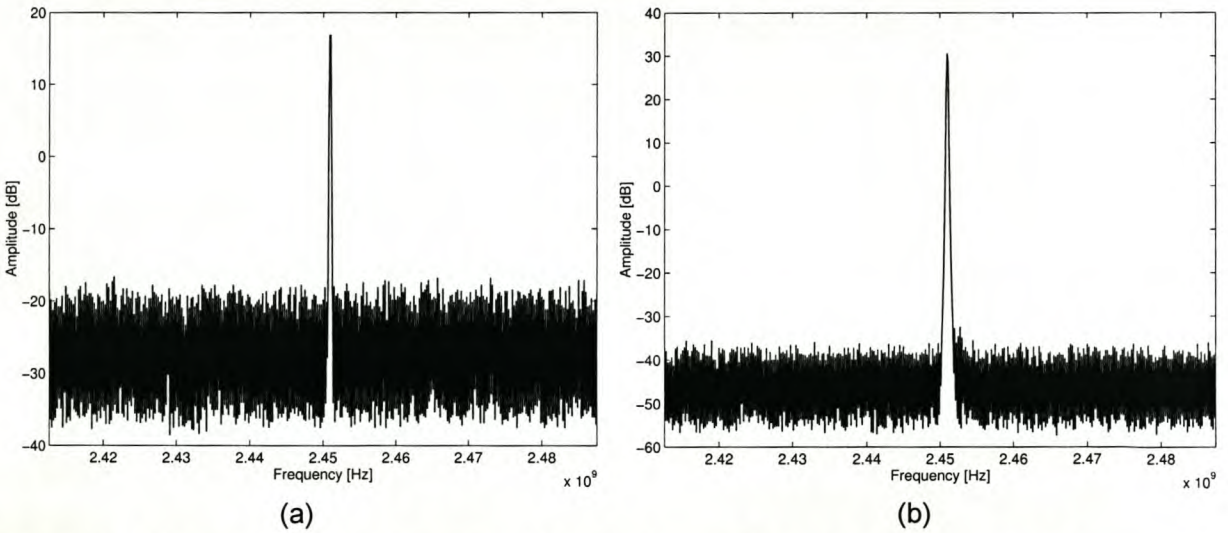

Figure 40: Magnitude versus frequency of injected signal (a) and locked source (b).

An injected signal amplitude of about 1.75% of a source's free running output power can lock the source. However, for practical reasons such as device tolerances, frequency drifts, and to accommodate supply fluctuations, an added safety margin is deemed appropriate to ensure locking in all cases. Therefore the injected signal power should be 3% of the SUT's output power, equivalent to 15 dB or 25 W for an 800 W source. This condition translates into a 25 W injected signal being required for 800 W (≈ 29 dB) emitted power. In order to achieve this, the de-coupling coefficient of the coupler shown in Figure 29 is 15 dB. The coupler's output signal serves as the reference signal injected into the secondary source.

The effects associated with the movement of the frequency of the injected signal towards the locking boundary, while maintaining constant amplitude, are also of interest.
In Figure 41, this frequency is shifted towards the lower boundary of the locking range. On the spectrum analyser it is observed that the secondary source drops out of locking (Figure 41a) and then re-engages locking (Figure 41b) as the frequency of the injected signal is moved slightly to either side of the boundary frequency. It is found that when disengaging lock, the spectrum appears to exhibit a less regular spacing between its sidebands. This is clear when comparing Figure 41a to Figure 41b.

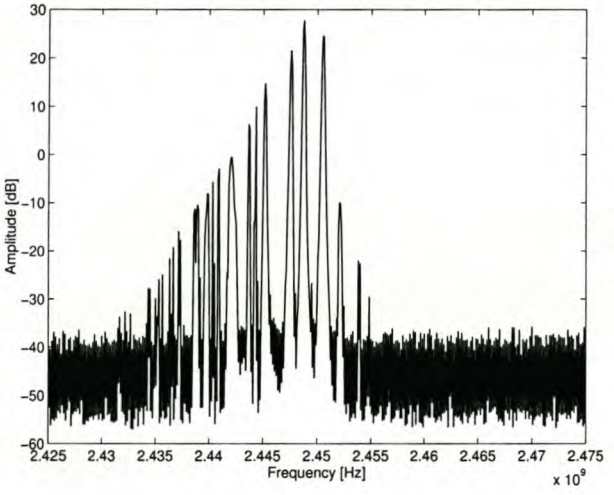

(a)

The source is about to drop out of lock, with the spectrum exhibiting a characteristic irregular Δf between the sidebands.

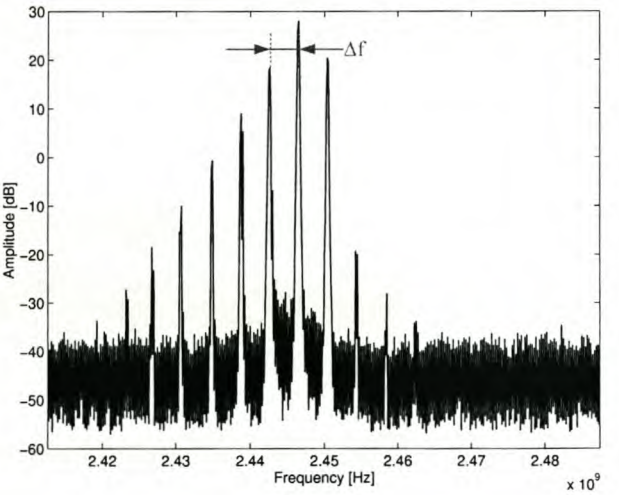

(b)

The source is about to lock. The sidebands are separated by a regularly spaced Δf. Note, the peak is still Δf away from the injected locking signal.

Figure 41: Sources about to lock (a) and unlock (b). The sum of the powers of the peaks is equal to the total output power of about 30 dB (see Figure 40b).

The frequency separation, Δf, is the frequency difference between the injected frequency and that of the SUT's own signal. The smaller the Δf, the faster the sources moved towards a locking condition. In fact, it is interesting to observe the response of the system to a suddenly applied, injected signal into the SUT, and to note how the Δf diminishes. The rate at which the sidebands converge on each

other increases as Δf decreases, until they all merge into one. At the same time, the powers of the individual sidebands merge and enforce the peak of the injected signal's frequency.

Moving the injected signal frequency even further, so that it goes beyond the locking boundary, generates a steady pattern of sidebands as shown in Figure 42. Again, Δf is the difference in frequency of the injected signal and SUT's own signal. As before, the sum of the signal powers contained in the sidebands must equal the total power of approximately 30 dB.

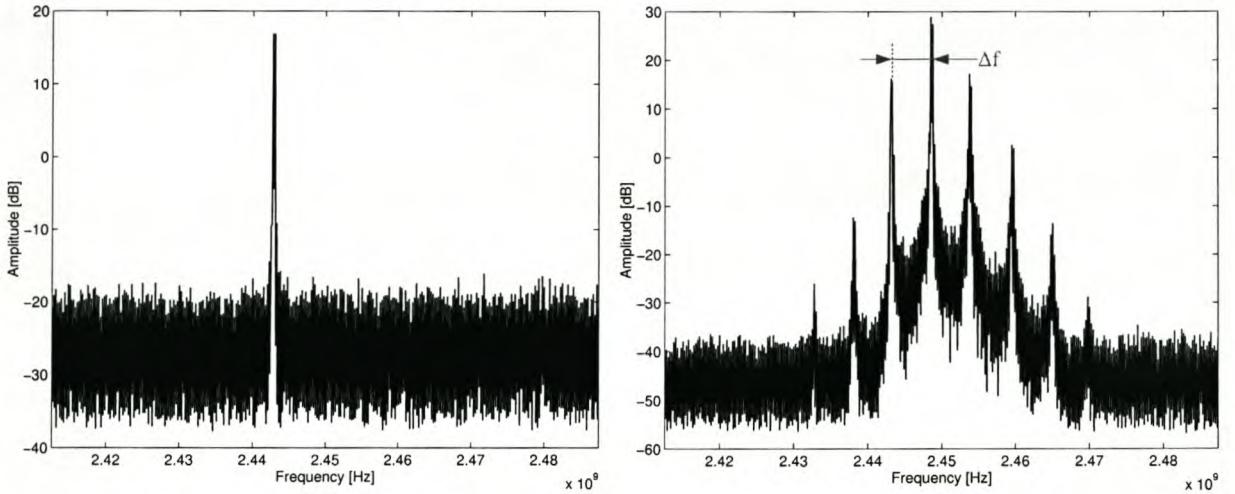

Figure 42: Sources do not lock because the injected signal frequency is outside the locking range. Only sidebands are generated. Again, Δf is the difference between the injected signal and produced frequency.

A time domain plot, revealing the phase difference between the injected signal and that of the SUT, may also be observed. Figure 43 illustrates the method by showing the same signal plotted against itself, producing 45° as the obvious angle of inclination in the X-Y plot. Ideally, the figure should be a straight line inclined at 45°. However a slight phase shift, introduced by the setup (mixer, local oscillator, cabling) between the measurement arms, turned the line slightly against the plane of the paper, revealing it to be a circle perpendicular to the page. For two signals 90° out of phase, a perfect circle would be produced. This condition is the boundary condition of the instantaneous phases for injected locking as is shown below (i.e. a perfect circle should not be obtained).

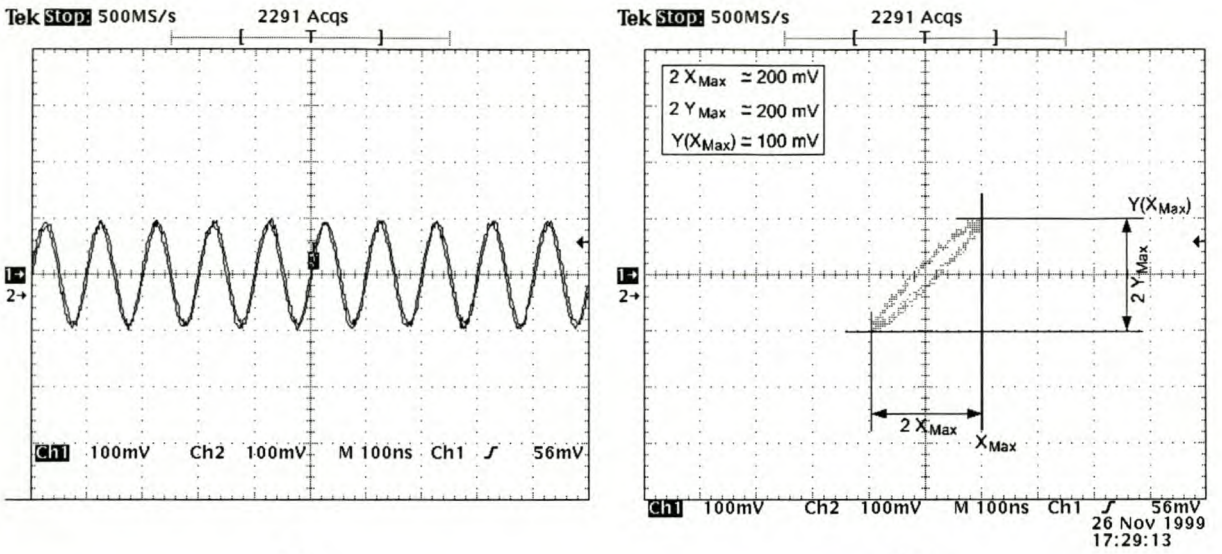

(a) (b)

Figure 43: The same signal received by the X and Y inputs (a) to the oscilloscope in Figure 37. The corresponding X-Y plot is shown in (b), from which the phase difference is found to be $\alpha = \arccos(Y(X_{Max})/Y_{Max}) \cong 0°$.

Figure 44 to Figure 46 show the progression as the injected signal frequency is moved slowly towards and then into the locking boundary. The nicely defined circle disintegrates into a bounded cloud of points. The distortion observed is a product of the sidebands as the oscillator tends to drop out of locking.
Figure 45 shows the source breaking out of lock. Note the distortion which is reminiscent of the sidebands in the frequency spectrum (see Figure 42).

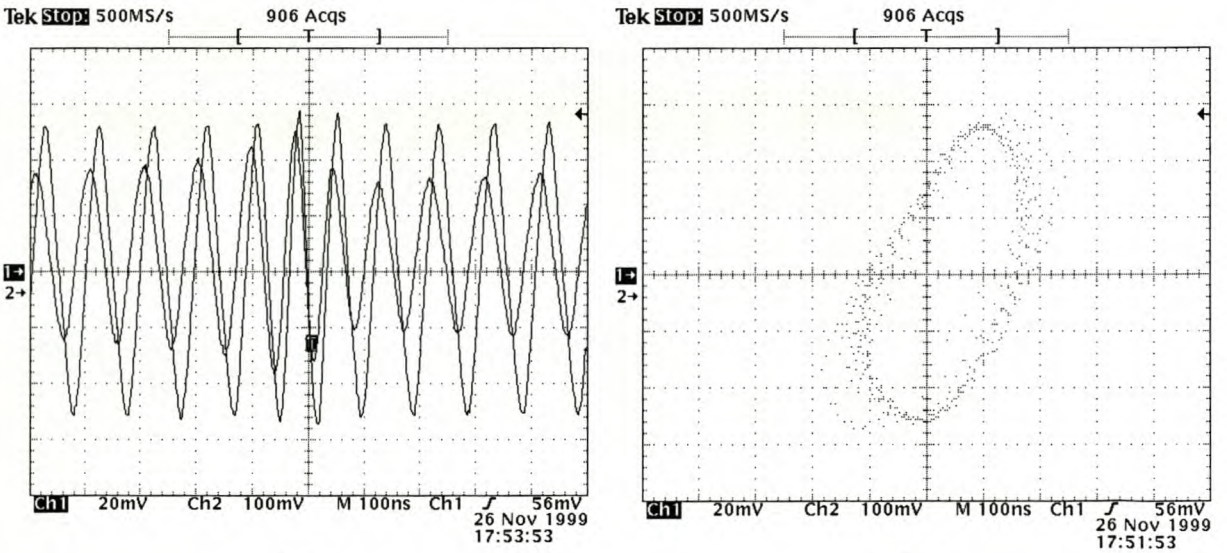

(a) (b)

Figure 44: On the locking boundary. At times, the oscillator locks when the instantaneous phase differences are sufficiently small for a particular beat frequency. The broader scatter in the top right and the bottom left quadrants in (b) is characteristic of the source dropping out of lock.

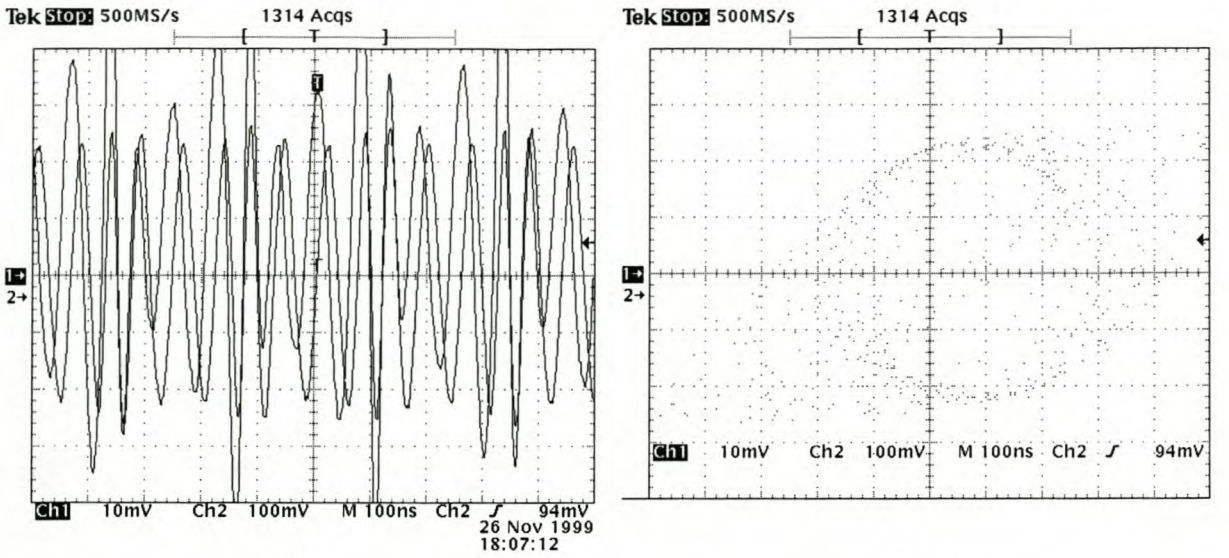

(a) (b)

Figure 45: Just outside the locking range. Similar to Figure 44, a brief temporary lock occurs for very small instantaneous phase differences. Note, the circular 'open' region in (b). This is reminiscent of the 90° instantaneous phase shift between the sources, representing the locking boundary which is predicted by theory (equation 7).

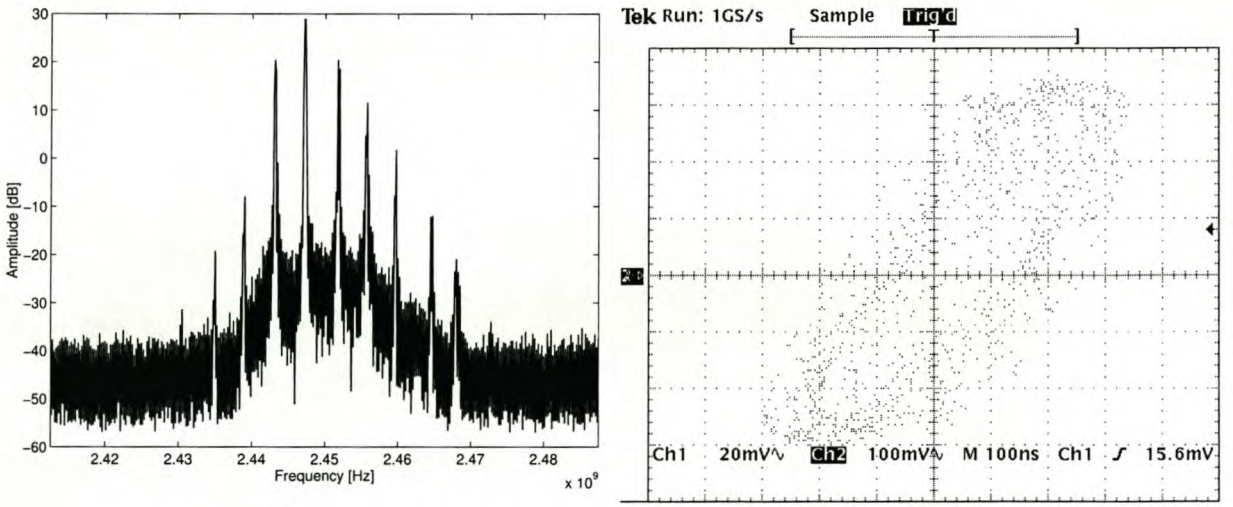

(a) (b)

Figure 46: Outside the locking range. The scattering region is bounded, but a line is no longer clearly discernable.

Having studied the phenomena at the locking boundary, the reference signal frequency is moved closer to 2450 MHz to produce a stable locking condition as shown in Figure 47. The frequency of 2445 MHz is close to, but still within, the locking boundary so that a stable lock is produced (refer to Figure 30).

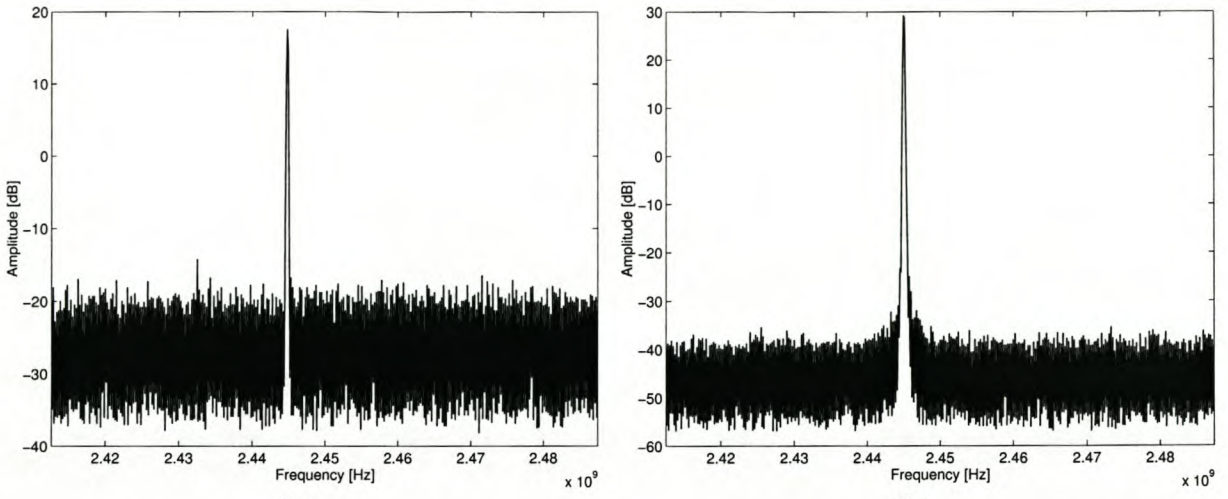

Figure 47: Frequency is set at about 2445 MHz to cause stable locking. The amplitude of the injected signal is the same as in Figure 42.

Figure 48 shows the X-Y plot of two injection locked signals. Figure 49 shows the same for the minimum injected power level required (see Figure 40) to produce a lock.

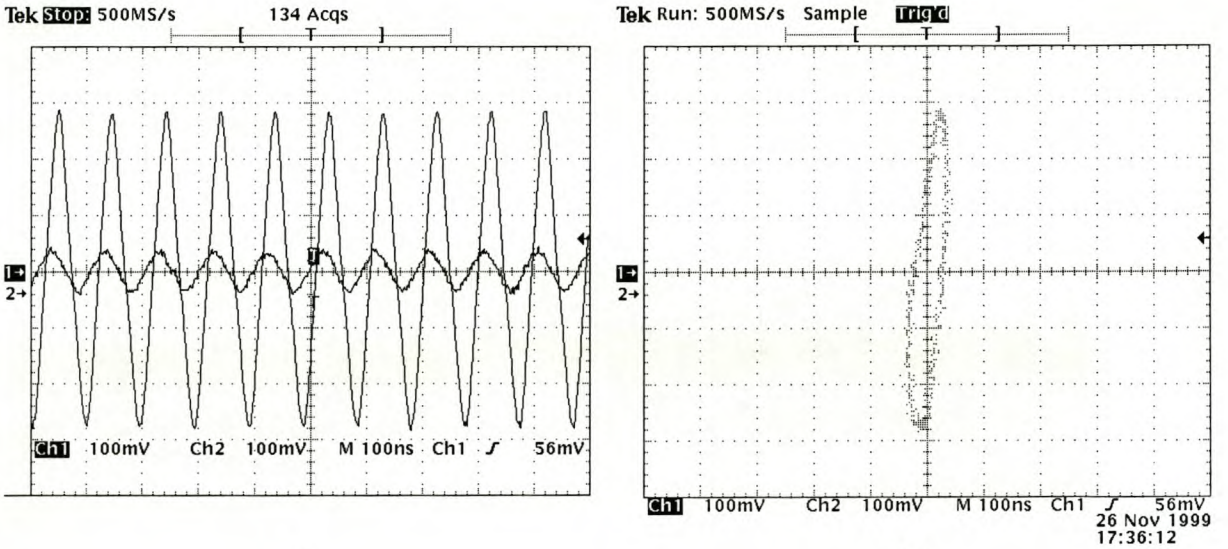

Figure 48: X-Y plot of injection locked source inside locking boundary. The instantaneous phase difference is $\alpha \cong 57°$.

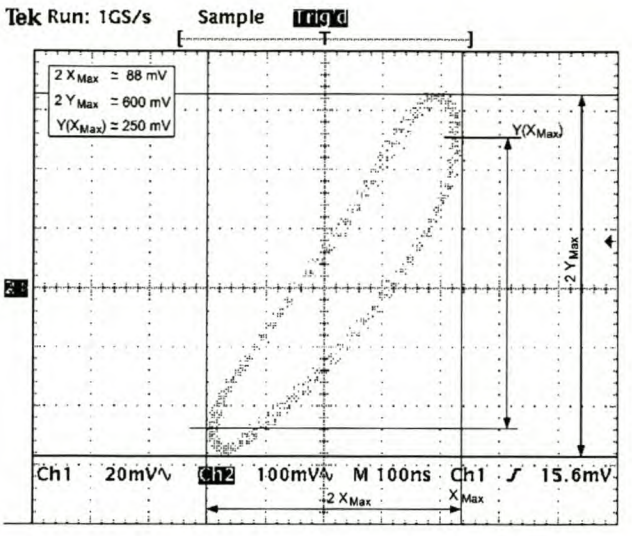

Figure 49: X-Y Graph of Figure 40a and b reveals that the two signals are frequency coherent. This is the X-Y Plot of a locked source with approximately 33° instantaneous phase difference.

4.3.1 Conclusion on Injection Locking Measurements

The effects of injected signal amplitude and frequency on the nearly locked and locked signal source were studied. Effects at the locking bounds were shown both in the frequency and time domains. The time domain X-Y plot proved to be a valuable tool, both to verify locking of the sources and to determine the instantaneous phase difference between the injected and locked sources.

In the case of the particular source under consideration, an 800 W magnetron tube, the minimum injected locking power at the optimum frequency of 2450 MHz was found to be 1.75% that of its output power. For the 800 W source, this amounts to approximately 15 W. To guarantee stable locking, taking environmental parameters and device tolerances into account, approximately 3% of the source's output power is considered to be necessary for the injected signal power. The optimum injected signal for locking is thus set to 25 W at 2450 MHz.

4.4 Introduction of a variable relative phase shift

Injection locking of magnetron tubes was predicted theoretically and verified by measurements. Similarly, the effect of a variable relative phase shift on the overall performance must be tested.

4.4.1 Variable relative phase between injection locked sources

Having established the conditions for, and achieved, reliable frequency coherence, the next step is to introduce a variable phase shift between the sources and to observe its effect on the overall performance. The setup shown in Figure 50 was used to allow concurrent observation of phase shift on an oscilloscope in the time domain, and frequency coherence on a spectrum analyzer (Notice that this configuration resembles that of Figure 37, used earlier). Mixers are used to down convert the signal from 2450 MHz to approximately 50 MHz and thereby to allow

concurrent observation of both source signals on a standard oscilloscope. Results from both the oscilloscope and the spectrum analyzer were recorded on a computer for post processing and display, and are shown in Figures 51 and 52.

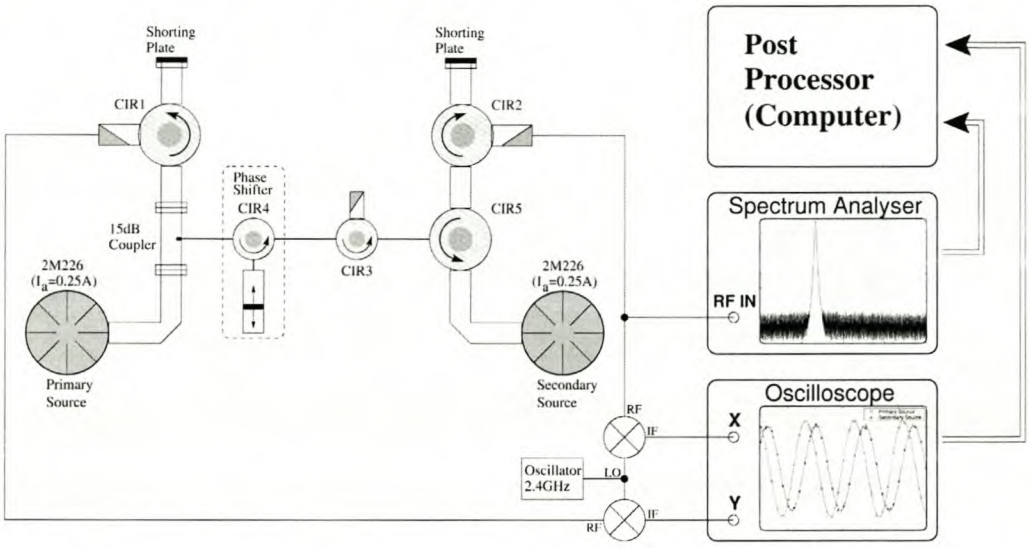

Figure 50: Setup for injection locking measurement suitable for interference modulation.

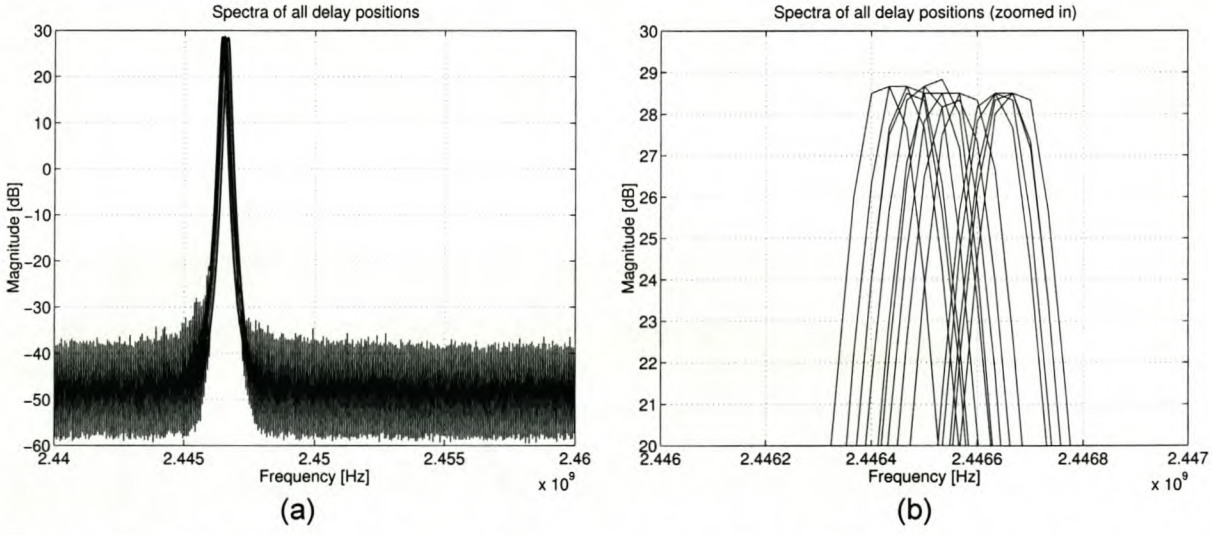

Figure 51: Spectrum of injection locked sources. The small frequency variations observed in the close-up during the measurements on the structure in Figure 50 is indicative of high isolation between sources. Note the scale in b). The frequency variation corresponds to ≈ 82 ppm, comparable to sources in communications equipment.

The small frequency variation in Figure 51 is known as 'short term jitter', and is most notably caused by PSU ripple feed through. At only ≈ ±100 ppm, however, this level of jitter is comparable to that of sources used in communications equipment (e.g. WLAN sources are specified at ±20 ppm).

Good frequency stability and coherence is observed from measurements presented in Figure 51. This is largely a result of the well filtered power supply (Figure 12) used for the primary source, and sufficient isolation of approximately 38 dB between primary and secondary sources.

Frequency coherence is a prerequisite for stable phase shifts. In Figure 52 phase shifts of over 540° have been measured, with larger phase shifts being possible but not essential for the production of interference modulation[10]. Phase and frequency performance is very satisfactory. Full and controlled coverage of over 360° phase shift required to move peaks and troughs to any position inside the applicator is achieved. The peaks and troughs correspond to high and low zones of energy concentrations as, for instance, shown earlier in Figure 21.

[10] The phase differences in Figure 52 are the actual phase shifts between the primary and secondary magnetron oscillator, and are not to be confused with the instantaneous phase difference between f_0 and f_{inj} used in (7), which allows for only a ±90° phase shift [87].

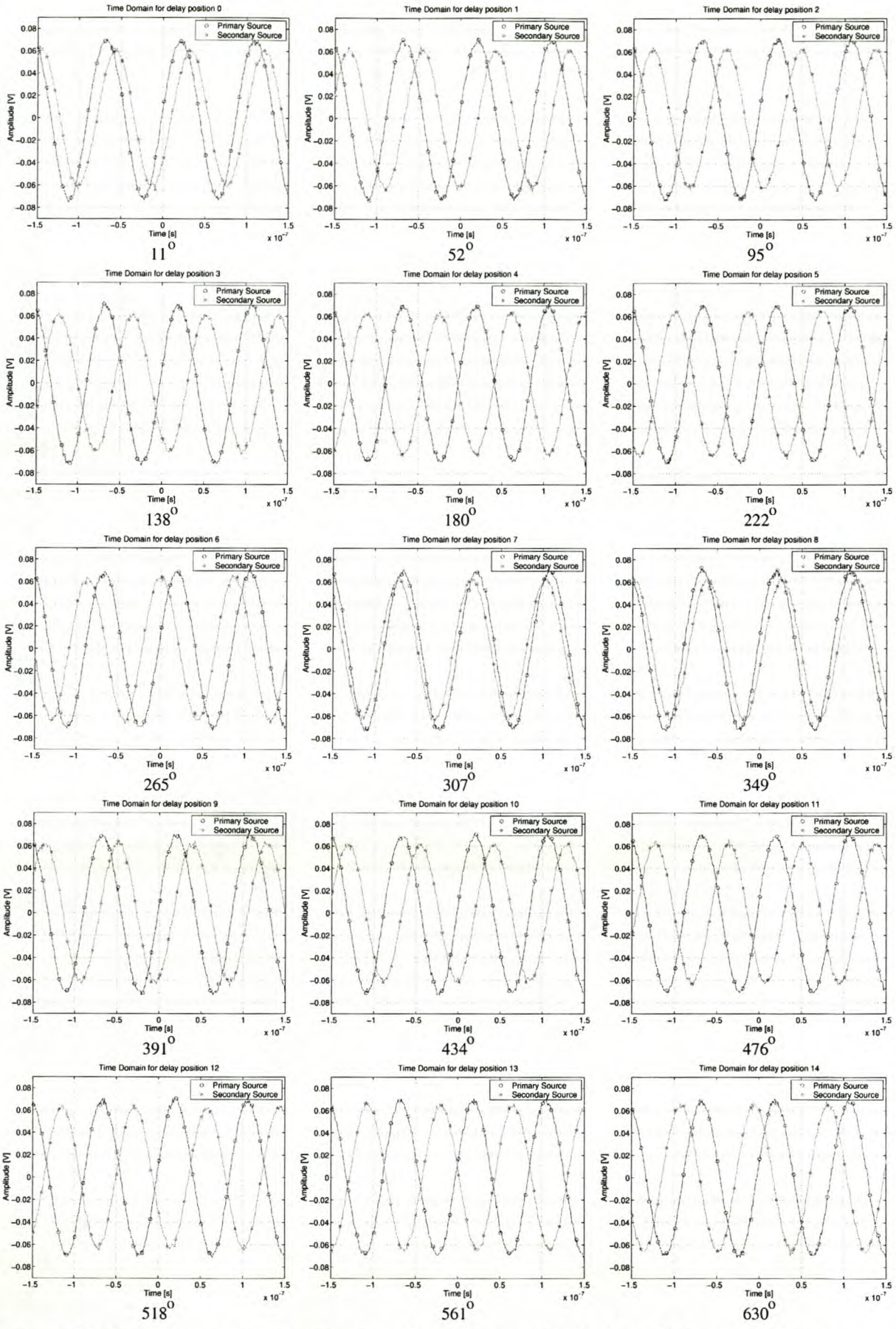

Figure 52: Time domain display showing phase progression for linearly increased delay settings.

4.4.2 Attaching the applicator

The applicator was attached to complete the structure as per Figure 29. Phase shift and frequency stability were tested again. When using an empty applicator strong frequency changes were initially observed for varying phase delays. At the same time, the maximum phase shift was constrained to ±90° and jumps in frequency were observed as the phase bounds were approached. These anomalies did not occur with a loaded applicator.

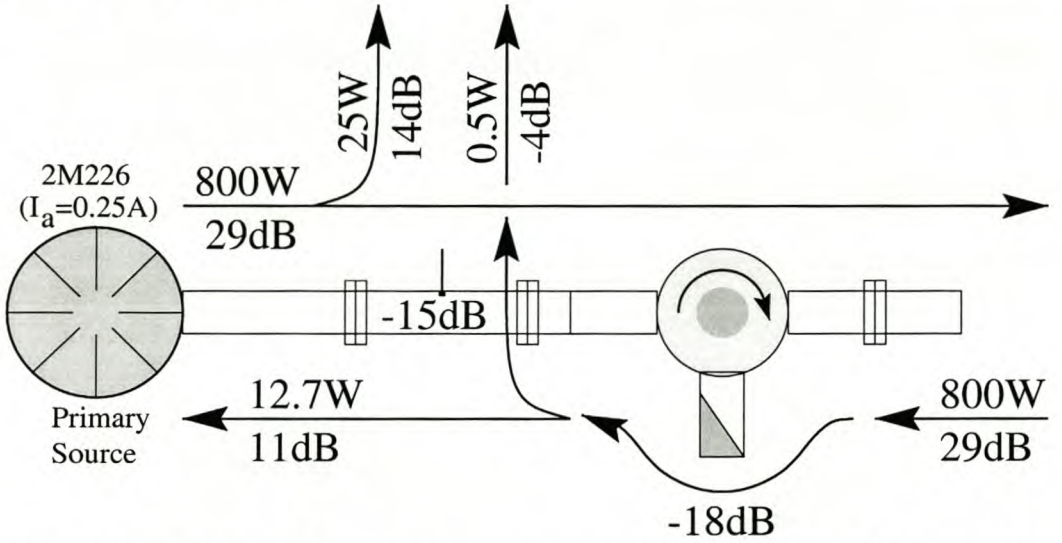

Figure 53: Analysis of power flow in the primary source's arm, performed to explain the isolators inadequate -18dB reverse transmission coefficient.

Analysis of the situation in Figure 53 reveals that the reverse isolation of approximately -18 dB provided by the isolators was insufficient. Of the approximately 800 W of power from the secondary source that was incident on the isolator of the primary source, approximately 13 W made its way through the isolator in the reverse direction, and became incident on the primary source. This signal power, applied to the reference source, is sufficient to injection lock it to the signal from the secondary source, which was itself being locked to the primary source, hence establishing an unintended 'injection-loop'. From the source's point of view, it was presented with a reflection coefficient of $\Gamma \cong \sqrt{12.7/800} = 0.125$. This corresponds to a Voltage Standing Wave Ratio (VSWR) of about 1.3 whose phase is determined by the phase shifter. The frequency contours of the 2M226, shown in Figure 31, show that a VSWR of 1.3, encircles a frequency range of about 10 MHz (frequency offset from -9 MHz to 1 MHz). This explains the strong frequency variation encountered with changes in phase (i.e. strong frequency-phase sensitivity).

Increasing the isolation between the sources along the high power applicator paths corrected the problem. Phase and frequency measurements with the changes in place are shown in Figure 54 and Figure 55. Again, over 360° of phase shift was achieved. The frequency variation increased to about 2.25 MHz, compared with the

lower variation shown in Figure 51, contributing up to ±10° to the phase shift [87]. This additional phase shift is inconsequential to the topology, but should be noted for the calculation of phase shifts. If desired, the added phase shift can be compensated for by increased isolation or with the variable phase shifter.

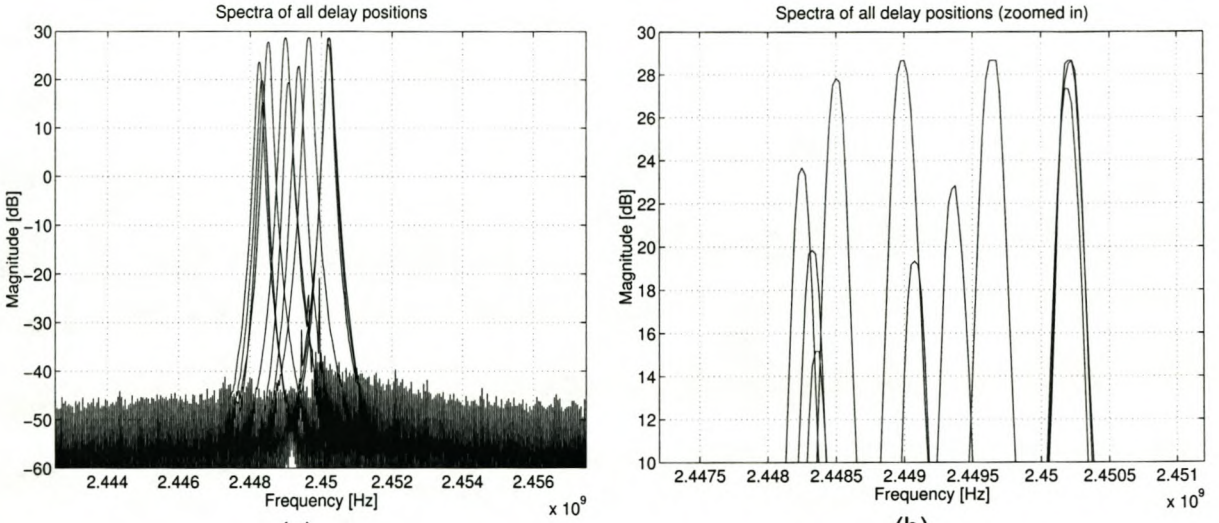

Figure 54: Spectrum of injection locked sources with improved isolation and applicator attached. The frequency variation for various delay settings can be observed in the close-up.

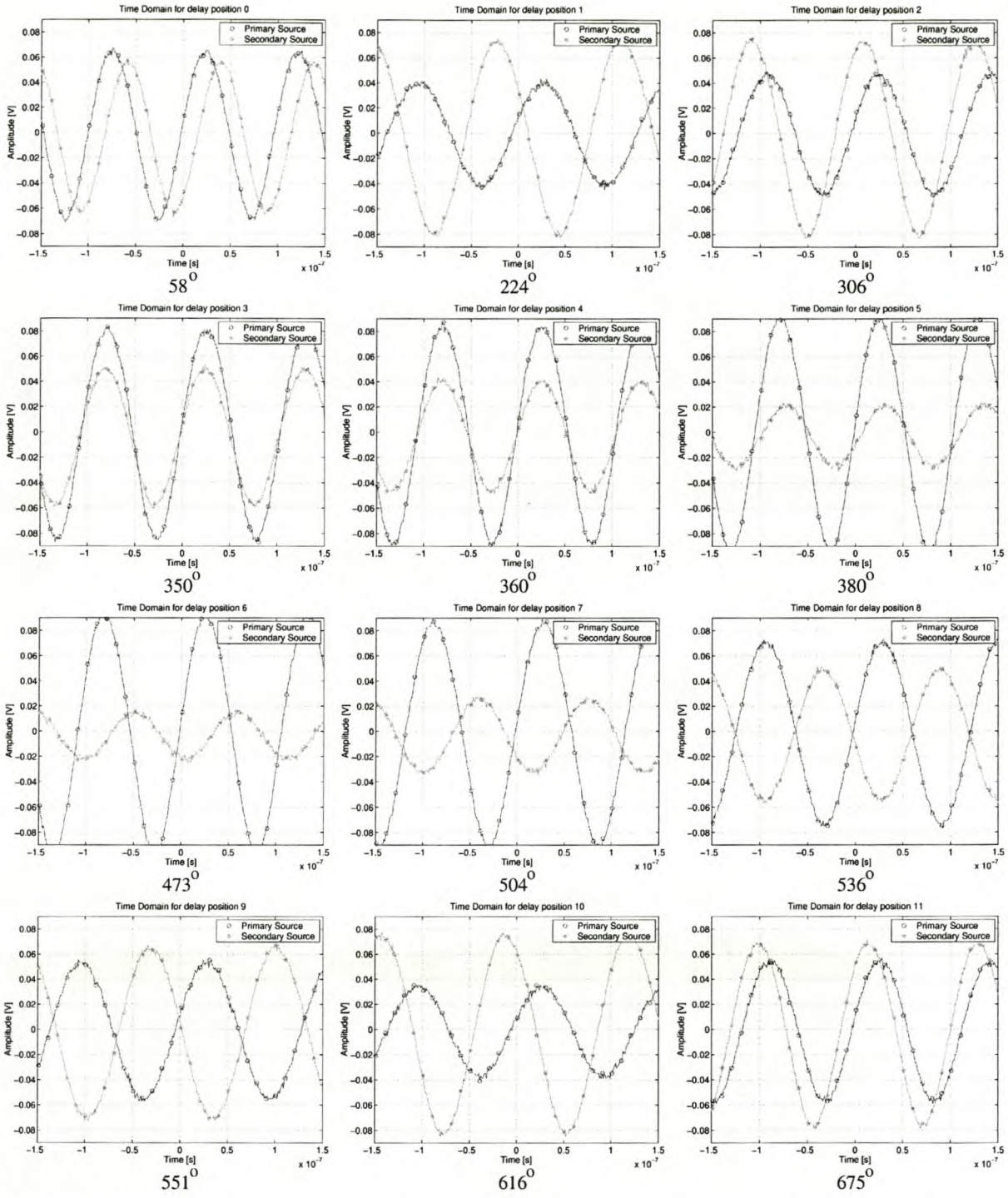

Figure 55: Time domain display showing phase progression for linearly increased delay settings for the setup in Figure 63.

Once the positions of peaks and troughs can be set, features can be synthesised inside the applicator. Patterns are then produced by varying the relative phase difference between sources and introducing time weighting factors.

4.5 Interference modulation

The subdivided single source in Figure 16a and the injection locked multi source topologies in Figure 16b have been implemented and their performance characterised. The applicator used in both instances was a 480 mm long slotted WR340 aluminium waveguide, into which carbon composite slabs with dielectric constant $\varepsilon_r = 10 - 2.5j$ [18][115] of 25 mm thickness were inserted. Microwaves from magnetron sources were incident on either side, and these interfered inside the applicator. A complementary approach between measurement and simulation was adopted to obtain reliable full 3-D field distributions inside the waveguide. The approach is a general one and is outlined as follows:

- Maxwell Eminence®[11] and HFSS®[11] with their independently adjustable sources [64][65][66] were used to obtain the various interference features.
- An adjustable high power microwave probe [120] measured field patterns along the slot.
- Measurements were compared with data obtained by simulation along the same slot dimensions.
- Agreement of measurement and simulation implies that simulated data is correct [121]. Close coupling exists amongst the values of the finite element matrices of the simulator. Therefore differences in the slot influence other values, which means that agreement with measurements performed along the same slot is a sufficient condition for validation.

In this way, measurements were used to confirm the reliability of the simulations. Having verified the simulations in this way, they could then be used with confidence to extract fine detail, which would have been difficult or impossible to obtain by measurement alone, due to the fact that the system would likely have been significantly perturbed by indiscriminately placed probes.

A field visualisation technique that indirectly measures microwave patterns and thus provides additional verification is introduced further on in this document.
Differences exist in the way incident signals are obtained in the single and the multi source implementations. They are thus treated separately in the following subsections, in which practical implementations and their results are presented.

4.5.1 Obtaining features in a single source topology

In the single source implementation the signal emitted by a magnetron is split into equal parts by a power divider. Subsequent isolators not only provide source protection but also make the signals incident onto the applicator appear independent of each other, i.e. they isolate them. For measurement of interference features, the high-power probe (E) seen atop the applicator (D) in Figure 56, can glide along the full length of the slot. Performance characteristics of the various components mentioned can be found in appendix E.

---

[11] © 1999, Ansoft Corporation, USA

Phase shift in this single source topology is achieved by offsetting the carbon composite slab from the centre position. These slabs are 25.4 mm thick, with a cross-section of 86.36 x 43.18 mm and have a relative dielectric constant of $\varepsilon_r = 10 - 2.5j$. Equation 37 relates physical offset in distance from the centre to the resulting relative phase shift between the sources. The required wavelength in the applicator was measured to be 171.1 mm, corresponding to a frequency of 2466 MHz in an empty applicator.

$$\angle\Theta^\circ = \frac{360^\circ 2x}{\lambda_g} \tag{37}$$

where

Θ° = Relative phase shift [°]
x = Offset [m]
λ_g = Wavelength in applicator [m]

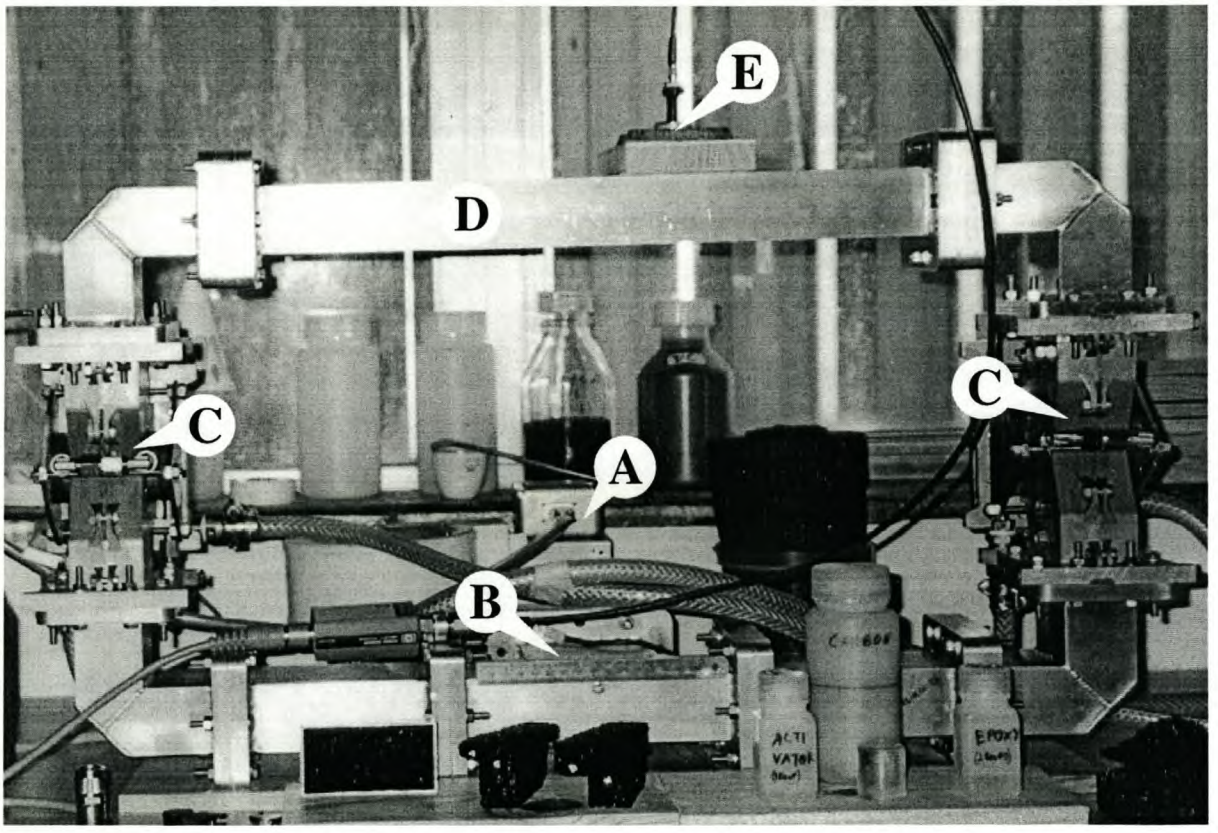

Figure 56: Picture of single source interferometer setup. A - magnetron source, B - compensated power splitter, C - two high-power isolators, one for each incident signal, D - applicator, E - measurement probe. Carbon composite samples can be seen in the foreground.

After the magnetron source acquired its steady-state operating condition, measurements were taken manually approximately every 2.5 mm along the length of the slot. In simulations carried out on the same applicator, it was assumed that:

- Reflection coefficients of the circulators below -25 dB from 2440 MHz to 2460 MHz (see Figure 97 in appendix A) are a good enough approximation to the perfect match provided by ports in the finite element modelling (FEM) packages used.
- Waveguides made from aluminium were used. Aluminium is sufficiently conductive to assume a perfect conductor (no noticeable changes in results were found, supporting the assumption).
- 2450 MHz is the operating frequency of the source.

Results of measurement and simulation are plotted beside each other in Figure 57, Figure 58 and Figure 59 for 0°, 106° and 188° relative phase shifts respectively. For purposes of comparison, they have been normalised by the average total power present in the applicator.

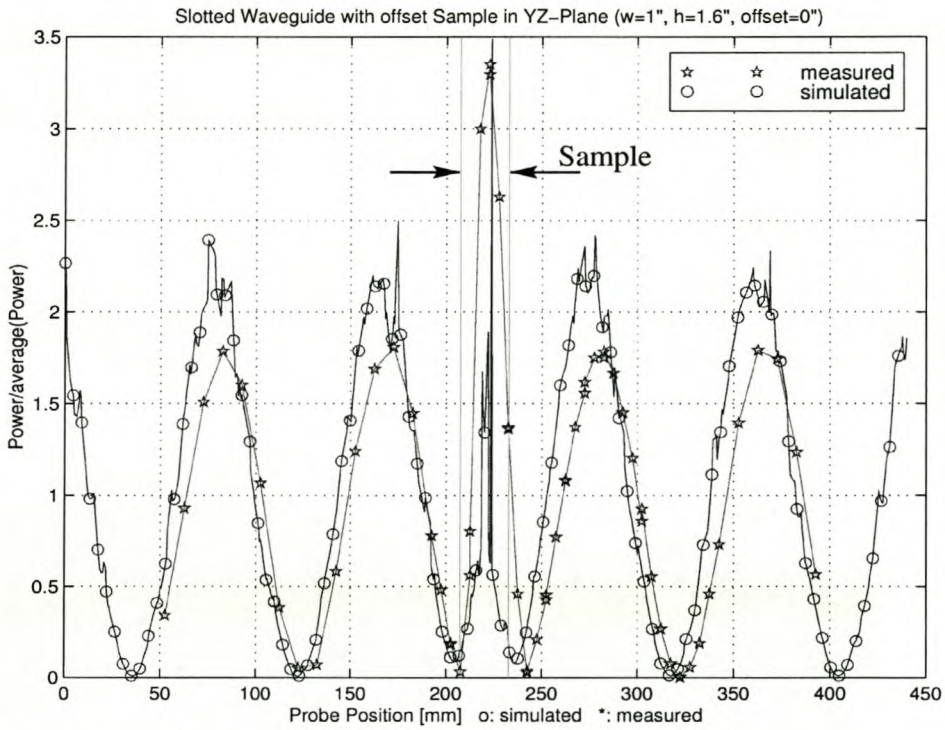

Figure 57: Measured and simulated results at 0° relative phase shift between signals incident onto carbon composite samples.

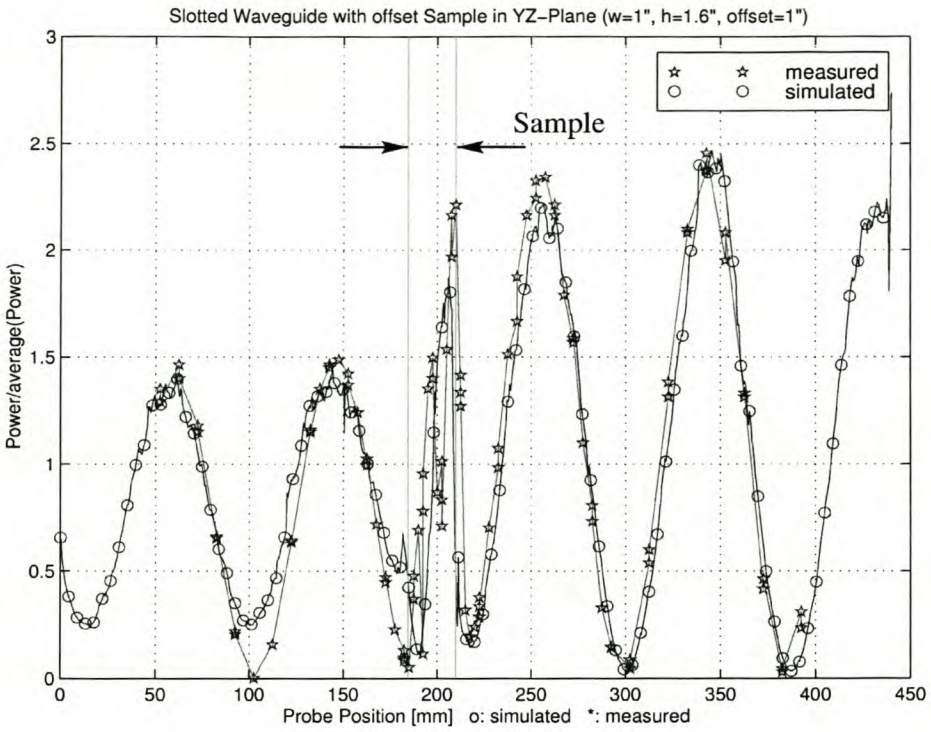

Figure 58: Measured and simulated results at 106° relative phase shift between signals incident onto carbon composite samples.

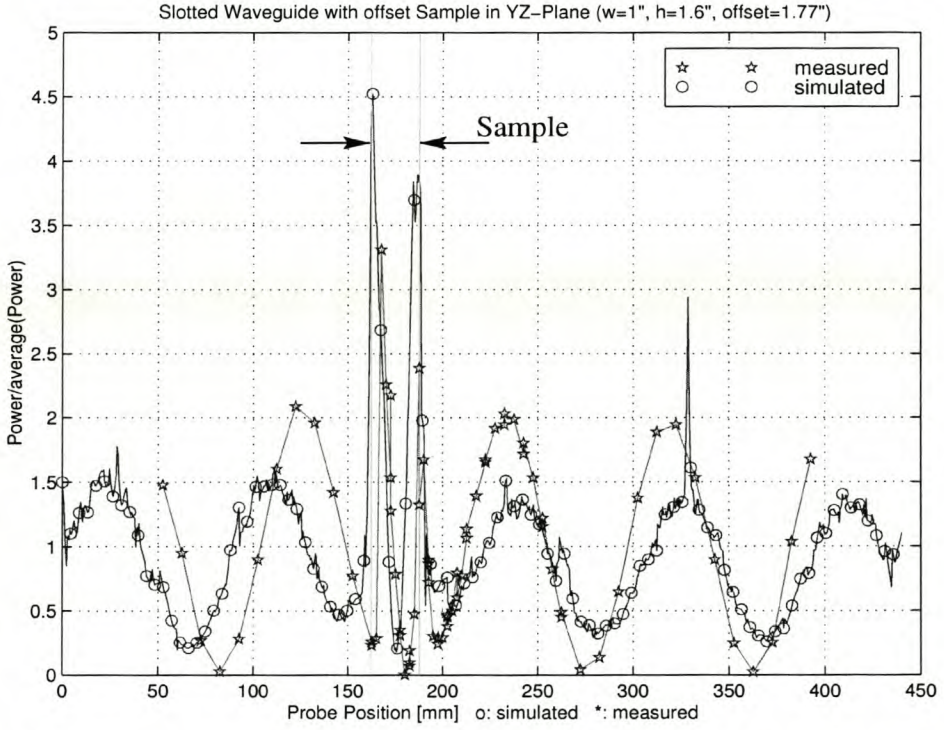

Figure 59: Measured and simulated results at 188° relative phase shift between signals incident onto carbon composite samples.

Good agreement in the frequency and position of peaks is shown in all cases, with a slightly larger discrepancy in Figure 59. Amplitude progressions are similar in shape, but differ by as much as 29% in Figure 57, and about 33% in Figure 59, with good

agreement in Figure 58. High sensitivity in the amplitudes during the manual measurement process can be traced to changes in supply conditions which influence frequency and output power, as well as to high sensitivity to the probe's position inside the 2 mm high slot, as shown in Figure 60.

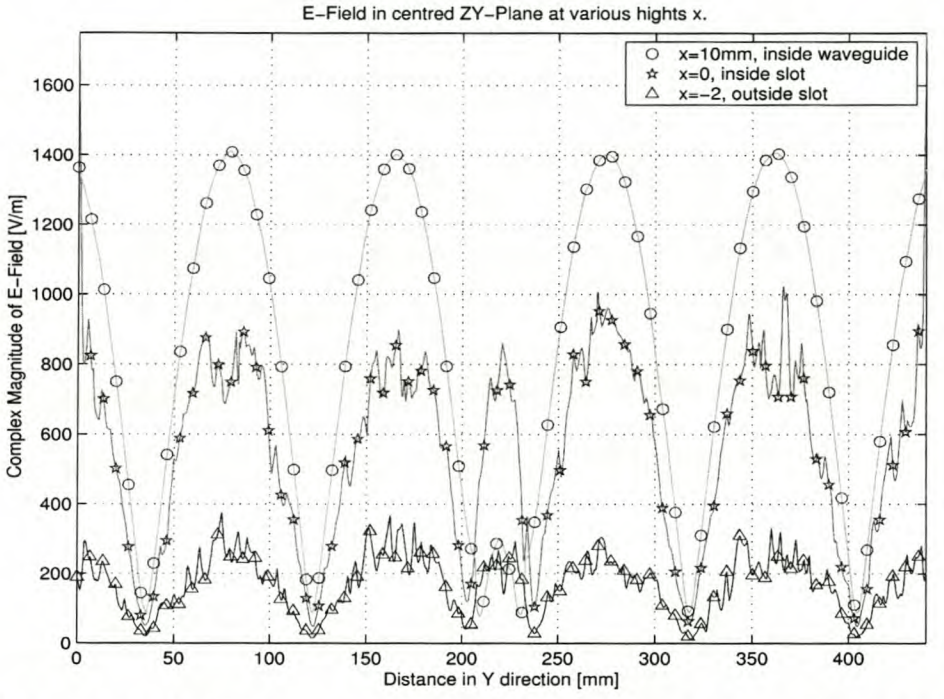

Figure 60: Magnitude of E-field along centred YZ-plane at various X positions to illustrate the steep change in the slot.

The assumption is often made that the probe is sufficiently flush with the inside surface of the wave guide so that slot effects can be neglected.
However, with vertical position of the probe, a strong change in field strength must logically occur, in order to suppress radiation to the outside. As Figure 60 shows, a strong change does indeed occur inside the slot, viz. a significant sensitivity to the vertical probe position is exhibited. Hence the probe's vertical position must be well controlled so that its position is maintained flush to the inside surface. If this is not ensured, then the following problems could occur:

a) If the probe protrudes too far into the waveguide, it will interfere with the electromagnetic fields, and
b) If the probe is too far inside the slot, then the variation of the measurement sensitivity increases.

The probe was therefore kept as flush to the surface as is mechanically possible.

In conclusion, agreement between simulation and measurement has been demonstrated. The positions of peaks inside the media, in particular, correspond well with each other. 3-D data obtained by computation therefore represents a valid model of the physical system.

The good agreement is further supported by the E-fields in the XY-plane of the carbon composite obtained by simulation (Figure 61) and by the theory presented in

section 3 (Figure 62). Aside from the roughness reminiscent of discretisation, both figures agree well.

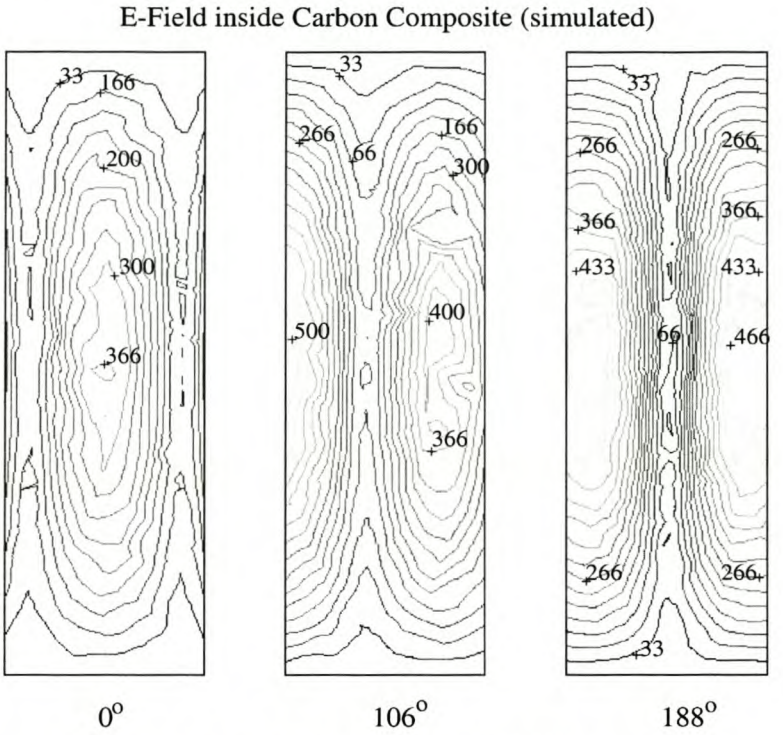

Figure 61: E-field in XY-plane inside carbon composite (simulated).

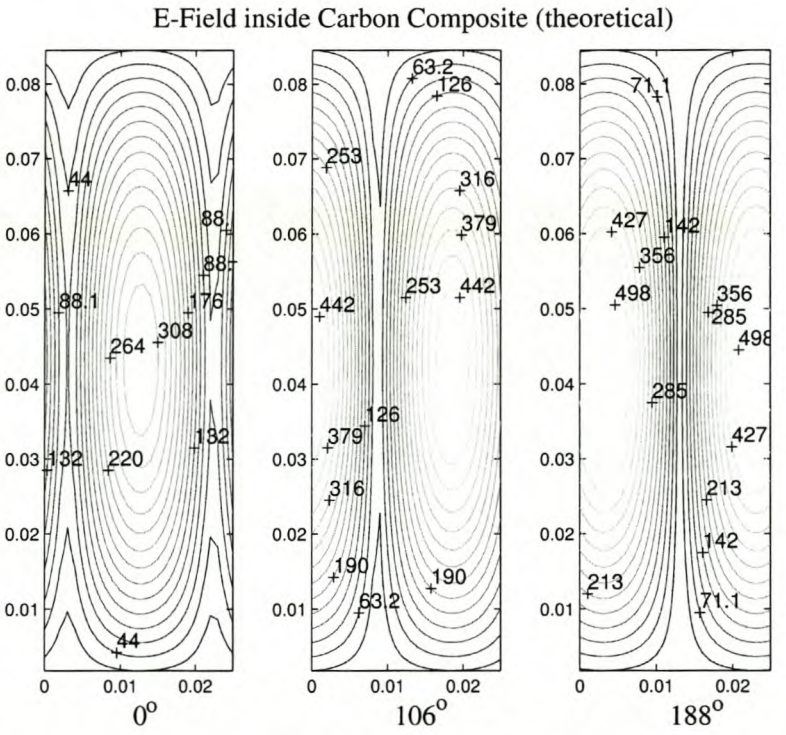

Figure 62: E-field in XY-plane inside carbon composite (theoretical).

Differences and errors are attributable to the differences between the model and the real, physical system. Other sources of error include problems encountered close to

metal boundaries, errors in the manual measurement process along the length of the slot (2.5 mm steps moved with about +/-1 mm precision), variations in the height of the probe, and moisture from samples – which at times condensed on the inside of the waveguide walls and the probe's tip, changing its measurement characteristic. The difference in source frequency between simulation and the physical system is negligible and was not a significant source of error, since the simulation frequency was 2450 MHz (i.e. λ_g=0.173 m) and source frequency in the physical setup was 2466 MHz, (i.e. λ_g=0.171 m). This corresponds to a discrepancy in wavelength of only 2 mm.

4.5.2 Obtaining features in the multi source topology

The multi source topology will be demonstrated using two injection locked magnetron based sources. A photograph and schematic diagram of the setup are shown in Figure 63 and Figure 64 respectively.

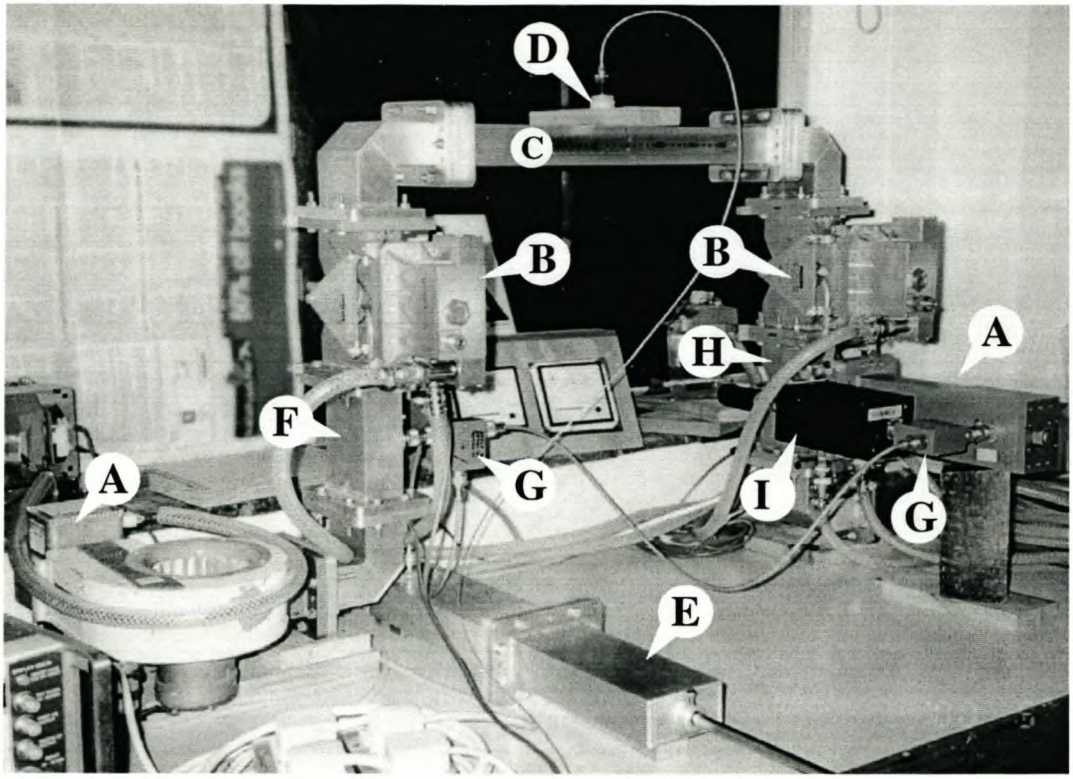

Figure 63: Experimental multi source interference modulation setup. A - magnetron sources, B - high-power isolators, one for each source, C - applicator, D - measurement probe, E - phase shifter, F - coupler, G - low-power circulators, H - circulator for reflection amplifier. The combination of low-power load (I) with low-power circulator (G) forms an isolator.

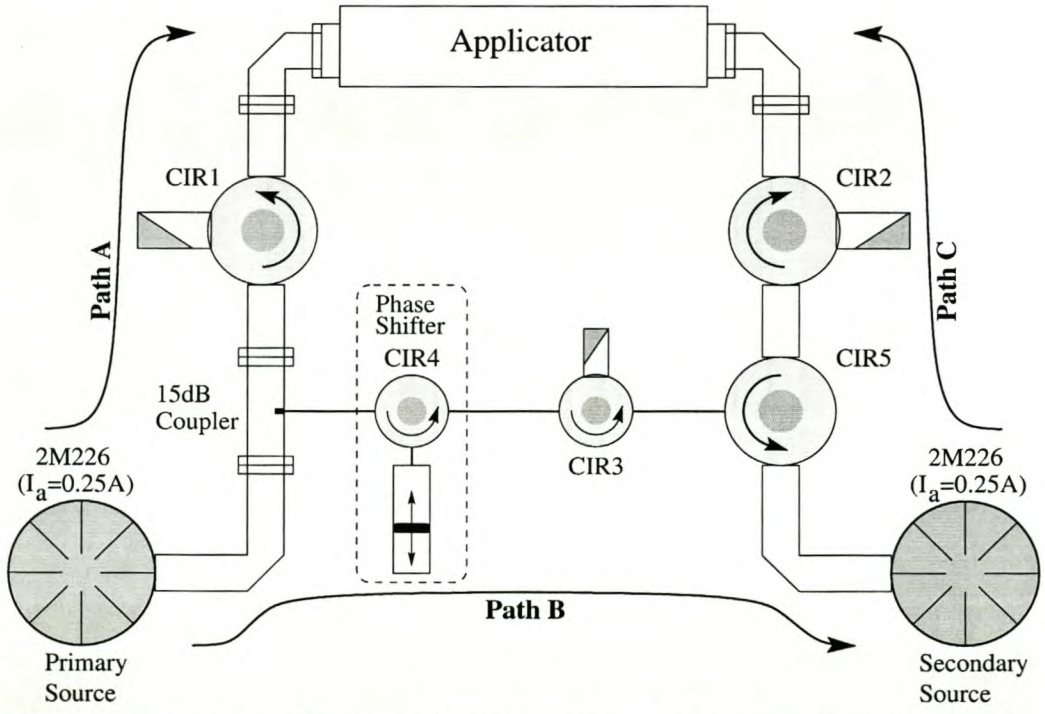

Figure 64: Configuration of experimental multi-source setup. The Paths indicate the flow of power.

Power emitted from the primary source is supplied to the applicator via Path A. Only a small fraction of its signal is decoupled to injection lock the secondary source via Path B. The secondary source's frequency coherent signal is supplied to the applicator via Path C. Isolators CIR1 to CIR3 protect the sources against incident signals and make them appear to be independent of each other, while circulator CIR4, together with a moving short, serves as a variable phase shifter. CIR5 places the secondary source into a reflection amplifier configuration. Important differences with respect to the single source implementation include:

- Sample now assumes a fixed position,
- Relative phase shift between sources is effected through the low power Path B in Figure 64, and
- Power from two or more sources, instead of a single source, is applied.

Both incident signals are interfered in the same slotted applicator used for the single source experiments. Measurements along the length of the slot for an empty applicator are compared with values from equation 27 in Figure 65. These agree well with each other. A comparison between measurement and HFSS simulations of the same setup, but with a carbon slab located at the centre position, produced good agreement for -70° relative phase shift shown in Figure 66a. The correlation is not as good for 195° as shown in Figure 66b, however the positions of peaks and troughs do correspond. Reasons for the discrepancy in the latter figure are likely related to the granularity of the meshing in the simulation. The apparent phase offset of approximately 12° between the graphs in Figure 66a can be attributed to the sensitivity of the manually adjustable delay, where a position error of only ±1 mm corresponds to a phase error of ≈ ±5°.

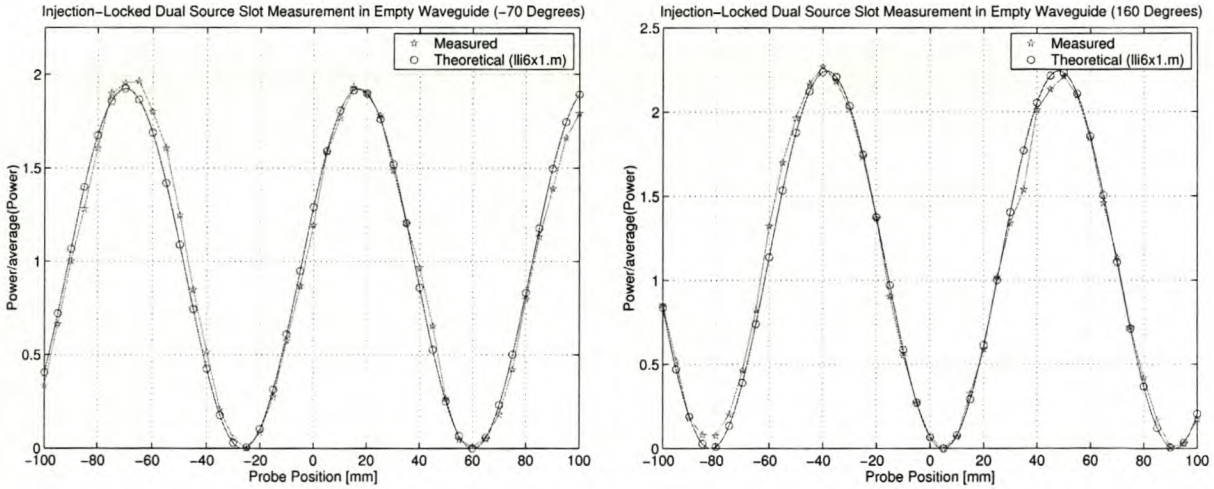

Figure 65: Comparison of measurements with values from equation 27 for two different relative phase shifts between sources in an empty applicator.

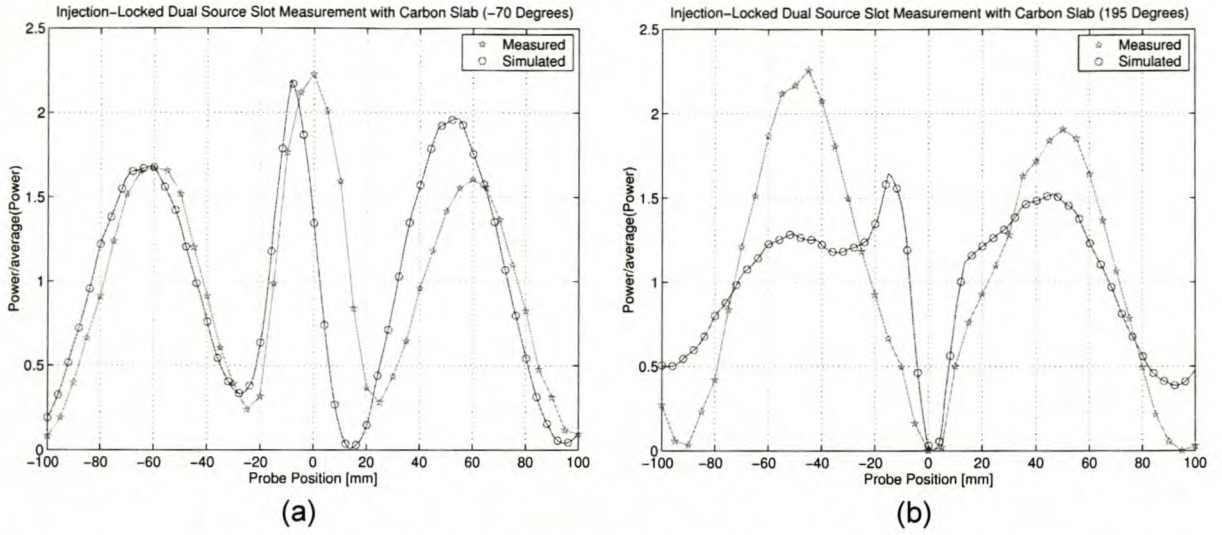

Figure 66: Comparison of measurements with results from HFSS® for two different relative phase shifts between sources in an applicator with carbon sample.

The field/heating patterns obtained inside the applicator are far more revealing. Sheets or blocks made from a specially developed paste consisting of silica gel impregnated with cobalt chloride (for preparation see appendix D) and bonded with cellulose produce a colour change from rose when moist to a deep cobalt blue in their dry state, with a continuous colour gradient in between. When placed into an applicator and exposed to microwave heating fields, areas of high field intensity dry the material and thereby produce a clearly noticeable change in colour — be it for a long slab or inside a block (Figure 67).

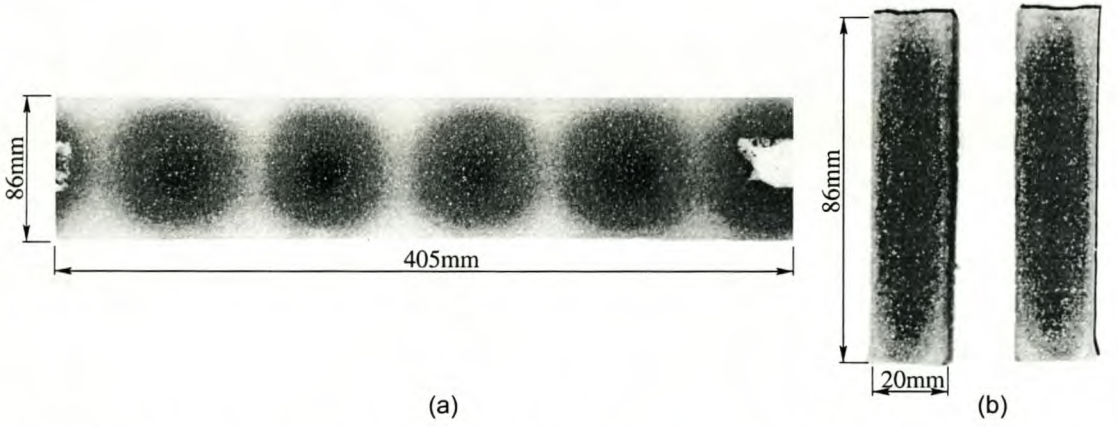

Figure 67: Paste made of silica gel impregnated with cobalt chloride can be cast into sheets (a) and blocks (b). Characteristic field and heating patterns can be made visible when these sheets or blocks are exposed to microwaves, here about 1500 W at 2449 MHz for close to 3 minutes in the interference modulation applicator of Figure 63. The dark patches indicate positions of high field intensity.

Changes in the relative phase difference between sources change the position of peaks and troughs. This is shown for three different phases in Figure 68, all three of which were applied continuously and for roughly the same length of time to synthesise an approximately uniform field pattern as shown Figure 69. A slight

attenuation towards the centre of the strip is evident. This is caused by an exponential loss in field intensity, as is expected.

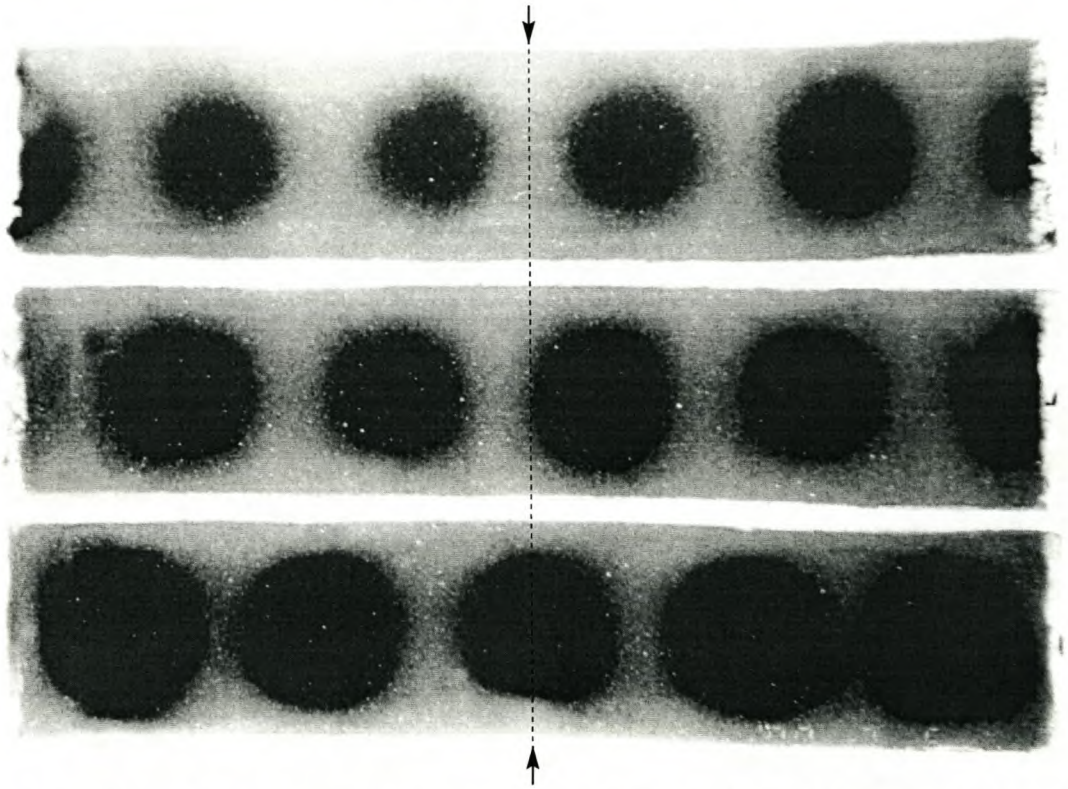

Figure 68: Features 'fixed' in silica gel impregnated with cobalt chloride. The relative phase difference of the features starting from the top is 180°, 120° and 0°.

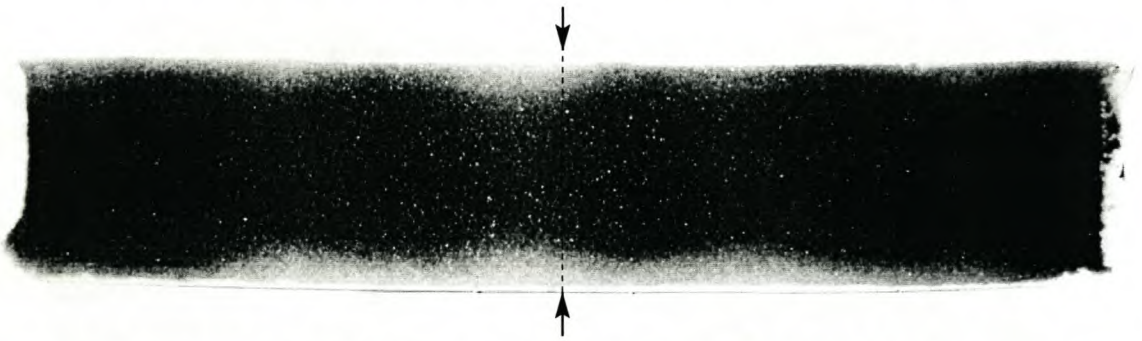

Figure 69: All features of Figure 68 applied to a cobalt chloride sheet with about the same time weight for a total exposure time of 6 minutes.

Simulations carried out with HFSS, and shown in Figure 70 and Figure 71, confirm the features obtained with cobalt chloride impregnated silica gel in Figure 68 and Figure 69.

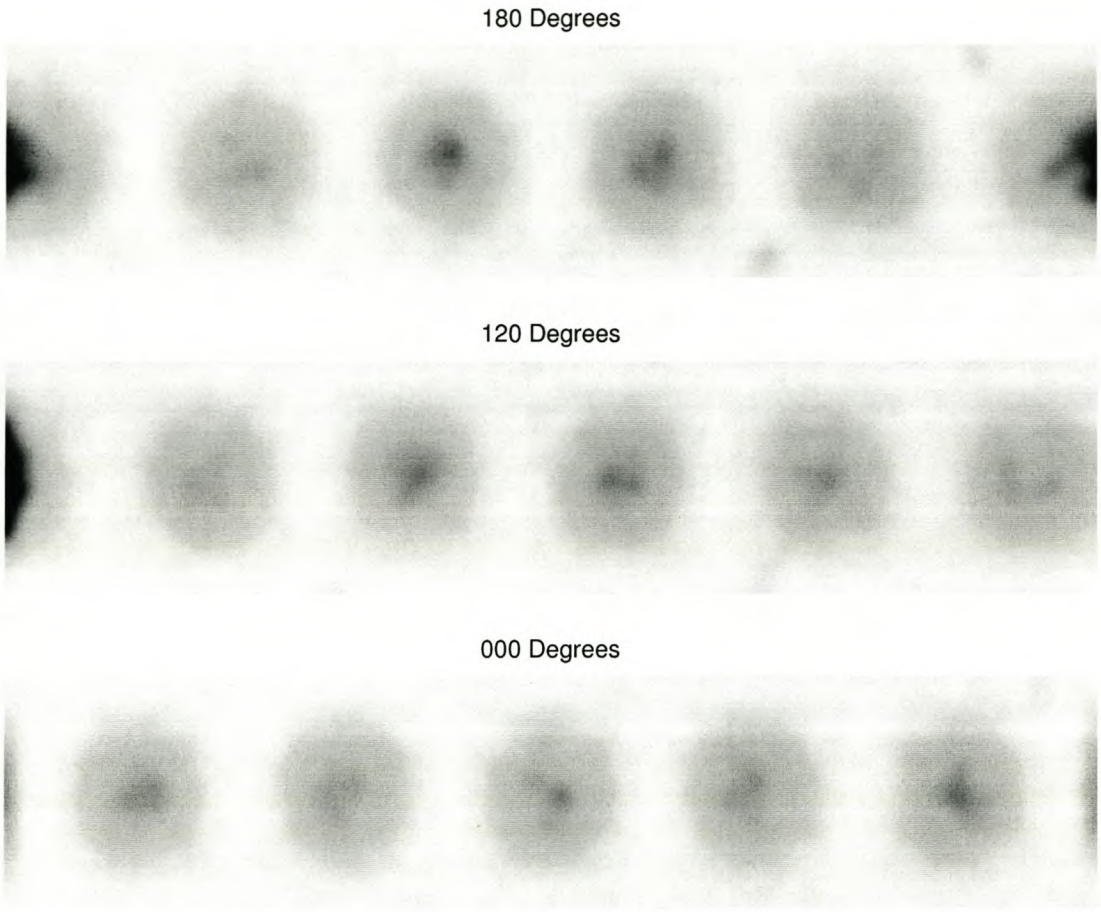

Figure 70: Simulation carried out on HFSS for the case depicted in Figure 68. A measured dielectric constant of $\varepsilon_r = 5.15 - 1.6\mathrm{j}$ was used for the cobalt chloride impregnated silica gel.

Figure 71: All features of Figure 70 applied to a cobalt chloride sheet with about the same time weight.

Though the cobalt chloride samples do not yield quantitative, numerical information, the direct visual confirmation of theory and simulation that they do provide is very satisfactory indeed. It shows that measurement, theory, simulation and visualisation of fields produced by interference modulation all concur.

4.6 Conclusion

In the single subdivided source topology, frequency coherence is inherent and interference modulation is merely a matter of setting the correct relative phase shift. Combining the power of multiple sources, however, requires them to be injection locked in order to achieve frequency coherence. It has been shown that injection locking does occur, and that the relative phase shift between the sources can be adjusted in the prototype produced. Initially, the phase could not be adjusted in a predeterminable manner. This was related to insufficient source-to-source isolation, and was corrected for. Thereafter, the system performed as predicted. Signals of the same frequency but with different phase were produced and applied to an interference modulation topology.

The gain-bandwidth based model can be used, as a numerical alternative to the Rieke diagram, representing the frequency, power and complex impedance behaviour of an oscillator, to model the performance of a magnetron for fixed bias conditions. The model was verified and was found to produce good results. An advantage of the model is its economical use of coefficients, making it suitable for the publication of magnetron data analogous to Spice semiconductor data. Currently magnetron device data is published solely in the form of graphs and plots.

Predicted, simulated, synthesized and measured patterns concurred well in both the single and dual source configurations. At first, interference modulation was verified in order to produce repeatable individual features that agreed with theory. Thereafter these features were applied to a synthesis method proposed, and again this compared favourably with predictions. Both lossless and lossy samples were used in the experiments. Here the lossy samples are of major concern, for they may inhibit the occurrence of interference, particularly within bulk material. Together lossiness and thickness of the bulk material, it is found, impose a resolution limit. For surface treatment, where the effective loss in the interference path is very low, the resolution limit is of little concern. In general, sufficient interference space is readily available above the material and interference patterns can be synthesized. Surface treatment was demonstrated visually for a sheet of lossy material and the results obtained confirmed simulations.

Chapter 5

Conclusion

Imposed electromagnetic waves produce a volumetric temperature change in matter. Reflections in the heating chamber, or the applicator, containing the material, result in the formation of particular modal patterns. As a consequence of these spatial patterns, localised hot spots, that mitigate against uniform heating throughout the material, are developed during the heating process. Hence, one of the most pressing and crucial issues in microwave heating is the need to realise uniform or predeterminable and controllable microwave heating patterns.

Traditionally, passive devices such as mode-stirrers and turn-tables have been used to enhance the heating and field uniformity within an applicator. Besides providing no guarantee of uniformity, they also do not provide a means of controlling the resulting field pattern. Furthermore, these crude, mechanical methods cause frequency variations of the source and provide no mechanism to compensate for system variations on a product to product basis.

Modern material synthesis applications call for control of the heating pattern. An active approach based on interference was conceived, adapted for microwaves and enhanced by way of a simple pattern synthesis technique. The topology has been demonstrated and shown successfully to synthesise uniform heating patterns as well as specific predetermined heating patterns. The forms of the synthesised patterns were shown to agree with theoretical predictions. Through applying a synthesis technique, the prototype was made suitable for automatic, online, adaptive control.

In the following two subsections findings with regard to the topology used for the prototype and recommendations for an industrial version of the system are detailed. Following this, is a summary of contributions and achievements. The chapter finishes with a summary of this section

5.1 Topology

Peaks and troughs of individual interference patterns, known as features, were shown to be functions of the relative phase shift between sources. The thermal momentum of target materials allows discrete or 'stepped' features to be used in synthesising a time averaged heating pattern by using weighted averaging of a fixed set of features.

Controllable features are produced by interference modulation, which requires frequency coherence and control of the relative phase difference between two incident sources. Once this is achieved, individual features may be produced. The proposed topology injection locks narrow band high power sources to a low power

phase control signal. This results in a simple and elegant solution, which caters for both coherence of the sources and precise control of the heating pattern. The topology also greatly relaxes requirements on the power handling capacity of the control components, since these run at relatively low power although they are capable of controlling high power, narrow band sources such as magnetron tubes.

Injection locking theory contributed to the development of the system's theory of operation, while concepts borrowed from feature extraction were adapted and applied to microwave dielectric heating for the first time.

The theory developed to describe the system was first validated, whereafter the proposed injection locking interferometer, with low-power control of the relative phase shift, was implemented and tested. The process entailed measurement of injection locking behaviour in the time and the frequency domains. The measurements were used to determine the optimum amplitude and frequency of the injected signal required to produce stable injection locking. Having established and verified these two important parameters, it was then possible to reliably produce interference in the applicator and to measure the resulting phases and field strengths produced. Phase measurements in the time domain, as well as field measurements at various pertinent relative phase differences, were made. A pattern visualisation technique was also applied to complement the field measurements and to serve as an additional means to verify the theoretical data. The technique provided direct visual confirmation of theory and simulation. These were all shown to have compared very satisfactorily indeed with the visualisation technique, having given particularly valuable, visual feedback. Theory, simulation and two different measurement techniques all support each other, thereby successfully validating the operation of the proposed topology.

In the same way that the advent of digital circuitry has shifted the focus of design away from hardware topologies and onto the software controlling it, the development of the proposed topology represents a step towards a scenario where the focus of the design in microwave heating equipment is on versatile DSP based software solutions, which can drive a multi-purpose applicator, as opposed to focussing on the design of application specific applicators.

5.2 Recommendations for an industrial system

An industrial system may call for increased microwave power capability. These requirements are addressed by the:

- Addition of multiple sources or the use of higher power sources,
- Control of the individual sources' power with compensation for frequency pushing effects,
- Use of vector modulators.

Multiple sources may also be configured so as to add the benefit of 'graceful degradation' and online serviceability. The schematic block diagram in Figure 72

shows the concept. In this topology, a low-power reference source resides in the low power section. The reference source may be semiconductor based but a magnetron based source is equally feasible.

Industrial applications require tighter control of the supply, since this has an influence on output frequency. A combination of load pulling and frequency pushing can be used to compensate for this effect and stabilize the frequency.

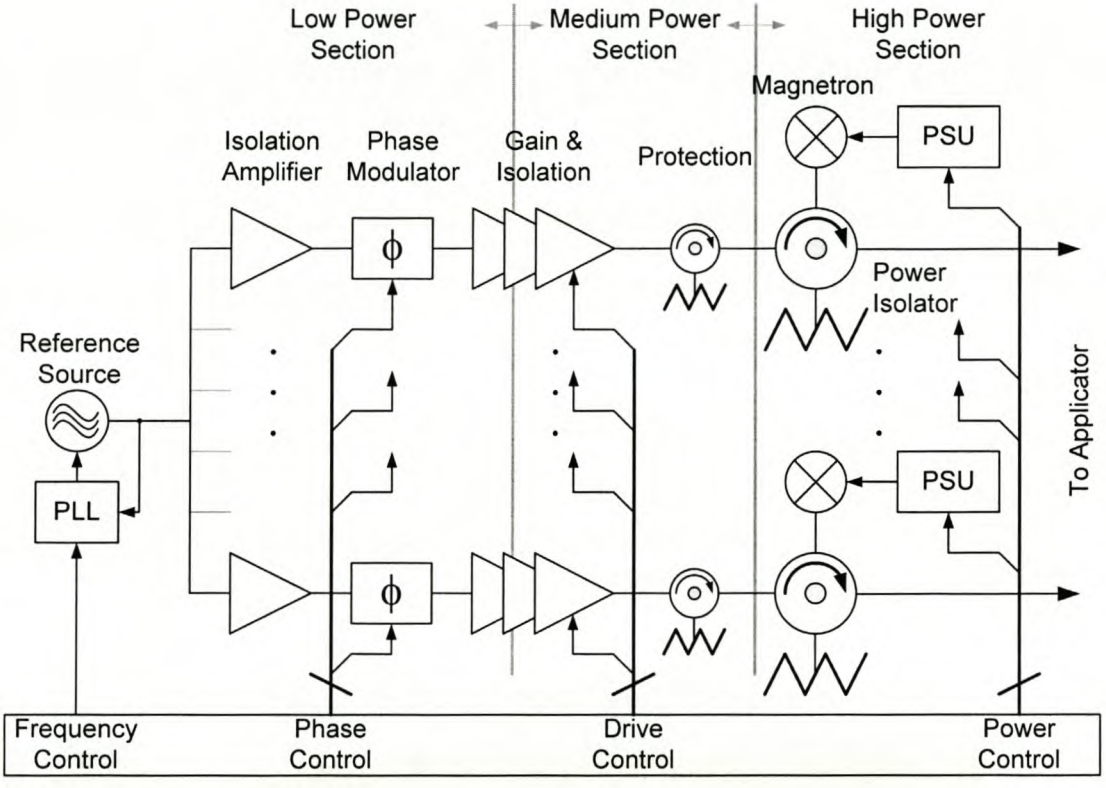

Figure 72: Industrial implementation of the interference modulation topology.

The combination of the suggestions made above result in a magnetron directional amplifier that may be considered and used as a relatively high integrity 'microwave power module'. The module implements full phase and amplitude control, thus making it is suitable for the task at hand.

Industrial set-ups have stringent safety requirements. Conventional measures, such as high-voltage protection and door-locks are not sufficient and external radiation measurements that trip system operation as soon as local safety limits are exceeded may need to be installed.

5.3 Summary of contributions, achievements and accomplishments

To build the proposed online adaptive microwave heating system, a number of new concepts and techniques were developed and described. The effort required that virtually all waveguide components and the high-voltage supplies be designed, built and tested by the author. The designs were produced in such a way as to make them easy to replicate. In addition to forming the essential backbone or infrastructure required to perform the research detailed in this thesis, the designs and their ease of reproduction made it possible for others to benefit from them in their own research into microwave dielectric heating. Similarly, the designs may be re-used by yet others in academia and industry to carry out further research in this field. Waveguide components produced include bends, power splitters, probes, launchers, measurement transitions and a calibration kit. A test bench with high voltage power supplies, filament supplies and high voltage meters for current and voltage, essential for the operation of magnetron based sources, was also constructed.

The microwave components were assembled into the interference modulation structures described. Injection locking measurements were carried out and these showed that:

- A low power signal of 3% of the magnetron oscillator's output power is guaranteed to lock it to said low power, from an external source. As a result, non-waveguide based components suffice to carry and further process the locking signal.
- The theoretical injection-locking bandwidth given by Adler's equations falls short of the actual measured bandwidth by about 20%. This is so because the derivations of van der Pol and Adler consider only linear contributions.

Injection-locking ensures that the magnetron based sources are frequency coherent and that their signal's phase can be set. Thereby, specific known phase differences were established between the sources' signals, and these were interfered to produce heating patterns, known as features.

Together with a synthesis technique, which decomposes a desired heating pattern into known features, the (linear) combination of appropriately weighted features by temporal superposition resulted in the overall heating pattern. This concept is distinctly different from current methods. In fact, it bears resemblance to the inverse of pattern recognition, but is adapted and applied to microwave dielectric heating to allow controlled and predetermined heating patters to be produced.

Both switched and continuous control of the features is possible with the injection-locking topology. The inherent thermal time constant of matter even allows a subset of specific discrete, non-continuous features to be used, as opposed to a continuous 'spectrum' of these feaures, making the topology particularly suitable for switching between features. This is significant, because it allows features to be switched, and hence simplifies control of the system.

5.4 Summary

The proposed topology makes use of injection-locked narrow-band microwave sources and components. Because of this, the design is simplified and the cost of the system kept low, when compared to broadband solutions. This narrow-band approach is well suited to high-power applications, especially since a low-power signal is sufficient to effect rapid control of the system. This control is exerted through injection-locking. Standard low-power microwave components, that are not necessarily waveguide based, form the control backbone of the interference modulation structure. As a result, magnetron based microwave sources can be located at or close to their point of application.

These benefits distinguish the proposed topology from others currently being employed and make it suitable for industrial processes which involve small numbers of high value materials, where change and adaptability of the heating process are of prime importance. Both uniform and relatively complex non-uniform heating profiles required for advanced material synthesis, the food industry, or 'Just-in-time' production of different items are possible with this design. Furthermore, this variation may be achieved on the same production line by changing software based parameters.

Bibliography

[1] John M. Osepchuk; 'A history of microwave heating applications'; IEEE Transactions on Microwave Theory and Techniques, Vol:32, No:9, September 1984, P:1200-1224.

[2] Steven Bradshaw; 'Introduction to microwave dielectric heating'; University of Stellenbosch, Department of Electrical Engineering, EHG-Laboratory, short course notes, April 1998.

[3] NRC; 'Microwave processing of materials'; National Materials Advisory Board, USA: Washington D.C, 1994, ISBN: 0-309-05027-8.

[4] 'Mikrowellenapparatur für Desinfektion und Schädlingsbekämpfung in Getreideprodukten und Lebensmitteln'; International Centre of Technological Cooperation, 1998.

[5] Philips E. Gawthop, Frank H. Sanders, Karl B. Nebbia, John J. Sell; 'Radio spectrum measurements of individual microwave ovens'; NTIA Report 94-303-1, Vol:1; U.S. Department of Commerce, 1994.

[6] 'EMC, The role and contribution of IEC standards'; International Electrotechnical Commission, February 2001.

[7] Imad Kobeissi; 'Noise reduction techniques for microcontroller-based systems'; AN1705, Motorola, 1999.

[8] 'Electromagnetic compatibility and radio spectrum matters (ERM), Electro Magnetic Compatibility (EMC) standard for radio equipment and services; Part 1: Common technical requirements'; European Telecommunications Standards Institute EN301486-1 V1.3.1, 2000

[9] Jon Binner, talk at University of Stellenbosch about material processing with microwaves, 1997.

[10] Jon G.P. Binner, Tom E. Cross, I.A.H Al-Dawery; 'Processing and characterisation of microwave and conventionally sintered bulk YGBCO high-Tc superconductors'; Microwave Processing of Materials V, Ed.: M.F. Iskander, E.R. Peteson, J.O. Kiggans, J.Ch. Bolomey, Proceedings of the Materials Research Society Spring Meeting, USA: San Francisco, April 1996.

[11] A. Cherradi, G. Desgardin, J. Provost, B. Raveau; 'Microwave sintering and texturing of high Tc superconductor YBaCuO'; CRISMAT, ISMRA and Université de CAEN, France: Caen, 1996.

[12] A. Cherradi, G. Desgardin, J. Provost, B. Raveau. Nouvelles Frontières de l'usage des micro-ondes pour le frittage des céramiques. ; CRISMAT, ISMRA and Université de CAEN, France: Caen.

[13] R. E. Newnham, S. J. Jang, Ming Xu, Frederick Jones; 'Fundamental interaction mechanisms between microwaves and matter'; The American Ceramic Society, Proceedings of the Symposium on Microwaves: Theory and Application in Material Processing, Cincinnati, USA, 1991, Vol:21, P:51-67, ISBN:0-944904-43-2.

[14] Christian Gerk, Monika Willert-Porada; 'Combination of laser and microwave heating - A new tool in ceramic processing'; Second World Congress on Microwave & Radio Frequency Processing, Orlando, Florida, USA, April 2000.

[15] Ernest Carl Okress; 'Microwave Power Engineering'; Academic Press, New York, USA, 1968, LCCN:68014655.

[16] V.N. Makarov, V.A. Nedel'ko, L.M. Nutovich; 'Modelling of the microwave heating of inhomogeneous media with phase transition'; Radiotekhnika i elektronika, No:5, 1991, P:960-964.

[17] Georges Roussy, John A. Pearce; 'Foundations and Industrial Applications of Microwaves and Radio Frequency Fields: Physical and Chemical Processes'; John Wiley & Sons, Chichester, England, UK, 1995, ISBN:0-471-93849-1.

[18] Ingolf Meier, Johann B. de Swardt; 'Synthesis of heating patterns by interference of microwaves'; International Journal of Electronics, Vol:87, No:6, 2000, P:725-734.

[19] Robert J. Lauf, Don W. Bible, Arvid C. Johnson, Carl A. Everleigh; '2 to 18GHz Broadband Microwave Heating Systems'; Microwave Journal, Vol:36, No:11, November 1993, P:24-34.

[20] Don W. Bible, Robert J. Lauf, Carl A. Everleigh, 'Multikilowatt variable frequency microwave furnace'; Materials Research Society Symposium Proceedings, Microwave Processing of Materials III, Editors: R.L. Beatty, W.H. Sutton, M.F. Iskander, Pittsburgh, Pennsylvania, Vol:269, P: 77-81.

[21] Tse V. Chow Ting Chan, Howard Charles Reader; 'Understanding microwave heating cavities'; Artech House, Boston, USA, 2000, ISBN:15805309X.

[22] Roger Meredith; 'Engineers' Handbook of Industrial Microwave Heating'; IEE Power Series 25, The Institute of Electrical Engineers, London, UK, 1998, ISBN:0-85296-916-3.

[23] Herbert Püschner; 'Heating with Microwaves, Fundamentals, Components and Circuit Technique'; Springer-Verlag, New York, USA, Series: Philips Technical Library, 1966, LCCN: 66018569.

[24] Robert F. Schiffmann; 'Microwave Technology a half-century of progress'; Food Product Design, Cover Story, May 1997.

[25] Magdy F. Iskander, Ray L. Smith, A. Octavio M. Andrade, Hal Kimrey Jr., Lee M. Walsh; 'FDTD simulation of microwave sintering of ceramics in multimode cavities'; IEEE Transactions on Microwave Theory and Techniques, Vol:42, No:5, May 1994, P:793-799.

[26] A.C. Metaxas, Roger J. Meredith; 'Industrial Microwave Heating'; Peregrinus, UK: London, 1988, ISBN:0906048893

[27] Vladimir Nedeljkovic; 'Statistical Pattern Recognition'; Lecture Notes, University of the Witwatersrand, 1994.

[28] Pierre A. Devijver, Josef Kittler; 'Pattern recognition: A statistical approach'; Prentice-Hall International, London, UK, 1982, ISBN: 0-13-654236-0.

[29] Robert S. Symons; 'Tubes: Still vital after all these years'; IEEE Spectrum, Vol:35, No:4, April 1988.

[30] 'ISTOK M-137 Magnetron'; ISTOK Microwave, Product note.

[31] William C. Brown; 'The sophisticated properties of the microwave oven magnetron'; IEEE Microwave Symposium Digest, Session:DD-5, USA: California, Long Beach, June 1989, P:871—874, ISSN:0149-645X.

[32] William C. Brown; 'The Magnetron -- A Low Noise, Long Life Amplifier'; Applied Microwave Journal, Summer 1990, P:117-121

[33] 'Electron Tubes: Book T4'; Philips Electronic Components, Eindhoven, The Netherlands, 1989.

[34] John D. Kraus; 'Electromagnetics'; 4th Ed, McGraw-Hill, New York, USA, 1991, ISBN:0-07-112991-9.

[35] Paul Hlawiczka; 'Introduction to Quantum Electronics'; Academic Press, London, UK, 1971, ISBN: 0-12-349950-X.

[36] Arthur Beiser; 'Concepts of Modern Physics'; McGraw-Hill International, Physics Series, Singapore, 1987, ISBN:0-07-100144-1.

[37] David M. Pozar; 'Microwave Engineering'; Addison-Wesley, 1990, ISBN:0-201-50418-9.

[38] Simon Ramo, John R. Whinnery, Theodore van Duzer; 'Fields and Waves in Communication Electronics'; John Wiley & Sons, New York, 1965, LCCN:65019477.

[39] Amnon Yariv; 'Quantum Electronics'; 3rd Ed, John Wiley & Sons, 1988, Singapore, ISBN:0-471-61771-7.

[40] Richard H. Pantell, Harold E. Puthoff; 'Fundamentals of Quantum Electronics'; John Wiley & Sons, New York, USA, 1969, ISBN:0-471-657905.

[41] Constantine A. Balanis; 'Advanced Engineering Electromagnetics'; John Wiley & Sons, New York, USA, 1989, ISBN:0-471-50316-9.

[42] Hendrik Wade Bode; 'Network Analysis and Feedback Amplifier Design'; D. van Nostrand Company, Boston, USA, 1945, LCCN:6464786.

[43] Hewlett-Packard; 'Basics of measuring the dielectric properties of materials'; Hewlett-Packard, USA, Application Note: 1217-1, 1992.

[44] Douglas C. Giancoli; 'Physics for Scientists and Engineers'; 2nd Ed, Prentice-Hall International, London, England, UK, 1988, ISBN:0-13-674045-6.

[45] Ingolf Meier, Johann B. de Swardt; 'Simple pattern synthesis for microwave dielectric heating'; IEEE Africon'99 Proceedings, Cape-Town, South-Africa, P:1121-1126.

[46] Ingolf Meier, Johann B. de Swardt; 'Pattern synthesis for microwave heating applications'; in Microwaves: Theory and Application in Materials Processing V, Ceramic Transactions, Vol:3, Editors: David E. Clark, Jon G.P. Binner, David A. Lewis, American Ceramics Society, March 2001, ISBN:1-574-98103-X.

[47] Ingolf Meier, Johann B. de Swardt; 'Interference modulation for microwave dielectric heating'; Proceedings of the AP/MTTS/RS Conference '98, Cape-Town, South Africa.

[48] EHG Laboratory, Department of Electrical and Electronic Engineering, University of Stellenbosch, 1999, Involvement of the author in the design of industrial multi-purpose applicators.

[49] A. W. Hull; 'The Effect of a Uniform Magnetic Field on the Motion of Electrons between Coaxial Cylinders'; Physical Review, 1921, Vol:18, No:1, P:31-57.

[50] Ingolf Meier, Johann B. de Swardt; 'Use of commercial magnetron tubes for industrial processes: Common failures and causes'; University of Stellenbosch, Department of Electrical and Electronic Engineering, Electro Heating Group, Technical Report: EHG-2, 30 September 1998.

[51] V.B. Bayburin, G.L. Sobolev; 'Analysis of the nonlinear region of a plane multi-resonator magnetron with space charge taken into account'; Radio Engineering and Electronic Physics, No:3, Vol:12, March 1967, P:440-448.

[52] George Briggs Collins; 'Microwave Magnetrons'; M.I.T. Radiation Lab. Series #6, 1st Ed., McGraw-Hill Book Co., USA, 1948, LCCN: 48007106.

[53] Ernest Carl Okress, et al; 'Crossed-Field Microwave Devices'; Academic Press, New York, USA, 1961, LCCN:60014270.

[54] George E. Dombrowski; 'Simulation of magnetrons and crossed-field amplifiers'; IEEE Transactions on Electron Devices, Vol:35, No:11, November 1988, P:2060-2067.

[55] English Electric Valve Ltd.; 'EEV Magnetrons', Brochure; English Electric Valve Ltd., Chelmsford, Essex, England, UK.

[56] K. Schünemann, A. Serebryannikov, D. Vavriv; 'Analysis of the Complex Natural Frequency Spectrum of the Azimuthally Periodic Coaxial Cavity'; Microwave and Optical Technology Letters, Vol:17, No:5, 5 April 1998, P:308-313.

[57] James Benford, John Swegle; 'High-Power Microwaves'; Artech House, Norwood, USA, 1992, ISBN: 0-8900-6415-6.

[58] Badford L. Smith, Michel-Henri Carpentier; 'The Microwave Engineering Handbook, Volume 1: Microwave Components'; Chapman & Hall, London, UK, 1993, ISBN: 0-4124-5660-5.

[59] K. Hinkel; 'Magnetrons'; Philips Technical Library, Series: Electronic valves, No:15, Eindhoven, The Netherlands, 1961.

[60] Carol L. Kory; 'The First International Vacuum Electronics Conference in Review'; Microwave Journal, January 2001, Vol:44, No:1, P:152—154, ISSN: 0192-6217.

[61] Katsumi Fukomoto, Masamitsu Nakajima, Jun-Ichi Ikenoue; 'Mathematical representation of microwave oscillator characteristics by use of the rieke diagram'; IEEE Transactions on Microwave Theory and Techniques, Vol:31, No:11, November 1983, P:954-959.

[62] Tetsuo Hirota, Masamitsu Nakajima, Jun-Ichi Ikenoue; 'A simple equivalent oscillator allowing for nonlinearity'; International Journal of Electronics, Vol:48, No:5, 1980, P:427-434.

[63] Balth van der Pol; 'The nonlinear theory of electric oscillators'; Proceedings of the Institute of Radio Engineers, Vol:22, No:9, September 1934, P:1051-1086.

[64] —; 'Getting Started - A Radiation Problem'; Ansoft Corporation, Maxwell Eminence, Revision 3.0, Sept 1994.

[65] —; 'Maxwell Control Panel - User's Reference'; Ansoft Corporation, Maxwell Eminence, Revision 1.3, May 1994.

[66] —; 'Maxwell Control Panel - Quick Reference'; Ansoft Corporation, Maxwell Eminence, Revision 1.3, May 1994.

[67] Thomas Ohlsson; 'Minimal processing of foods with electric heating methods'; Processing Foods: Quality Optimization and Process Assessment, Edited by: Fernanda A.R. Oliveira and Jorge C. Oliveira, CRC Press, USA, 1999, P:101-102, ISBN:0-8493-7905-9/99.

[68] Carlo Kopp; 'A Doctrine for the use of Electromagnetic Pulse Bombs'; RAAF APSC Working Paper #15, Australia, July 1993.

[69] Carlo Kopp; 'An Introduction to the Technical and Operational Aspects of the Electromagnetic Bomb'; Air Power Studies Centre, Fairbairn, Australia, November 1996.

[70] A. Palevsky, G. Bekefi, A. T. Drobot; 'Numerical simulation of oscillating magnetrons'; Journal of Applied Physics, Vol:52, No:8, August 1981, P:4936-4941.

[71] S. B. van der Geer, M. J. de Loos; 'The General Particle Tracer code: Design, Implementation and Application'; Technische Universiteit Eindhoven, 2001, ISBN: 90-386-1739-9.

[72] J. Krall, V. Serlin, M. Friedman, Y. Y. Lau; 'Simulated Studies of Particle Acceleration Powered by Modulated Intense Relativistic Electron Beams'; Particle Accelerators, Vol:25, 1989, P:43-56.

[73] John L. Warren, Mary T. Menzel, Grenfell Boicourt, Helen Stokes, Richard K. Cooper; 'POISSON/SUPERFISH Reference Manual'; LA-UR-87-126, Los Alamos National Laboratory, Los Alamos, NM, USA, January 1987.

[74] Massachusetts Institute of Technology, Department of Electrical Engineering; 'Applied Electronics: A first course in electronics, electron tubes and associated circuits'; John Wiley & Sons, New York, USA, 1954, LCCN: 7918477.

[75] George C. Southworth; 'Graphical analysis of microwave components, Part II'; Microwave Journal, July 1959, P:33-39.

[76] H. Takahashi, I. Namba, K. Akiyama; 'Magnetron Rieke diagram plotting and application'; Journal of Microwave Power, Vol:14, No:3, 1979, P:261-268.

[77] H. Takahashi, I. Namba, K. Akiyama; 'Automatic plotting of magnetron Rieke diagram'; Microwave Power Symposium Digest, 1978, P:124-126.

[78] Balth van der Pol; 'Forced oscillations in a circuit with non-linear resistance (Reception with reactive triode)'; Philosophical Magazine and Journal of Science, Taylor and Francis, London, England, UK, Series:7, Vol:3, No:13, January 1927, P:65-80.

[79] Robert Adler; 'A study of Locking Phenomena in Oscillators'; Proceedings of the IRE and Waves and Electrons, June 1946, P:351—357.

[80] H.L. Thal, R. G. Lock; 'Locking of magnetrons by an injected RF signal'; IEEE Transactions on Microwave Theory and Techniques, Vol:MTT-13, No:6, November 1965, P:836-846.

[81] K. Kurokawa; 'Microwave solid state oscillator circuits'; published in: 'Microwave devices: Device circuit interactions', edited by M. J. Howes, D. V. Morgan, John Wiley & Sons, London, UK, 1976, Chpt:5, ISBN:0-471-41729-7.

[82] K. Kurokawa; 'An introduction to the theory of microwave circuits'; Academic Press, New York, USA, 1969, Chpt:9.

[83] K. Kurokawa; 'Some basic characteristics of broadband negative resistance oscillator circuits'; American Telephone and Telegraph Company, The Bell System Technical Journal, Vol:48, No:6, July--August 1969, P:1937-1955.

[84] Eric Holzman, Ralston Stewart Robertson; 'Solid-state microwave power oscillator design'; Artech House, Boston, USA, 1992, ISBN:0-890-06487-3.

[85] E.M. Guttsayt, L.N. Karpova, V.N. Makarov; 'Magnetron synchonization band'; Radio Engineering and Electronic Physics, Vol:13, No:10, 1968, P:1611-1615.

[86] W. Woo, J. Benford, D. Fittinghoff, B. Harteneck, D. Price, R. Smith, H. Sze; 'Phase locking of high-power microwave oscillators'; Journal of Applied Physics, Vol:65, No:2, January 1989, P:861-866.

[87] L. Sivan; 'Microwave tube transmitters'; Chapman & Hall, New York, USA, 1994, ISBN:0-412-5795-02, P:183-191.

[88] S. Sarkar, O.S. Gupta; 'Dependence of the multiple-device oscillator injection-locking range on the number of constituent devices'; IEEE Transactions on Microwave Theory and Techniques, Vol:34, No:7, July 1986, P:839-840.

[89] Robert E. Collin; 'Foundations for microwave engineering'; McGraw-Hill, Singapore, 1992, ISBN:0-07-011811-6, P:481-485.

[90] George D. Vendelin, Anthony M. Pavio, Ulrich L. Rohde; 'Microwave circuit design using linear and nonlinear techniques'; John Wiley & Sons, New York, USA, 1990, ISBN:0-471-58060-0, Sec:6.3.

[91] Max Sucher, Jerome Fox; 'Handbook of microwave measurements'; 3rd Ed., Polytechnic Press of the Polytechnic Institute of Brooklyn, New York, USA, 1963, Vol:II, Chpt:20.

[92] V.N. Danilov; 'The theory of a relativistic magnetron'; Radio Engineering and Electronic Physics, December 1966, P:1906-1919.

[93] V.B. Bayburin, G.L. Sobolev; 'Design of basic electrical parameters of multicavity magnetrons'; Radio Engineering and Electronic Physics, No:9, September 1967, P:1493-1498.

[94] J.C. Slater; 'The phasing of magnetrons'; Massachusetts Institute of Technology, Research Laboratory of Electronics, Technical Report No. 35, 3 April 1947.

[95] E.E. David, Jr.; 'RF phase control in pulsed magnetrons'; Proceedings of the IRE, June 1952, P:669-685.

[96] Ihor O. Bohachevsky, Mark E. Johnson, Myron L. Stein; 'Generalized simulated annealing for function optimization'; The American Statistical Association and the American Society for Quality Control, Technometrics, Vol:28, No:3, August 1986, P:209-217.

[97] A. Patnaik, R.K. Mishra; 'ANN techniques in microwave engineering'; IEEE Microwave Magazine, Vol:1, No:1, March 2000, ISSN:1527-3342, P:55-60.

[98] V. Nguyen Tran; 'Continuous microwave re-working of defective confectionary'; Second World Congress on Microwave & Radio Frequency Processing, Renaissance Orlando Resort, Orlando, Florida, USA, April 2000.

[99] E.O. Goksoy, C. James, S.J. James; 'Non-uniformity of surface temperatures after microwave heating of poultry meat'; Journal of Microwave Power and Electromagnetic Energy, Vol:34, No:3, 1999, P:149-160.

[100] 'VFM processing: Rapid cure techniques for the electronic packaging industry'; Lambda Technologies, Product Application and Description, 2000, Reference: G.D. Smith, Lambda Technologies, Second World Congress on Microwave & Radio Frequency Processing, Renaissance Orlando Resort, Orlando, Florida, USA, April 2000.

[101] R. L. Schulz, G. G. Wicks, David E. Clark; 'Microwave remediation of emissions resulting from treatment of electronic components'; Second World Congress on Microwave & Radio Frequency Processing, Orlando, Florida, USA, April 2000.

[102] Paola Veronesi, Cristina Leonelli, Anna Bonamartini Corradi; 'Restoring of catalytic alumina porous spheres by microwave treatments'; University of Modena and Reggio Emilia, Italy, Second World Congress on Microwave & Radio Frequency Processing, Orlando, Florida, USA, April 2000.

[103] 'Recovery of metals'; EMR Microwave Technology Corporation, Canada, www.emrmicrowave.com.

[104] Ilja Graulich; 'Microwave technology used to unlock mineral wealth', Business Day, South Africa, 10 September 1999.

[105] Yoshio Nikawa, Keiji. Kawai, Shigeyuki. Ebisu; 'Application of microwaves to dental caries treatment'; Second World Congress on Microwave & Radio Frequency Processing, Renaissance Orlando Resort, Orlando, Florida, USA, April 2000.

[106] S. Rhee, G. Link, Manfred Thumm; 'Dilatometric measurements of nanoscaled ceramics in a 30GHz millimeter wave field'; University of Karlsruhe, Germany, Second World Congress on Microwave & Radio Frequency Processing, Orlando, Florida, USA, April 2000.

[107] Dorothee Vinga Szabo, Dieter Vollath; 'Nanocomposites from coated nanoparticles'; Advanced Materials, Vol:11, No:15, P:1313, Oct 1999.

[108] S. Aravindan, J. Ramkumar, R. Krishnamurthy; 'Microwave joining of Al_2O_3 and SiC with glass interlayer'; Second World Congress on Microwave & Radio Frequency Processing, Orlando, Florida, USA, April 2000.

[109] R. Borchert, Monika Willert-Porada; 'Pressureless microwave sintering of functional gradient materials'; The American Ceramic Society, Ceramic Transactions, VOl:94, Innovative Processing and Synthesis of Ceramics, Glasses, and Composites II, 1999, P:57-67, ISBN: 1-57498-060-2.

[110] Kenneth Frederick Sander; 'Microwave components and systems'; Addison-Wesley, Wokingham, England, UK, 1987, ISBN: 0-201-14544-8, Chpt: 5.11.

[111] 'The PIN diode circuit designers' handbook'; Microsemi Corporation, Watertown, Massachusetts, USA, 1998, Chpt:5.

[112] W.L. Teeter, K. R. Bushore; 'A variable-ratio microwave power divider and multiplexer'; IRE Transactions on Microwave Theory and Techniques, October 1957, P:227-229.

[113] Gernot Kubin; 'Fundamentals of Digital Signal Processing'; Course Notes, Austria: Villach, September 2001

[114] Alan V. Oppenheim, Ronald W. Schafer, John R. Buck; 'Discrete-time Signal Processing'; 2nd Ed., Prentice Hall, USA: New York, 1999, ISBN:0137549202

[115] Ingolf Meier; 'Simple discussion of results: Measured electrical properties of activated carbon'; Laboratory Report 199703170008, Department of Electrical and Electronic Engineering, University of Stellenbosch, Stellenbosch, South Africa, 17 March 1997.

[116] Erwin Kreyszig; 'Advanced engineering mathematics'; 5th Ed, John Wiley & Sons, New York, USA, 1983, ISBN:0471862517.

[117] David B. Fogel; 'What is evolutionary computation'; IEEE Spectrum, February 2000, P:26--32.

[118] Donald A. Pierre; 'Optimization Theory with Applications'; Dover Publications, New York, USA, 1986, ISBN:048665205.

[119] Thomas Coleman, Mary Ann Branch, Andrew Grace; 'Optimization Toolbox: For use with Matlab'; 3rd printing, The MathWorks Inc., Natick, Massachusits, USA, January 1999.

[120] S. Burkhart; 'Coaxial E-field probe for high-power microwave measurement'; IEEE Transactions on Microwave Theory and Technique, Vol:33, 1985, P:262-265.

[121] André P. C. Fourie; 'Antennas in Practice'; Handbook, Givati Fourie & Associates and University of the Witwatersrand, March 1994.

[122] Stephen Barnett, Timothy Mathew Cronin; 'Mathematical Formulae for Engineering and Science Students'; 4th Ed., Longman Scientific & Technical, Burnt Mill, Harlow, England, UK, 1992, ISBN: 0-582-44758-5.

[123] M.C. Hatfield, J.G. Hawkins; 'Design of an electronically steerable phased array for wireless power transmissions using a magnetron directional amplifier'; IEEE MTT-S International Microwave Symposium 1999, Anaheim, California, USA, June 1999, M04B-6, P:341-344, ISSN:0-7803-5135-5/99.

[124] Dean A. Frickey; 'Conversions between S, Z, Y, h, ABCD, and T parameters which are valid for complex source and load impedances'; IEEE Transactions on Microwave Theory and Techniques, Vol:42, No:2, February 1994, P:205-211.

[125] Jaroslaw Uher, Jens Bornemann, Uwe Rosenberg; 'Waveguide components for antenna feed systems: Theory and CAD'; Artech House, Boston, USA, 1993, ISBN:0-89006-582-9.

[126] Zhewang Ma, Taku Yamane, Eikichi Yamashita; 'Analysis and design of H-Plane waveguide bends with compact size, wide-band and low return loss characteristics'; IEEE Symposium Digest, 1997, Session:WE1B-6, P:417—420; ISBN:0-7803-3814-6.

[127] James J. Campbell, William R. Jones; 'Symmetrically truncated right-angle corners in parallel-plate and rectangular waveguides'; IEEE Transactions on Microwave Theory and Techniques, Vol:16, No:8, August 1968, P:517—529.

[128] R. Melville, D. Long, V. Gopinathan, P. Kinget; 'An injection locking scheme for precision quadrature generation'; ESSCIR 2001.

[129] Irving Kalet; 'Digital Cellular Communications: The Radio Interface - Towards the third generation'; CEI-Europe, Course 139I, March 2001, Germany: Munich.

[130] C. Rapp; 'Effects of HPA-Nonlinearity on a 4-DPSK/OFDM-Signal for a digital Sound Broadcasting System'; Proceedings of the Second European Conference on Satellite Communications, Liege, Belgium, 22-24 October 1991.

Appendices

Appendix A

Derivation of Injection Locking Equations: Van der Pol, Adler and Locking-Time

Derivations of the famous Van der Pol and Adler equations are given in this appendix. These are frequently used; however the derivation is not as simple and straight forward as their result. Thus, for purpose of clarity and completeness, all intermediate steps in the derivation are shown.
In addition, the general solution to the second order differential equation of an oscillator is verified by comparison to known results and at the same time the solution in (40a) is verified. This solution, in turn, forms the basis for deriving Adler's equation and from it the locking time equation of oscillators.

A.1 Van der Pol Equation

The derivation of a general equation describing an oscillator is derived in (2), Section 2.3.1. It is reproduced here, for convenience, as equation 38. The non-linear gain characteristic $\mathrm{I}(\mathrm{V}(\mathrm{t}))$ is included in (39).

$$\frac{\mathrm{d}^2}{\mathrm{dt}^2}\mathrm{V}(\mathrm{t})+\frac{\omega_0}{\mathrm{Q}}\frac{\mathrm{d}}{\mathrm{dt}}\left(\mathrm{V}(\mathrm{t})-R\,\mathrm{I}_{\mathrm{Res}}(\mathrm{V}(\mathrm{t}))\right)+\omega_0^2\,\mathrm{V}(\mathrm{t})=0 \tag{38}$$

$$\mathrm{I}_{\mathrm{Res}}(\mathrm{t})=\mathrm{I}(\mathrm{V}(\mathrm{t}))+\mathrm{I}_{\mathrm{inj}}(\mathrm{t}) \tag{39}$$

Equation 40a represents a general solution to (34) (see also equation 4) – the symbol '$*$' indicating convolution. The equations are derived in the time domain, under the same assumptions made by Balth van der Pol in [63] and [78].

Applying (39) to (40a) produces $\mathrm{V}(\mathrm{t})$ in (40b). $Z(\mathrm{t})$, the impulse impedance response of the resonator, as given earlier in (4), is evaluated in (37).

$$\mathrm{V}(\mathrm{t})=\mathrm{I}_{\mathrm{Res}}(\mathrm{t})*\frac{\mathrm{d}}{\mathrm{dt}}\mathrm{Z}(\mathrm{t}) \tag{40a}$$

$$=\mathrm{I}(\mathrm{V}(\mathrm{t}))*\mathrm{Z}'(\mathrm{t})+\mathrm{I}_{\mathrm{inj}}(\mathrm{t})*\mathrm{Z}'(\mathrm{t}) \tag{40b}$$

$$\mathrm{Z}(\mathrm{t})=\mathrm{L}^{-1}\langle\mathrm{Z}(\mathrm{s})\rangle=\mathrm{L}^{-1}\left\langle\frac{\mathrm{R}\,\omega_0}{\mathrm{Q}\,\mathrm{s}^2+\omega_0\,\mathrm{s}+\mathrm{Q}\,\omega_0^2}\right\rangle$$

$$=\frac{\mathrm{R}\omega_0}{\mathrm{Q}}\,\frac{\mathrm{e}^{-\frac{\omega_0}{2\mathrm{Q}}\mathrm{t}+\frac{\omega_0}{2\mathrm{Q}}\sqrt{1-4\mathrm{Q}^2}\,\mathrm{t}}-\mathrm{e}^{-\frac{\omega_0}{2\mathrm{Q}}\mathrm{t}-\frac{\omega_0}{2\mathrm{Q}}\sqrt{1-4\mathrm{Q}^2}\,\mathrm{t}}}{\frac{\omega_0}{\mathrm{Q}}\sqrt{1-4\mathrm{Q}^2}} \tag{41}$$

In the case of oscillators and low-loss resonators Q, the quality factor of the resonator, is much greater than unity such that the term $\sqrt{1-4Q^2}$ is approximated by $\sqrt{-4Q^2} = j2Q$, which yields (42).

$$\begin{aligned} Z(t) &= \frac{R\omega_0}{Q}\,\frac{e^{-\frac{\omega_0}{2Q}t+j\omega_0 t} - e^{-\frac{\omega_0}{2Q}t-j\omega_0 t}}{2\,j\omega_0} \\ &= \frac{R}{Q}\,e^{-\frac{\omega_0}{2Q}t}\left(\frac{e^{+j\omega_0 t} - e^{-j\omega_0 t}}{2j}\right) \\ &= \frac{R}{Q}\,e^{-\frac{\omega_0}{2Q}t}\,\sin(\omega_0 t) \quad \forall\, Q >> 1 \end{aligned} \tag{42}$$

An important element of the Laplace transform [122] is the notion of causality, that is no signal energy prior to t=0. This introduces the transient term $e^{-(\omega_0/2Q)t}$ in (42), which disappears with time.

Before the terms in (40b) can be solved for, it is necessary to shown that convolution does not produce additional frequency components. In other words, it must be shown that convolution is a linear operator.

Consider the convolution of '$a\sin(\omega_a t)$' with '$b\sin(\omega_b t)$' in (43).

$$\begin{aligned} a\sin(\omega_a t) * b\sin(\omega_b t) &= \int_0^t a\sin(\omega_a u)\, b\sin(\omega_b (t-u))\, du \\ &= \frac{a\,b}{\omega_a^2 - \omega_b^2}\left(\omega_a \sin(\omega_b t) + \omega_b \sin(\omega_a t)\right) \end{aligned} \tag{43}$$

Prior to the convolution, signals at ω_a and ω_b were present with RMS^2 amplitudes of $\frac{1}{2}a^2$ and $\frac{1}{2}b^2$ respectively; Afterwards the same frequency components were found but with RMS^2 amplitudes of $\frac{1}{2}\left(\frac{a\,b\,\omega_b}{\omega_a^2-\omega_b^2}\right)^2$ and $\frac{1}{2}\left(\frac{a\,b\,\omega_a}{\omega_a^2-\omega_b^2}\right)^2$ respectively. No additional new components occurred because the convolution operator obeys commutative, distributive and associative laws of mathematics [116]. Differentiation too can not introduce additional harmonics, only the non-linearity of $I(V)$ in (40b) can. Therefore in the case of an oscillator with an injected signal the output is approximated by equation 44, at least for small signals.

$$V(t) = a(t)\sin(\omega_0 t + \alpha) + b(t)\sin(\omega_i t + \beta) \tag{44}$$

A non-linearity can be approximated by polynomial sum (45). Van der Pol [63] found that a third order polynomial (46b) is sufficient to obtain sustained stable oscillation.

$$I(V(t)) = \sum_{k=0}^{\infty} p_k\, V(t)^k \tag{45}$$

$$I(V(t)) = \sum_{k=0}^{3} p_k \, V(t)^k$$

$$= \left(\tfrac{3}{4} p_3 a(a^2 + 2b^2) - p_1\right)\sin(\omega_0 t + \alpha) +$$

$$+ \left(\tfrac{3}{4} p_3 b(b^2 + 2a^2) - p_1\right)\sin(\omega_0 t + \beta) \qquad (46a)$$

$$= a_i \sin(\omega_0 t + \alpha) + b_i \sin(\omega_0 t + \beta) \qquad (46b)$$

In (46a) both $a = a(t)$ and $b = b(t)$ are assumed quasi-static. The following simplifications have been made by [63]:

- The polynomial constants are taken to be '$p_1 = 0$' and '$p_3 = 1$, i.e. $I(V(t)) = V(t)^3$, and
- The injected equivalent signal current is $I_{inj}(t) = I_i \cos(\omega_i t) = (\omega_i E/\gamma)\cos(\omega_i t)$. Here the cos-term appears because current is used, while [63] used the differential component, that is sin-component, corresponding to voltage.

Combining (40b) and (46b) one arrives at (47).

$$V(t) = a_i \sin(\omega_0 t + \alpha) * Z'(t) +$$

$$+ b_i \sin(\omega_i t + \beta) * Z'(t) +$$

$$+ \frac{\omega_i E}{\gamma} \cos(\omega_i t) * Z'(t) \qquad (47)$$

Next, the convolution terms of (47) are evaluated in (50), (51) and (52). Resulting $e^{-(\omega_0/(2Q))t}$ terms which tend to zero for t sufficiently large have been removed and the substitutions in (48) and (49) have been adopted to simplify the equations.

$$\alpha = -\frac{\omega_0}{Q} \qquad (48)$$

$$\gamma = \alpha R \qquad (49)$$

$$I_{inj}(t) * Z'(t) = -\omega_i E \left(\frac{-\omega_i \, \omega_i^2}{\alpha^2 \omega_i^2 + (\omega_i^2 - \omega_0^2)^2} + \frac{\omega_i^3}{\alpha^2 \omega_i^2 + (\omega_i^2 - \omega_0^2)^2} \right) \sin(\omega_i t) +$$

$$+ \frac{\omega_i^3 \, E \, \alpha}{\alpha^2 \omega_i^2 + (\omega_i^2 - \omega_0^2)^2} \cos(\omega_i t) \qquad (50)$$

$$a_i \sin(\omega_0 t + \alpha) * Z'(t) = \sin(\omega_0 t) \qquad (51)$$

$$
\begin{aligned}
b_i \sin(\omega_i t + \beta) * Z'(t) = & \frac{b_i \gamma \omega_i}{\alpha^2 \omega_i^2 + (\omega_i^2 - \omega_0^2)^2} \\
& (\omega_i^2 \cos(\beta)\cos(\omega_i t) - \omega_i^2 \sin(\beta)\sin(\omega_i t) - \\
& - \omega_0^2 \cos(\beta)\cos(\omega_i t) + \omega_0^2 \sin(\beta)\sin(\omega_i t) + \\
& + \omega_i \alpha \sin(\beta)\cos(\omega_i t) + \omega_i \alpha \cos(\beta)\sin(\omega_i t)) \\
= & \frac{b_i \gamma \omega_i}{\alpha^2 \omega_i^2 + (\omega_i^2 - \omega_0^2)^2} (\omega_i^2 \cos(\omega_i t + \beta) - \\
& - \omega_0^2 \cos(\omega_i t + \beta) + \omega_i \alpha \sin(\omega_i t + \beta))
\end{aligned} \tag{52}
$$

Substituting into (40b) yields:

$$
\begin{aligned}
V(t) = & \frac{a_i \gamma}{\alpha} \sin(\omega_0 t) + \\
& + \frac{b_i \gamma \omega_i}{\alpha^2 \omega_i^2 + (\omega_i^2 - \omega_0^2)^2} (\omega_i^2 \cos(\omega_i t + \beta) - \\
& - \omega_0^2 \cos(\omega_i t + \beta) + \omega_i \alpha \sin(\omega_i t + \beta)) + \\
& + \frac{E\omega_0^2 \omega_i^2 - E\omega_i^4}{\alpha^2 \omega_i^2 + (\omega_i^2 - \omega_0^2)^2} \sin(\omega_i t) + \frac{\omega_i^3 E \alpha}{\alpha^2 \omega_i^2 + (\omega_i^2 - \omega_0^2)^2} \cos(\omega_i t)
\end{aligned} \tag{53}
$$

Equating equal frequency terms in (44) and (53), two new equations (54) and (55) are obtained.

$$
a \sin(\omega_0 t + \alpha) = \frac{a_i \gamma}{\alpha} \sin(\omega_0 t) \tag{54}
$$

$$
\begin{aligned}
b \sin(\omega_i t + \beta) = & \frac{b_i \gamma \omega_i (\omega_i^2 - \omega_0^2)}{\alpha^2 \omega_i^2 + (\omega_i^2 - \omega_0^2)^2} \cos(\omega_i t + \beta) + \\
& + \frac{b_i \gamma \omega_i^2 \alpha}{\alpha^2 \omega_i^2 + (\omega_i^2 - \omega_0^2)^2} \sin(\omega_i t + \beta) + \\
& + E\omega_i^2 \frac{(\omega_i^2 - \omega_0^2)}{\alpha^2 \omega_i^2 + (\omega_i^2 - \omega_0^2)^2} \sin(\omega_i t) + \\
& + E\omega_i^2 \frac{\omega_i \alpha}{\alpha^2 \omega_i^2 + (\omega_i^2 - \omega_0^2)^2} \sin(\omega_i t)
\end{aligned} \tag{55}
$$

Being only interested in the power at the respective frequencies, the RMS^2 is taken, values for a_i and b_i from (46b) substituted, and evaluated leading to (56) and (57). Equation (58) is identical to the one obtained by [63].

$$
a = \frac{a_i \gamma}{\alpha} \tag{56}
$$

$$
a = \frac{\frac{3}{4}\gamma}{\alpha} a(a^2 + 2b^2) \tag{57}
$$

Let $a_0^2 = \frac{\alpha}{(3/4)\gamma}$ and solve (57) for a^2 to obtain:

$$a^2 = a_0^2 - 2b^2 \tag{58}$$

One proceeds similarly with (55). To simplify (55) both sides are first multiplied by $\alpha^2\omega_i^2 + (\omega_i^2 - \omega_0^2)^2$ and subsequently simplified with $z = (\omega_0^2 - \omega_i^2)/\omega_i$ to arrive at (59), before taking the RMS[2].

$$\left(b(\alpha^2\omega_i^2 + \omega_i^2 z^2) - b_i\gamma\omega_i^2\alpha\right)\sin(\omega_i t + \beta) + b_i\gamma\omega_i^2 z\cos(\omega_i t + \beta) = \\ = E\omega_i^2\left(\omega_i z\sin(\omega_i t) + \omega_i\alpha\cos(\omega_i t)\right) \tag{59}$$

$$\left(b(\alpha^2\omega_i^2 + \omega_i^2 z^2) - b_i\gamma\omega_i^2\alpha\right)^2 + (b_i\gamma\omega_i^2 z)^2 = E^2\omega_i^4\left((\omega_i z)^2 + (\omega_i\alpha)^2\right) \tag{60}$$

Dividing by ω_i^4, substituting for b_i from (46b), expanding polynomials and simplifying:

$$b^2\left(\left(\left(\alpha^2 + z^2\right) - \frac{b^2 + 2a^2}{a_0^2}\alpha^2\right)^2 + \left(\frac{b^2 + 2a^2}{a_0^2}\alpha z\right)^2\right) = E^2\omega_i^2\left(\alpha^2 + z^2\right) \tag{61}$$

After polynomial manipulation, the desired result in (62) follows from (61). The result is also found in [63].

$$b^2\left(z^2 + \alpha^2\left(1 - \frac{b^2 + 2a^2}{a_0^2}\right)^2\right) = E^2\omega_i^2 \tag{62}$$

Together with (58) an approximation of the gain required to achieve a particular locking bandwidth is possible. Under locked conditions the natural frequency ceases to exist, hence $a = 0$, and (58) turns into $b^2 = a_0^2/2$. Substitution into (62) yields:

$$\frac{a_0^2 z^2}{2} + \frac{a_0^2\alpha^2}{8} = \omega_i^2 E^2 \tag{63}$$

The left hand side of (63) contains amplitude modifying term $a_0^2\alpha^2/8$ which is related to the lossiness of the circuit. For high-Q circuits this term becomes negligible leading to (65), which relates bandwidth, circuit gain and injected signal amplitude. Equation 65 is frequently found in the literature including [63].

$$\frac{2E}{a_0\sqrt{2}} = \frac{\omega_0^2 - \omega_i^2}{\omega_i^2} \approx \frac{2(\omega_0 - \omega_i)}{\omega_i} \tag{64}$$

$$\frac{E}{a_0\sqrt{2}} = \frac{\omega_0 - \omega_i}{\omega_i} \tag{65}$$

In this appendix, two aims were achieved: It was shown that application of the general solution to the Van der Pol equation yields identical equations found by Balth van der Pol in [63], and in the trade literature [86]. A full derivation of these often cited and used equations was also presented.
The assumptions made by [63] were stated as well. It could also be seen that the solution in the literature represents an approximation to the linear case. It is

therefore important to realise that the result in (65) is but an approximation and should be treated as such.

A.2 Adler's equation and oscillator locking time

Previously the amplitude required by an injected signal to suppress the oscillator's natural frequency was considered. Robert Adler [79] was interested in the signal amplitude and its instantaneous phase constraints resulting in locking of a source into which an external signal is injected.
To improve understanding, Adler's equation is 'rediscovered', based on the differential equation of an oscillator. The first aim is to derive Adler's equation, and thereafter an expression for the injection locking time. Adler's equation is important to injection locking because it links instantaneous phase and amplitude of an oscillator to its injected signal which it tracks.
The injection locking time sets bounds on the phase velocity within which locking is maintained. If the instantaneous phase difference were to changed more rapidly than these bounds suggest, the oscillator would drop out of lock as it can no longer track the phase change.

The starting point is again the general differential equation of an oscillator in (66), with an injected signal.

$$\frac{d^2}{dt^2}V(t)+\underbrace{\frac{\omega_0}{Q}\left(\frac{d}{dt}V(t)-R\frac{d}{dt}I(V(t))\right)}_{\frac{\omega_o}{Q}\left(1-R\frac{d}{dV}I(V)\right)\frac{d}{dt}V(t)}+\omega_0^2\,V(t)=\frac{\omega_0 R}{Q}\frac{d}{dt}I_{inj}(t) \qquad (66)$$

It is assumed that the injected signal $I_{inj}(t)$ can lock the oscillator; the condition to satisfy this constraint will be derived. Hence $f_{osc}=f_{inj}$ and $V(t)=V_0(t)\cos(\omega_i t+\varphi(t))$,where $\varphi(t)$ is the instantaneous phase difference between the oscillators free-running and the injected signal. Hence $I_{inj}(t)=k\,V(t)$ applies to the synchronous case, turning equation (66) into (67).

$$\frac{d^2}{dt^2}V(t)+\frac{\omega_o}{Q}\left(1-R\frac{d}{dV}I(V)\right)\frac{d}{dt}V(t)+\omega_0^2\,V(t)=\frac{\omega_0 R}{Q}k\frac{d}{dt}V(t) \qquad (67)$$

Similar to (46), the assumed non-linearity is represented by a third order polynomial: $I(V(t))=p_3\,V(t)^3-p_1\,V(t)$, whereby one arrives at:

$$\frac{d^2}{dt^2}V+(\alpha-2\beta V^2)\frac{d}{dt}V+\omega_0^2 V=kk\frac{d}{dt}V \tag{68}$$

where

$$\alpha=\frac{\omega_0}{Q}(1+R\,p_1)$$

$$\beta=R\frac{\omega_0}{Q}p_3$$

$$kk=\frac{\omega_0 R}{Q}k$$

Use was not yet made of $V(t)=V_0(t)\cos(\omega_i t+\varphi(t))$. For ease of use later, first and second order derivatives of $V(t)$ are determined separately in (69) and (70).

$$\begin{aligned}\frac{d}{dt}V(t)&=\frac{d}{dt}\left(V_0(t)\right)\cos(\omega_i t+\varphi(t))+V_0(t)\frac{d}{dt}\left(\cos(\omega_i t+\varphi(t))\right)\\&=\frac{d}{dt}\left(V_0(t)\right)\cos(\omega_i t+\varphi(t))-\omega_i\sin(\omega_i t+\varphi(t))V_0-\sin(\omega_i t+\varphi(t))\frac{d}{dt}\left(V_0(t)\right)\end{aligned} \tag{69}$$

$$\begin{aligned}\frac{d^2}{dt^2}V(t)&=\frac{d^2}{dt^2}\left(V_0(t)\right)\cos(\omega_i t+\varphi(t))+\frac{d}{dt}\left(V_0(t)\right)\frac{d}{dt}\left(\cos(\omega_i t+\varphi(t))\right)-\\&\quad-\left(\frac{d}{dt}\left(V_0(t)\right)\left(\omega_i+\frac{d}{dt}\varphi(t)\right)\sin(\omega_i t+\varphi(t))+\right.\\&\quad\left.+V_0(t)\frac{d}{dt}\left(\omega_i+\frac{d}{dt}\left(\varphi(t)\right)\sin(\omega_i t+\varphi(t))\right)\right)\\&=\frac{d^2}{dt^2}\left(V_0\right)\cos(\omega_i t+\varphi(t))-\omega_i\sin(\omega_i t+\varphi(t))\frac{d}{dt}\left(V_0\right)-\\&\quad-\sin(\omega_i t+\varphi(t))\frac{d}{dt}\left(\varphi\right)\frac{d}{dt}\left(V_0\right)-\omega_i\sin(\omega_i t+\varphi(t))\frac{d}{dt}\left(V_0\right)-\\&\quad-\sin(\omega_i t+\varphi(t))\frac{d}{dt}\left(\varphi\right)\frac{d}{dt}\left(V_0\right)-\sin(\omega_i t+\varphi(t))\frac{d^2}{dt^2}\left(\varphi\right)V_0-\\&\quad-\omega_i\cos(\omega_i t+\varphi(t))\frac{d}{dt}\left(\varphi\right)V_0-\cos(\omega_i t+\varphi(t))\left(\frac{d}{dt}\left(\varphi\right)\right)^2 V_0\end{aligned} \tag{70}$$

A meaningful and solvable solution can be obtained if linear and first order terms of V_0 and φ are considered. Under this condition, substitution of (69) and (70) into (68) yields equation (71).

$$-\sin(\sim)2\omega_i \frac{d}{dt} V_0 - \cos(\sim)\left(\omega_i \frac{d}{dt}(\varphi) V_0\right) +$$
$$+(\alpha - 3\beta V^2)\left(\cos(\sim)\frac{d}{dt} V_0 - \sin(\sim)(\omega_i V_0 + \frac{d}{dt}(\varphi) V_0)\right) + \omega_0^2 V_0 \cos(\sim) =$$
$$= kk\left(\cos(\sim)\frac{d}{dt} V_0 - \sin(\sim)\right)\left(\omega_i V_0 + \frac{d}{dt}(\varphi) V_0\right) \qquad (71)$$

where

$$\sim = \omega_i t + \varphi$$

Making use of trigonometric identities in (72) and (73), $\sin$ terms of (71) are collected to produce equation (74).

$$\sin(\omega_i t + \varphi) = \sin(\omega_i t)\cos(\varphi) + \cos(\omega_i t)\sin(\varphi) \qquad (72)$$
$$\cos(\omega_i t + \varphi) = \cos(\omega_i t)\cos(\varphi) - \sin(\omega_i t)\sin(\varphi) \qquad (73)$$
$$\sin(\varphi)\left(\omega_i \frac{d}{dt}(\varphi) V_0 - \frac{d}{dt}(V_0)(\alpha - 3\beta V_0^2) - \omega_0^2 V_0\right) = -\frac{\omega_0 R V_i \omega_i}{Q} \qquad (74)$$

Equation 75 follows from (74), assuming V_0 to be quasi-constant, dividing both sides by V_0, and noting that $|\Gamma| = |V_i|/|V_0| = \sqrt{P_{In}/P_{Out}}$.

$$\frac{d}{dt}(\varphi)\sin(\varphi) - \frac{\omega_0^2}{\omega_i} = -\frac{\omega_0 |\Gamma|}{Q_E} \qquad (75)$$

Expressing ω_0 / ω_i in terms of bandwidth as in (76) and substituting into (75):

$$\frac{\omega_0}{\omega_i} = \frac{BW/2}{\omega_0} = \frac{|\omega_i - \omega_0|}{\omega_0} \qquad (76)$$
$$\frac{d}{dt}(\varphi) = |\omega_i - \omega_0| - \frac{\omega_0 |\Gamma|}{Q_E \sin(\varphi)} \qquad (77)$$

Under locked conditions $\frac{d}{dt}(\varphi) = 0$ from which (78) is obtained.

$$|\omega_i - \omega_0| = \frac{\omega_0 |\Gamma|}{Q_E} \qquad (78)$$

The bandwidth BW of a resonator is half the distance between its 3dB points, that is: $BW = 2|\omega_i - \omega_0|$, and (80) results, which is found in the literature [87]. It is the theoretical locking bandwidth under 'linear' conditions.[12]

$$BW_{radian} = \frac{2\omega_0 |\Gamma|}{Q_E} \qquad (79)$$

[12] Under linear conditions no oscillation can take place. However, it can be argued that this is the contribution of the linear term to the bandwidth. Higher order terms have been neglected in the derivation because they would greatly increase the difficulty of solving the equations without yielding further insight. Hence the equation provides a good estimate but is by no means exact!

$$BW_{hertz} = \frac{2 f_0 |\Gamma|}{Q_E} \tag{80}$$

The locking speed in (81) is obtained by integration of (77) for $\sin(\varphi) = \pm 1$. It corresponds with results provided in [53].

$$t = \frac{2\frac{\omega_0 |\Gamma|}{Q_E |\omega_i - \omega_0|}}{\left(\left(\frac{\omega_0 |\Gamma|}{Q_E}\right)^2 - |\omega_i - \omega_0|^2\right)^{\frac{1}{2}}} \tag{81}$$

A.3 Associative law applied to differentiated convolutes

Earlier, (4) and (40) used the relationship: $a' * b = a * b'$. Its proof is now derived. $L\langle\ \rangle$ and '$*$' are the Laplace transform and the convolution operator respectively.

It is to be shown that

$$\frac{d}{dt}(a(t)) * b(t) = a(t) * \frac{d}{dt}(b(t)) = \frac{d}{dt}(a(t) * b(t)) \tag{82}$$

for all initial conditions being zero.

$$L\left\langle \frac{d}{dt}(a(t)) * b(t) \right\rangle = L\left\langle \frac{d}{dt}(a(t)) \right\rangle L\langle b(t)\rangle = sL\langle a(t)\rangle L\langle b(t)\rangle \tag{83}$$

$$L\left\langle a(t) * \frac{d}{dt}(b(t)) \right\rangle = L\langle a(t)\rangle L\left\langle \frac{d}{dt}(b(t)) \right\rangle = L\langle a(t)\rangle s\langle b(t)\rangle \tag{84}$$

$$L\left\langle \frac{d}{dt}(a(t) * b(t)) \right\rangle = sL\langle a(t) * b(t)\rangle = sL\langle a(t)\rangle L\langle b(t)\rangle \tag{85}$$

From (83) equal (84) equal (85) follows (82), completing the proof.

Equation 40 can therefore be written in the following three forms:

$$V(t) = \frac{d}{dt}(I_{res}(V(t))) * C(t) = \frac{d}{dt}(I_{res}(V(t)) * C(t)) = I_{res}(V(t)) * \frac{d}{dt}(L(t)) \tag{86}$$

Appendix B

Time harmonic equation for energy conservation

Faraday's (87) and Ampère's (88) law, both as modified by Maxwell and including magnetic conduction σ_M serve as a starting point [41][44].

$$\nabla \times E = -M_S - \sigma_M H - j\omega\mu H \tag{87}$$

$$\nabla \times H = J_S + \sigma_E E + j\omega\varepsilon E \tag{88}$$

where

M_S =supplied magnetic current density [V/m^2]

J_S =supplied electric current density [A/m^2]

σ_M =magnetic conductivity [V/A m]

σ_E =electric conductivity [A/V m]

μ =permeability [Wb/A m]

ε =permittivity [C/V m]

Permittivity (89) and permeability (90) are complex quantities to allow for dielectric and magnetic loss.

$$\varepsilon = \varepsilon(1 - j\tan\delta_E) \tag{89}$$

$$\mu = \mu(1 - j\tan\delta_M) \tag{90}$$

where

$\tan\delta_E$ =electric loss tangent [1]

$\tan\delta_M$ =magnetic loss tangent [1]

Combining conduction into (87) and (88) we arrive at (91) and (92).

$$\nabla \times E = -M_S - (\sigma_M + \omega\mu\tan\delta_M + j\omega\mu)H \tag{91}$$

$$\nabla \times H = J_S + (\sigma_E + \omega\varepsilon\tan\delta_E + j\omega\varepsilon)E \tag{92}$$

Comparing (91) and (92) to vector identity (93) [122], (91) and the conjugate of (92) are dot multiplied with the conjugate of H and E respectively, to obtain the instantaneous time harmonic equation for energy conservation (94).

$$\nabla \bullet (A^* \times B) = B \bullet (\nabla \times A^*) - A^* \bullet (\nabla \times B) \tag{93}$$

$$\begin{aligned}\nabla \bullet (H^* \times E) &= E \bullet (\nabla \times H^*) - H^* \bullet (\nabla \times E) = -\nabla \bullet (E \times H^*) = \\ &= E \bullet J_S^* + (\sigma_E + \omega\varepsilon\tan\delta_E - j\omega\varepsilon)|E|^2 + \\ &\quad + H^* \bullet M_S + (\sigma_M + \omega\mu\tan\delta_M - j\omega\mu)|H|^2\end{aligned} \tag{94}$$

[34] and [41] show that the average is ½ the instantaneous value.
Integrating over the volume to which H and E are applied and using the 'divergence theorem of Gauss' [122], the link between the applied field and power is established in (95). (96) states that all energy supplied is either dissipated (converted to another form), stored, or passes through the media.

$$\underbrace{-\frac{1}{2}\iint_S (E\times H^*)dS}_{P_E} =$$

$$= \underbrace{\frac{1}{2}\iiint_V (E\bullet J_S^* + H^*\bullet M_S)dV}_{-P_S} +$$

$$+ \underbrace{\frac{1}{2}\iiint_V (\sigma_E + \omega\varepsilon\tan\delta_E)|E|^2 + (\sigma_M + \omega\mu\tan\delta_M)|H|^2\,dV}_{P_D} +$$

$$+ \underbrace{\frac{1}{2}j\omega\iiint_V (\mu|H|^2 - \varepsilon|E|^2)dV}_{P_P} \qquad (95)$$

$$P_S = P_E + P_D + P_P \qquad (96)$$

where

P_S =Power supplied [W]

P_E =Power exiting or not absorbed [W]

P_D =Power dissipated or absorbed [W]

P_P =Power potential, stored as energy [W]

Appendix C

Source Codes

The source code of the programs to calculate the interference in the waveguide and to perform the simulated annealing algorithm is given below.

C.1 Matlab code for interference in a waveguide

The Matlab™ code used to simulate interference in a waveguide, and to generate figures in section 3.2 is given below. It allows for adaptation to other structural dimensions or materials. As shown, active carbon with $\varepsilon_r = 10 - 2.5j$ in a WR340 waveguide of dimensions 86.36 mm by 43.18 mm (3.4" by 1.7") with a sample length of 25.4 mm (1") is used.

```
clear all;
% Calculate |E| of interference in waveguides
% Waveguide dimensions, modes and material
% characteristics can be set.
% Plots |E|^2, but can be changed.
%
% Ingolf Meier, 2000 04 21 14 02
%
j=sqrt(-1);     % jmath ... to make sure
f=2450e6;       % Frequency in [Hz]
w=2*pi*f;       % convert to rad/sec
c=299792458;    % Speed of light [m/s]

% Set EM material constants
% NOTE: Absolute constants used!!!
eps=1/(4*pi*1e-7*c^2)*(10-j*2.5); %epsilon
mu=4*pi*1e-7; % OK, taken here as mu_0 %mu
sig=0; %sigma = conduction

% Set waveguide dimensions [m]
z1=3.4*25.4e-3; % z1 dimension of WR340
y1=1.7*25.4e-3; % y1 dimension of WR340

% Length of applicator [m]
applilen=(25.4e-3*1);%Length of applicator [m]

% Relative phase shift between incident waves
deg=0:30:180; %degrees
deg=[0,106,188];

% Resolution for plot
step=1e-3;
Z=0:step:z1;
X=0:step:applilen;

% Set modes  m=1, n=0 is TE10 mode
m=1;
n=0;

% Set initial magnetic field
% Magnitude scaling constant
H0=1;  % magnetic field

% Select if normalisation should be used
% then H0=1 has no meaning
% 0=No, 1=Yes
normit=0;

% Obtain beta cutoff
bc=sqrt((m*pi/z1)^2+(n*pi/y1)^2); % beta
cutoff

% Convert offset degrees into radians
offrad=pi.*deg./180;

% Obtain Real of eps and mu
epsd=real(eps);
mud=real(mu);

% Waveguide related values
fc=1/(2*z1*sqrt(epsd*mud)); % cutoff
frequency for TE10 mode [1/s]
eeff=1-(fc./f).^2; %eff dielec const in WG [1]
mueff=1; %effective magnetic constant

% Epsilon and Mu in waveguide ...
eps_g=eps*eeff;
mu_g=mu*mueff;

% Gamma in material filled waveguide
% gamma=alpha+j*beta;
gamma2=j.*w.*mu_g.*(sig+j.*w.*eps_g);
gamma=sqrt(gamma2);

% Impedance of material filled WG
Zw_g=sqrt((j.*w.*mu_g)./(sig+j.*w.*eps_g));
Zyz=Zw_g;

% Compute common part P(Y,Z) ... see thesis
p=(gamma*Zyz*H0./(bc.^2)).*(pi./z1).*sin(pi*Z
./z1);

if normit > 0,
  % Let's normalize P to make comparison
easier .... i.e. |E|=1
  pmax=max(max(abs(p)));
  p=p./pmax;
end;

% Length away from Port A is Xa, away from
Port B is Xb
Xa=X;
Xb=applilen-X;

% Fields emanating from Port A and B are
% Eya and Eyb respectively
Eya=p'*exp(-gamma.*Xa);
Eyb=p'*exp(-gamma.*Xb);
```

```
% Do computation for all phases in 'deg'
qq=exp((-1)*sqrt(-1)*offrad);
for cnt=1:length(deg),
% Relative phase difference between
% sources only of significance
% Apply phase offset to Eyb, keep Eya as is.
%%% Note there is an UNWRAP problem
%%% because of MATLAB!!!!!
 Eybs=Eyb.*qq(cnt);

 % Interfere waves
 Ey(:,:,cnt)=Eya+Eybs;

 % Obtain |Ey|^2
 magEy2(:,:,cnt)=Ey(:,:,cnt).* ...
           conj(Ey(:,:,cnt)); % abs(Ey)^2
 magEy(:,:,cnt)=sqrt(magEy2(:,:,cnt)./(2*pi));
end;

% Show a pretty picture
numcol=16;
for cnt=1:length(deg),
 Vmin=min(min(min(magEy(:,:,cnt))));
 Vmax=max(max(max(magEy(:,:,cnt))));
 V=Vmin:(Vmax-Vmin)/(numcol-1):Vmax;
 Hfig(cnt)=figure;
 [cs,h]=contour(X,Z,magEy(:,:,cnt),V);
 % Only label every second contour.
 VV=V(1:2:length(V));
 clabel(cs,VV,'fontsize',12', ...
             'color','k', ...
             'rotation',0);
 titletext=['E-Field inside Carbon Composite
for offset: ', num2str(deg(cnt))];
 title(titletext);
 colorbar;
 caxis    % set colour limits on plot
          % NOTE: After caxis REDO colorbar!!!
 caxis([0,350]); colorbar;
 colormap(gray) % better for printing
 axis image;
 %fn=['smplwglssy_',num2str(deg(cnt)),'.eps'];
 %print(Hfig(cnt),'-depsc',fn);
end;
```

C.2 Matlab and C code of the annealing algorithm

The annealing algorithm used for parameter extraction of the magnetron model was initially implemented in Matlab. Due to the abundance of loops, the Matlab code performed relatively slowly. Implementation as a MEX function written in C improved speed about fourfold. Shifting often called Matlab routines into the MEX implementation (i.e. into C code) would further improve performance by removing the calling overhead.

The annealing algorithms in Matlab and C below were implemented according to [96].

```
function
[xbest,fbest]=ANNEAL(FUN,x0,dr,beta,g,...
fmin,estop,N,P1,P2,P3,P4,P5,P6,P7,P8,P9,P10)
% ANNEAL tries to implement simulated
% annealing for function optimization.
%
% [x]=ANNEAL(FUN,x0,dr,beta,g,fmin,estop,N,
%                              P1, ... P10)
% fmin = value of FUN at global minimum
% estop = Optimization halts if error<estop
% N = max number of iterations
% x0 = Starting point
% dr = step length, the radius of hypersphere
% beta = determines 'temperature' and hence
%        probability to attain higher
%        energy state
% g = arbitrary negative number. g=0 for
%     standard annealing.
%     It is essentially the fkt that links
%     FUN to the 'energy field'.
%     (exp(-beta*I^g*.....
% P1 ... Pn: parameters passed along to fkt.
%

% ------------Initialization----------------
% Put together function string with x and
% parameters P1 ... Pn
evalstr = [FUN];
if ~any(FUN<48)
       evalstr=[evalstr, '(x'];
   for i=1:nargin-8,
       evalstr = [evalstr,',P',int2str(i)];
   end;
       evalstr = [evalstr, ')'];
end;

% Initialise x with x0.
x=x0;

% Evaluate function with parameters
f=abs(eval(evalstr));

fbest=f;
xbest=x;

true=1;
false=0;
loopagain=true;
NN=0;

% Chk if Main loop is necessary
  % Main loop
  % if loopagain is false then we stop
  while ~any([loopagain==false, NN>=N]),
    NN=NN+1;
    if abs(fbest)>abs(f),
      fbest=f; xbest=x0; end;
    disp(f);
    if abs(fmin)>abs(f), fmin=f; end;
    inbounds=false;
    % if xnew is outside allowed bounds
    % then redo it
    while (inbounds==false),
      % New random direction about
      % n-dimensional hypersphere
      Y=randn(size(x0(:)))+
```

```
        sqrt(-1)*randn(size(x0(:)));
    h1=sqrt(sum(Y.*conj(Y)));
    U=Y/h1; % Normalise values
    clear h1 Y;

    % New X value to test
    xnew=x0+(real(dr)*real(U)+
        sqrt(-1)*imag(dr)*imag(U));

    % Chk if xnew is within bounds
    % if not, get new random direction
      % not implemented at the moment.
      % Use a while loop for this
      inbounds=true;
      %if any([xnew>1 xnew<-1]),
    % inbounds=false; disp('Out of bounds');
      %end;
  end;
  % Evaluate function using xnew
  x=xnew;
  fnew=abs(eval(evalstr)-fmin);

  % delta fkt=difference between new
  % and old fkt value
  df=fnew-f;

  % Based on df and a random value, xnew
  % is accepted or rejected
  %% In the first instance, it is chked
  %% if fnew is an improvement over f
  %% if so, it is accepted.  Then chk
  %% for estop or continued optim follow
  if fnew<=f,
    x0=xnew;
    f=fnew;
    error=abs(f-fmin);
    if error>=estop,
%       disp('+++');
      loopagain=true;
    else
%       disp('---');
      loopagain=false;
    end;
  else % Use probability do decide if
       % poor value is accepted or rejected
    % 'Thermal' distribution
    p=exp(-beta*(f.^g)*df);
    V=rand(1,1);
    if V>=p,
      loopagain=true; % Value rejected
%       disp('reject');
      x0=x0;
      f=f;
    else
      x0=xnew;
      f=fnew;
      loopagain=true; % Value accepted
%       disp('accept');
    end;
  end;
end;

xx=x0;

disp(NN);
disp(fmin);
x=xbest;
fbest=eval(evalstr);
disp(fbest);
disp(xbest);
```

The C implementation in the MEX file below is, to a large extent, concerned with parameter passing. Coding of the annealing algorithm is straight forward and tracks the Matlab code closely.

```
/*
  Simulated annealing as described in
  reference:
    Ihor O. Bohachevsky, Mark E. Johnson,
    Myron L. Stein; `Generalized simulated
    annealing for function optimization';
    Technometrics, Vol:28, No:3,
    August 1986, P:209
*/

/* In Matlab it is to be called like this:
  [Xbest,Fbest,Naccept,Nreject]=...
  ANNEAL(FUN,X0,dr,beta,g,Fmin,Estop,N,...
                              P1,...Pxx);
  where:
    Xbest: Best value found so far
    Fbest: Function value at Xbest
    Naccept: Number of detri steps accepted
    Nreject: Number of detri steps rejected
    FUN: String, name of fkt to 'anneal'
    X0: Starting value
    dr: step size
    beta: determines probability of
          accepting or rejecting
          detrimental steps
    g: arbitrary negative number.
       g=0 for standard annealing.
       g=-1 normalizes F(xnew)-F(xprevious)
    Fmin: minimum value of FUN.  Not
          critical, ANNEAL will try and
          find it.
    Estop: minimum acceptable difference
          between subsequent values of FUN
    N: maximum number of iterations
    P1 ... Pxx: Additional arguments
       passed to FUN
*/


#include <math.h>
#include "mex.h"

#define max_P_options 10

/* true=1; false=0; */
#define TRUE 1
#define FALSE 0

typedef struct
  {
   double real;
   double imag;
  } Complex;

typedef struct
  {
   mxArray *ptr;
   double *realptr;
   double *imagptr;
   int rows;
   int cols;
  } GenDatStruc;
```

```
/* Global variables */
int Pnumber;

/* Complex Arithmetic functions */
double real(Complex x)
  {return x.real;}

double imag(Complex x)
  {return x.imag;}

double cabs(Complex x)
  {
   double helpr, helpi, help;
   helpr=x.real*x.real;
   helpi=x.imag*x.imag;
   help=sqrt(helpr+helpi);
   return help;
  }

double riabs(double r, double i)
  {
   double helpr, helpi, help;
   helpr=r*r;
   helpi=i*i;
   help=sqrt(helpr+helpi);
   return help;
  }

/* Random functions */
/* uniform, 0 to 1  */
double random(double *seed)
  {
   mxArray *output[1], *input[2];
   int rows, cols;
   double result, help1, help2;

   rows=1;
   cols=1;
   output[0]=
   mxCreateDoubleMatrix(rows, cols, mxREAL);

   if
(mexCallMATLAB(1,output,0,NULL,"rand")!=0)
     mexErrMsgTxt("Problem: random");

   result=*(mxGetPr(output[0]));
   mxDestroyArray(output[0]);
   return result;
  }

/* Normal or Gauss */
double randomn(double *seed)
  {
   mxArray *output[1], *input[2];
   int rows, cols;
   double result, help1, help2;

   rows=1;
   cols=1;
   output[0]=
   mxCreateDoubleMatrix(rows, cols, mxREAL);

   if
 (mexCallMATLAB(1,output,0,NULL,"randn")!=0)
     mexErrMsgTxt("Problem: randomn");

   result=*(mxGetPr(output[0]));
   mxDestroyArray(output[0]);
   return result;
  }

/* Our functions */
void usrfkt(char *FUNstring,
            mxArray *result[],
            mxArray *X0[],
            mxArray *P[])

/* The M or MEX file called in Matlab    */
/* should be of the form:                */
/*   Result=FUN(X0,P1 ... Pxx);          */
/* No other fancies are catered for!!!   */
  {
   int num_input,cnt;
   mxArray *input[1+max_P_options];

   num_input=1+Pnumber;
   input[0]=X0[0];
   if (Pnumber > 0)
     for (cnt=0; cnt<Pnumber; cnt++)
       input[cnt+1]=P[cnt];

   if (mexCallMATLAB(1, result, num_input,
input, FUNstring) != 0)
     mexErrMsgTxt("Problem: Function");
   if (mxIsComplex(result[0]))
     mexErrMsgTxt("FUN returned complex
value.  Must be real!");
  }


/*
  [Xbest,Fbest,Naccept,Nreject]=
  ANNEAL(FUN,X0,dr,beta,g,Fmin,Estop,N,Px);
*/

void anneal(double *Xbestreal,
            double *Xbestimag,
            int XbestN, int XbestM,
            double *Fbestreal,
            double *Naccept,
            double *Nreject,
            char *FUNstring,
            double *X0real,
            double *X0imag,
            int X0N, int X0M,
            double *drreal, double *drimag,
            double beta,
            double g,
            double Fminreal,
            double Estop,
            long int N,
            mxArray *P[])
  {
   long int cnt;
   int Xlength;
   double *Xreal, *Ximag, *freal;
   double *Xnewreal, *Xnewimag, *fnewreal;
   mxArray *X, *f, *Xnew, *fnew;
   int loopagain, inbounds;
   long int NN, Ndisp;
   double help1, help2, df, error, p, V;
   double *seed;

   /* initialize */
   XbestN=X0N;
   XbestM=X0M;
   Xlength=X0N*X0M;

   /* Now if we write to either,
      it should change the other */
  X=mxCreateDoubleMatrix(X0M,X0N,mxCOMPLEX);
   Xreal=mxGetPr(X);
   Ximag=mxGetPi(X);

   Xnew=mxCreateDoubleMatrix(X0M,X0N,
mxCOMPLEX);
   Xnewreal=mxGetPr(Xnew);
   Xnewimag=mxGetPi(Xnew);

   freal=mxCalloc(1,sizeof(double));
   fnewreal=mxCalloc(1,sizeof(double));

   /* x=x0 */
   /* xbest=x */
```

```
for (cnt=((long int)Xlength-1);
     cnt >= 0; cnt--)
  {
   *(Xreal+cnt)=*(X0real+cnt);
   *(Xbestreal+cnt)=*(Xreal+cnt);
   if (X0imag!=NULL)
     *(Ximag+cnt)=*(X0imag+cnt);
   else *(Ximag+cnt)=0;
   *(Xbestimag+cnt)=*(Ximag+cnt);
  }

/* f=abs(usrfkt(X,P)) */
usrfkt(FUNstring, &f, &X, P);
*freal=mxGetScalar(f);
help1=(*freal)*(*freal);
*freal=sqrt(help1);

/* fbest=f */
*Fbestreal=*freal;

/* loopagain=TRUE; NN=0; ndisp=0;
   naccept=0; nreject=0; */
loopagain=TRUE;
NN=0;
Ndisp=0;
*Naccept=0.0;
*Nreject=0.0;

/* Main loop */
/* while~any([loopagain==false,NN>=N])*/
while (loopagain==TRUE && NN<N)
  {
   NN++;
   /* if abs(fbest)>abs(f), fbest=f;
      xbest=x0; end; */
   help1=((*Fbestreal)*(*Fbestreal));
   help2=((*freal)*(*freal));
   if (help1>help2)
     {
      *Fbestreal=*freal;
      /* xbest=x0 */
      for (cnt=((long int)Xlength-1);
           cnt >= 0; cnt--)
        {
         *(Xbestreal+cnt)=*(X0real+cnt);
         if (X0imag!=NULL)
         *(Xbestimag+cnt)=*(X0imag+cnt);
         else
           *(Xbestimag+cnt)=0;
        }
     }

   /* if abs(fmin)>abs(f),
         fmin=f; end; */
   help1=((Fminreal)*(Fminreal));
   help2=((*freal)*(*freal));
   if (help1>help2)
     {
      Fminreal=*freal;
     }

   inbounds=FALSE;
   while (inbounds==FALSE)
     {
      /* New random directions for
         n-dimensions */
      for (cnt=((long int)Xlength-1);
           cnt >= 0; cnt--)
        {
         /* Y=randn(size(X0))+
            sqrt(-1)*randn(size(X0)) */
         /* New X value to test */
         /* xnew=x0+(real(dr)*real(U)+
           sqrt(-1)*imag(dr)*imag(U)) */
         *(Xnewreal+cnt)=*(X0real+cnt)+
            ((*drreal)*(randomn(seed)));
         if (X0imag!=NULL)
           *(Xnewimag+cnt)=*(X0imag+cnt)+
          ((*drimag)*(randomn(seed)));
           else
             *(Xnewimag+cnt)=0;
         }
       /* Chk if xnew is within bounds,
        if not, new random direction */
       inbounds=TRUE;
       /* ************************* */
             }

/* Evaluate function using Xnew */
/* x=xnew */
/* fnew=abs(usrfkt(X,P)-fmin) */
usrfkt(FUNstring, &fnew, &Xnew, P);
*fnewreal=mxGetScalar(fnew);
help1=(*fnewreal-Fminreal)*
      (*fnewreal-Fminreal);
*fnewreal=sqrt(help1);
/* delta fkt=difference between
   new and old fkt value */
/* NOTE: fnew and f should be REAL
   and ABS values only!!!! */
/*Enforce this right at the source!*/
df=(*fnewreal)-(*freal);

/* Now determine if Xnew is better
   than X0 */
if (*fnewreal<=(*freal))
  {
   /* x0=xnew */
   for (cnt=((long int)Xlength-1);
        cnt >= 0; cnt--)
     {
      *(X0real+cnt)=*(Xnewreal+cnt);
      if (X0imag!=NULL)
        *(X0imag+cnt)=*(Xnewimag+cnt);
     }
   /* f=fnew */
   *freal=*fnewreal;
   /* error=abs(f-fmin) */
   help1=(*freal)-Fminreal;
   help1=help1*help1;
   error=sqrt(help1);
   if (error<Estop) {loopagain=FALSE;}
  }
else
  {
   /* Use probability to decide if
      poor value is accepted or
      rejected */
    % Boltzmann distribution */
   /* p=exp(-beta*(f.^g).*df);
   help1=pow((*freal),double((int)g));
   help2=(-1)*beta*help1*df;
   p=exp(help2);
   V=random(seed);
   if (V>=p)
     {/* Value rejected */
      loopagain=TRUE;
      *Nreject+=1.0;
      /* X0=X0; f=f */
     }
   else
     {/* Value accepted */
      loopagain=TRUE;
      *Naccept+=1.0;
      /* x0=xnew; f=fnew; */
      for (cnt=((long int)Xlength-1);
           cnt >= 0; cnt--)
        {
         *(X0real+cnt)=
           *(Xnewreal+cnt);
         if (X0imag!=NULL)
           *(X0imag+cnt)=
             *(Xnewimag+cnt);
        }
```

```
            *freal=*fnewreal;
           }
        }
      }
    /* x=xbest */
    for (cnt=((long int)Xlength-1);
         cnt >= 0; cnt--)
      {
       *(Xreal+cnt)=*(Xbestreal+cnt);
       *(Ximag+cnt)=*(Xbestimag+cnt);
      }
    /* fbest=usrfkt(X,P) */
    usrfkt(FUNstring, &fnew, &X, P);
    *Fbestreal=mxGetScalar(fnew);

    /* ********************** */
    /* Chk which mxArrays can be
mxDestroyArrayed-ed */
    /* Note pointer passing!!! */
   }



/* The matlab 'main' fkt is 'mexFunction'
*/
void mexFunction( int nlhs, mxArray *plhs[],
          int nrhs, const mxArray *prhs[] )
{
 /* Declare all variables and structures
    before the executable statements    */
 /* Matlab will otherwise complain!     */
 GenDatStruc FUN, X0, dr;
 mxArray *P[max_P_options];
 GenDatStruc Xbest, Fbest, Naccept, Nreject;

 int FUNlength;
 char *FUNstring;

 double beta, g, Fmin, Estop;
 long int N;
 int rows;
 int cols;
 double random_value;

 /* General purpose counter */
 int cnt;
 Complex a={0.0, 0.0};

 /* Chk nrhs and nlhs bounds */
 if (nlhs > 4)
     mexErrMsgTxt("Too many output
                  arguments. (Maximum: 4");
 if (nrhs < 8)
     mexErrMsgTxt("Insufficient input
                  arguments. (Minimum: 8)");
 /* Find number of Px values and chk
    their number */
 Pnumber=nrhs-8;
 if (Pnumber > max_P_options)
   mexErrMsgTxt("Too many optional
              parameters. (Maximum: 10)");

 /* Additional chks (complex, double, real,
                     string, size, etc.) */
 /* FUN: array of characters */
 if (!mxIsChar(prhs[0]))
   mexErrMsgTxt("FUN must be a function
         name or inline function object.");
 /* X0: matrix, complex or real, double */
 if (!mxIsDouble(prhs[1]))
   mexErrMsgTxt("X0 should be double
        precision floating point number.");
 /* dr: either (double, scalar) or (like X0)
*/
 /* currently: scalar only, real or complex,
double */
 if ( !mxIsDouble(prhs[2]) ||
      !(mxGetM(prhs[2])==1 &&
        mxGetN(prhs[2])==1) ||
     !(mxIsComplex(prhs[1])==
       mxIsComplex(prhs[2])))
   mexErrMsgTxt("dr should be scalar and
        real/complex depending on X0.");
 /*beta: scalar, real, double */
 if ( !mxIsDouble(prhs[3]) ||
      !(mxGetM(prhs[3])==1 &&
mxGetN(prhs[3])==1) ||
      mxIsComplex(prhs[3]) )
   mexErrMsgTxt("beta should be scalar and
                                 real.");
 /* g: scalar, real, double */
 if ( !mxIsDouble(prhs[4]) ||
      !(mxGetM(prhs[4])==1 &&
mxGetN(prhs[4])==1) ||
      mxIsComplex(prhs[4]) )
   mexErrMsgTxt("g should be scalar, real
   and double precision floating point.");
 /* Fmin: scalar, real or complex, double
*/
 if ( !mxIsDouble(prhs[5]) ||
      !(mxGetM(prhs[5])==1 &&
        mxGetN(prhs[5])==1) )
   mexErrMsgTxt("Fmin should be scalar and
       double precision floating point.");
 /* Estop: scalar, real, double */
 if ( !mxIsDouble(prhs[6]) ||
      !(mxGetM(prhs[6])==1 &&
        mxGetN(prhs[6])==1) ||
        mxIsComplex(prhs[6]) )
   mexErrMsgTxt("beta should be scalar,
     real and double precision floating
     point.");
 /* N: double, real, scalar, integer(N)=N,
                (double)((long int)N)=N */
 /* No chk for integer yet.  ceil or
                 typecasting could chk */
 if ( mxIsComplex(prhs[7]) ||
      !(mxGetM(prhs[7])==1 &&
       mxGetN(prhs[7])==1) ||
      !mxIsDouble(prhs[7]) )
   mexErrMsgTxt("N should be scalar, real
         and double precision integer.");
 /* P1 to Px are just passed on.  No chk on
    type or content */


 /* Sort out data from Matlab */
 /*
(FUN,X0,dr,beta,g,Fmin,Estop,N,P1,...Pxx)
*/
 FUN.ptr=(mxArray *)prhs[0];
 FUN.realptr=NULL;
 FUN.imagptr=NULL;
 FUN.rows=mxGetM(FUN.ptr);
 FUN.cols=mxGetN(FUN.ptr);

 FUNlength=(FUN.rows*FUN.cols)+1;
 FUNstring=mxCalloc(FUNlength,
                    sizeof(char));
 if (mxGetString(FUN.ptr, FUNstring,
                  FUNlength) != 0)
   mexErrMsgTxt("Problem: FUNstring");

 X0.ptr=(mxArray *)prhs[1];
 X0.realptr=mxGetPr(X0.ptr);
 X0.imagptr=mxGetPi(X0.ptr);
 X0.rows=mxGetM(X0.ptr);
 X0.cols=mxGetN(X0.ptr);

 dr.ptr=(mxArray *)prhs[2];
 dr.realptr=mxGetPr(dr.ptr);
 dr.imagptr=mxGetPi(dr.ptr);
 dr.rows=mxGetM(dr.ptr);
 dr.cols=mxGetN(dr.ptr);
```

```
beta=mxGetScalar(prhs[3]);
g=mxGetScalar(prhs[4]);
Fmin=mxGetScalar(prhs[5]);
Estop=mxGetScalar(prhs[6]);
N=(long int)mxGetScalar(prhs[7]);

if (Pnumber > 0)
  for (cnt=0; cnt<Pnumber; cnt++)
    P[cnt]=(mxArray *)prhs[8+cnt];

/* Create arrays for variables to be
    returned to Matlab (mxCreate) */
/* same size as X0, complex */
Xbest.ptr=mxCreateDoubleMatrix(X0.rows,
                  X0.cols, mxCOMPLEX);
Xbest.realptr=mxGetPr(Xbest.ptr);
Xbest.imagptr=mxGetPi(Xbest.ptr);
Xbest.rows=mxGetM(Xbest.ptr);
Xbest.cols=mxGetN(Xbest.ptr);

/* scalar, complex */
Fbest.ptr=mxCreateDoubleMatrix(1, 1,
                           mxREAL);
Fbest.realptr=mxGetPr(Fbest.ptr);
Fbest.imagptr=NULL;
Fbest.rows=mxGetM(Fbest.ptr);
Fbest.cols=mxGetN(Fbest.ptr);

/* scalar, real */
Naccept.ptr=mxCreateDoubleMatrix(1, 1,
                              mxREAL);
Naccept.realptr=mxGetPr(Naccept.ptr);
Naccept.imagptr=NULL;
Naccept.rows=mxGetM(Naccept.ptr);
Naccept.cols=mxGetN(Naccept.ptr);

/* scalar, real */
Nreject.ptr=mxCreateDoubleMatrix(1, 1,
                              mxREAL);
Nreject.realptr=mxGetPr(Nreject.ptr);
Nreject.imagptr=NULL;
Nreject.rows=mxGetM(Nreject.ptr);
Nreject.cols=mxGetN(Nreject.ptr);

/* Process it using our routines */

/*
 usrfkt(FUNstring, &Xbest.ptr, &X0.ptr, P);
*/

 anneal(Xbest.realptr, Xbest.imagptr,
        Xbest.rows, Xbest.cols,
        Fbest.realptr,
        Naccept.realptr,
        Nreject.realptr,
        FUNstring,
        X0.realptr, X0.imagptr, X0.rows,
        X0.cols,
        dr.realptr, dr.imagptr,
        beta, g,
        Fmin,
        Estop,
        N, P);
   a.imag=0;
   a.real=mxGetScalar(X0.ptr);
   a.real=cabs(a);
   mexPrintf("Input: %g \n", a.real);
   a.real=mxGetScalar(Xbest.ptr);
   mexPrintf("Output: %g \n", a);


 /* Sort out data to be rtned to Matlab */
 /* Have to chk this with nlhs          */
 plhs[0]=mxDuplicateArray(Xbest.ptr);
 if (nlhs > 1)
   {
    plhs[1]=mxDuplicateArray(Fbest.ptr);
    if (nlhs > 2)
      {

plhs[2]=mxDuplicateArray(Naccept.ptr);
       if (nlhs >3)
         {

plhs[3]=mxDuplicateArray(Nreject.ptr);
         }
      }
   }

 /* Remove data before exiting           */
 /* Make sure it is first 'deep' copied! */
 mxDestroyArray(Xbest.ptr);
 mxDestroyArray(Fbest.ptr);
 mxDestroyArray(Naccept.ptr);
 mxDestroyArray(Nreject.ptr);
 mxFree(FUNstring);
}
```

Appendix D

Silica gel – Cobalt chloride preparation

The salts of the transition metals iron, nickel, cobalt and copper change their colour with moisture content. Cobalt-Chloride ($CoCl_2$) was found to be most suitable because it changes its colour from a strong blue – cobalt blue – when dry to red/pink when moist. The effect is best visible if Cobalt-Chloride is absorbed in a suitable material permeable to moisture, such as high quality filter paper or silica gel.

Silica gel crystals are readily available as pellets, clear or colour coded with cobalt-chloride. Even if colour coded, the effect needs to be enhanced.

Good contrast and adequate pattern resolution is obtained for silica gel crystals between 500 µm and 250 µm in diameter. For this purpose the pellets are ground in ball mills first.

D.1 Recipe for mouldable Cobalt-Chloride Silica Gel Blocks

Components used for the preparation are:

a) 150 g Silica Gel, dried, grain-size: 500 µm to 250 µm

b) 50 ml of Cobalt-Chloride solution which is prepared as follows: 30 g $CoCl_2 \cdot 6\ H_2O$ dissolved in 100 ml water

c) 2 g Wallpaper paste powder (type Polycell) dissolved in 50 ml water

d) 10 g Potato or Corn Starch mixed with 10 ml water

e) 10 g Potato or Corn Starch mixed in 60 ml water and boiled until thick (Similar to thickening sauces in the kitchen, it must be constantly stirred!)

A patty like mass from which sheets or blocks are produced is prepared as follows:

- Mix a) and b), add c), mix, add d), mix, add e), mix thoroughly.
- Pour into moulds (*Do not use metal moulds unless coated!*)
- Heat to about 80 °C to 90 °C but not above 100 °C until thickened. 150 g take about half an hour.
- Remove from mould and dry at 80 °C to 90 °C degrees Celsius until blue.

Component d) ensures that the mixture can be easily potted. It will thicken in the mould when heated. Alternatively it is possible to combine the ground silica gel with an open pored foam.

Measured data of the relative permittivity and skin depth are available in Figure 73 and Figure 74. Their values vary with moisture content.

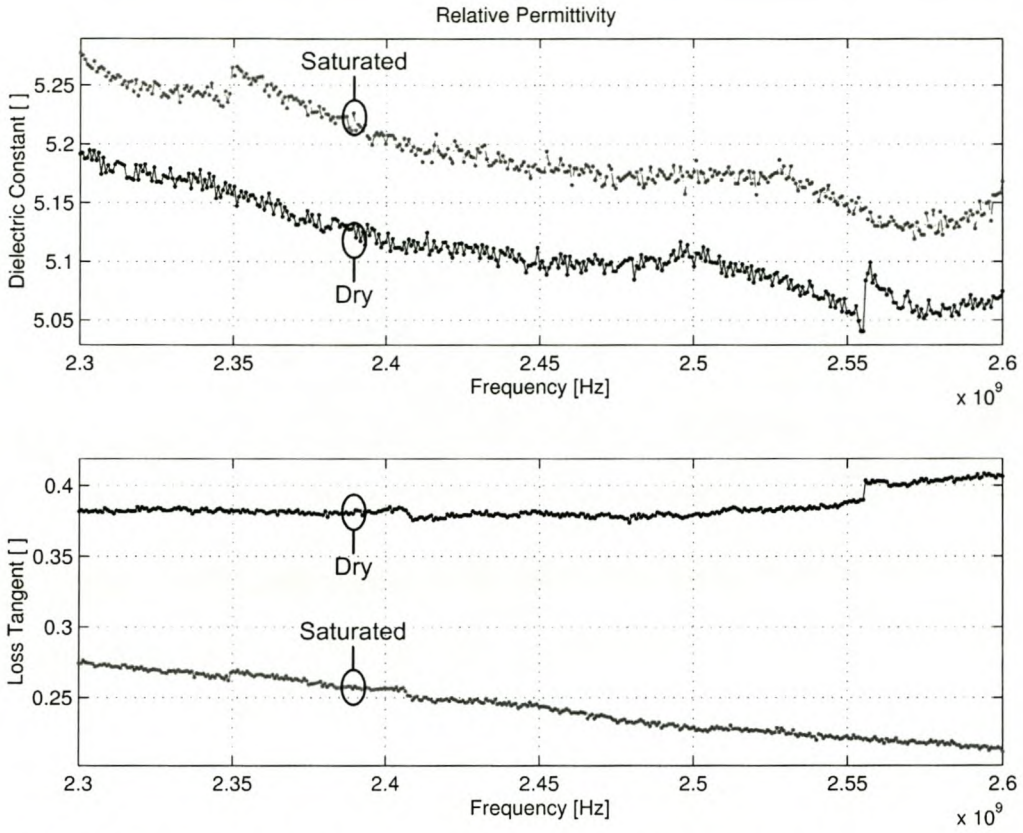

Figure 73: Relative permittivity of moist and dry cobalt chloride paste.

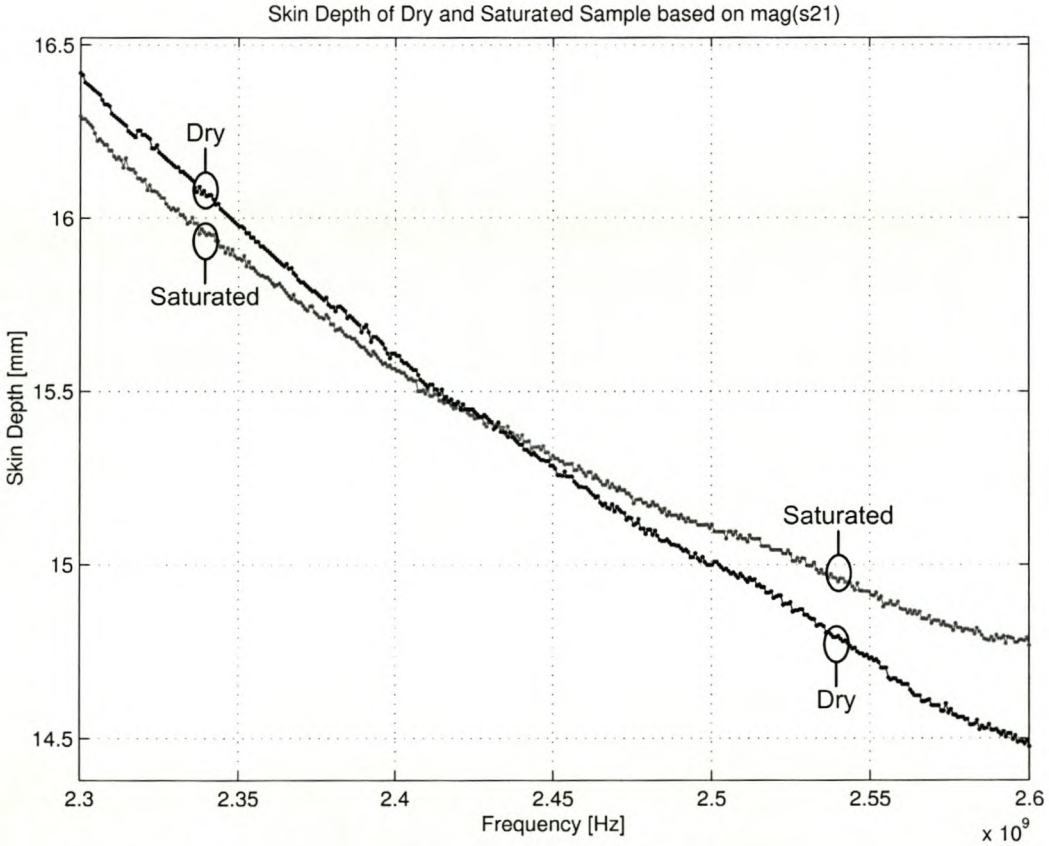

Figure 74: Skindepth of moist and dry cobalt chloride.

Appendix E

Waveguide components

A number of waveguide components were designed and evaluated to construct the topologies discussed in chapter 4 and to measure their performance. The following components were of prime importance:

- Flanges for WR340 aluminium and brass waveguide in Figure 75.
- Transitions from coaxial to WR340 waveguide in Figure 77 and Figure 78.
- WR340 launchers for the magnetron tubes in Figure 82.
- Coaxial high power probe for slotted waveguide measurement in Figure 83. The probe was mounted into a wooded slide located atop a slotted waveguide.
- T-piece with phase and magnitude compensation used as power splitter in Figure 84.
- Bends in both E and H plane in Figure 89 and Figure 93 respectively allowed circular structures to be built.
- 15 dB coupler for injection locking decoupling (Figure 94 and Figure 95).
- Double slug tuner in Figure 76 for Rieke Diagram measurements used in conjunction with a slotted waveguide.
- Three stub tuner intended for automatic Rieke Diagram characterisation (Figure 96).

Of particular importance were flanges and a pair of measurement quality transitions for waveguide component characterisation together with a WR340 waveguide calibration kit. The latter is not described herein but consisted of three offset shorts of 0 mm, $\lambda/8$ and $\lambda/4$ offset and a matched load which was built from anechoic chamber cones as absorbing material of 300 mm length and cut to fit into a 300 mm long offset short. Its performance was about 30 dB match and better.

All other components dimensions and characteristics are shown in the figures below, save for the Philips high power circulator, measurements of which are shown in Figure 97 to Figure 100.

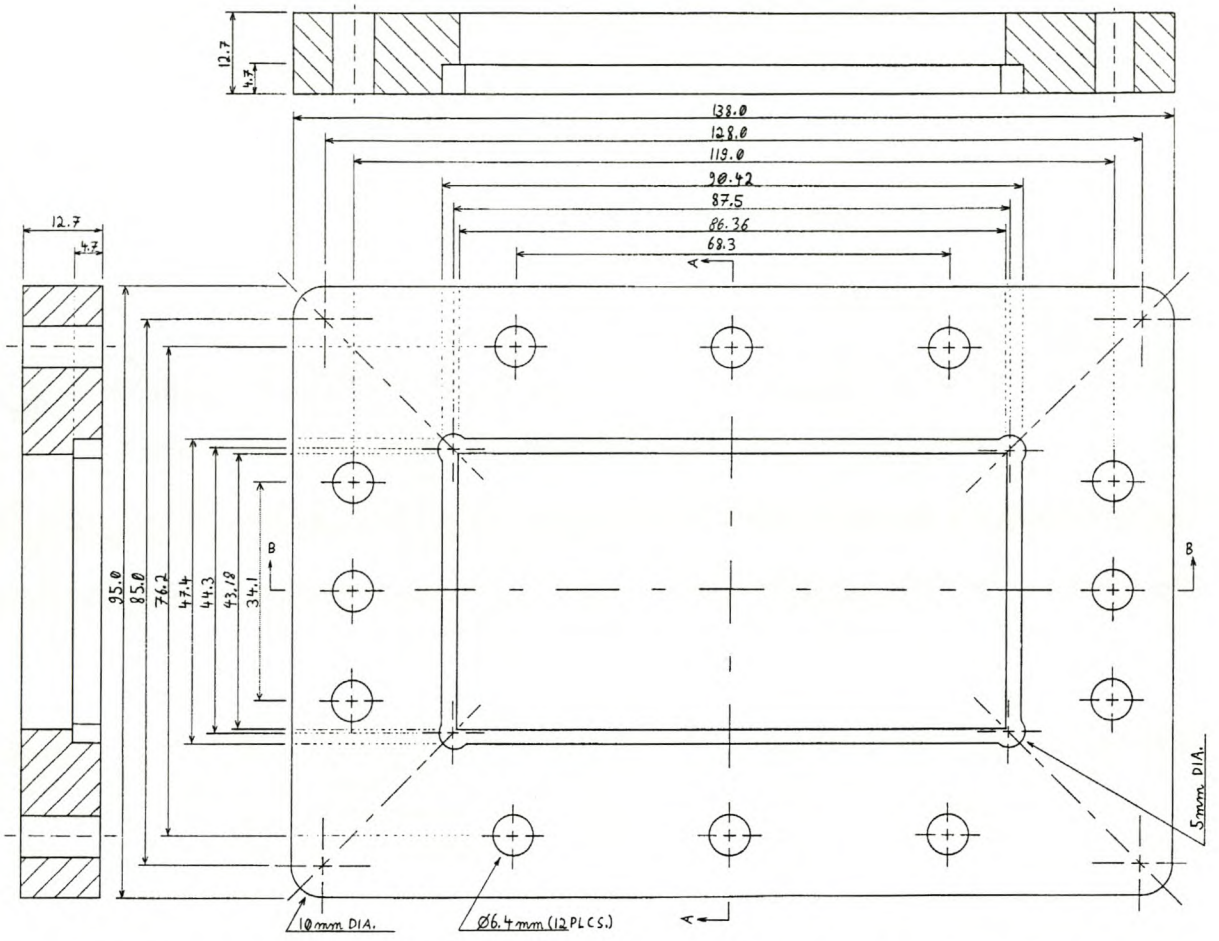

Figure 75: Dimensions of WR340 flange suitable for aluminium and brass waveguides.

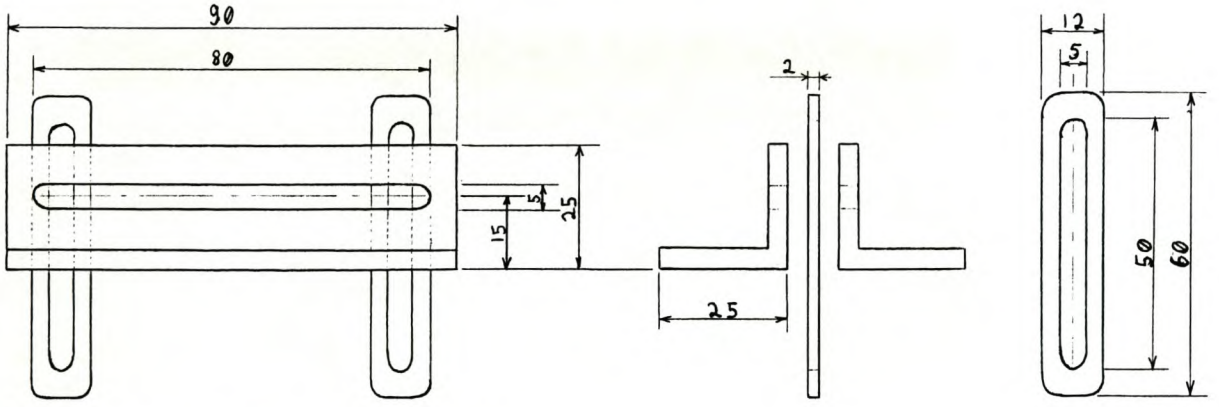

Figure 76: Dimensions double slug tuner.

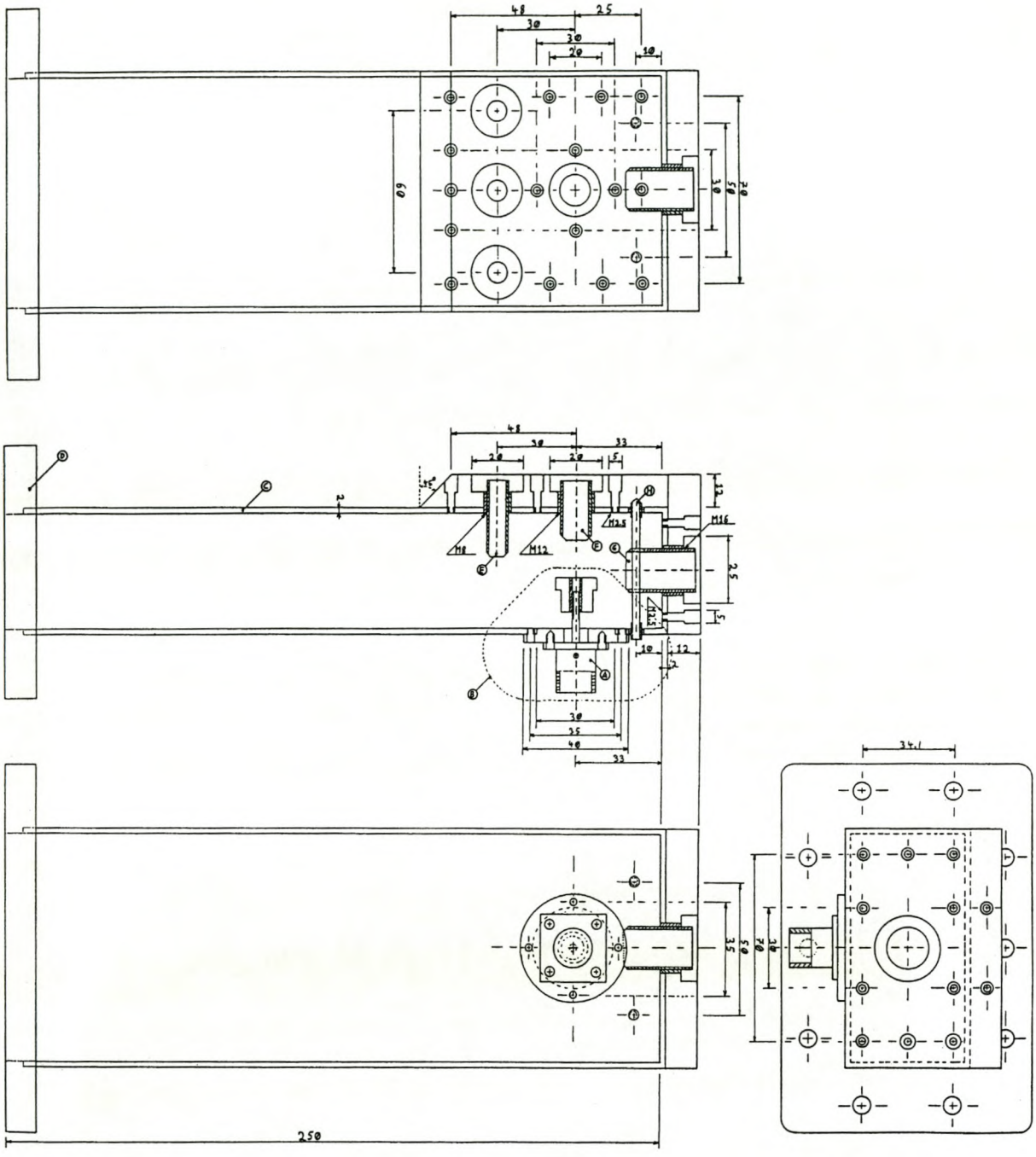

Figure 77: Dimensions of N-type to WR340 transition.

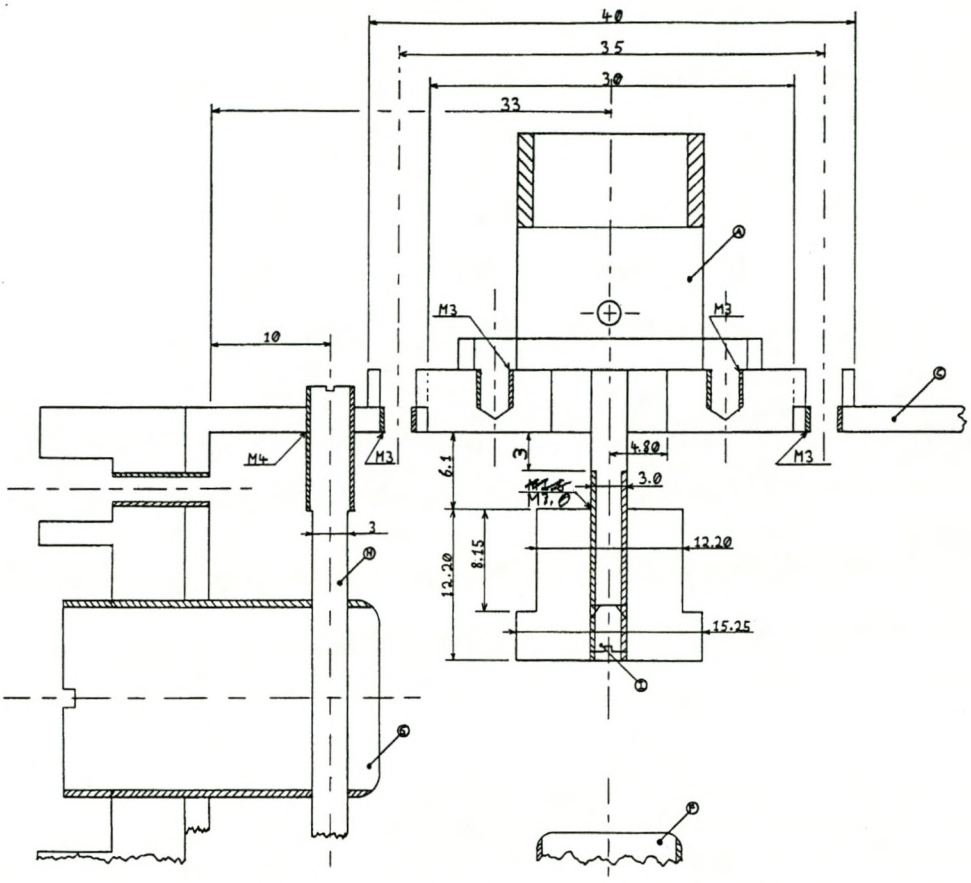

Figure 78: Dimensions of transition region with a view of the 'doorknob'.

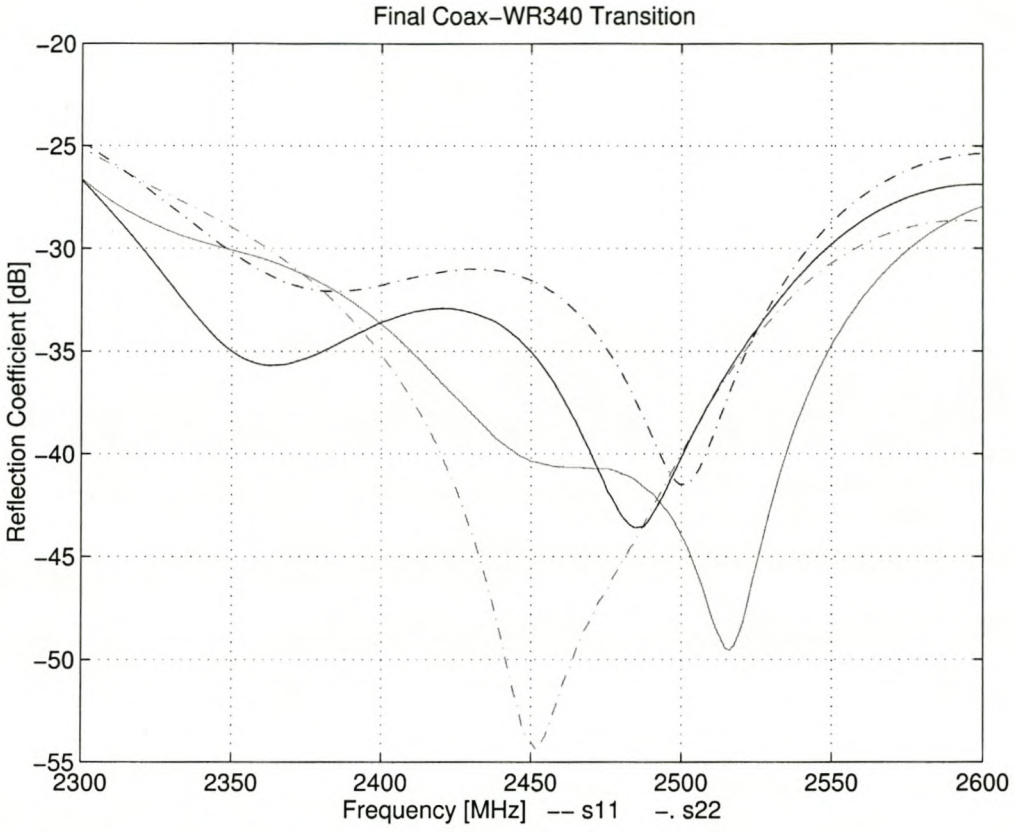

Figure 79: Reflection coefficient of back-to-back mounted pair of transitions.

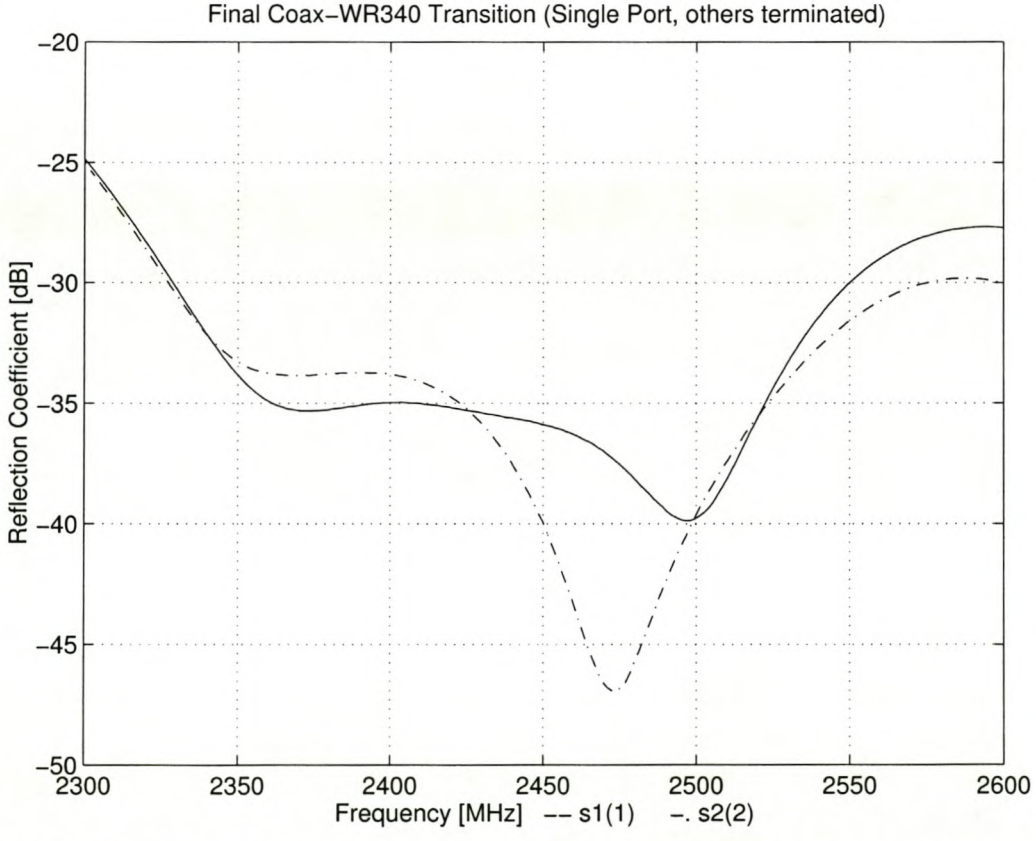

Figure 80: Reflection coefficient of transitions terminated with matched load on WR340 side.

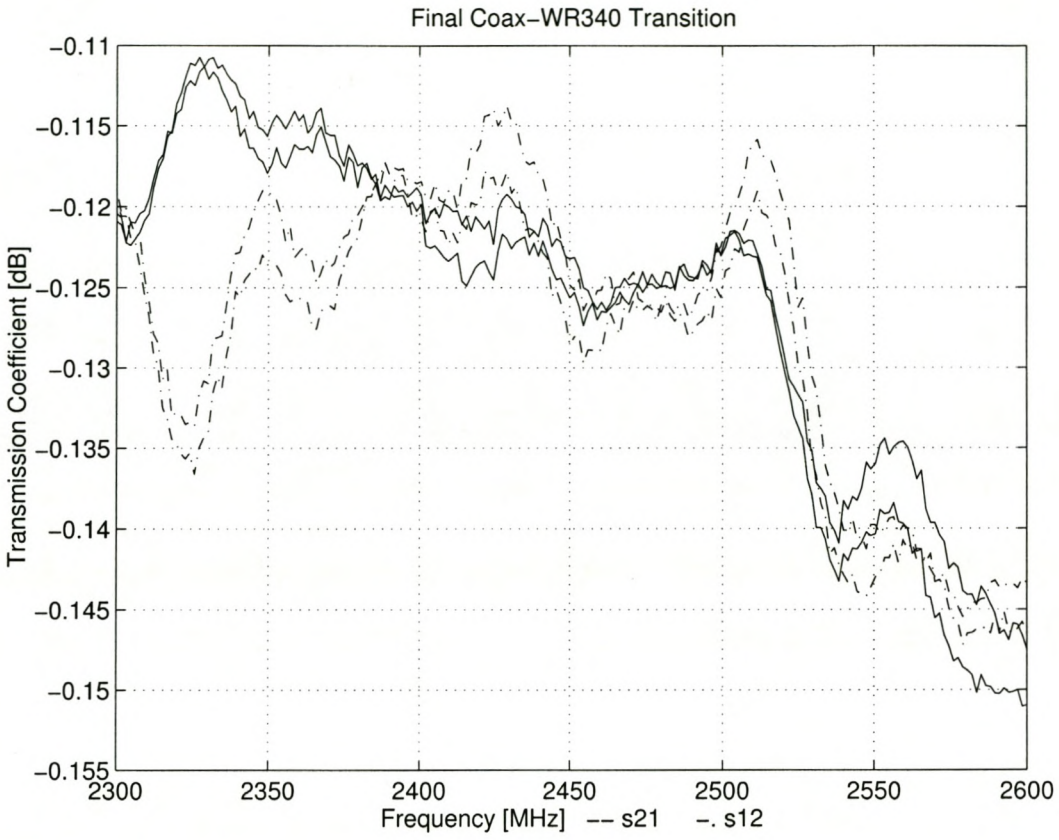

Figure 81: Transmission coefficient of transitions.

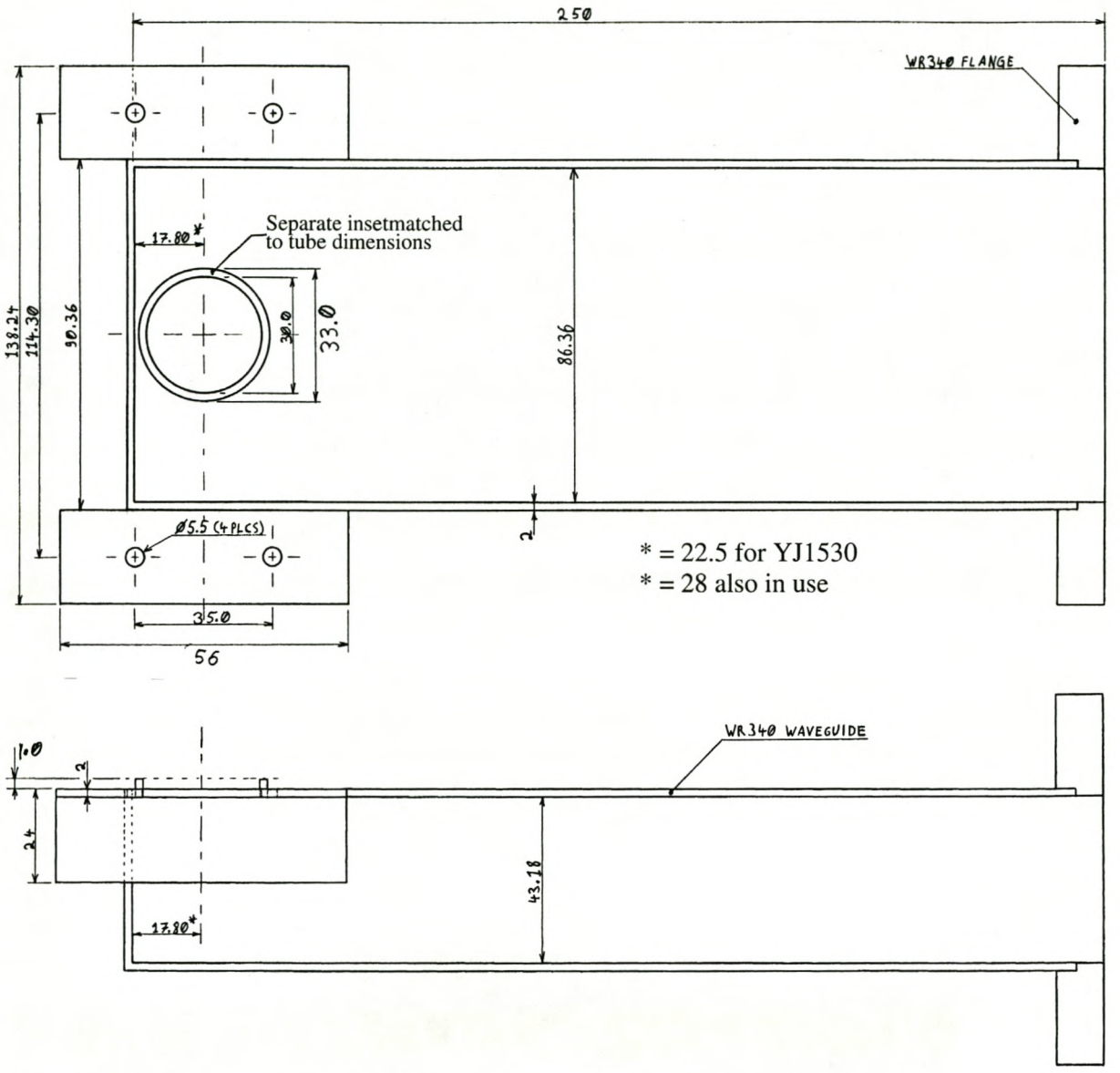

Figure 82: Dimensions of launcher for magnetron tubes. Dimensions for different tubes are indicated.

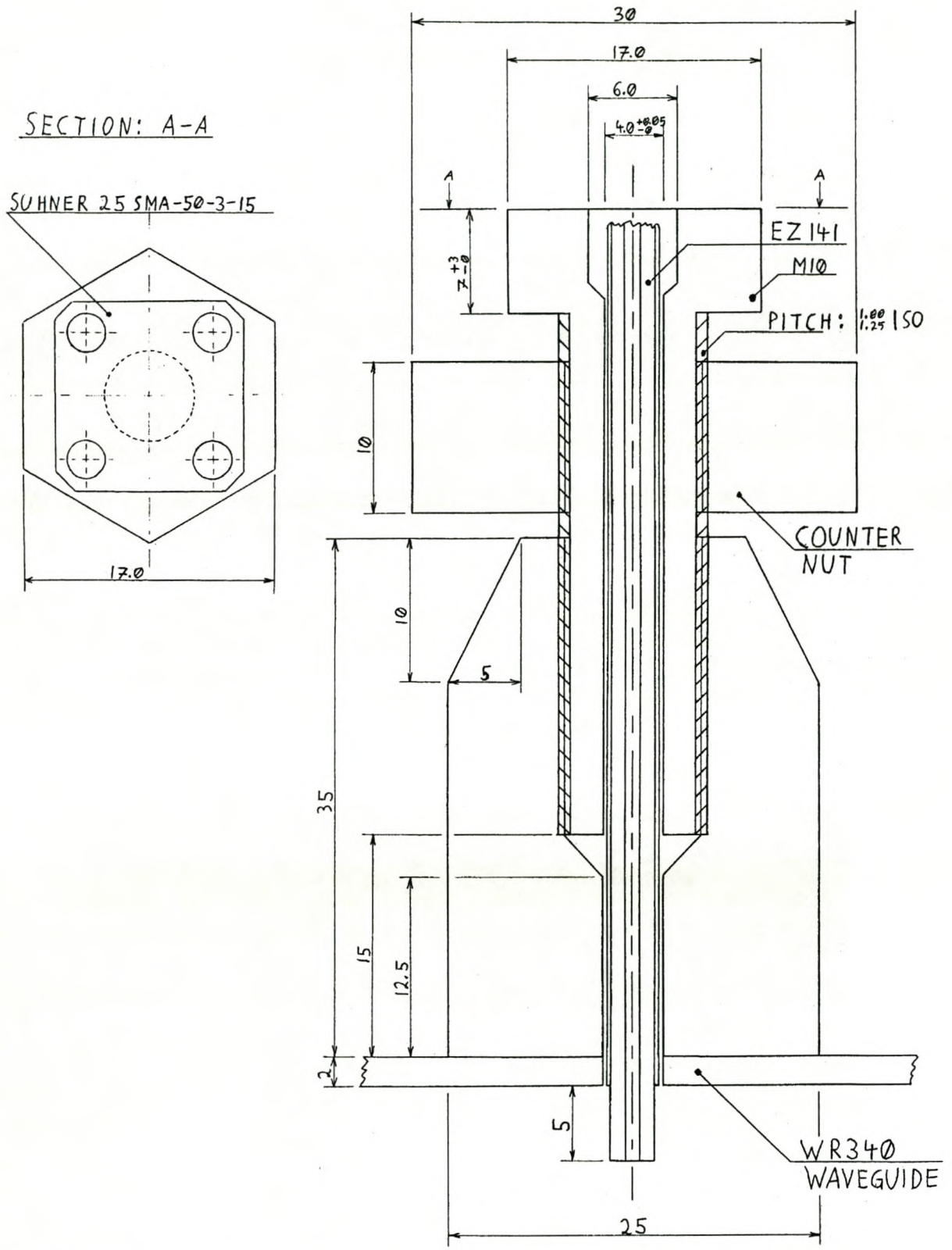

Figure 83: Dimensions of high power probe with variable coupling ratio.

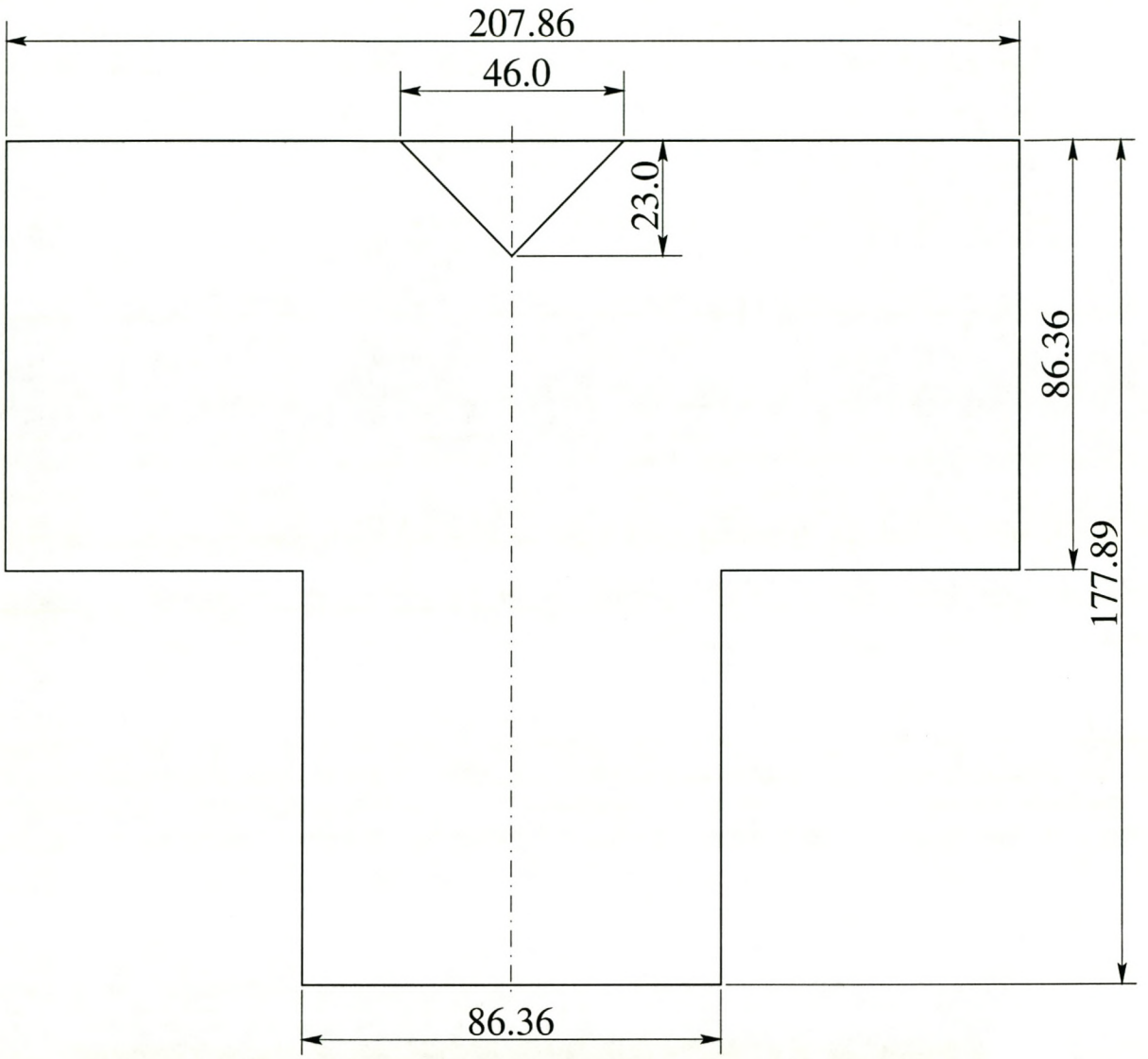

Figure 84: Dimensions of phase and magnitude compensated H-plane T-piece. All ports have got the same electrical characteristic.

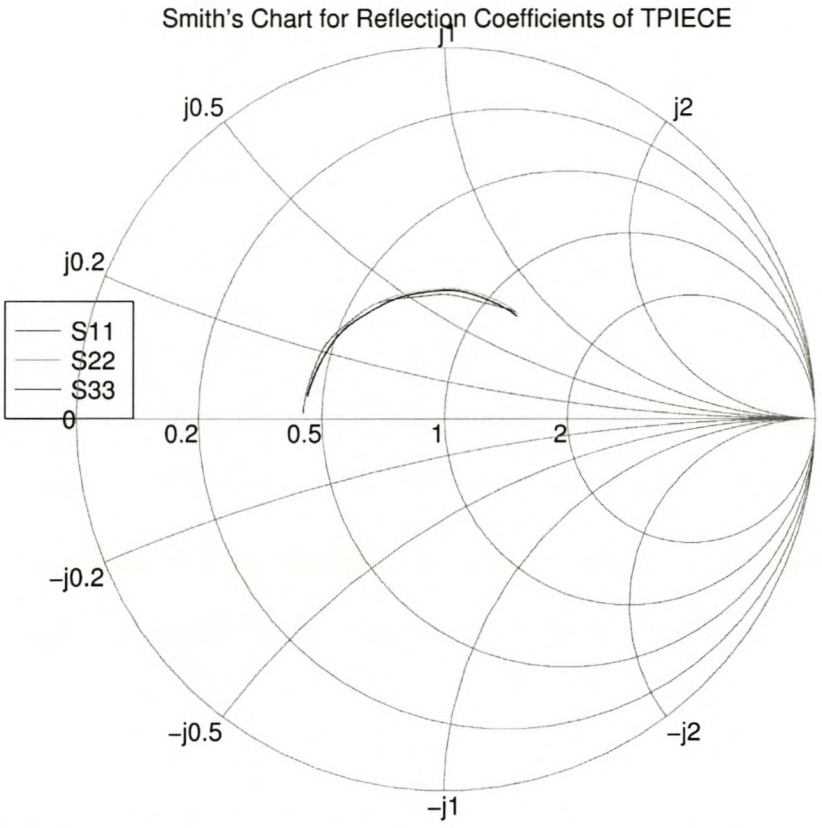

Figure 85: Measured reflection coefficient of T-piece ports plotted on a Smith Chart.

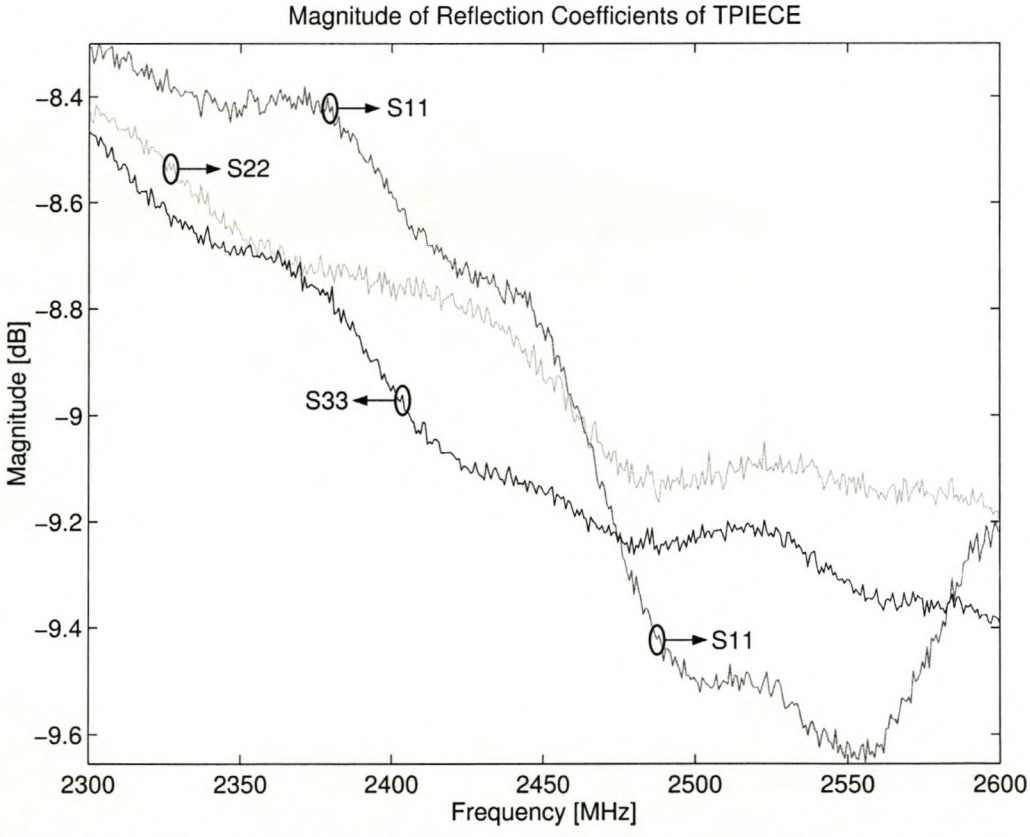

Figure 86: Magnitude versus frequency plot of measured reflection coefficient of T-piece ports.

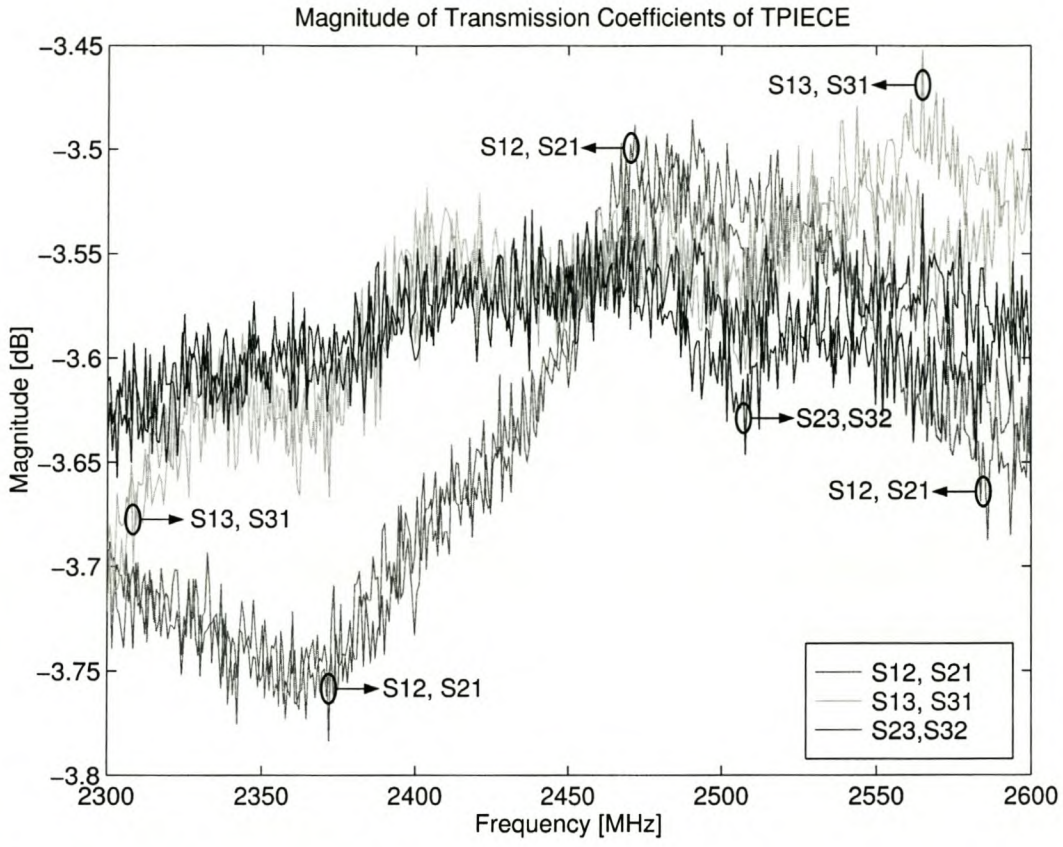

Figure 87: Magnitude of transmission coefficient of T-piece.

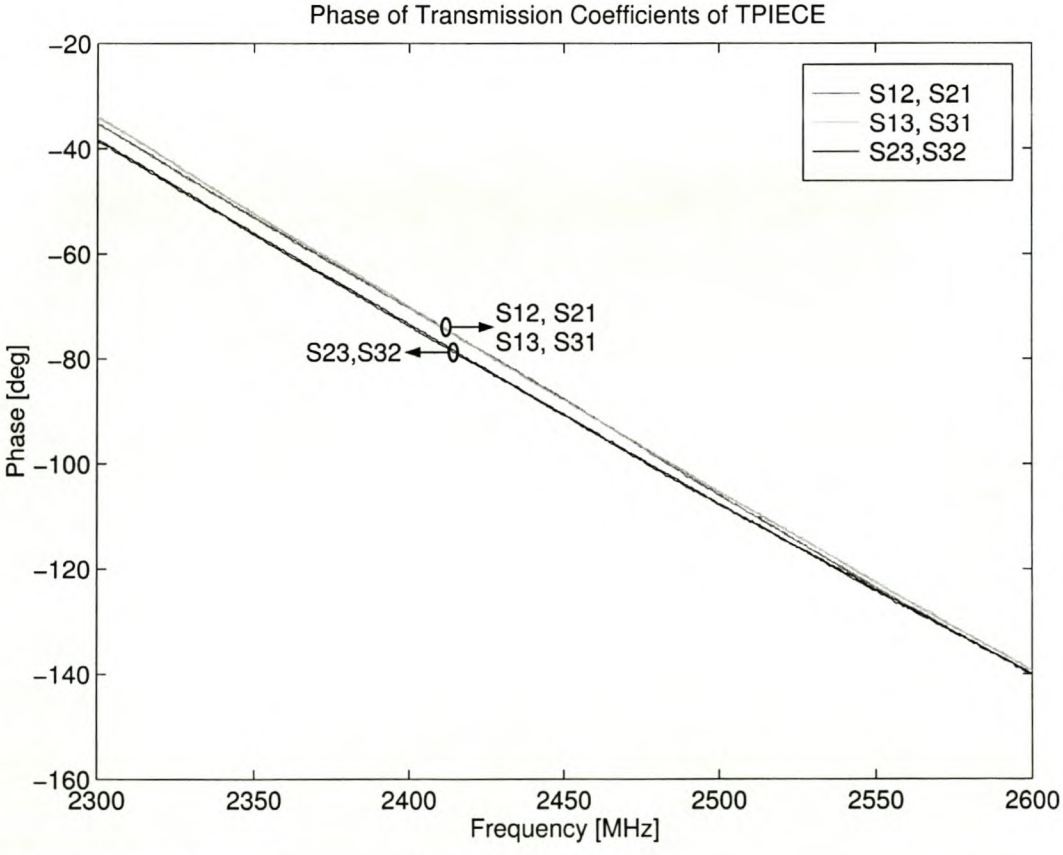

Figure 88: Phase of transmission coefficient of T-piece.

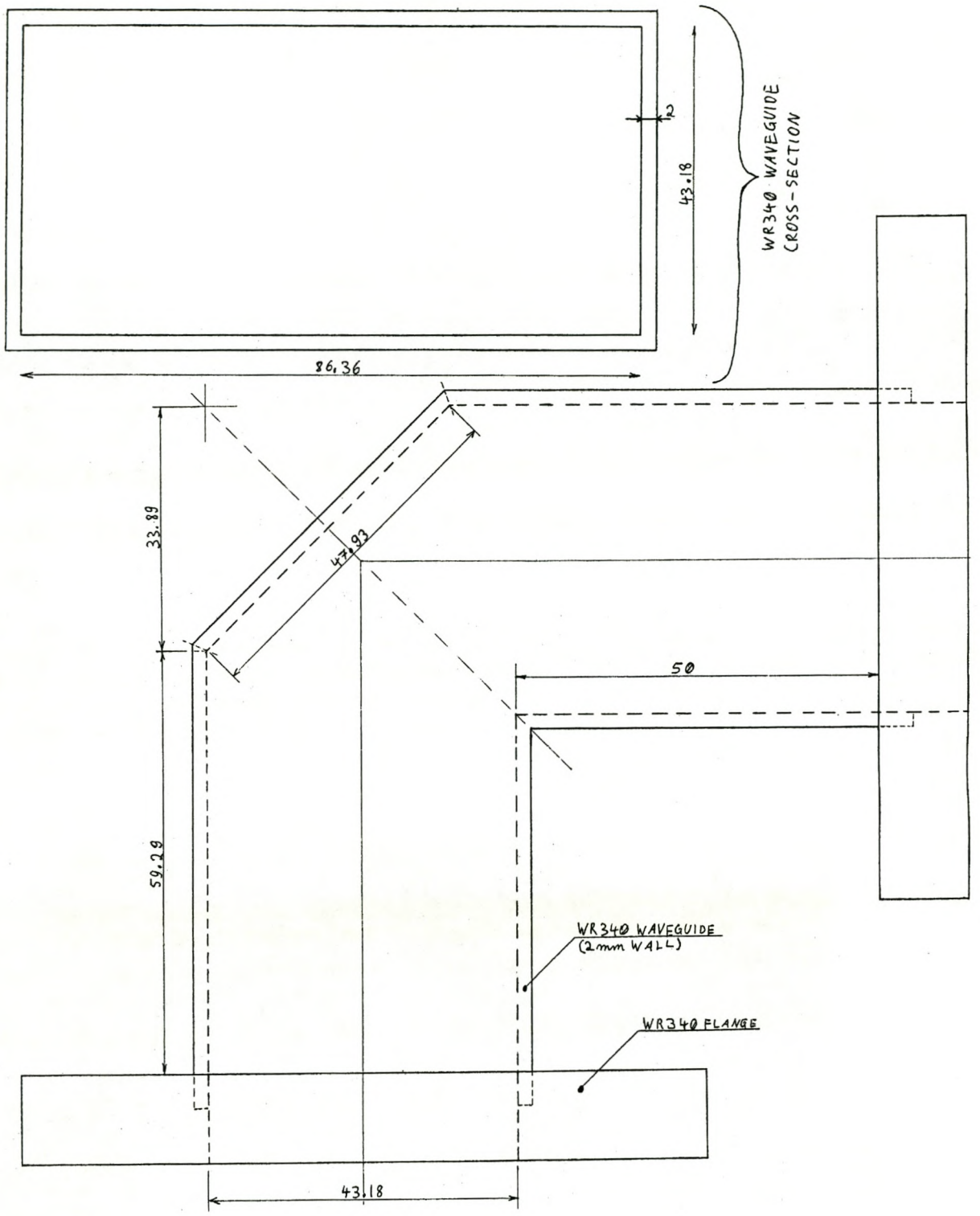

Figure 89: Dimensions of E-plane bend.

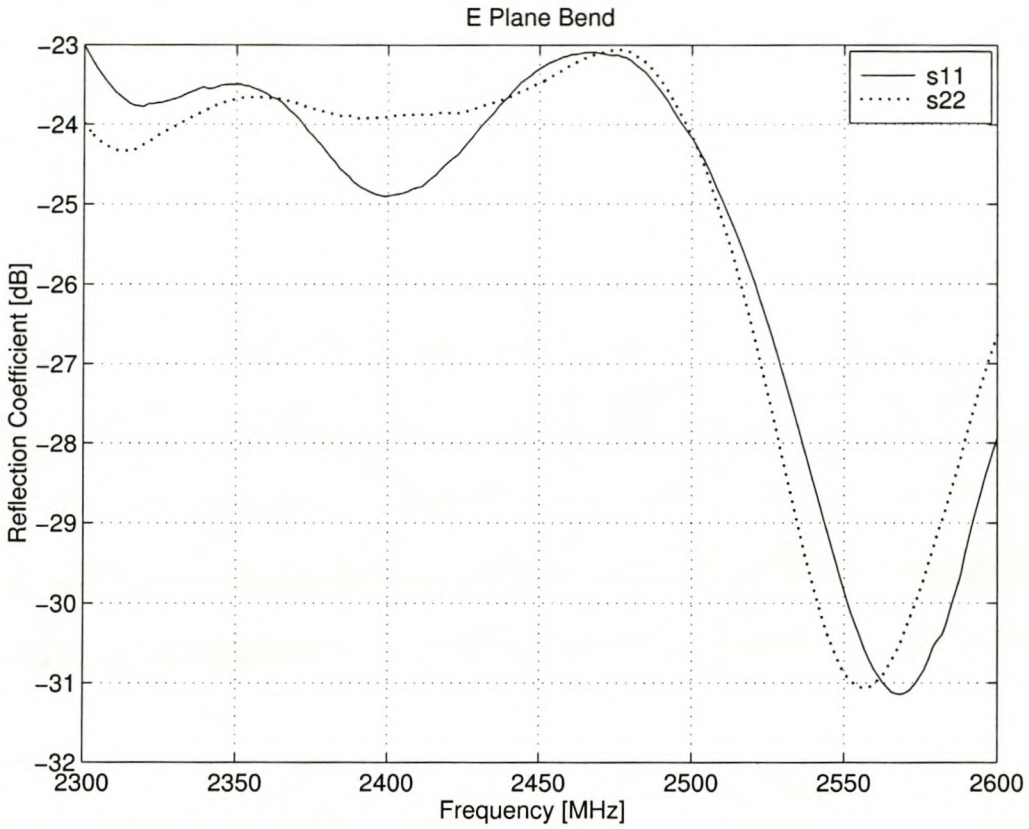

Figure 90: Reflection coefficient of E-plane bend.

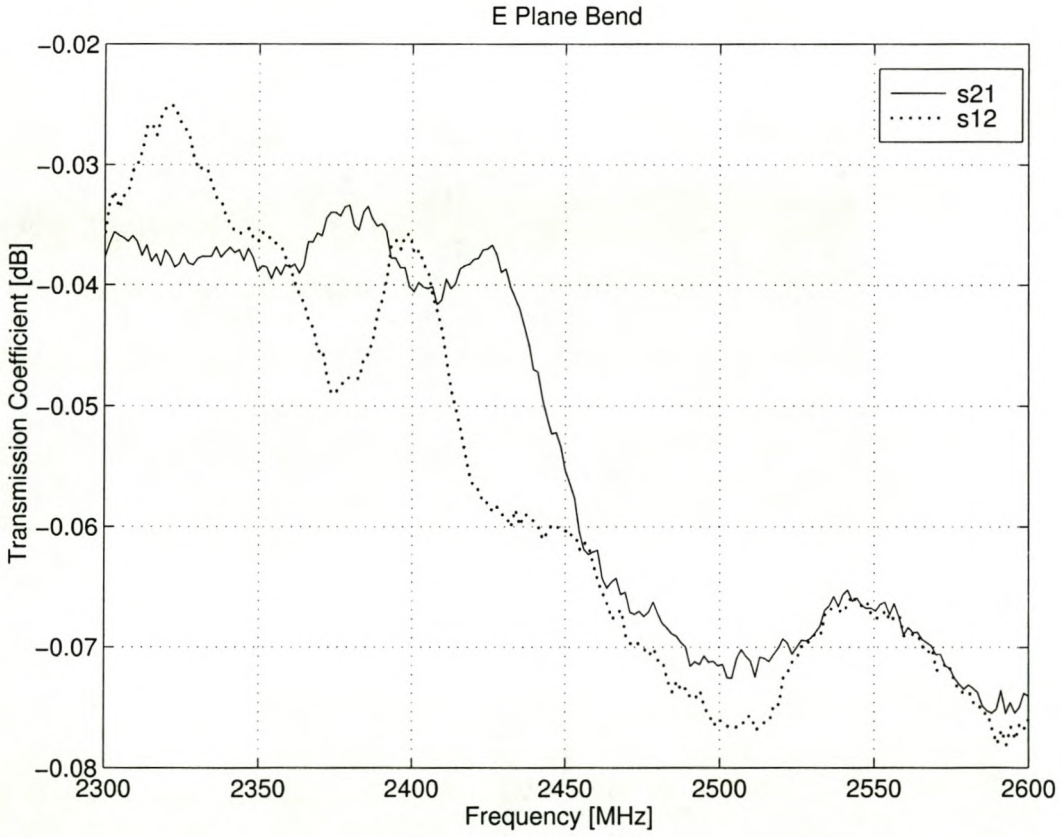

Figure 91: Transmission coefficient of E-plane bend.

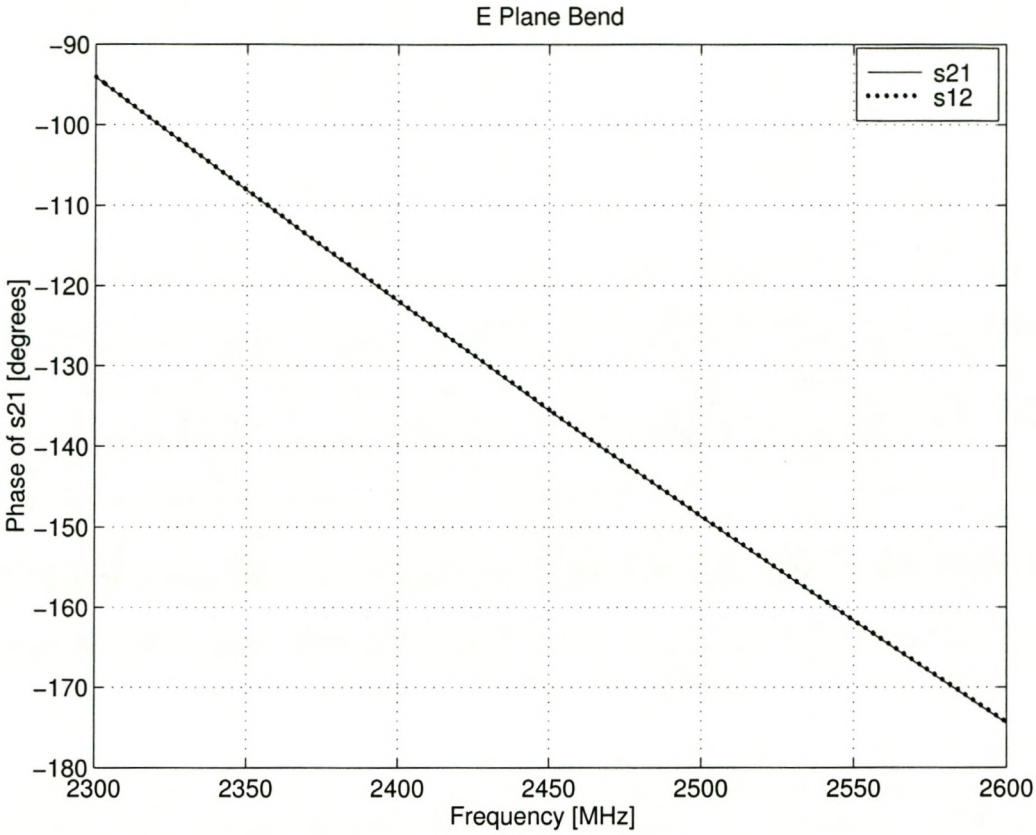

Figure 92: Phase of transmission coefficient of E-plane bend.

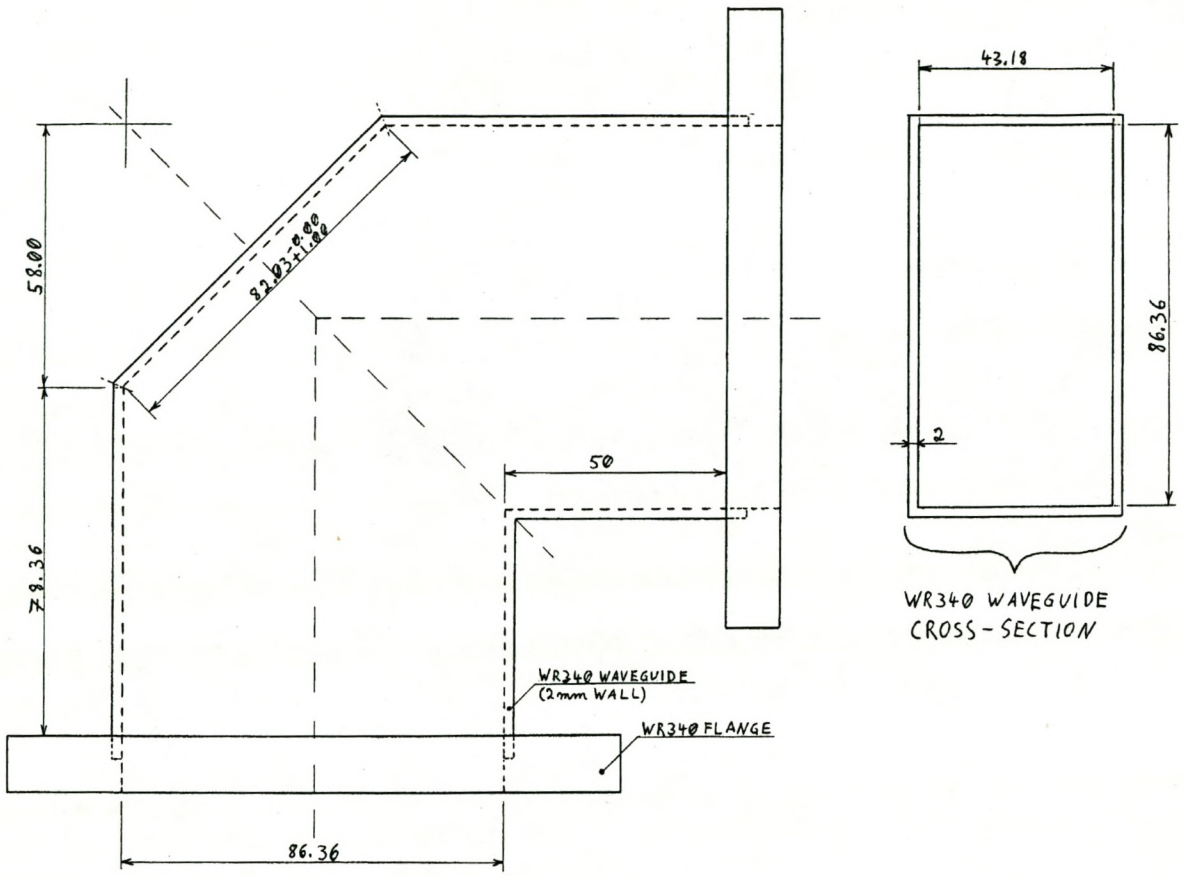

Figure 93: Dimensions of H-plane bend.

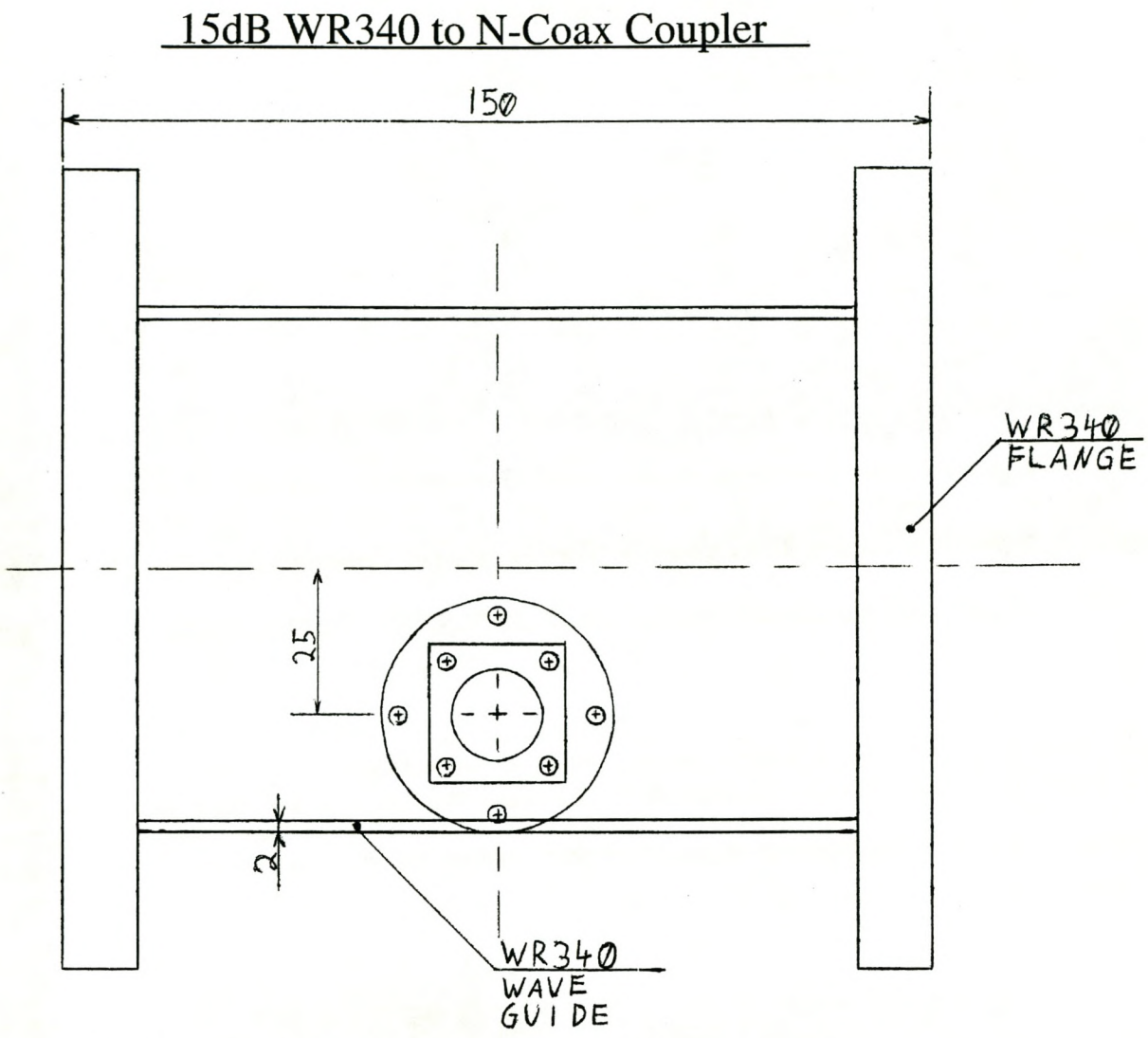

Figure 94: Dimensions 15dB coupler (Drawing 1 of 2).

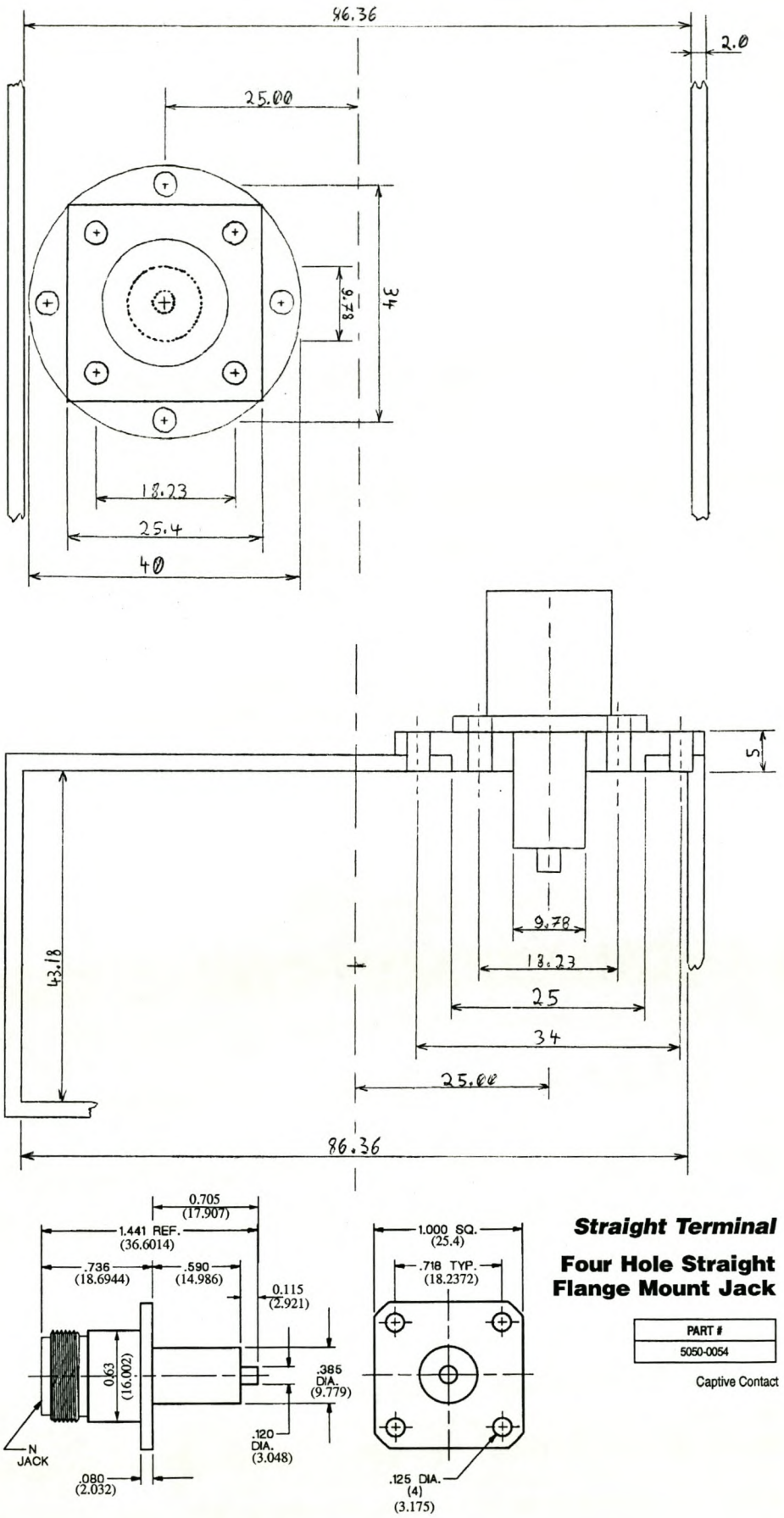

Figure 95: Dimensions 15dB coupler (Drawing 2 of 2).

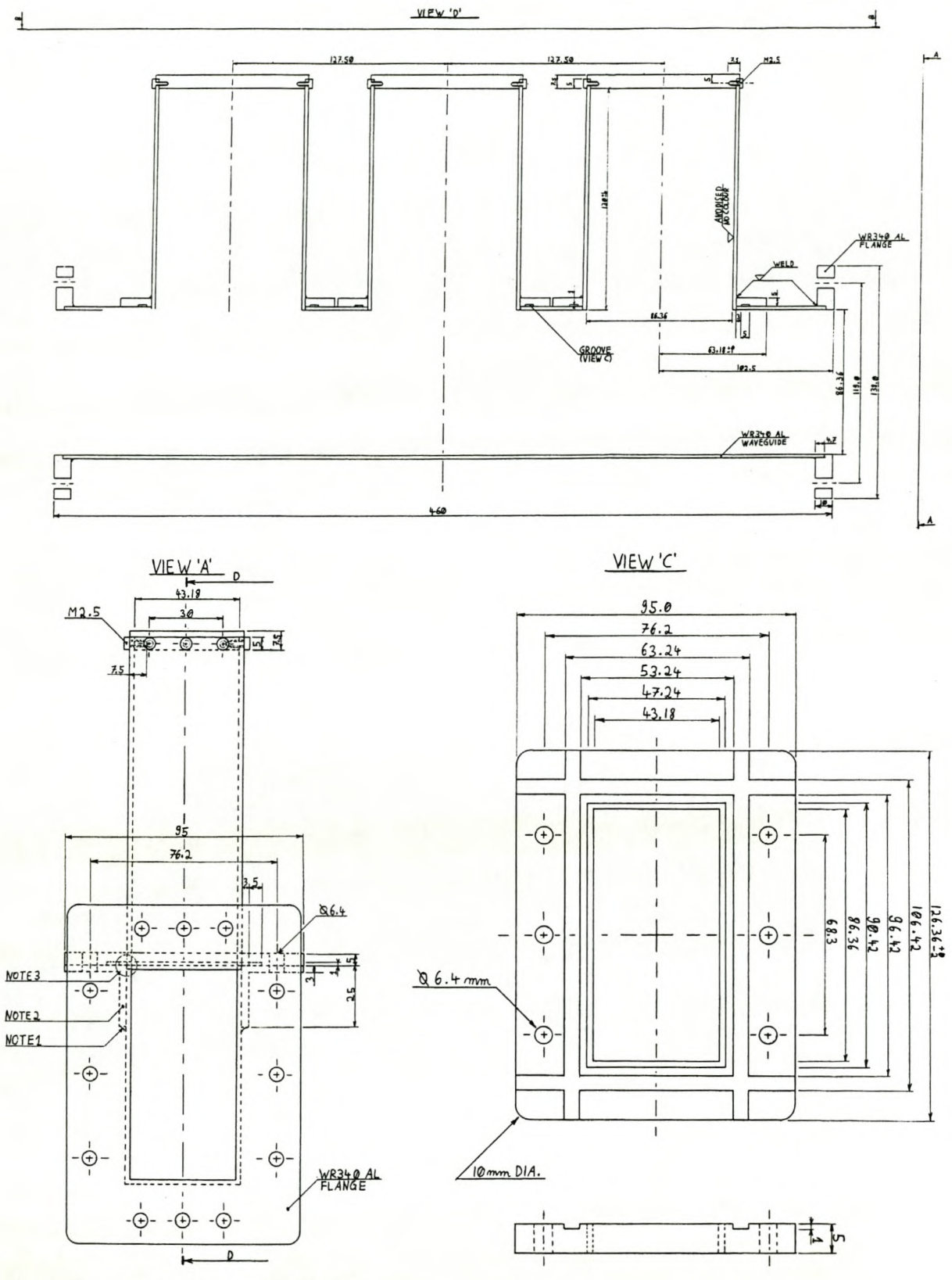

Figure 96: Dimensions 3 stub tuner.

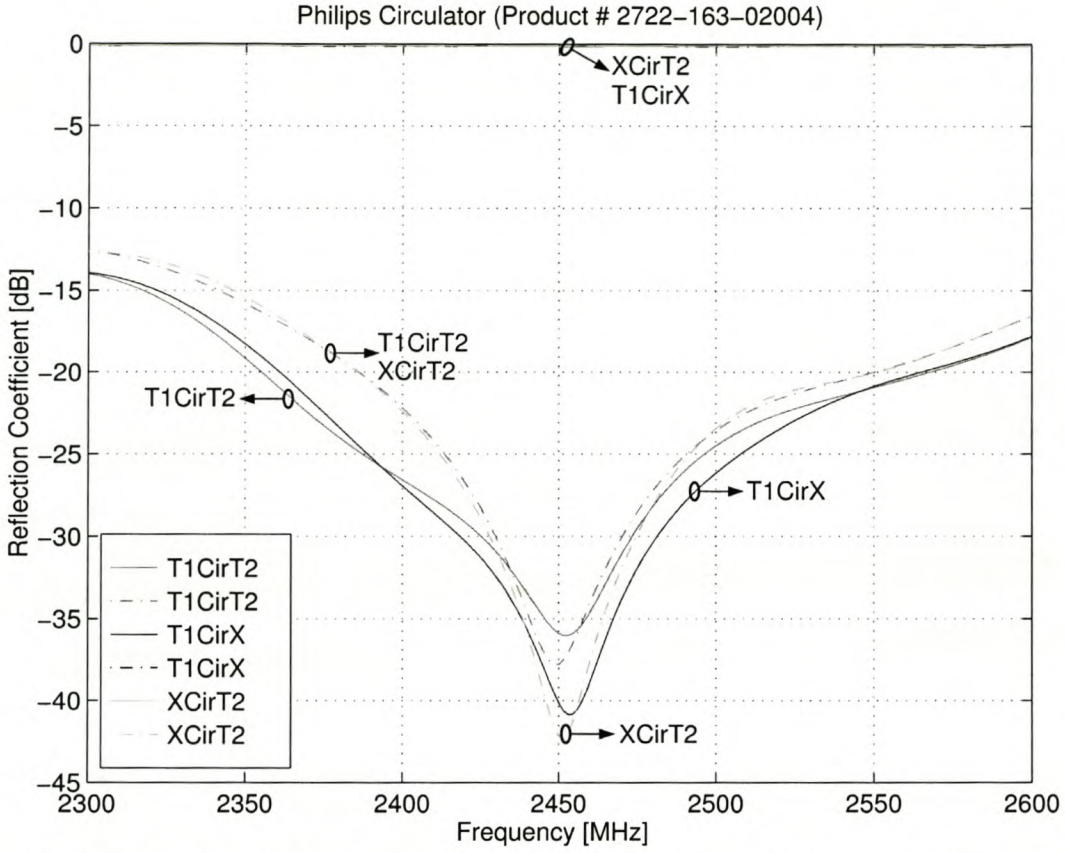

Figure 97: Reflection coefficient of Philips circulator (PN: 2722-163-02004) in dB.

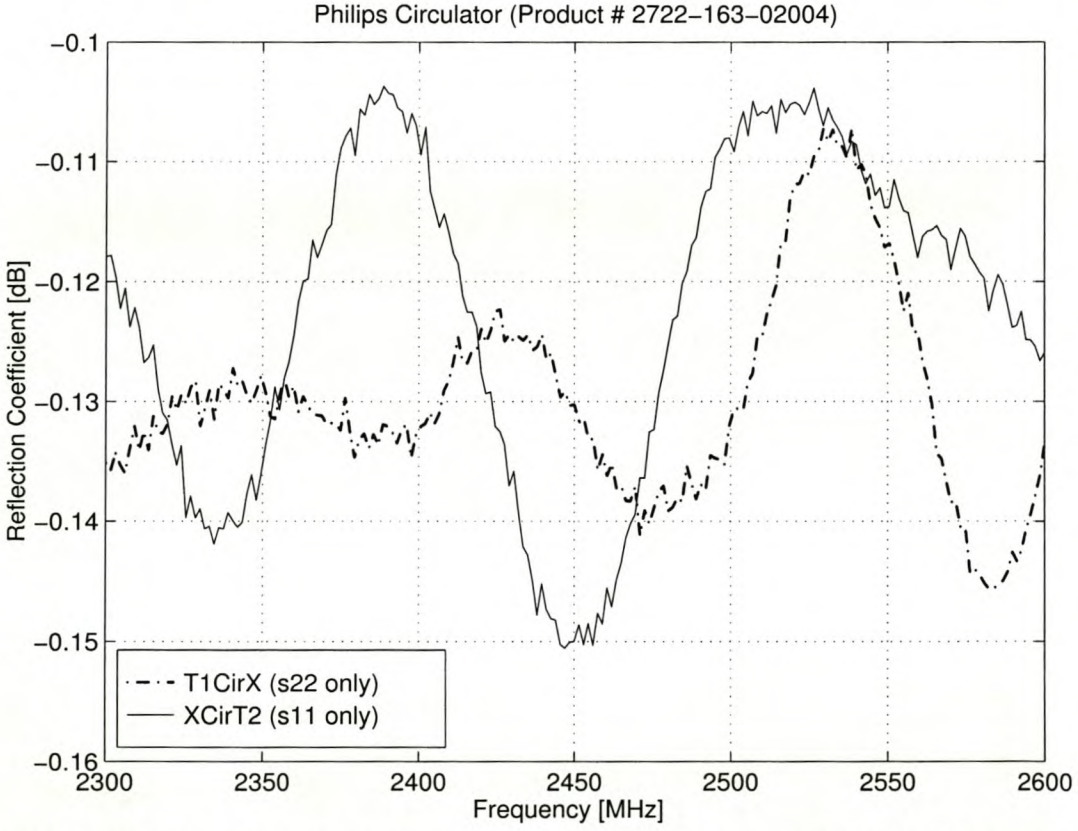

Figure 98: Reflection coefficient of probing port on Philips circulator (PN: 2722-163-02004).

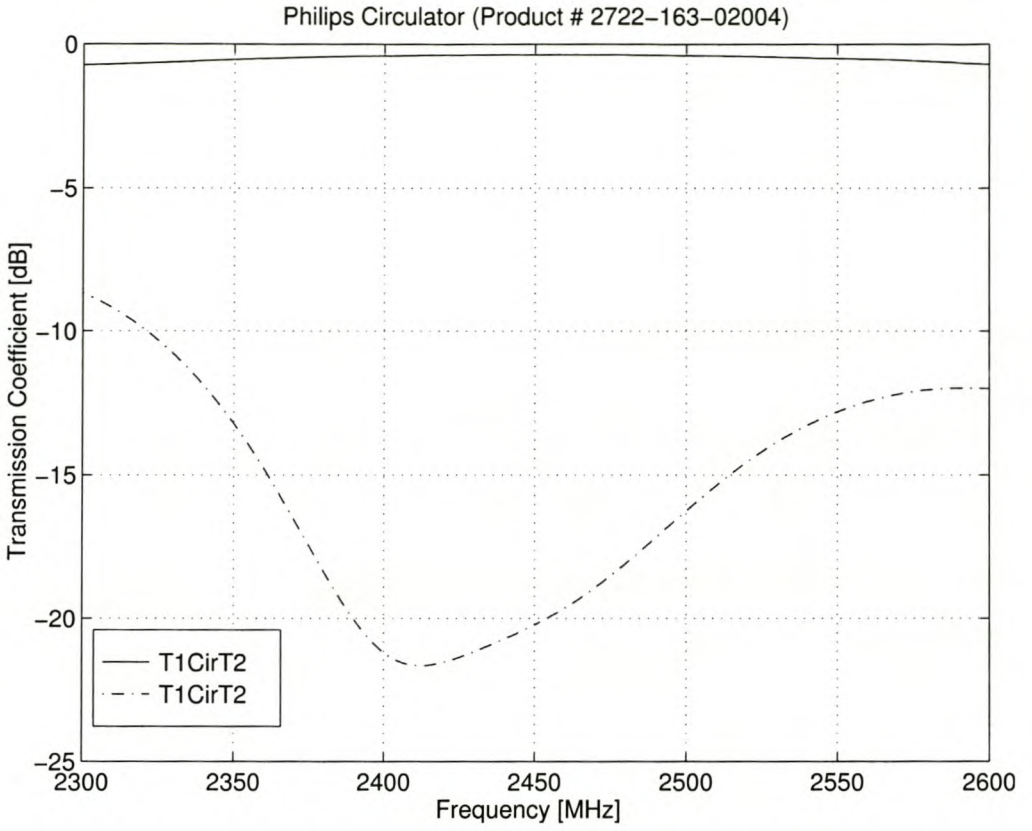

Figure 99: Transmission coefficient of Philips circulator (PN: 2722-163-02004) in dB.

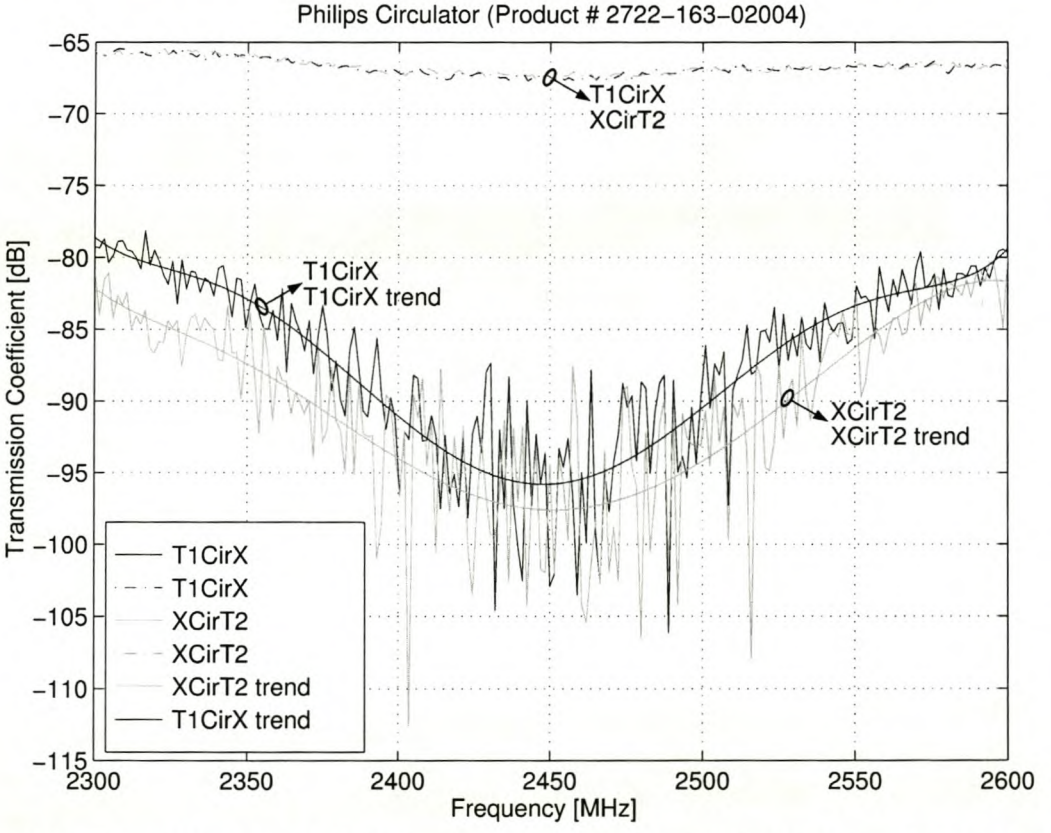

Figure 100: Transmission coefficient of probing port to main ports on Philips circulator (PN: 2722-163-02004) in dB.